Advanced experimental methods for the characterization of welded structures

Thesis

The Open University

Faculty of Mathematics, Computing and Technology

Department of Design, Development, Environment and Materials

ADVANCED EXPERIMENTAL METHODS FOR THE CHARACTERIZATION OF WELDED STRUCTURES

by

Mehmet Emin KARTAL

September 2008

A THESIS SUMMITTED TO THE DEPARTMENT OF MATERIALS ENGINEERING OF THE OPEN UNIVERSITY FOR THE DEGREE OF DOCTOR OF PHILOSOPHY

Submission date: 5 Sept 2008
Date of award: 23 Dec 2008

ABSTRACT

Welding is one of the most prevalent techniques for mechanical fastening of metals. Recent developments in welding technology have led to welding techniques being more readily employed in safety-critical engineering structures. Since the existence of residual stresses and material property variation around welds affects the mechanical performance and thereby structural integrity, it is essential to improve our knowledge in understanding and modelling the mechanical response of the welded structures. The present work focuses on mechanical characterizations of such structures. This work can be broadly classified into two parts; the first part investigates the residual stress distribution in welded specimens of different metals and the second part presents investigations of mechanical properties in welded specimen using full-field optical techniques.

A newly invented destructive technique for residual stress measurement, the contour method, was used for the investigations of the residual stress in welded joints in this study. The principle of the contour method is based on a variation of Bueckner's superposition theory. By means of a single straight cut, the 2D residual stress component normal to the region of interest can be determined. In this work, first the numerical simulations of the contour method using two and three dimensional bodies have been demonstrated. The contour method was then applied to one-pass and three-pass groove weld specimens and the results obtained from the contour method were compared to those obtained by the neutron diffraction strain measurement technique.

The capability of the contour method to measure multiple residual stress components was also investigated in this project. A recent development of the contour method of stress measurement, the multi-axial contour method, permits measurement of the 3D residual stress distribution in a body, based on the assumption that the residual stresses are due to an inelastic misfit strain (eigenstrain) that does not change when a sample containing residual stresses is sectioned. The eigenstrain is derived from measured displacements due to residual stress relaxation when the specimen is sectioned. By carrying out multiple cuts, the full residual stress tensor in a continuously processed body can then be determined. In this study, finite element simulations of the technique were carried out to verify the method numerically. The method was then used to determine the residual stresses in a VPPA-welded sample, and the results were validated by neutron diffraction measurements.

As part of the characterization of the welded structures, a study was undertaken to develop a method of extracting local mechanical properties from weld metal by strain mapping using the digital image correlation (DIC) technique. The feasibility of determining local stress-strain behaviour in the weld zone of a 316H stainless steel pipe with a girth weld was investigated by tensile tests on miniature and standard tensile test specimens. In addition, electron speckle pattern interferometry (ESPI) was utilized to obtain the full-field strain maps of a standard tensile specimen during loading and compared to those obtained in the same specimen by digital image correlation in order to verify the DIC measurements.

ACKNOWLEDGEMENT

I would like to express sincere appreciation my supervisors Dr. Salih Gungor, Prof. Mike Fitzpatrick and Prof. Lyndon Edwards. Without their constant support, guidance and encouragement this work would not have finished.

I am especially indebted to The Open University for its financial support to carry out this project.

I also express my deepest gratitude to Dr. David Liljedahl, who is a great real scientist, for supplying useful discussions which have been helpful during the course of this study. I wish to thanks Dr. Mark Turski for stimulating questions and discussions.

My greatest debt is to Peter Ledgard and Stan Hiller for their help in specimen preparation and metallography.

I wish to acknowledge my colleges Dr. Moshiur Rahman, Dr. Brahim Nadri, Dr. Joao Gomes, Dr. Supriyo Ganguly, Dr. Sumit Pratihar, Dr, Mulyadi, Olivier Zanellato, David Sefton, and other fresh students, members and staffs in Materials Engineering Department for their friendship and support which made my three years stay worthwhile and memorable.

Finally, I would like to express my appreciation to my wife and my family for their support and encouragement.

Mehmet Emin KARTAL
December 2008

AUTHOR'S DECLARATION

This thesis is submitted for the degree of Doctor of Philosophy of The Open University, United Kingdom. The work described in this thesis was performed in the Department of Materials Engineering, Faculty of technology, between October 2004 and December 2008, under the supervision of Dr. Salih Gungor, Professor Michael Edward Fitzpatrick and Professor Lyndon Edwards.

It is entirely the work of the author except where clearly referenced. None of this work has been submitted for a degree or other qualification at this or any other university. Some of the results of this work have been published in academic journals and conference proceedings as listed below:

1 Kartal M.E., Liljedahl C.D.M., Gungor S., Edwards L. and Fitzpatrick M.E. (2008). Determination of the Profile of the Complete Residual Stress Tensor in a VPPA Weld Using the Multi-Axial Contour Method. Acta Materialia, vol. 56, pp. 4417-4428.

2 Kartal M., Molak R., Turski M., Gungor S., Fitzpatrick M.E. and Edwards L. (2007). Determination of Weld Metal Mechanical Properties Utilising Novel Tensile Testing Methods. Applied Mechanics and Materials, vol. 7-8. pp. 127-132.

3 Molak R., Kartal M., Kalinowski A., Pakiela Z., Manaj W., Turski M., Hiller S., Gungor S., Edwards L. and Kurzydlowski K.J. (2007). Use of micro tensile test samples in determining the remnant life of pressure vessel steels. Applied Mechanics and Materials, vol. 7-8, pp. 187-194.

4 Kartal M., Turski M., Johnson G., Fitzpatrick M.E., Gungor S., Withers P.J. and Edwards L. (2006). Residual stress measurements in single and multi-pass groove weld specimens using neutron diffraction and the contour method. Materials Science Forum, vol. 524-525, pp. 671-676.

Mehmet Emin KARTAL
December 2008

TABLE OF CONTENTS

NOMENCLATURE

Symbol	Description
Roman	
2D	Two dimensional
3D	Three dimensional
A	Unknown coefficient of the Legendre polynomials of the first kind; Proportional limit; Current cross sectional area
AA	Aluminium alloy
$\overline{A}$, $\overline{B}$	Calibration constants
A_0	Original cross sectional area
a	Slot depth
B	Unknown coefficient of the Legendre polynomials of the second kind; A sub-region size; Yield point
C	Compliance matrix; Correlated coefficient; Stiffness tensor
CAE	Computer-Aided-Engineering
CCD	Charge coupled device
CMM	Coordinate Measurement Machine
CNC	Computer numerically controlled
C_{ijkl}	The anisotropic elastic tensor
C_y	Characteristic material parameter
c_1, c_2, c_3, c_4	constants for determination of the grey level value
curl	Curl of a vector field
DIC	Digital Image Correlation
div	Divergence of a vector field
ds	Displacement vector
dW	Total work increment
dW^e	Elastic work increment
dW^p	Plastic work increment
dx, dy, dz	Dimensions of an infinitesimal cubic element
E	Modulus of elasticity; Eulerian finite strain tensor
EDM	Electro-discharge wire machining
ESPI	Electron speckle pattern interferometry

e	Random error
$d\lambda$	Proportionality factor
F	Applied load
FEM	Finite element method
FFT	Fast Fourier transform
F_i	Body forces
f	Undeformed grey level value distribution; Loading function
f_d	Deformed grey level value distribution
g	The plastic potential
HAZ	Heat affected zone
h	General function of stress and strain flow
K	Acousto-elastic constant
k	Experimental constant
L	Length; Current gauge length; Lagrangian finite strain tensor
L_0	Original gauge length
MMA	Manual metal arc
m, n	Integer numbers
N	Order of the Tensor
n	Unit normal vector
P	Legendre polynomials of the first kind
Parent1	The position of the micro specimen extracted from the region 1
Parent2	The position of the micro specimen extracted from the region 2
Parent3	The position of the micro specimen extracted from the region 3
Q	Legendre polynomials of the second kind
QM	Quadratic mean suquare
r	Number of the points measured on the cur surface
S	Bivariate polynomials; A sub-region; Compliance tensor
SIF	Stress-intensity factor
s_{ij}	Deviatoric stress component
T	Temperature; Traction
TIG	Tungsten inert gas
T_x, T_y	Surface traction in the x and y directions respectively
t	Thickness
UTS	Ultimate tensile strength

u	Displacement
u_f	Fit displacement
u_m	Measured displacement
u_{normal}	Displacement vector caused by the release of the normal stress component
u_{shear}	Displacement vector caused by the release of the shear stress component
u_x, u_y	Displacement components in the x and y directions respectively
V	Volume of a specimen
v	Altering tensor
W^p	Total plastic work
w	Width
XYZ	Original Cartesian coordinate system
$X^*Y^*Z^*$	Deformed Cartesian coordinate system
x, y, z	Horizontal, vertical and normal axes
x_0	A reference point
x'	A nearby point after deformation
y_0	A reference point
y'	A nearby point after deformation

Greek

α	Coefficient of thermal expansion; Angle
β	Angle
∂	Partial differentiation symbol
ε	Strain
ε^*	Eigenstrain
ε^e	Elastic strain
ε^p_{EQ}	Equivalent plastic strain
$\varepsilon^p{}_{\text{true}}$	True plastic strain
φ	Gradient of a scalar field
Δ	Difference
ΔT	Temperature difference
$\Delta\theta$	Change in angle
δ	Kronecker's delta function: $\delta_{ij} = \{1, \text{ for } i = j \ ; \ 0, \text{ for } i \neq j)$

δL	Elongation in the gauge length
Φ	Diameter
γ	Magnitude of correlation peak
∇	Vector operator
λ	Wavelength
θ	Angle
ν	Poisson ratio
σ	Stress; Speckle size
σ_{EQ}	Equivalent stress
σ_T	True stress
σ_y	Yield stress
τ	Shear stress component

SUPERSCRIPT

e	Elastic component
left	Left part
p	Plastic component
right	Right part

Subscript

0	Reference state; initial
1, 2, 3	Principal directions
EQ	Equivalent
f	Fit
i	Initial
i,j,k,l,s,t	Matrix index
max	Maximum
min	Minimum
normal	Normal components
shear	Shear components
T	True
y	Yield stress

CHAPTER 1

INTRODUCTION

Residual stresses are those stresses that can exist within a material in the absence of any externally applied loads or self load. They can be introduced into the material by virtually all manufacturing processes that cause thermal or compositional gradients or that involve plastic deformation. Thus, they can be produced by forming, joining, machining, heat treatment, abrasion and many other relatively simple processes. The importance of residual stresses in the structural integrity of materials and components is due to the fact that they can have the same effects on a material as stresses generated by applied loads. They can add to an externally applied load to cause yield, for example, even though the external load on its own may not be high enough to do so. As they can cause premature failure if they are not accounted for, it is imperative that their magnitude and distribution within materials are known in safety-critical structures.

Although numerical methods are now commonly employed to model residual stress generation, experimental measurements are often required to validate the predictions. This is especially true when the material in question has gone through a complicated fabrication process, such as welding. The measurement methods can be classified into two categories. Destructive techniques are based on the principle that

the strain measured in a material as a result of sectioning, or removing, part of the material is directly related to the residual stresses in the material before the cut is made. Examples include hole drilling, layer removal, compliance and contour methods. Non-destructive methods rely on the measurement of the change in certain physical properties of the material, such as lattice spacings or magnetic properties, due to the residual stresses. Diffraction methods, which use X-rays or neutrons, are currently amongst the most popular measurement techniques, though they do have some limitations. For example, although neutron diffraction is non-destructive and provides multi-axial stress components, it is time consuming and sensitive to microstructural changes.

Many manufacturing processes, such as welding do not only generate residual stresses but also cause changes in the microstructure. These changes include local variations in size, shape and crystallographic orientations of grains, and size and distribution of precipitates, which have strong influence on mechanical properties and global performance of the material. It is therefore essential to determine the mechanical behaviour of material at the local level. These local variations in properties are usually very steep and their measurement therefore requires techniques with high special resolution. Optical techniques for strain measurements, such as speckle interferometry, moiré interferometry and digital image correlation, are well suited for this purpose. Once the local stress strain curves are obtained, the global performance of a welded structure can then be determined by successfully implementing the constitutive stress-strain response in the weld region, together with the residual stress information, into numerical modelling codes.

One of the aims of this work was to measure residual stresses in welded materials. For this purpose, the newly invented contour method, which allows a map of 2D residual stress component normal to a cut surface to be determined, is used as a measurement tool. In addition, potential improvements to the contour method have been investigated. This involved the use of the eigenstrain concept to calculate the full original stress tensor on the first cut of the specimens. Furthermore, the digital image correlation technique is utilized to investigate the mechanical properties of cross weld samples.

The outline of this work is briefly presented below

Chapter 1 includes the motivation of this project work done in this thesis.

Chapter 2 introduces the major concepts that have been extensively used in this project. They are the theories of elasticity and plasticity, and the subject of residual stresses along with a brief description of the different techniques used to measure them. The welding technology together with a brief description of the different welding methods is also given in this chapter.

In chapter 3, some popular optical techniques are briefly described. Then, the principle of the digital image correlation method (DIC) is given in detail. Finally, the experimental validation of the DIC with the help of strain gauge measurement on a tensile specimen made of 2024–T351 aluminium alloy is presented.

Chapter 4 gives the details of the study where the digital image correlation method was used to investigate the variation of mechanical properties in a stainless steel pipe girth weld manufactured by multi-pass arc welding, by performing tensile tests on micro mechanical test specimens cut out from various positions in the welded pipe. The results obtained from these micro-specimens were compared with the standard cross-weld tensile specimen. In addition, electron spackle pattern interferometry (ESPI) was used to obtain the full-field strain map of a standard tensile specimen together with digital image correlation in order to see the agreement level between two independent strain measurement methods.

In chapter 5, the theoretical background to the contour method is given. Then, the fundamental steps of the contour method and their experimental procedures are explained. Next, numerical validations of this technique on 2D and 3D bodies are demonstrated. Then the results of the measurement using contour method on 1-pass and 3-pass groove weld specimens are given. Finally, these results are compared to those obtained using neutron diffraction technique.

Chapter 6 focuses on the numerical exploration of the multi-axial contour method. The definition of eigenstrain and the methodology of the multi-axial contour method are given in detail. Then a numerical validation of the technique for 2D and 3D geometrical specimens is undertaken using finite element simulation.

In chapter 7 an investigation on the capability of the multi-axial contour method using a residually stressed sample is presented. The residual stress in a VPPA

AA2024-T351 weld is investigated and the results obtained by the multi-axial contour method are compared with neutron diffraction results.

Finally, overall conclusions are drawn and future work is given in Chapter 8.

CHAPTER 2

INTRODUCTION TO STRESS ANALYSIS

2.1 Introduction

In this chapter the background knowledge which is specially required for the research work in this dissertation is given. The tensor analysis, the theory of elasticity, along with the description of stress and strain and their relation in the perspective of continuum mechanics are described. Then, an overview of the origin of residual stress, its types and measuring techniques are given in this chapter. Finally, a brief description of weld technology together with popular welding techniques is given.

2.2 Tensor Analysis

Tensors, independent of the choice of any coordinate system, enable the expression of physical quantities in array form, such as stress components at a point, which it is not possible to show as a vector field. Tensors are described by their order. The number of components in a tensor is determined by 3^N, where N is the order (or rank) of the tensor.

Some physical quantities which possess magnitude only and are independent of any reference coordinates (direction) are known as scalars and have one component

(tensor of order zero). Quantities having magnitude and direction are called vectors. Vectors are tensors of order one and have three components in the tensor. There are higher order tensors in mathematical concepts such as the stress-strain field at a point, altering (permutation) tensor, and stiffness-compliance matrix illustrated as follow.

Scalars: Tensor of order zero, 1 component

Vectors: Tensor of order one, u_i: i=1:3, 3 components

Stress-Strain: Tensors of order two $\sigma_{ij}, \varepsilon_{ij}$, 9 components

Alternating Tensor: Tensors of order three v_{ijk}, 27 components

Stiffness-Compliance: Tensors of order four C_{ijkl}, S_{ijkl}, 81 components

2.2.1 Indicial Notation

Indicial notation is widely utilized to represent general equations in single expressions. Consider an arbitrary vector $\vec{u} = (u_x, u_y, u_z)$ whose components are indexed by the coordinate labels x, y and z. This vector can also be expressed as $\vec{u} = (u_1, u_2, u_3)$ or just u_i (i=1, 2, 3). The range of index i is a set of integer values 1 to 3. When the index i is not repeatable in a term, it is called a free index. When an index appears twice in a term, it is comprehended to sum over the range of index and called a dummy index.

There are two important tensor functions used in indicial notation: Kronecker's delta function and the permutation symbol. Kronecker's δ function is defined as

$$\delta_{ij} = \begin{cases} 1 & if\ i = j \\ 0 & if\ i \neq j \end{cases} \tag{2.1}$$

Eq. (2.1) clearly shows that the value is non-zero only if $i=j$. In other words, the Kronecker's function gives an identity matrix. The other useful function in continuum mechanics is the permutation symbol. This third order tensor is defined by

$$v_{ij} = \begin{cases} +1 & if\ i = j \quad \text{if } i,j,k \text{ are an even permutation of 1,2,3} \\ -1 & if\ i \neq j \quad \text{if } i,j,k \text{ are an odd permutation of 1,2,3} \\ 0 & if\ i = j \quad \text{if } i,j,k \text{ are not a permutation of 1,2,3} \end{cases} \tag{2.2}$$

A Schematic showing the even and odd cyclic permutations is given in Figure 2.1. In the case of even permutation, *ijk* is one of the options 123, 231 or 312 that swap indices of 123. For an odd permutation, *ijk* is indexed as 132, 321 or 213. If any two values of indices get the same number such as 112 then the value of the permutation symbol is zero.

There is a relationship between Kronecker's delta and the permutation symbol [1], specified by

$$v_{ijk} v_{ist} = \delta_{js}\delta_{kt} - \delta_{jt}\delta_{ks}\ , \tag{2.3}$$

where *k, l, s* and *t* are the indices.

2.2.2 Vector operations

In most cases, perpendicular axes are typically defined by a coordinate system and any vector can be articulated by base vectors. If we consider the coordinate system (Figure 2.2) with its operator, one can be written as

$$\vec{u} = u_1\vec{i}_1 + u_2\vec{i}_2 + u_3\vec{i}_3,$$
$$\vec{v} = v_1\vec{i}_1 + v_2\vec{i}_2 + v_3\vec{i}_3, \tag{2.4}$$

in which $\vec{u}$ and $\vec{v}$ are vectors and $\vec{i}_1$, $\vec{i}_2$ and $\vec{i}_3$ are unit base vectors. The scalar or dot product of the two vectors in Eq. (2.4) is given by

$$\vec{u}\cdot\vec{v} = \left(u_1\vec{i}_1 + u_2\vec{i}_2 + u_3\vec{i}_3\right)\cdot\left(v_1\vec{i}_1 + v_2\vec{i}_2 + v_3\vec{i}_3\right) = u_i v_i = u_1v_1 + u_2v_2 + u_3v_3, \tag{2.5}$$

or the dot product with the Kronecker delta can be expressed by

$$\vec{u}\cdot\vec{v} = \sum_{i=1}^{3}\sum_{j=1}^{3} u_i v_i \delta_{ij}. \tag{2.6}$$

The vector or cross product of the same two vectors is given by

$$\vec{u}\times\vec{v} = \begin{vmatrix} \vec{i}_1 & \vec{i}_2 & \vec{i}_3 \\ u_1 & u_2 & u_3 \\ v_1 & v_2 & v_3 \end{vmatrix} = (u_2v_3 - u_3v_2)\vec{i}_1 + (u_3v_1 - u_1v_3)\vec{i}_2 + (u_1v_2 - u_2v_1)\vec{i}_3 \tag{2.7}$$

using the permutation symbol, the cross product can be written in indicial notation by

$$\vec{u}\times\vec{v} = v_{ijk}u_j v_k. \tag{2.8}$$

The differentiation of tensor components with respect to the coordinates is known as the vector operator ∇ and expressed by

$$\nabla = \vec{i}_1\frac{\partial}{\partial x_1} + \vec{i}_2\frac{\partial}{\partial x_2} + \vec{i}_3\frac{\partial}{\partial x_3}, \tag{2.9}$$

Eq. (2.9) is written in the conventional form

$$\nabla = i_j\frac{\partial}{\partial x_j}. \tag{2.10}$$

There are several important differentiation operators seen in mathematical concepts [2] and given by

- Gradient of a scalar field $\varphi(x_1, x_2, x_3)$

$$\vec{\nabla}\varphi = \frac{\partial\varphi}{\partial x_1}\vec{i}_1 + \frac{\partial\varphi}{\partial x_2}\vec{i}_2 + \frac{\partial\varphi}{\partial x_3}\vec{i}_3 = \varphi_{,i}\,. \tag{2.11}$$

- Divergence of a vector field $\vec{u}(x_1, x_2, x_3)$

$$div\vec{u} = \vec{\nabla}\cdot\vec{u} = \frac{\partial u_1}{\partial x_1} + \frac{\partial u_2}{\partial x_2} + \frac{\partial u_3}{\partial x_3} = u_{i,i}\,. \tag{2.12}$$

- Curl of a vector field

$$curl\vec{u} = \vec{\nabla}\times\vec{u} = \begin{vmatrix} \vec{i}_1 & \vec{i}_2 & \vec{i}_3 \\ \dfrac{\partial}{\partial x_1} & \dfrac{\partial}{\partial x_2} & \dfrac{\partial}{\partial x_3} \\ u_1 & u_2 & u_3 \end{vmatrix} = v_{ijk}u_{k,j}\,. \tag{2.13}$$

- Laplace operator for gradient of a scalar field $\varphi(x_1, x_2, x_3)$

$$\nabla^2\varphi = (\nabla\cdot\nabla\cdot\varphi) = \frac{\partial^2\varphi}{\partial x_1^{\,2}} + \frac{\partial^2\varphi}{\partial x_2^{\,2}} + \frac{\partial^2\varphi}{\partial x_3^{\,2}} = \varphi_{,ii}\,, \tag{2.14}$$

where a comma denotes partial differentiation with respect to the variable x_i.

2.3 Elasticity and Plasticity Theories of Solids

The behaviour of materials under load depends on the extent of deformation. The theory of elasticity is concerned with mechanical behaviour of materials when the external forces applied do not exceed a certain limit, the so-called yield stress. The theory of plasticity deals with the mechanical response of materials under loads which are above the yield limit. In this section, the theories of elasticity and plasticity will be given.

2.3.1 The Stress-Strain Curve

Solid bodies which are subjected to a small load deform. On removal of the applied load, solids return to the undeformed configuration, and this is known as elastic deformation. Such deformation depends only on a stress magnitude and not loading history. When the load exceeds a certain threshold value known as the elastic limit, or yield stress (σ_y), permanent dimensional changes begin and this is known as plastic deformation. For a uniaxial tension test, experiments show a typical stress-strain relationship as given in Figure 2.3. In this plot, σ characterizes engineering stress obtained as

$$\sigma = \frac{F}{A_0}, \tag{2.15}$$

in which F is the applied load and A_0 is the original cross sectional area normal to the tensile test direction, and ε_0 is engineering strain defined as

$$\varepsilon_0 = \frac{L - L_0}{L_0}, \tag{2.16}$$

where L_0 is the original gauge length of the specimen and L is the current gauge length of the specimen.

In Figure 2.3, the stress-strain curve is separated by the yield point B into two different ranges which are the elastic range and the plastic range. In the elastic range, with an increase in load, the stress-strain-state point moves upward along the curve and with a decrease in load the point moves downward along the same path. Until the proportional limit A, there is a constant ratio between stress and strain, which is described by the so-called Hooke's Law. Between the proportional limit A

and elastic limit B, the material is elastic but the stress-strain relationship is not constant any longer.

In the plastic range, however, for a decrease in load from a point such as C, the point moves downward along the path CD, essentially parallel with the linear elastic portion of the curve. At D, the stress becomes zero and the permanent plastic strain ε^p remains.

The recoverable elastic strain from C is labelled ε^e in Figure 2.3. A reloading from D back to C would follow very closely the path CD. On a return to C, a load increase is required to cause further deformation, a condition referred to as work hardening or strain hardening. It is clear in the plastic range that the stress for a given strain depends on the entire loading history. With further increasing of the load, the stress reaches a maximum value, called the ultimate stress, at point E and the specimen begins to neck. Beyond the ultimate load the material flows and at a point F in the curve of Figure 2.3 the specimen breaks.

During the test, the original dimensions of the specimen change depending on the load. For small deformations, the change in the cross sectional area is negligible. Therefore, the initial cross sectional area is used to calculate engineering stress-strain values and it is chosen as constant in engineering applications. However, the case is different for plastic deformation. The change in cross sectional area is significant. Hence, the use of true stress-strain curves takes this into account [3]. The relationship between true and engineering stresses or strains are determined by the

assumption that the volume of the deformed specimen remains constant during the plastic deformation such that

$$V = A_0 L_0 = AL, \tag{2.17}$$

where V is the volume of specimen and A is the current cross sectional area. The true stress is expressed in terms of engineering stress by

$$\sigma_T = \frac{F}{A} = \frac{F}{A_0}\frac{L}{L_0} = \sigma\frac{L_0 + \delta L}{L_0} = \sigma(1+\varepsilon_0), \tag{2.18}$$

in which δL is the elongation in the gauge length. In a similar manner, the relationship between true strain and engineering strain is given by

$$\varepsilon = \int_{L_0}^{L}\frac{dx}{x} = \ln(L) - \ln(L_0) = \ln\frac{L}{L_0} = \ln\frac{L_0 + \delta L}{L_0} = \ln(1+\varepsilon_0). \tag{2.19}$$

In a tensile test, true stress is greater than engineering stress and true strain is smaller than the engineering strain.

2.3.2 Components of Stress

Consider a deformable body in equilibrium being subjected to external forces as shown in Figure 2.4. Due to these external forces, internal distribution of forces per unit area are produced that balance and react to the external forces acting on the body. The amount of the internal force per unit area is defined by stress. Stress is a tensor of order two hence it has nine components.

Taking an infinitesimal cubic element at any arbitrary point in the body such as the point P, the stress components at that point can be expressed in matrix form

$$\sigma_{ij} = \begin{bmatrix} \sigma_{xx} \sigma_{xy} \sigma_{xz} \\ \sigma_{yx} \sigma_{yy} \sigma_{yz} \\ \sigma_{zx} \sigma_{zy} \sigma_{zz} \end{bmatrix}, \tag{2.20}$$

in Eq. (2.20), the nine quantities are known as the Cartesian components of stress. The first index of each component implies the direction of the normal to the plane and second index indicates stress component acting in that plane. The components perpendicular to the planes are called normal stresses ($\sigma_{xx}, \sigma_{yy}, \sigma_{zz}$) and the components acting in the plane are called shear stresses ($\sigma_{xy}, \sigma_{yx}, \sigma_{xz}, \sigma_{zx}, \sigma_{yz}, \sigma_{zy}$).

2.3.2.1 Equation of Equilibrium

In the simplest way, the equilibrium equations can be obtained by means of an infinitesimal cubic element with dimensions *dx*, *dy* and *dz* as given in Figure 2.5. The stress components acting on the surfaces for both positive and negative directions are denoted in the figure. (The partial differentiation terms on each positive surface are due to the continuity of stresses in a body [1]).

In order to satisfy equilibrium in this infinitesimal parallelepiped, the net force in each direction must be zero. Force components for each surface are calculated by multiplying the area of the side by stress components acting on that surface. For the *X* direction total force is

$$\begin{aligned} &\left(\sigma_{xx} + \frac{\partial \sigma_{xx}}{\partial x} dx\right) dydz - \sigma_{xx} dydz + \left(\sigma_{yx} + \frac{\partial \sigma_{yx}}{\partial y} dy\right) dxdz - \sigma_{yx} dxdz \\ &+ \left(\sigma_{zx} + \frac{\partial \sigma_{zx}}{\partial z} dz\right) dxdy - \sigma_{zx} dxdy + F_x dxdydz = 0. \end{aligned} \tag{2.21}$$

Simplifying Eq. (2.21), we get

$$\frac{\partial \sigma_{xx}}{\partial x}+\frac{\partial \sigma_{yx}}{\partial y}+\frac{\partial \sigma_{zx}}{\partial z}+F_x=0. \tag{2.22}$$

Similarly, the equilibrium equations for the other two directions are found as

$$\frac{\partial \sigma_{xy}}{\partial x}+\frac{\partial \sigma_{yy}}{\partial y}+\frac{\partial \sigma_{zy}}{\partial z}+F_y=0, \tag{2.23}$$

$$\frac{\partial \sigma_{xz}}{\partial x}+\frac{\partial \sigma_{yz}}{\partial y}+\frac{\partial \sigma_{zz}}{\partial z}+F_z=0, \tag{2.24}$$

Where, F_x, F_y and F_z are body forces in *X*, *Y* and *Z* directions respectively. Eqs. (2.22–2.24) can be expressed in notation form as

$$\sigma_{ij,i}+F_j=0. \tag{2.25}$$

In addition, the resultant moment on the cube must be zero to satisfy equilibrium. Taking the moment of the forces about each coordinate axis and simplifying the result [1], one can obtain the relation:

$$\sigma_{ij}=\sigma_{ji}. \tag{2.26}$$

This proves that the stress tensor is symmetric.

2.3.3 Deformation and Strain Tensor

Figure 2.6 demonstrates both the undeformed configuration of a material continuum with coordinate system $OX_1X_2X_3$ and deformed (spatial) configuration of the same continuum with coordinate system $OX_1^*X_2^*X_3^*$. Any arbitrary point such as point *B* moves to B^* after deformation and the vector *u* which links the points *B* and B^* is a known displacement vector and can be expressed as

$$u_i=X_i^*-X_i. \tag{2.27}$$

In Eq. (2.27) the displacement vector u_i can be denoted as a partial differential equation with respect to the initial (undeformed) configuration to get the material displacement gradient as

$$\frac{\partial u_i}{\partial X_j} = \frac{\partial X_i^*}{\partial X_j} - \delta_{ij}, \tag{2.28}$$

or with respect to the deformed configuration to obtain the spatial displacement gradient as

$$\frac{\partial u_i}{\partial X_j^*} = \delta_{ij} - \frac{\partial X_i}{\partial X_j^*}. \tag{2.29}$$

The position in the deformed configuration can be expressed by using undeformed coordinate variables as

$$X_i^* = X_i^*(X_1, X_2, X_3). \tag{2.30}$$

Eq. (2.30) is known as the Lagrangian description [4]. On the other hand, the expression of the location in the undeformed configuration by means of the deformed coordinate system is called the an Eulerian description and written as

$$X_i = X_i(X_1^*, X_2^*, X_3^*). \tag{2.31}$$

Assuming differentially small lines such as $\overline{AB}$ of length dX remain as differentially small lines $\overline{A^*B^*}$ of length dX^* after deformation, the differential distances dX and dX^* are

$$dX_i = \frac{\partial X_i}{\partial X_j^*} dX_j^*, \tag{2.32}$$

$$dX_i^* = \frac{\partial X_i^*}{\partial X_j} dX_j. \tag{2.33}$$

The square of the differential lengths of Eqs. (2.32 – 2.33) are

$$(dX)^2 = \delta_{ij} dX_i dX_j, \tag{2.34}$$

$$(dX^*)^2 = \delta_{ij} dX_i^* dX_j^*, \tag{2.35}$$

or this expressions can be shown in the open form as follows

$$(dX)^2 = \frac{\partial X_k}{\partial X_i^*} \frac{\partial X_k}{\partial X_j^*} dX_i^* dX_j^*, \tag{2.36}$$

$$(dX^*)^2 = \frac{\partial X_k^*}{\partial X_i} \frac{\partial X_k^*}{\partial X_j} dX_i dX_j. \tag{2.37}$$

Using the square of differential lengths (2.34) and (2.37) the difference $(dX^*)^2 - (dX)^2$ for two small line segments are found as

$$(dX^*)^2 - (dX)^2 = 2L_{ij} dX_i dX_j. \tag{2.38}$$

Alternatively, by means of Eqs. (2.35) and (2.36), Eq. (2.38) can be written as

$$(dX^*)^2 - (dX)^2 = 2E_{ij} dX_i^* dX_j^*, \tag{2.39}$$

where L_{ij} and E_{ij} are second order tensors

$$L_{ij} = \frac{1}{2}\left(\frac{\partial X_k^*}{\partial X_i} \frac{\partial X_k^*}{\partial X_j} - \delta_{ij} \right), \tag{2.40}$$

$$E_{ij} = \frac{1}{2}\left(\delta_{ij} - \frac{\partial X_k}{\partial X_i^*} \frac{\partial X_k}{\partial X_j^*} \right), \tag{2.41}$$

and called Lagrangian and Eulerian finite strain tensors respectively. Substituting material displacement gradient (2.28) into Eq. (2.40) and spatial displacement gradient (2.29) into Eq. (2.41), Lagrangian and Eulerian finite strain tensors may be expressed by displacement gradients as

$$L_{ij} = \frac{1}{2}\left(\frac{\partial u_i}{\partial X_j} + \frac{\partial u_j}{\partial X_i} + \frac{\partial u_k}{\partial X_i} \frac{\partial u_k}{\partial X_j} \right), \tag{2.42}$$

$$E_{ij} = \frac{1}{2}\left(\frac{\partial u_i}{\partial X_j^*} + \frac{\partial u_j}{\partial X_i^*} - \frac{\partial u_k}{\partial X_i^*}\frac{\partial u_k}{\partial X_j^*} \right). \tag{2.43}$$

If the displacement gradient terms in the Lagrangian and Eulerian finite strain tensors are small enough compared to the body, then the product terms can be neglected since they are much smaller than the displacement gradient terms. Therefore the Lagrangian and Eulerian finite strain tensors will be nearly equal and expressed by the strain tensor as

$$\varepsilon_{ij} = \frac{1}{2}\left(\frac{\partial u_i}{\partial X_j^*} + \frac{\partial u_j}{\partial X_i^*} \right). \tag{2.44}$$

2.3.4 Generalized Hooke's Law for Anisotropic Bodies

The linear relationship between stress and strain is called the Hooke's Law. Cauchy generalized the Hooke's law for three dimensional elastic bodies, which states that the nine components of stress are linearly related to the nine components of strain. The stress-strain relationship is shown as

$$\sigma_{ij} = C_{ijkl}\,\varepsilon_{kl}, \tag{2.45}$$

$$\varepsilon_{ij} = S_{ijkl}\,\sigma_{kl}. \tag{2.46}$$

Here S_{ijkl} is the compliance tensor and C_{ijkl} is stiffness tensor. The relation between these tensors is

$$C_{ijkl}\,S_{ijkl} = \delta_{im}\delta_{jn}. \tag{2.47}$$

C_{ijkl} and S_{ijkl} have 81 constants. However, due to symmetry of the infinitesimal strain tensors, $i \Leftrightarrow j$ and $l \Leftrightarrow k$, the stiffness and the compliance tensors have only 36 independent constants. In addition, the compliance and stiffness matrices can be

written as contracted notation. For instance, the stress-strain relationship for the stiffness matrix is

$$\sigma_i = C_{ij}\varepsilon_j, \tag{2.48}$$

or in matrix form

$$\begin{bmatrix}\sigma_1\\ \sigma_2\\ \sigma_3\\ \sigma_4\\ \sigma_5\\ \sigma_6\end{bmatrix} = \begin{bmatrix}C_{11} & C_{12} & C_{13} & C_{14} & C_{15} & C_{16}\\ C_{21} & C_{22} & C_{23} & C_{24} & C_{25} & C_{26}\\ C_{31} & C_{32} & C_{33} & C_{34} & C_{35} & C_{36}\\ C_{41} & C_{42} & C_{43} & C_{44} & C_{45} & C_{46}\\ C_{51} & C_{52} & C_{53} & C_{54} & C_{55} & C_{56}\\ C_{61} & C_{62} & C_{63} & C_{64} & C_{65} & C_{66}\end{bmatrix}\begin{bmatrix}\varepsilon_1\\ \varepsilon_2\\ \varepsilon_3\\ \varepsilon_4\\ \varepsilon_5\\ \varepsilon_6\end{bmatrix}. \tag{2.49}$$

Conservative materials have a strain energy density function [5] and as a result, the stiffness and compliance matrices are symmetric. i.e. $C_{ij} = C_{ji}$ and $S_{ij} = S_{ji}$. Hence, only 21 stiffness components are actually independent and the most extreme case is a triclinic material where there is no elastic symmetry.

If there is a plane of elastic symmetry in a body then the elastic constants have the same values. Let 1-2 plane shown in Figure 2.2 be the plane of symmetry. Then, elastic properties in the positive 3-direction are the same as those in the negative 3-direction [6] and hence the stiffness matrix becomes

$$C_{ij} = \begin{bmatrix}C_{11} & C_{12} & C_{13} & 0 & 0 & C_{16}\\ C_{12} & C_{22} & C_{23} & 0 & 0 & C_{26}\\ C_{13} & C_{23} & C_{33} & 0 & 0 & C_{36}\\ 0 & 0 & 0 & C_{44} & C_{45} & 0\\ 0 & 0 & 0 & C_{45} & C_{55} & 0\\ C_{16} & C_{26} & C_{36} & 0 & 0 & C_{66}\end{bmatrix}. \tag{2.50}$$

A material having one plane of symmetry is known as a monoclinic material and has 13 independent components. If an anisotropic material has two orthogonal planes of

symmetry, then it is called an orthotropic material. Suppose the 1-2 and 2-3 planes are the planes of symmetry, then we get

$$C_{ij} = \begin{bmatrix} C_{11} & C_{12} & C_{13} & 0 & 0 & 0 \\ C_{12} & C_{22} & C_{23} & 0 & 0 & 0 \\ C_{13} & C_{23} & C_{33} & 0 & 0 & 0 \\ 0 & 0 & 0 & C_{44} & 0 & 0 \\ 0 & 0 & 0 & 0 & C_{55} & 0 \\ 0 & 0 & 0 & 0 & 0 & C_{66} \end{bmatrix}. \tag{2.51}$$

An orthotropic materials have 9 independent elastic constants. If a material has two orthogonal planes of symmetry, it will automatically have a third orthogonal plane of symmetry. Hence, an orthotropic material has 3 orthogonal planes of symmetry.

If a material is elastically equivalent in three directions, it is known as an isotropic material and has 2 independent elastic constants which are C_{11} and C_{12}. Suppose a material is subjected to an external tensile force along the direction 1 (uniaxial state of stress), this applied load results in strain along that direction. The relationship between stress and strain is expressed as

$$\varepsilon_{11} = \frac{\sigma_{11}}{E}, \tag{2.52}$$

where E is known as the Elastic Young's Modulus. The other two strain components will have negative values as follows

$$\varepsilon_{22} = \varepsilon_{33} = -\nu\varepsilon_{11} = -\nu\frac{\sigma_{11}}{E}, \tag{2.53}$$

in which ν is called the Poisson's ratio. In general case, Hooke's Law for isotropic bodies for these two elastic constants becomes

$$\varepsilon_{ij} = \frac{1+\nu}{E}\sigma_{ij} - \frac{\nu}{E}\delta_{ij}\sigma_{kk}, \tag{2.54}$$

or with inverse solution

$$\sigma_{ij} = \frac{E}{1+\nu}\left(\varepsilon_{ij} + \frac{\nu}{1-2\nu}\delta_{ij}\varepsilon_{kk}\right). \tag{2.55}$$

2.3.5 Yield Condition

Yield condition is defined as a mathematical relationship among the stress components at a point that must be satisfied for the onset of plastic behaviour at the point. Of the numerous yield conditions which have been proposed, two are reasonably simple mathematically and accurate enough to be highly useful for the initial yield of isotropic materials. These are the Tresca yield condition (Maximum Shear Theory) and the von Mises yield condition (Distortion Energy Theory).

According to the Tresca [7] yield condition, when the maximum shear stress reaches the prescribed value, yielding occurs. For given principal stresses, $\sigma_1 > \sigma_2 > \sigma_3$, the Tresca yield condition is expressed in its simple form

$$\frac{1}{2}(\sigma_1 - \sigma_3) = C_y, \tag{2.56}$$

where C_y is a characteristic material parameter denoting the yield limit. In simple tension, the maximum shear is equal to half of the yield stress: $\sigma_y/2$. Thus, Tresca's yield condition becomes

$$\sigma_1 - \sigma_3 = \sigma_y. \tag{2.57}$$

According to the von Mises Yield Condition [8], when the second deviator stress invariant reaches a specified value, yielding occurs. In terms of the principal stresses, the von Mises yield condition states

$$(\sigma_1 - \sigma_2)^2 + (\sigma_2 - \sigma_3)^2 + (\sigma_1 - \sigma_3)^2 = 6C_y. \tag{2.58}$$

In simple tension, the Eq.(2.58) becomes

$$(\sigma_1-\sigma_2)^2+(\sigma_2-\sigma_3)^2+(\sigma_1-\sigma_3)^2=2\sigma_y. \quad (2.59)$$

When stress components other than the principal stresses are employed, there are several variations for presenting equation 2.59.

2.3.6 Plastic Stress-Strain Equations

When initial yield is reached, elastic equations can no longer be used owing to plastic strains, which depend on the loading history. For plastic stress-strain relations, there are two approaches which are incremental strain theories and total strain theories. Plastic stress-strain relations are usually given in terms of incremental strain which produce more realistic theories [9].

A general relationship between the strain increments and the stresses was developed by Lévy [10]. Later on, the same relations were studied independently by von Mises. According to the Levy-Mises equations, as they are known, the total strain increments $d\varepsilon_{ij}$ relate to the deviatoric stress components s_{ij} as follows

$$d\varepsilon_{ij}=s_{ij}d\lambda, \quad (2.60)$$

in which dλ is proportionality factor meaning that finite stress components are related to incremental strains [11]. During the loading history dλ can change thus it is not a fixed constant. In equation (2.60), the elastic portion is neglected and it is assumed that the principal axes of strain increments coincide with the principal stress axes. The Levy-Mises equations are valid for a rigid plastic material, as it is assumed that the total strain increments equal the plastic strain increments.

Prandtl [12] extended Eq (2.60) to include the elastic strain. Then, Reuss [13] assumed the plastic strain increments $d\varepsilon_{ij}{}^{p}$ are related to the deviatoric stress components s_{ij} by

$$d\varepsilon_{ij}^{p} = s_{ij} d\lambda . \tag{2.61}$$

Eqs. (2.61) is known as the Prandtl-Reuss equations. It provides a relationship between the plastic strain increments and the current stress deviators. These equations are valid for an elastic-plastic material.

In order to obtain general stress-strain relations, two assumptions are used as follows

1. There is a loading function $f(\sigma_{ij})$ and plastic deformation takes place only for $f(\sigma_{ij}) = k$ and $df > 0$, where k depends on the existing state of stress and the strain history.
2. The relation between infinitesimal of stress and plastic strain is linear. If $df = 0$ neutral loading occurs in this case plastic strain does not increase.

For the second condition, there is an assumption such that [14]

$$d\varepsilon_{ij}^{p} = G_{ij} df , \tag{2.62}$$

where G_{ij} are the components of a second order symmetric tensor which are functions of the stress components. If G_{ii} is taken to be zero, the change in the plastic strain is zero and by means of [14]:

$$G_{ij} = h \frac{\partial g}{\partial \sigma_{ij}}, \tag{2.63}$$

where h is a general function of stress and strain flow, and g is known as the plastic potential which is a scalar function of the stress. Substituting Eq. (2.63) in Eq. (2.62) it is obtained:

$$d\varepsilon_{ij}^{p} = h\frac{\partial g}{\partial \sigma_{ij}} df \,, \tag{2.64}$$

taking $g = f$ [14]:

$$d\varepsilon_{ij}^{p} = \frac{\partial f}{\partial \sigma_{ij}} d\lambda \,. \tag{2.65}$$

These equations are known as the associated flow rule.

2.3.7 Plastic Work

The work increment per unit volume may be written as:

$$dW = \sigma_{ij} d\varepsilon_{ij} \,. \tag{2.66}$$

If strain increments are separated into two parts as elastic and plastic portions:

$$d\varepsilon_{ij} = d\varepsilon_{ij}^{e} + d\varepsilon_{ij}^{p} \,, \tag{2.67}$$

and substituting Eq. (2.67) into the Eq.(2.66) we get:

$$dW = \sigma_{ij} d\varepsilon_{ij}^{e} + \sigma_{ij} d\varepsilon_{ij}^{p} = dW^{e} + dW^{p} \,. \tag{2.68}$$

If a material is plastically incompressible, the plastic work increment may be written as:

$$dW^{p} = \sigma_{ij} d\varepsilon_{ij}^{p} = s_{ij} d\varepsilon_{ij}^{p} \,. \tag{2.69}$$

For a material obeying Eq. (2.62), the plastic work increment may be expressed as [15]:

$$dW^{p} = \sigma_{EQ} d\varepsilon_{EQ}^{p} \,, \tag{2.70}$$

where σ_{EQ} is equivalent stress and $d\varepsilon_{EQ}^{p}$ is equivalent plastic strain.

In order to compute the current yield stress under isotropic strain hardening plastic flow, there are two approaches. The first is the work-hardening hypothesis and

assumes that the equivalent stress is a function of the total plastic work which is done per unit volume:

$$\sigma_{EQ} = F(W^P), \tag{2.71}$$

where:

$$W^P = \int \sigma_{ij} d\varepsilon_{ij}^P . \tag{2.72}$$

The other hardening hypothesis is the strain-hardening hypothesis and assumes that the equivalent stress is a function of the amount of the plastic strain:

$$\sigma_{EQ} = H(\varepsilon_{EQ}^P), \tag{2.73}$$

where H is a function depending upon the material and can be determined experimentally. ε_{EQ}^P is the total equivalent strain and is equal to:

$$\varepsilon_{EQ}^P = \int d\varepsilon_{EQ}^P . \tag{2.74}$$

2.4 Physical Basis of Plasticity and Elasticity at the Atomic Scale

It should be appreciated that so far the theories of elasticity and plasticity have been given from a mechanics point of view since the study in this thesis is concerned with the view of mechanics. The macroscopic and microscopic views of matter are wide, however, and recent developments in metallurgical science provide an understanding of many features of engineering experiments. Hence, this section is dedicated to understanding the behaviour of metals on the atomic scale without going into detail.

In metals, atoms arrange in simple regular array in crystals. A crystal is a solid in which the constituent atoms, molecules, or ions are packed in a regularly ordered pattern extending in all three spatial dimensions. Between each adjacent atom, attractive and repulsive interactions exist. Both these effects are extremely nonlinear with distance and atoms have equilibrium spacing for unstressed metal under this effect.

When a metal is subjected to load in the elastic range, the bonds between the atoms are strained, resulting in relatively small movements and it can be assumed that this relative movement is reversible and there is a linear relation between attractions and change of movement from the undeformed (equilibrium) position. Therefore, there is a linear relationship between changes of load and deformation. On the other hand, the behaviour of crystals in the elastic range are not perfect due to misfits and gaps in the crystal lattice. In addition, since there are many crystals with arbitrary orientations, there are mismatches at the crystal boundaries [16].

When a larger load is applied, misfit atoms move position in response to the load. In principle the movement of one atom results in the misfit of neighbouring atoms. Hence, chains of movement may occur by a series of flips of individual atoms. Imperfections in crystal structure are known as dislocations and the movement of dislocations, driven by shear stress, results in permanent plastic deformation of the material. If the load causing plastic deformation is removed, the dislocation movement is not generally reversible since the force is relieved on the next atom in line and changes are only accommodated elastically. Hence the plastic deformation

is irreversible. Because atomic bonds are transferred when atoms move, the elastic properties of the material remain unaffected by plastic deformation [16].

2.5 Residual Stresses

2.5.1 Definitions, Causes and Importance

Stresses acting in a body can be divided into two groups. The first kind of stresses, referred to as applied stresses, occur in materials during the application of load. They balance with external loading stresses. The second kind of stresses, so-called residual stresses, is the stresses which remain in a stationary body after removal of external loads. They are self-equilibrating where the resultant force and moments are zero.

Residual stresses can be classified according to the scale over which they act [17]. This category allows us to select the type of residual stress measurement technique to be implemented on a material. Three kinds of residual stresses are thus defined. Type *I* denotes the almost homogenous distribution of residual stresses over many grains of materials. These are called macrostresses. This type of stresses can be detected by destructive methods such as the contour, hole drilling or layer removal techniques etc.

Type *II* residual stresses are nearly homogenous over a few grains. Type *III* residual stresses range over several atomic distances within a grain. Type *II* and type *III* residual stresses are collectively known as microstresses. These three different kinds

of residual stresses in multi-phase or composite materials equilibrated over different length scales are given in Figure 2.7 [18].

Even though microstresses can contribute to failures in engineering components these stresses are generally localized in particular grains and therefore Type *I* residual stresses are generally taken into account for the design of engineering applications since they are equilibrated within a whole body.

Almost all manufacturing processes introduce residual stresses into engineering components. Manufacturing processes are the most common causes of residual stress and can be classified into three main categories [19]:

(i) Plastic deformation or forming which includes rolling, drawing, extruding, bending, pressing etc.

(ii) Manufacturing processes such as welding, machining, coating, joining, etc.

(iii) Heat treatment such as carburizing, hardening, nitriding etc.

Different manufacturing processes causing residual stress are given in Figure 2.8 [20]. On the other hand, the existence of residual stresses may be advantageous for engineering components depending on the sign and magnitude. It is known that cold expansion and shot peening cause compressive residual stresses that have a beneficial effect on the fatigue life and stress corrosion since they delay crack initiation.

Since residual stresses are locked-in stresses, the standard measurement techniques used for materials under externally applied loads are not applicable to measure residual stresses. The residual stress measurements require more sophisticated methods, which will be discussed in the next section.

2.5.2 Residual Stress Measurement Methods

Because of the importance of residual stresses, many measurement techniques have been developed. In general, these techniques can be broadly divided into two groups: destructive and non-destructive. All residual stress measurement methods have their advantages and disadvantages. There is no such technique that overwhelms all the other techniques. There are many critical parameters to determine which technique needs to be chosen. Some of the important parameters are: the type of residual stresses, time, cost of the measurement, cost of the material, structure of the material, the variation of the residual stresses with depth from the surface, the geometry of the part, the laboratory facilities, etc.

2.5.2.1 Destructive methods

Destructive methods involve mechanical processes and residual stresses can be determined from the measurement of relaxed deformation. These methods include three main steps:

(i) altering the stress state by means of machining,

(ii) redistribution of stress state introduces deformation which is measured in terms of displacement or strain,

(iii) the original residual stress field is generated from the displacement or strain field by using the theory of elasticity.

Some important destructive techniques in terms of their prevalent industrial applications and new developments are: the hole-drilling method, the ring core technique, the layer removal method, contour method and compliance method.

2.5.2.1.1 Hole-Drilling Methods

Hole-drilling is one of the most common techniques amongst the destructive residual stress measurement methods since this technique can provide a simple measurement of residual stress having a sharp gradient through the thickness of specimen with a minimal amount of material damage. Therefore it is occasionally termed a "semi-destructive residual stress measurement method". Hole-drilling is a fully standardized method by ASTM (American Society for Testing and Materials) E387-92 [21].

A specially designed strain gauge rosette as shown in Figure 2.9 is installed on the surface of the material where the residual stress components are to be measured and a hole is incrementally drilled at the centre of the strain gauge. While drilling, the residual stresses are partly relieved and the resulting change in strain state is measured by the strain gauge. An analytical equation between initial residual stresses and radial strains measured around the hole is given [22],

$$\varepsilon = (\sigma_{max} + \sigma_{min})\overline{A} + (\sigma_{max} - \sigma_{min})\overline{B}\cos(2\beta), \qquad (2.75)$$

in which σ_{max} and σ_{min} are the maximum and minimum principal stresses, β is the angle between the X axis and the maximum principal direction and $\overline{A}$ and $\overline{B}$ are calibration constants depending upon the experimental settings.

For a thin plate, three strain results from the three-element strain gauge are sufficient to derive three equations in the form of equation (2.75) simultaneously to get the principal stresses at each increment of depth. In many cases, however, a drilled hole is a blind hole where hole is incrementally drilled on one side of the surface and the length of the drill does not reach the other side of the surface due to thickness of material and it causes enough complex geometry to obtain analytical solution by using Eq. (2.75). Hence, numerical methods such as finite element are employed to predict the residual stresses along the depth of hole.

2.5.2.1.2 Crack Compliance Method

The crack compliance method involves a small slot cut incrementally across the thickness of a part which contains residual stresses. The slot releases residual stresses on the crack opening faces. The changing of the strains at the surface of the body can be measured by means of strain gauges which are attached at suitable measurement points, and strains are assessed as a function of slot depth a.

Figure 2.10 shows typical crack-compliance specimen [23]. A slot is introduced incrementally from the top surface of the specimen by electro-discharge machining (EDM) and strain gauges on the top and bottom surfaces record strain values at each successive slot depth a. From these measurements, the residual stress component normal to the cut surface (σ_y) can be determined through the thickness of the specimen (X-direction). In order to get residual stress from strains measured, the stress-intensity factor (SIF) is determined as a function of cut depth a and, by using inversion techniques such as Schindler's inversion technique [24-25], residual stress can be calculated. The cut can be considered as a perfect crack therefore basic

equations relating to fracture mechanics can be used to evaluate analytical investigation.

2.5.2.1.3 Layer Removal Method

The curvature technique is used to calculate residual stresses in simple geometries. The theory of the method is founded on the static equilibrium of internal forces and moments [26]. When layers of the material are progressively removed from a plate, the static equilibrium is unbalanced and the plate consequently bends owing to redistribution of residual stress. The shape of the curvature (Figure 2.11) depends upon the sign of the surface stress which exists in the layer.

The implementation of this method is rapid and determination of curvature geometry requires a simple computation in order to obtain residual stress. Depending on experimental conditions, measurement of the curvature can be done by using strain gauges, coordinate measurement machine (CMM), laser scanning, or optical methods. Due to its simple implementation, this technique is widely used to determine residual stress especially in polymeric composites and coatings. Layer removal is valid solely in plate specimens and Type *I* stresses are detectable by using this method.

2.5.2.1.4 Sectioning Method

Sectioning is another destructive technique commonly used to measure residual stresses. There are two kinds of sectioning approaches for measurement of residual stress. The first approach is a standard sectioning method where a body is sectioned and the deformation due to stress relief is measured [27]. The sectioning is repeated

until there is no change of strain observed. The principle of the other approach is based on measuring eigenstrain. Previous studies show that the source of residual stress in a body is due to an incompatible strain field that is called eigenstrain (or inherent strain) [28-29]. By using this methodology, sectioning does not need to be repeated since the eigenstrain can be predicted theoretically from surface strains. The aim of using eigenstrain for measuring residual stress is that the changing of the geometry of the specimen alters the residual stress but it does not change the eigenstrain distribution. This will be discussed in detail in chapter 6 when the multi-axial contour method is introduced.

One assumption of the eigenstrain approach is that residual stress along the longitudinal direction does not vary, which is the case in a continuously processed body. Figure 2.12 shows such a welded joint. Very thin sliced plates perpendicular to the Z-axis (L_i) and the X-axis (T) are cut out from a large original specimen R. During the cutting process, elastic strains are directly observed at the points where strain gauges are attached.

By the assumption that cutting does not introduce any further plastic strain, the eigenstrain components measured by the strain gauges on the specimens L_i and T are strains due to relaxation of residual stresses. Since the specimens are sufficiently thin, the eigenstrain component normal to the cut planes does not contribute any residual stress. Therefore, specimens L_i only contain the eigenstrain components ε^*_{xx} and ε^*_{zz}. The source of the residual stress in specimen T is due to the component of eigenstrains $\varepsilon^*_{yy}, \varepsilon^*_{zz}$ and ε^*_{yz}. The resulting residual stress in the specimens T and L

are determined by means of these eigenstrain components and the three-dimensional residual stress $\{\sigma\}$ can be expressed by the sum of the stress in T and L specimens.

2.5.2.2 Non-Destructive Methods

Non-destructive techniques are founded on the association between the residual stress and physical parameters [19]. The main advantage of these methods is that they do not involve any destruction. In other words, the initial geometry of a sample is conserved after an experiment which allows a repeatability of measurements on the same specimen. There are a number of non-destructive methods prevalently used to measure residual stress and strain, including X-ray diffraction, neutron diffraction, ultrasonic and magnetic methods. These techniques allow residual stress of Type *I*, *II* and *III* to be measured.

2.5.2.2.1 X-ray diffraction

In diffraction based stress analysis a crystalline lattice is used as if it is an atomic strain gauge. In this case, strains can be measured in the bulk of engineering materials. The measurement depth depends upon the power of the source used in diffraction methods such as X-ray, neutron etc. Diffraction arises when a wave motion is incident on a set of regularly spaced scattering objects, as long as the wavelength of the incoming wave is of the same order of magnitude as the repeat distance between the scattering centres [30].

One of the most popular diffraction techniques is X-ray diffraction which is utilized to determine residual stresses near to a surface. The maximum penetration of laboratory based X-rays for most materials is only about 5-50 μm from the surface.

Although this is a main limitation of this method apart from complexity of the equipments used in experiments, X-rays diffraction is widely used on engineering materials due to its standardized method.

X-ray diffraction technique is founded on Bragg's Law [31]. If a monochromatic X-ray beam of wavelength λ is incident on the surface of the crystalline material as shown in Figure 2.13, the following relation must be satisfied:

$$\lambda = 2d\sin(\theta). \tag{2.76}$$

This is known as the Bragg's Law, where d is the distance between diffracting lattice planes and θ is the angle between the diffracting plane and the incident beam.

If the wavelength λ and the change in diffracting angle θ are known, then the interplanar spacing d is calculated by means of Bragg's Eq. (2.76) in order to calculate strain ε as follows

$$\varepsilon = \frac{d - d_0}{d_0} = -\cot\theta\Delta\theta, \tag{2.77}$$

Where d_0 is the stress free lattice spacing, and $\Delta\theta$ is the change in angle.

2.5.2.2.2 Synchrotron X-ray Diffraction

The synchrotron or hard X-rays for non-destructive strain measurement method uses a very high intensity of X-rays. As a result, the penetration of the beam into a material is much deeper than that of the conventional X-ray technique [20]. Depending on the material type, the depth of penetration from a material surface can be 50 mm or more. In addition, the spatial resolution of synchrotron X-rays is much

higher owing to the ability to use a narrow beam size. Furthermore, the measurements are much quicker than the X-ray technique.

The synchrotron comprises a circular vacuum pipe which is called a storage ring [32] (Figure 2.14). High intensity X-rays are created by means of accelerating electrons. The electrons are inserted into the storage ring where their speed nearly reaches the speed of light. Electrons are directed from one straight section (insertion device) to another via dipole magnets. Insertion devices, which consist of a periodic array of electro magnets, are the source of synchrotron radiation. Electro magnets subject the electron beam to an oscillating magnetic field. This causes electron beams to follow a sinusoidal path in the orbital plane of a storage ring inside the insertion device. The energy that is lost by the electron beam through the production of high energy X-rays is compensated by radio frequency cavities in the storage ring.

2.5.2.2.3 Neutron Diffraction

The neutron diffraction method is one of the most prevalent non-destructive residual stress evaluation techniques, the principle of which for residual stress measurement is identical with X-ray diffraction [33]. The crucial advantage of using neutron diffraction over X-ray is much deeper penetration depths. This enables residual stress to be measured in engineering materials with thicker sections [34]. For instance, the penetration of neutrons can reach up to 250 mm in aluminium alloys and 37 mm in steel.

There are two kinds of neutron diffraction techniques which are conventional $\theta/2\theta$ scanning and time of flight approaches. The first one uses a continuous monochromatic beam from a reactor source and the shift in the angle 2θ is monitored [35]. The time of flight approach utilizes a pulsed beam from a spallation source, where the diffraction angle is kept constant and there is variation in the incident wavelength [36].

A schematic diagram of neutron diffraction is given in Figure 2.15. Incident neutron beams are collimated by passing through Söller Slits. The dimensions of the incoming beam are determined by an aperture, which is known as an incident slit. The area where strains are to be measured is determined via a translation system on which the specimen is mounted. Incoming beams passing into specimen are diffracted. The diffracted beam may pass through Söller Slits or an aperture. Slits on the incoming and diffracted beams determine the measurement area which is known as the gauge volume.

2.5.2.2.4 Ultrasonic Method

The principle of this method is based on the variation of ultrasonic speed the change of which in structural materials depends upon the stress magnitude. The stress is assessed by means of the variation of wave speed. The relationship between the ultrasonic speed and stress is given by [37]

$$V = V_0 + K\sigma, \tag{2.78}$$

where V_0 is the velocity of a wave in the unstressed form of the material, σ is the stress, and K is the acousto-elastic constant which can be determined by experiment.

There are several kinds of experimental configurations used in experiments to measure wave speed.

Figure 2.16 shows a schematic configuration of the ultrasonic method for surface pitch-catch. The wave is launched by a transmitting transducer, passes through a zone of material and reaches the receiving transducer. As the distance between the two transducers is constant, ultrasonic travel time instead of speed can be used as a parameter for stress measurements [38].

The main advantage of using the ultrasonic method is that interior stresses can be obtained. Depending on the configuration of unit and materials, stress can be measured within 3-150 mm thickness. Furthermore, the ultrasonic method is cheap to undertake and portable.

2.5.2.2.5 Magnetic Methods

Owing to the range of magnetic signals sensitivity to residual stresses and microstructures, residual stresses in magnetic materials can be non-destructively deduced by association between these signals and elastic strains. The most popular magnetic technique used for residual stress measurement is the Barkhausen method [39].

The principle of the Barkhausen method is based on the analysis of ferromagnetic domain wall motion. Ferromagnetic materials comprise magnetically ordered zones, so-called domains. When a magnetic field or mechanical force is applied to a ferromagnetic material, the domain orientations are altered, causing domains most

nearly oriented to a tensile stress to grow (positive magnetostriction) or shrink (negative magnetostriction) [20]. The abrupt reorientation of magnetic domains due to the presence of a stress field is converted to an electrical pulse and the signal recorded is known as Barkhausen noise. This is used to determine residual stress in magnetic materials.

2.6 Weld Technology

Welding is one of the most prevalent fabrication processes, widely used in industrial applications to join two or more materials. This process is typically achieved by melting the workpieces and adding a filler material, which then forms a molten material which cools to form a strong join to create the weld. The most common geometrical shapes of the weld can be either in the form of butt or V-joints. For the welding process, many kinds of energy sources are used. Examples include electron beams, friction, electric arc and laser beams [40].

Welding process, similar to other heat treatment processes, such as quenching, hot rolling or forging, do not change the chemical compositions of welded material but modify the metallurgical structure of the parent material which results in altering the mechanical properties in and around the weld region. Whichever welding techniques are used, welded material typically can be divided into three regions: parent, weld and heat-affected zones. Each of them possesses their own physical properties.

In addition to the effect of the welding process on modifying mechanical properties of the welded materials, residual stresses develop in a weld due to the non-homogeneous temperature field between the weld zone and the parent zone of the

material [41]. During the welding procedure, the region surrounded by the weld is subjected to high temperature which results in a volume expansion. This volume expansion is restricted by the cooler material and causes thermal stress. After the thermal stresses reach the yield point, the material locally yields. When the heated weld metal shrinks during solidification, it is restrained by the colder material around the weld region. This brings about a tensile residual stress around the weld region, balanced by compressive residual stress in a region further away from the weld region. During cooling, phase transformations, such as from austenite into martensite, can affect the residual stress distribution. These phase transformations are associated with a volume expansion which in turn is hindered by the surrounding materials, producing a compressive residual stress [42].

The magnitude and distribution of the residual stresses depends mostly upon the type of welding process, the constraint of the weld material, the phase transformation and the cooling rate [41]. Moreover, the degree of preheat of the surfaces prior to the welding, the number of weld passes, heat input, welding speed and welding voltage also have substantial effect on the residual stress variation.
Since the welding process affects the mechanical performance of the metals and causes the residual stresses, mechanical characterization of the weld metal has to be taken into account for safety of engineering designs. There are numerous researches that have been carried out in previous years and many investigations are in progress to study the weld residual stress distribution and the mechanical performance in different alloys. Some of the important weld techniques are reviewed in the following paragraphs.

Friction Welding is a solid state welding process, where two parts having circular cross sections are brought in contact by a friction pressure while one of them rotates. Friction between the parts brings about heating at their ends. A forge pressure is implemented to create the joint. Since friction welding is implemented in the solid state, defects related to the melting and solidification do not occur. Applications of friction welding are found in the areas of turbine shafts in engines of next generation aircraft [43].

Friction Stir Weld (FSW), a solid state joining process developed at The Welding Institute (TWI) in 1991 [44], is often used for butt and lap joints. In general, the process is carried out by rotating and slowly plunging a friction stir weld tool into the interface of two clamped sheets. The frictional heat from the tool shoulder and deformation heat from the tool pin are utilized for bonding under applied normal force [45]. This process is successfully implemented for welding of precipitation hardening aluminium alloys of 2xxx and 7xxx series [46]. It is observed that FSW causes lower residual stress comparing to other fusion welding techniques.

Tungsten Inert Gas (TIG) welding is a fusion welding process that uses a non-consumable tungsten electrode to produce the weld. In this process an arc is formed between a non-consumable tungsten electrode and the metal welded. Argon, hydrogen or helium can be utilized as an inert gas. The weld area is preserved from atmospheric contamination by a shielding gas [40]. TIG welding is generally used to weld thin parts of stainless steel and lighter materials such as aluminium alloys. Since TIG welding uses a more intense heat source, nearly undistorted welds can be

obtained. For many applications TIG welding can not be completed with other welding methods such as electron or laser beam welding. [43].

Laser beam welding (LBW) is based on high heat density welding technologies that enable joining of materials with a concentrated coherent light beam impinging on the surfaces. Since the beam power can focus on with a very small spot diameter, the LBW process provides smaller heat affected zones, lower distortions, residual stresses and strains as compared to other traditional welding processes [47].

Electron beam welding (EBW) is an arc welding process where a high-velocity beam is incident on the metals being welded. As the applied electrons are transformed into heat on impact, the work-pieces melt to form part of the weld. The welding process needs to be conducted in vacuum to prevent dispersion of the electron beam. The main advantage of this technique over the laser process is that it has no problems with beam reflection on the molten metal [43].

Metal Inert Gas (MIG) welding is a form of fusion welding in which a consumable electrode with a constant speed is used to form an arc between the consumable electrode and the work-piece. Although widely used due its flexibility, the high input heat source changes the mechanical properties of materials in this technique, therefore, it is not suitable for safety critical applications, e.g. in manned aircraft manufacture.

Variable Polarity Plasma Arc (VPPA) welding uses a non-consumable tungsten electrode which forms one side of the arc whilst the base material forms the other

side [43]. Since a highly constricted arc is utilized in this technique, it results in fusion and subsequent joining of the work piece. The constriction of the arc can be achieved by a constricting nozzle or a high current density within the arc that generates a powerful magnetic field.

2.7 REFERENCES

[1] Fung Y.C. (1965). Foundation of Solid Mechanics, Prentice-Hall, Inc., Englewood Cliffs, N.J.

[2] Arfken, G.B. and Weber H.J. (2001). Mathematical Methods for Physicists, 5th edition. A Harcourt Science and Technology, San Diego.

[3] Dieter, G.E. (1976). Mechanical Metallurgy. McGraw-Hill, New York, Inc.

[4] Hunter S.C. (1976). Mechanics of Continuous Media. John Willey & Sons, New York.

[5] Christensen R.M. (1979). Mechanics of Composite Materials. Willey & Sons, New York.

[6] Green, A.E. and Zerna W. (1968). Theoretical Elasticity. Oxford University Press, New York.

[7] Tresca H. (1868). Mémoire sur l'Écoulement des Corps Solides. Mémoires. Présentes par Divers Savants, vol. 18, pp. 733–799, cited by Fung Y.C. [1].

[8] von Mises R. (1913). Mechanik der festen Körper im plastisch deformablen Zustand, Nachrichten der Gesellschaft der Wissenschaften in Göttingen, Mathematisch- Physikalische Klasse, pp. 582-592, cited by Fung Y.C. [1].

[9] Mase G.E. (1970). Schaum's Outline of Theory and Problems of Continuum Mechanics. McGraw-Hill, New York, Inc.

[10] Levy M. (1870). Mémoire sur les Équations Générales des Mouvements Intérieurs des Corps Solides Ductile au delà Limites ou l'élasticité Pourrait les Ramener à leur Premier État, Comptes. Rendus, vol. 70, pp. 1323-1325, cited by Fung Y.C. [1].

[11] Chen W.F. and Han. D.J. (1988). Plasticity for Structural Engineers, Springer-Verlag, New-York.

[12] Prandtl L. (1925). Spannungsverteilung in plastischen Körpern. Proceedings of the 1st International Congress on Applied Mechanics, Delft, pp. 43-54, cited by Fung Y.C. [1].

[13] Reuss A. (1930). Berücksichtigung der elastischen Formänderung im der Plastizitätstheorie. Zeitschrift für Angewandte Mathematik und Mechanik, vol. 10, pp. 266–274, cited by Fung Y.C. [1].

[14] Hill R. (1950). The Mathematical Theory of Plasticity. Oxford University Press, London.

[15] Bland D.R. (1957). The Two Measures of Work-Hardening, 9th International Congress of Applied Mechanics, Université Libre de Bruxelles, vol. 8, pp. 45-50.

[16] Calladine C. R. (1969). Engineering Plasticity. Pergamon press, Oxford.

[17] Cullity B.D. (1977). Some Problems in X-Ray Stress Measurements. Advances in X-Ray Analysis, vol. 20, pp. 259-271.

[18] Fitzpatrick M.E., Hutchings M.T. and Withers P.J. (1997). Separation of Macroscopic, Elastic Mismatch and Thermal Expansion Misfit Stresses in Metal Matrix Composite Quenched Plates from Neutron Diffraction Measurements. Acta Materialia, vol. 45, pp. 4867-4876.

[19] James M.R. and Lu J. (1996). Introduction. In Handbook of Measurement of Residual Stresses, Editor Lu J. Fairmont Press, Senlis.

[20] Withers P.J. and Bhadeshia H.K.D.H. (2001). Residual Stress: Part 1 – Measurement Techniques. Materials Science and Technology A, vol. 17, pp. 355-365.

[21] ASTM E387-92 (1992). Standard Test Method for Determining Residual Stresses by the Hole-drilling Strain-Gage Method. Annual Book of ASTM Standards, Section 3, vol. 3(1), pp. 747–753.

[22] Schajer G.S., Flaman M.T., Roy G. and Lu J. (1996). Hole-Drilling and Ring Core Methods. In Handbook of Measurement of Residual Stresses, Editor Lu J. Fairmont Press, Senlis.

[23] Prime M.B. (1999). Residual Stress Measurement by Successive Extension of a Slot: The Crack Compliance Method. Applied Mechanics Reviews, vol. 52(2), pp.75-96.

[24] Schindler H.J (1995). Determination of Residual Stress Distributions from Measured Stress Intensity Factors. International Journal of Fracture, vol. 74(2), pp. R23-R30.

[25] Schindler H.J, Cheng W. and Finnie I. (1997). Experimental Determination of Stress Intensity Factors Due to Residual Stresses. Experimental Mechanics, vol. 37(3), pp. 272-277.

[26] Flavenot J.F. (1996). Layer Removal Method. In Handbook of Measurement of Residual Stresses, Editor Lu J. Fairmont Press, Senlis.

[27] Ueda Y. (1996). Sectioning Methods. In Handbook of Measurement of Residual Stresses, Editor Lu J. Fairmont Press, Senlis.

[28] Ueda Y. and Fukuda K. (1986). New Measuring Method of Axisymmetric Three-Dimensional Residual Stresses Using Inherent Strains as Parameters. Journal of Engineering Materials and Technology, vol. 108(4), pp. 328-334.

[29] Mura T. (1987). Micromechanics of Defects in Solids. Kluwer, Massachusetts.

[30] Cullity B. D. (1978). Elements of X-ray Diffraction, 2nd edition. Addison-Wesley, London.

[31] Noyan I.C. and Cohen J.B. (1987). Residual Stress-Measurement by Diffraction and Interpretation. Springer-Verlag, New York.

[32] Riekel C. (2003). The Use of Synchrotron Radiation for Materials Research. In Analysis of Residual Stress by Diffraction Using Neutron and Synchrotron Radiation. Editor Fitzpatrick M.E. and Lodini A. Taylor and Francis, London.

[33] Holden T.M. and Ray G. (1996). The Application of Neutron Diffraction to the Measurement of Residual Stress and Strain. In Handbook of Measurement of Residual Stresses, Editor Lu J. Fairmont Press, Senlis.

[34] Lodini A. (2001). The Recent Development of Neutronic Techniques for Determination of Residual Stresses. Radiation Physics and Chemistry, vol. 61, pp.221-233.

[35] Pintschovius L. (2003). Neutron Diffraction Using a Constant wavelength. In Analysis of Residual Stress by Diffraction Using Neutron and Synchrotron Radiation. Editor Fitzpatrick M.E. and Lodini A. Taylor and Francis, London.

[36] Ezeilo A.N. and Webster G.A. (1999). Advances in Neutron Diffraction for Engineering Residual Stress Measurements. Textures and Microstructures, vol.33, pp. 151-171.

[37] Thompson R.B., Lu Y. and Clark A.V. (1996). Ultrasonic Methods. In Handbook of Measurement of Residual Stresses, Editor Lu J. Fairmont Press, Senlis.

[38] Ya M., Marquette P., Belahcene F. and Lu J. (2004). Residual Stresses in Laser Welded Aluminium Plate by Use of Ultrasonic and Optical Methods. Materials Science and Engineering A, vol. 382, pp. 257-264.

[39] Titto S. (1996). Magnetic Methods. In Handbook of Measurement of Residual Stresses, Editor Lu J. Fairmont Press, Senlis.

[40] Weman K. (2003). Welding Processes Handbook. CRC Press, New York.

[41] Nitschke T. and Wohlfahrt H. (2002). Residual Stresses in Welded Joints-Sources and Consequences. 6th European Conference on Residual Stresses, Coimbra, Portugal, vol. 404-407, pp. 215-224.

[42] Nitschke T. and Wohlfahrt H. (1991). The Generation of Residual Stresses due to Joining Processes. In Residual Stresses: Measurement, Calculation, Evaluation, Editor Hauk V., Hougardy H. and Macherauch E. Informationsgesellschaft, Verlag, Oberursel, Germany, pp. 121-133.

[43] Mendez P.F. (2000). New Trends in Welding in the Aeronautic Industry. Proceedings of the Conference New Trends for the Manufacturing in the Aeronautic Industry, Hegan/Inasmet, San Sebastián, Spain, pp. 21-38.

[44] Thomas W.M., Nicholas E.D., Needham J.C., Church M.G., Templemith P. and Dawes C.J. (1991). International Paten Application No. PCT/GB92/02203 and GB Patent Application No. 9125978.8.

[45] Schneider J., Beshears R. and Nunes Jr. A.C. (2006). Interfacial Sticking and Slipping in the Friction Stir Welding Process. Materials Science and Engineering A, vol. 435-436, pp. 297-304.

[46] Dawes C.J. and Thomas W.M. (1996). Friction Stir Process Welds Aluminium Alloys. The Welding Journal, vol. 3(75), pp. 41-46.

[47] Moraitis G.A. and Labeas G.N. (2008). Residual Stress and Distortion Calculation of Laser Beam Welding for Aluminum Lap Joints. Journal of Materials Processing Technology, vol. 198, pp. 260–269.

2.8 FIGURES

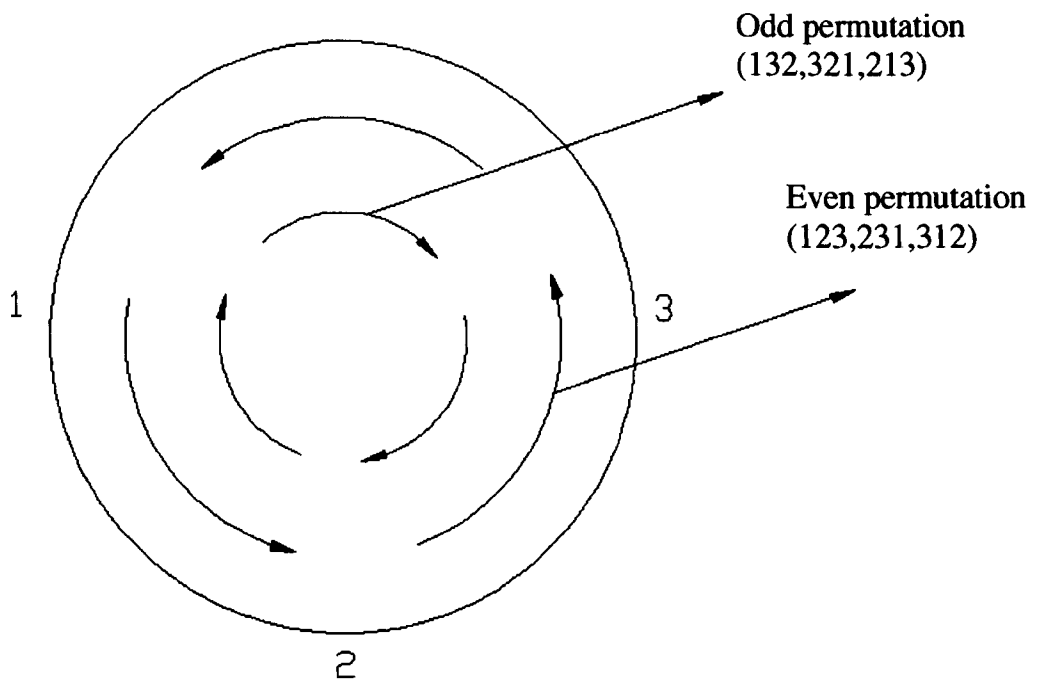

Figure 2.1 Schematic showing of even and odd cyclic permutations.

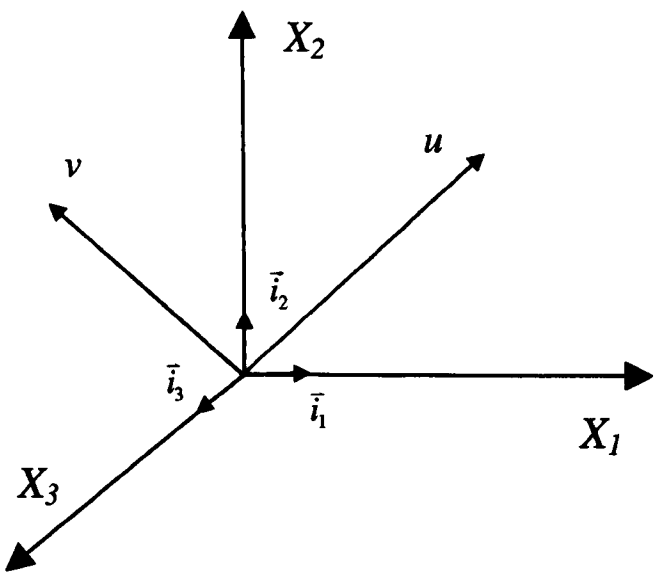

Figure 2.2 Cartesian coordinate system with its unit base vectors.

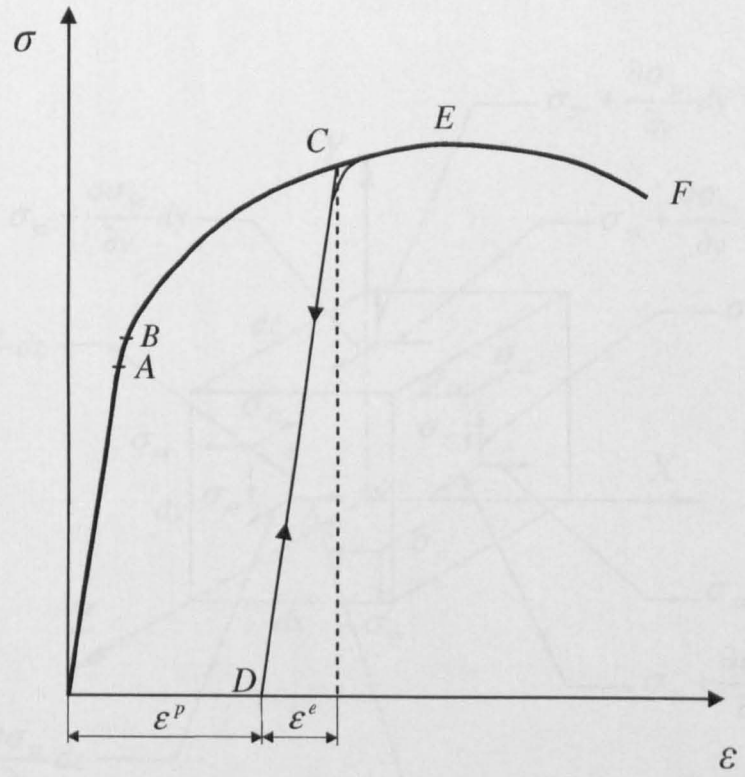

Figure 2.3 The stress-strain curve.

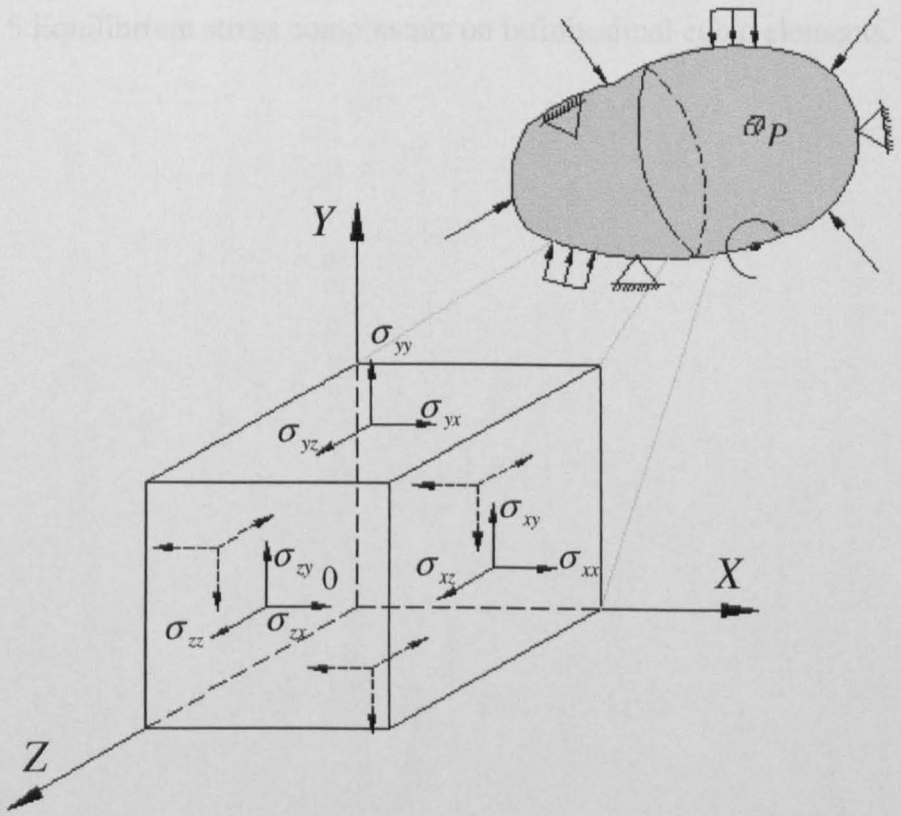

Figure 2.4 A 3D deformable body in equilibrium, and the stress components on an infinitesimal cubic element.

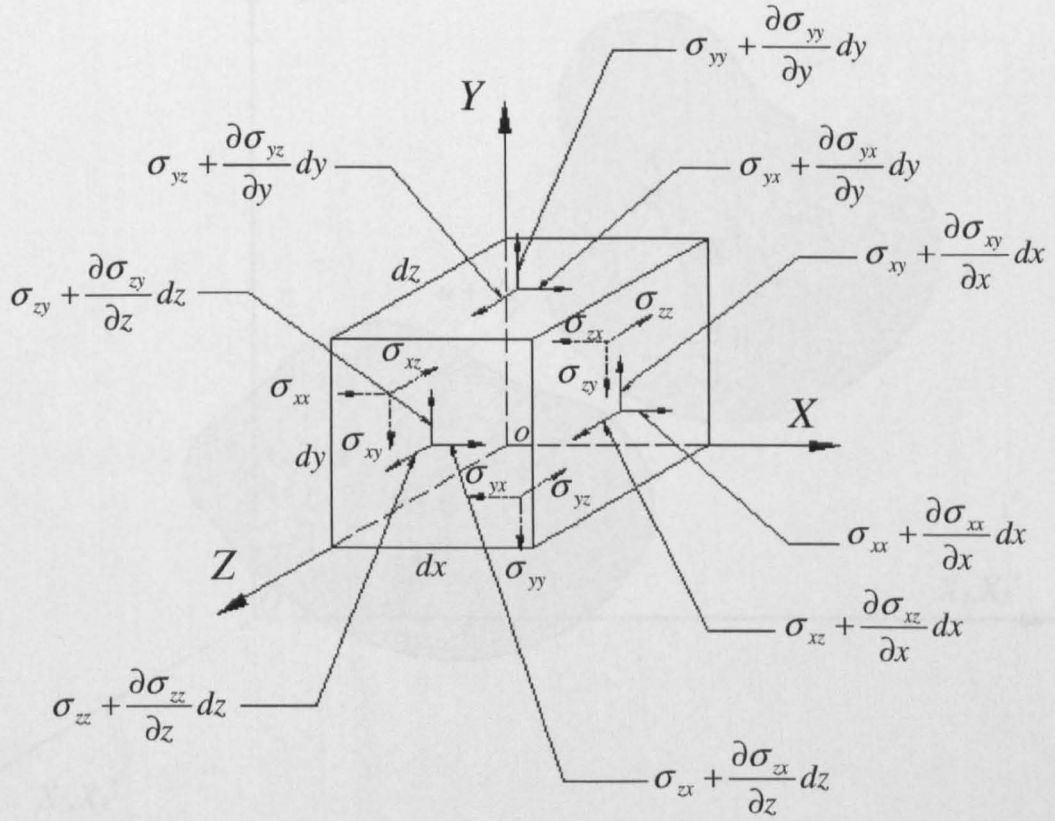

Figure 2.5 Equilibrium stress components on infinitesimal cubic elements.

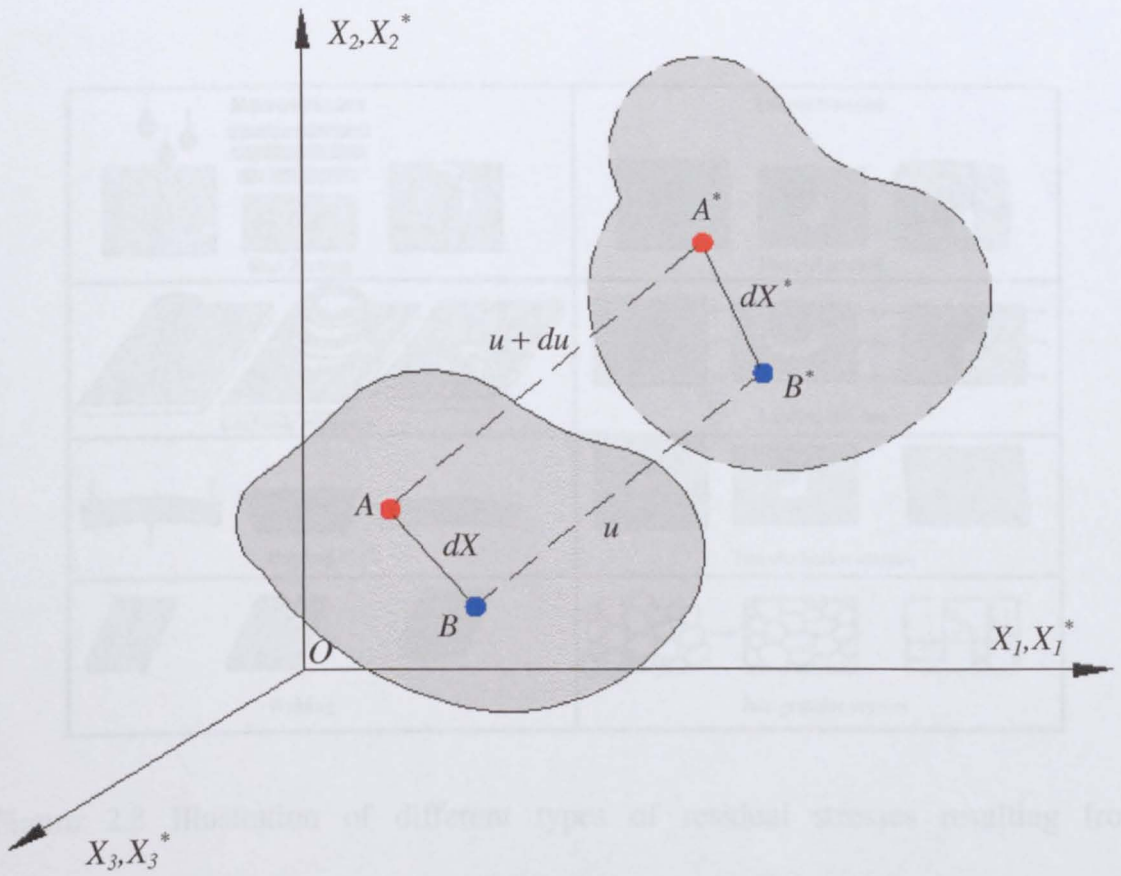

Figure 2.6 Undeformed and deformed configuration of a material continuum.

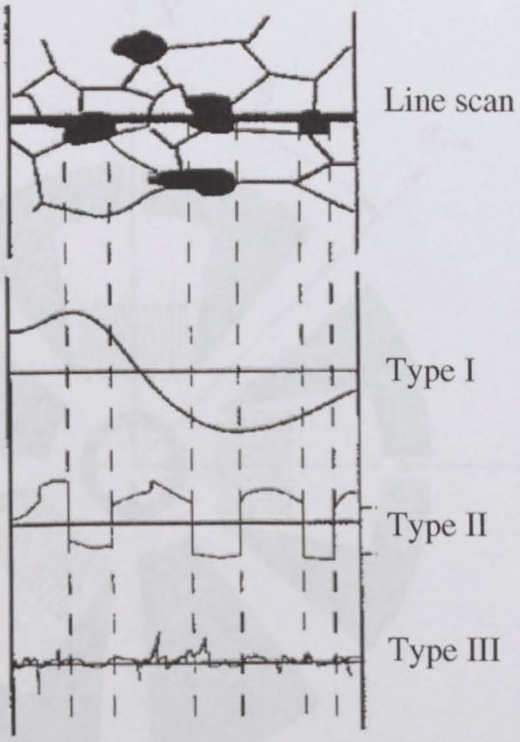

Figure 2.7 Schematic variation of Type I, II and III residual stresses over length scale [18].

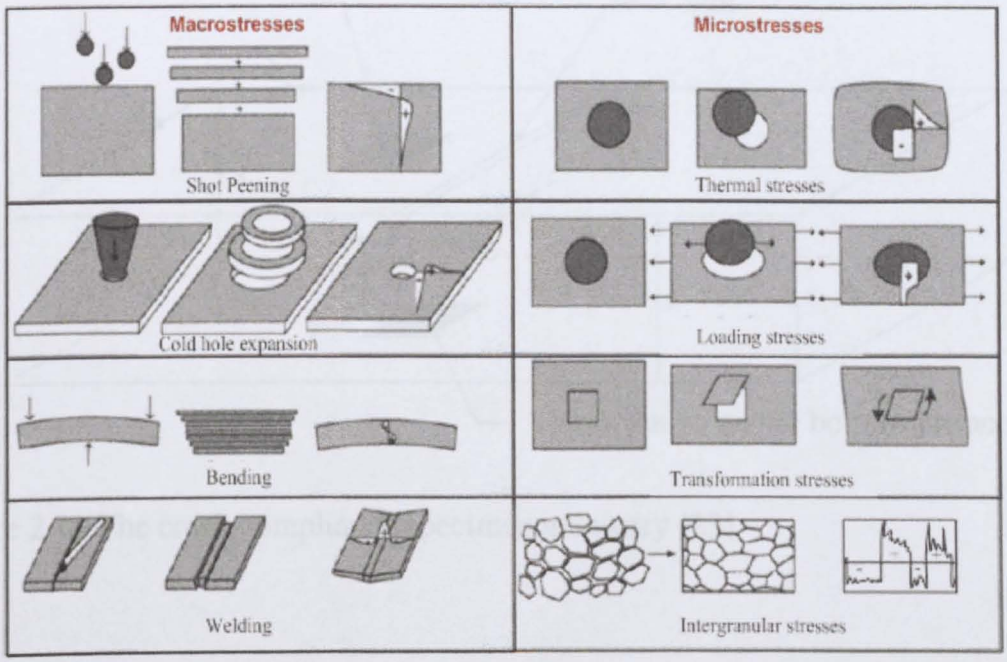

Figure 2.8 Illustration of different types of residual stresses resulting from manufacturing processes [20].

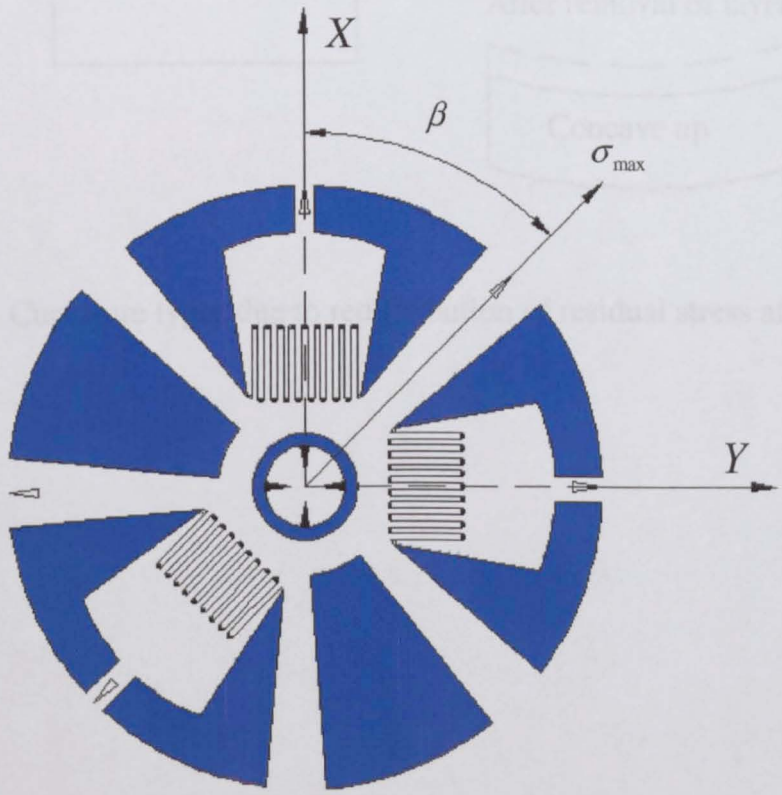

Figure 2.9 ASTM type hole drilling strain gauge rosette [22].

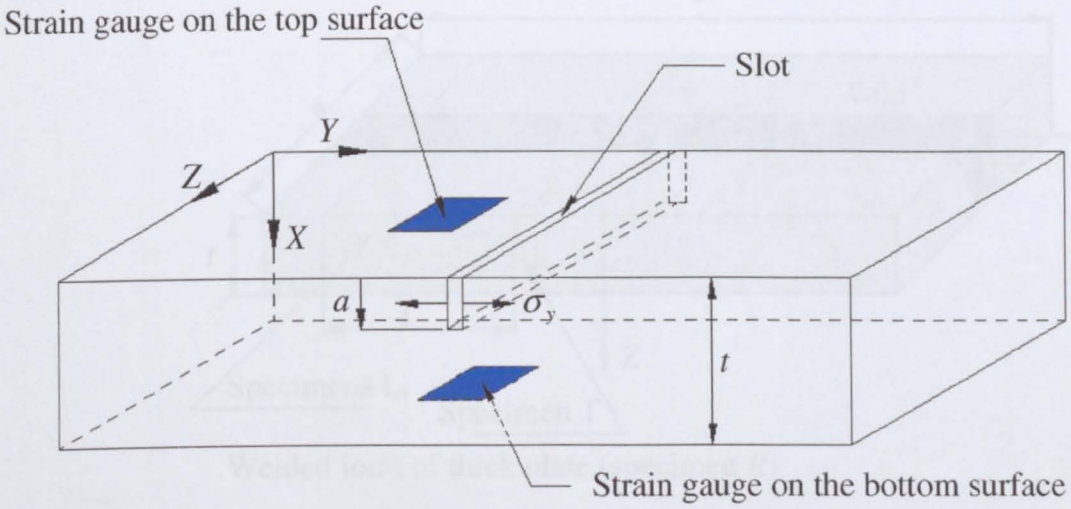

Figure 2.10 The crack compliance specimen geometry [23].

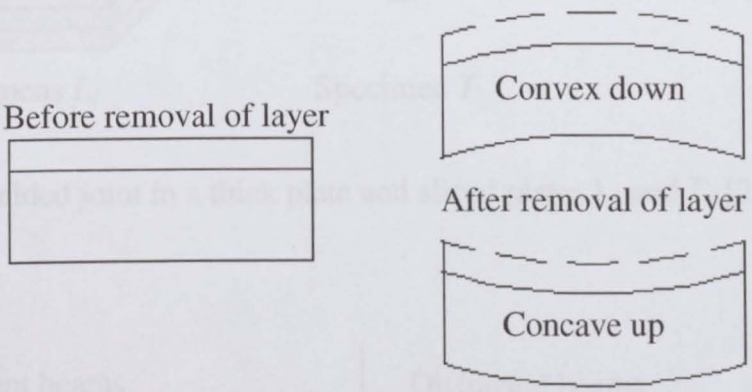

Figure 2.11 Curvature types due to redistribution of residual stress after removal of a layer.

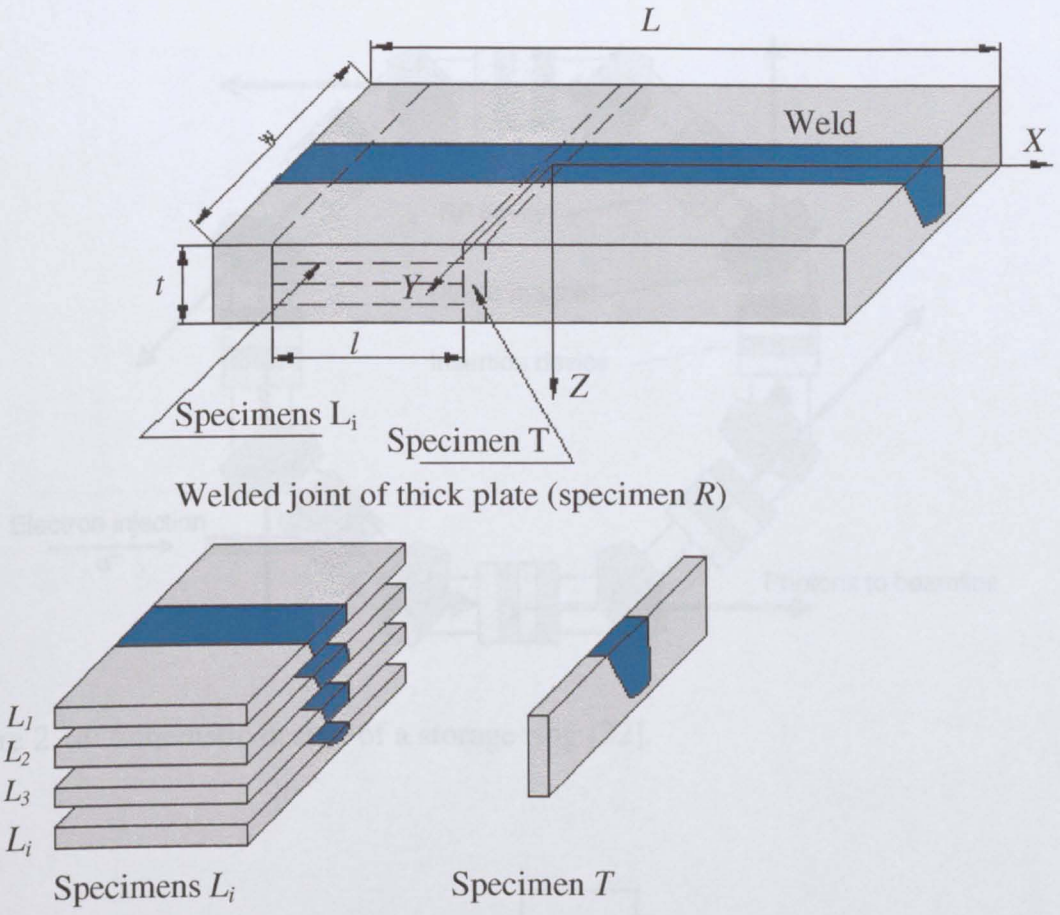

Figure 2.12 Welded joint in a thick plate and sliced plates L_i and T. [27].

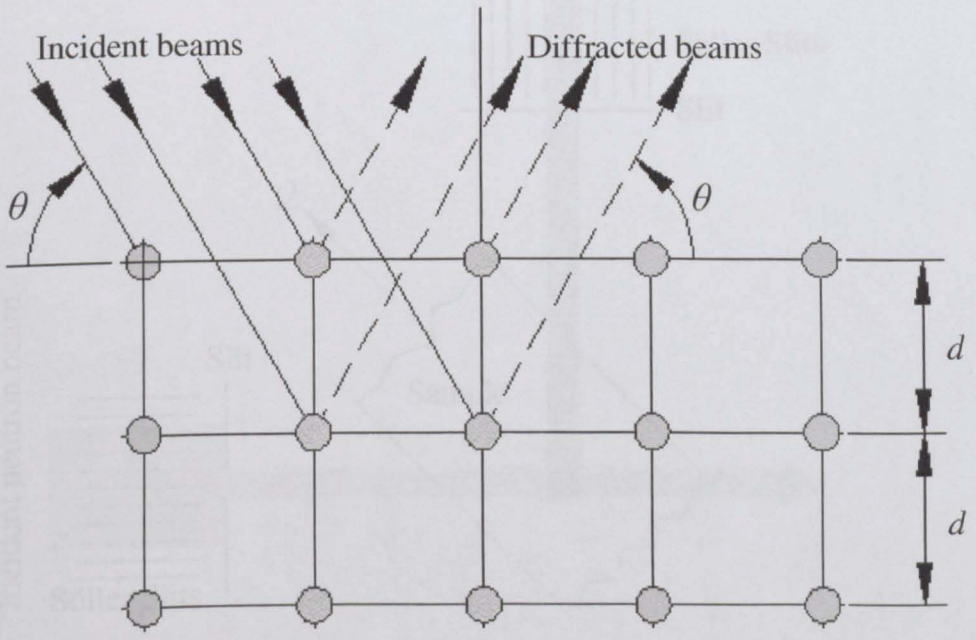

Figure 2.13 Bragg's Law - Diffraction of X-rays by a crystal.

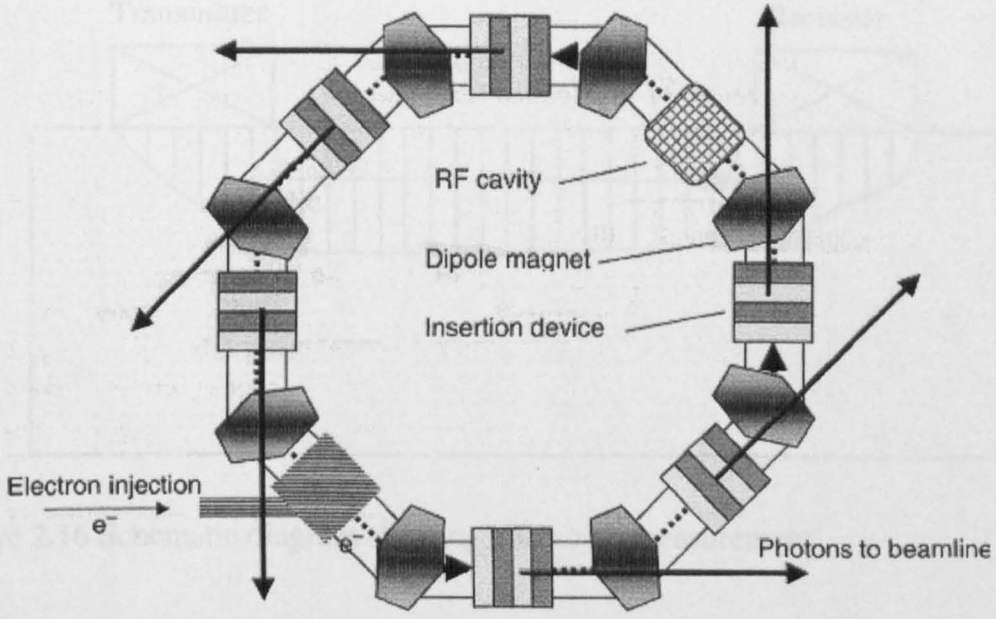

Figure 2.14: Schematic design of a storage ring [32].

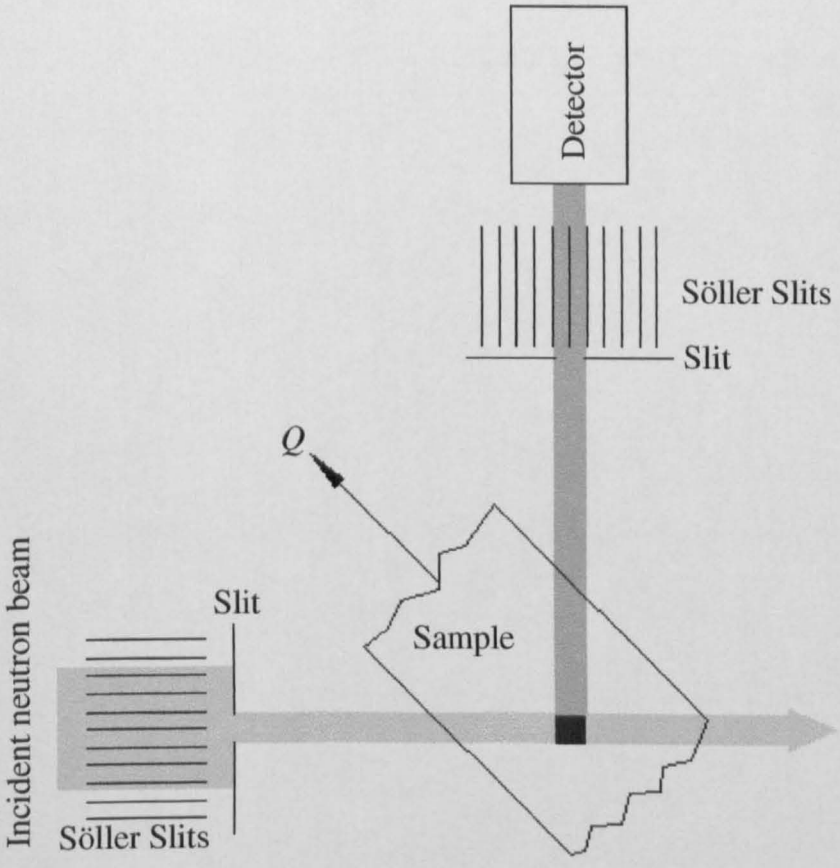

Figure 2.15 Schematic diagram of a neutron diffraction setup.

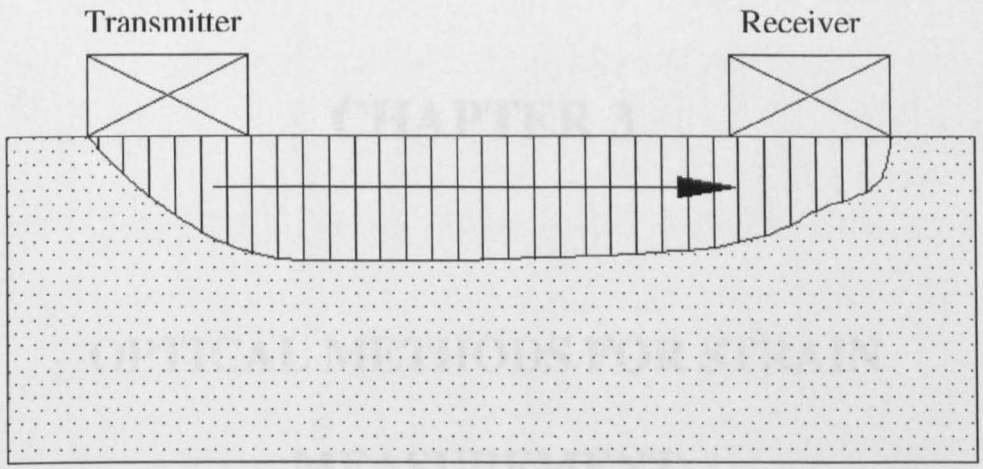

Figure 2.16 Schematic diagram showing ultrasonic measurement.

CHAPTER 3

OPTICAL METHODS FOR STRAIN MEASUREMENT

3.1 Introduction

Conventional techniques for measuring surface strains and displacements utilize strain gauges, extensometers, LVDTs and various other mechanical and electrical devices. These techniques have the capability to measure surface strains with very high sensitivity and accuracy. In this way load-strain relationships can be monitored by applying these devices to regions along which the strain variation is known to be uniform.

With the rapid developments of complex industrial applications in recent years, these strain measurement techniques have become inadequate for measuring the surface strains and mechanical properties of materials in most engineering applications. For instance, most conventional methods are unsuitable to be used in thermo–mechanical experiments due to their limitations at high temperatures. Another example is for welded joints; determination of the mechanical properties and performance of welded joints require strains in large regions to be measured with high accuracy due to the high strain gradients. However, traditional strain

measurement methods provide averaged information over limited regions. Therefore to build up an overall image of the strain or displacement distribution requires many separate measurements in a welded joint experiment. In the case of contact mechanics problems, the contact length can be very small, especially under small loading, and measuring the strain for this region might be very difficult, inaccurate and time consuming.

Although inexpensive and effective for some applications, conventional techniques of measuring strain-displacement provide only localized information and cannot be applicable for complex industrial applications owing to their limitations as explained above. Using conventional methods in these cases also requires careful and skilful application and are time consuming.

As alternatives to conventional strain measurement techniques, there have been many innovative developments in experimental mechanics in recent decades. Many of these developments involve optical techniques for the assessment of strains or displacements, and they comprise either significant advances in the capabilities of existing methods such as in the area of applied photoelasticity, or novel techniques such as digital image correlation and electronic speckle pattern interferometry. Specifically, with the help of computerized systems which enable to evaluate images they have made feasible the development of many innovative and complex optical measurement techniques.

The stimulating innovations in the experimental mechanics nevertheless have not been fully reflected in industry for structural integrity applications. The main issue is

because of lack of fully standardization of these techniques. The standards in this field are given by ASTM E2208 [1]. Instead of adopting modern advances in optical methods for evaluating full-field strain measurements by industry, using the data from the experiments to validate numerical experiments has been progressively more recognized. For this purpose, many industries use Computer-Aided-Engineering (CAE) tools to reduce the number of prototype builds and to accelerate the development cycle. These analytical and numerical methods are relatively inexpensive to utilize and faster to apply than expensive experimental techniques. However, the limitation with many numerical tools is that they can not sufficiently quantity the mechanical properties of the materials. To put it in a different way, these properties in many cases are given as input values to the Finite Element Method (FEM) and used to predict the reactions of materials under specific case problems, especially complex structures, providing severe challenges to reliable modelling.

Therefore, efficient physical experimental techniques are still necessary for component design validation, particularly for new materials. However, since their working principles are firmly based on the basic principles of optical phenomena, any real and measurable progress in optical methods is dependent on a deeper understanding of the phenomena underlying these techniques.

In this chapter I will briefly explain some optical techniques that have found wide usage in industry. Later, the principle of the digital image correlation (DIC) method will be given in detail. Finally, the experimental verification of DIC with the help of strain gauge measurements on 2024–T351 aluminium alloy will be demonstrated.

3.2. Optical Methods

3.2.1 Photoelasticity

Amongst the many optical methods of stress or strain analysis, photoelasticity is one of the oldest and the easiest techniques to implement for experiments. The principle of the method is based on the property of birefringence, which is displayed by certain transparent materials, such as glass or plastic. Birefringence is a property arising from the fact that a ray of light passing through a birefringent material experiences two refractive indices.

In order to utilize birefringence in stress analysis, the model is placed between two crossed polarising filters as shown in Figure 3.1. The first filter (polariser) produces a linearly polarized light source for the sample. When this polarised light is incident onto an unstressed photoelastic model, it passes through unaffected and might be entirely extinguished by the second polarising filter (analyser) whose axis is perpendicular to that of the first polariser (Figure 3.1). When the material is under stress, the source ray is to split into ordinary and extraordinary components which are so-called double refracting [2]. Their directions at any point coincide with the directions of the principal stresses at that point. These two rays travel at different velocities and can interfere with each other, which results in a phase difference. The analyser takes components of the ordinary and extraordinary rays, only their horizontal component is transmitted as shown in Figure 3.1 and these will combine to produce fringes. As the level of birefringence is proportional to the stress, differently stressed areas will have different a number and density of fringes. To

illustrate this, the optical pattern visible within a circular disc of epoxy resin that is in compression across its vertical diameter is given in Figure 3.2 [3].

Photoelasticity is especially useful for the analysis of geometries with unconventional boundaries and stress concentrations. The method is applied on a two dimensional model manufactured from a birefringent material. For stress concentration experiments, for example, regions of high stress can be determined in general by simple observation. However, precise analysis of tension, compression, and shear stresses and their strain values at any point on the sample requires more advanced techniques. Photoelasticity is typically utilized on models which are stressed in two planar directions (biaxial), but with additional modifications it can be used for the samples subjected to stresses in three spatial directions.

3.2.2 Moiré and Moiré Interferometry

The moiré methods are optical techniques commonly used for measuring strains and displacements with very high accuracy in solids subjected to mechanical deformations. Moiré is a generic name used for full-field measurement techniques that involve gratings which can be formed as line, cross and circular. The moiré phenomenon occurs whenever multiple gratings lie in contact with a small angle between the grating lines, and a fringe pattern which has a lower frequency than for the individual gratings is seen. This is an example of the moiré effect and the resulting fringes are called moiré fringes or moiré pattern [4]. Figure 3.3 shows formation of moiré fringes by superimposing two line patterns which vary in line spacing and rotation [5].

It has been shown that moiré fringes are interference patterns produced by the superposition of two sinusoidal gratings. If the mathematical expressions for two grating lines that produce the moiré pattern are known, then the moiré patterns can be described analytically. In the implementation of the moiré methods to determine strain or displacement fields, only one of the gratings is expressed analytically. When the material is under stress, the grating on the specimen and the moiré pattern show a complex shape depending upon the deformation of a specimen. The relation between the grating lines and the moiré fringes can be acquired by utilizing some parametric properties with the help of mechanical and numerical procedures [6]. Since the fringes are formed from the mechanical crossing of the two gratings, the moiré effect is therefore often termed mechanical interference. [6]

Numerous moiré techniques have been developed to measure displacement by two displaced gratings, or to measure in-plane deformations and strains, or even out-of-plane deformations [4]. In the case of the geometric moiré technique, which involves relatively coarse gratings of 40 lines/mm or even coarser, a minimum of 0.025 mm of deformation is required to generate a single fringe. This density would perhaps be adequate to measure large deformations. In the case of small deformations, such as elastic deformations however, a much higher density is required. Moiré interferometry extends the capacity of classic moiré techniques in to higher sensitivity domains.

Figure 3.4 illustrates the principle of moiré interferometry. In this technique [7], a very fine diffraction grating is placed on the specimen. Two laser beams symmetrically illuminate a specimen grating such that diffracted beams materialize

normal to the surface of the grating. When the grating is undeformed, diffraction from the beams emerges perpendicular to the grating with an undeformed wavefront and there is no interference occurring. During mechanical or thermal loading of the specimen, the grating deforms together with the specimen, and thus deformation of the grating represents the deformation of the specimen. These two beams create the virtual reference grating in their intersection zone. The deformed grating and reference grating interact to produce a moiré fringe which is visualized as contour map of the displacement and is analysed to obtain the specimen deformation.

Moiré interferometry offers an exclusive combination of high sensitivity, good contrast, and spatial resolution, and shows noteworthy advances in optical methods for stress analysis. The frequency of the specimen grating is typically 1200 lines/mm up to 4000 lines/mm, corresponding to a displacement resolution of 0.2 μm and this significantly improves the sensitivity of the moiré method. The sensitivity of moiré interferometry can be improved further by employing what is known as phase shifting interferometry [8]. This technique allows the fractional fringe values, i.e. those values in between the full fringes, to be determined very accurately hence it effectively increases the displacement sensitivity of the moiré interferometry. The application of the method requires that the optical phase of one of the beams be shifted relative to the other in three or more steps. Each fringe pattern, with a constant phase shift between them, is digitally captured and the consequent set of intensity values at each pixel is solved to give the relative displacement from fringe centre to fringe centre. It has been reported that the improvement in resolution of phase with this method can be as high as two orders of magnitude [8]. Therefore,

displacements as small as 5 nm may be detected with the proper implementation of the phase stepping technique.

3.2.3 Speckle Methods

The 'speckle' phenomenon is a generic name for the two optical techniques for measurement of the full-field displacement. These are speckle photography and speckle interferometry. A 'speckle' can be described as a spot having unique shape and intensity. It is generated by means of the interference of multiple lights reflected from the test surface. The properties of the speckle are due to the local surface imperfections of the specimen.

Speckle techniques can be divided into two main groups: incoherently superposed or coherently superposed. If the speckle technique does not posses a reference beam and if it employs incoherent recording of two speckle fields, then it is so called speckle photography. If the speckle technique utilizes optical interferometers which are based on the coherent addition of speckle fields diffracted by a specimen and if a reference beam exists, two resulting interference fields can be correlated. The comparison of these two fields denotes the state of the specimen before and after deformation. Each one is generated by coherent superposition of the reflected speckle and a reference wave. This is so called speckle interferometry [9].

A significant type of speckle interferometry is electronic speckle pattern interferometry (EPSI). The basic theory of ESPI, which was developed in the early 1970s [10-12], is based on the generation of fringe patterns.

The generic system of ESPI consists of two parts: optical parts and electronic parts. The optical parts include a coherent beam of light which is typically a laser, the beam path to arrange the illumination direction, and a beam splitter to split the laser beam into two beams. The electronic part includes a charge coupled device (CCD) camera, fringe generation and fringe analysis. This part provides the information encoded in the interferograms.

Figure 3.5 shows a typical example of an ESPI system to measure the full-field displacement in the X direction [13]. The specimen is illuminated by the laser beam at an angle θ to the surface normal to the test specimen. Since the test surface of the specimen is optically rough, the speckle image of the undeformed specimen is formed by CCD camera controlled along the Z axis. A reference wave, which is scattered at the surface of the sample, and nominally of normal incidence, is added to the image. By interference between the specimen speckle pattern and the reference field, a new speckle pattern emerges on the CCD target [14]. This is recorded into the computer as a reference pattern.

When the specimen is subsequently subjected to load, the test specimen undergoes deformation along the X direction and the beam is again scattered on the surface, which causes a change in the speckle patterns and interference patterns which are again imaged by CCD camera and stored in memory.

The ESPI software is then employed to produce displacement maps from the speckle pattern. First of all, the image of the speckle is subtracted from the reference pattern (before deformation) to obtain the resulting interferogram of alternate light and dark

fringes, which are called correlation fringes as they are acquired by correlating the intensities of the resulting speckle patterns recorded before and after deformation. Typically, this is performed during the acquisition process. These fringes represent contours of equal displacement in the direction of the X-axis. The spacing of the fringes is inversely proportional to the displacement. Two successive dark or bright fringes represent a displacement whose exact value deepens upon the wavelength of the laser light source used in the ESPI.

Since ESPI was invented, the algorithms to simplify measurement procedures have been continuously developed. The analysis of the intensity is mathematically performed using fringe wrapping and unwrapping [15]. The utilization of the phase-shifting technique [16] as in the case of moiré interferometry, provides a simple and easy approach to facilitating use of ESPI. The basic principle of the phase-shifting technique is based on shifting the phase of one laser beam and producing speckle patterns which corresponds to the given phase-shifting values. Then, the phase related to the deformation of the specimen can be determined by retrieving the phase-shifting intensities. For each measurement, three phase shifted images are created: 0°, 90°, and 180°. They are combined to form a final pattern to be evaluated by fringe wrapping to yield a 2π phase distribution map. Then the surface displacement map is determined from the phase map by fringe unwrapping.

The spatial resolution in ESPI depends on the resolution of the CCD array used to obtain the pattern, and the dimension of the specimen. This means that the maximum feasible spatial resolution for the displacement measurement would be equal to one point per pixel. However, in most experiments, the displacement is not

measured with such resolution. Instead of pixel size, the spatial resolution actually relates to the speckle pattern. If the speckle is very small (about pixel size), decorrelation will occur and pattern quality consequently reduces. This results in noise in the displacement. Therefore, the spatial resolution is considerably larger than the pixel size.

3.3 Digital Image Correlation

3.3.1 Introduction

Digital image correlation (DIC) is an optical technique used to measure deformation on a sample surface, based on modern digital image acquisition and processing technology. The method uses a natural or artificial surface speckle pattern and cross-correlates two slightly different images obtained before and after the deformation, to provide the whole field deformation of an object.

Conventional techniques, such as photoelasticity, moiré and speckle interferometry are widely used to measure macroscopic parameters of materials, such as strain and stress. Although, they are utilized in many industrial applications, all these interferometric methods have limitations: it is difficult to provide stability and they are required to make effort to satisfy parameters related to stability.

As compared to special requirements of these traditional optical measurements, DIC has some advantages over the interferometric methods [17]. One of the main benefits is that digital image correlation is optically less demanding. Only ordinary incoherent light is necessary to implement this technique. Another advantage with

this method is that the optical components such as beam splitters, spatial filters, piezoelectric transducers, etc. are not required. Finally, use of a vibration isolation table is not essential. Perhaps because of advantages including non contact, real time, avoidance of exhaustive phase information and interferometric treatment in addition to the other benefits explained above, DIC has attracted much interest in recent years.

On the other hand, an important advantage of the interferometric techniques is that they normally give much higher sensitivity than DIC, so smaller displacements/strains can be measured. One way of DIC overcoming this disadvantage is to capture images with higher resolution cameras, or optically zooming into the areas of interest.

The development of digital image correlation can be dated back to early 1980s for full-field displacement or strain measurements. In the literature, Peters and Ranson [18] are seen first to employ DIC for displacement measurement where they investigated two and four displacement gradients for in-plane deformations. However, they assumed that the speckle intensity before and after deformation had one to one correspondence. Sutton et al. [19] later described a correlation coefficient by means of the intensity difference of the two digital images for a 2D displacement field. Chu et al. [20] measured rigid body rotation and rigid body translation of the specimen in order to test the accuracy of the interpolation techniques used in the methods. They found that bilinear interpolation gave better results than higher order polynomial interpolation. Among these publications, the searching tool was a coarse-fine iterative technique.

Research interest has lately been focused on improving DIC for reduced computational complexity and achieving high accuracy with reduced computational cost. In this manner, many implementations have been proposed to improve the correlation algorithms [21-22] with the Newton–Raphson iterative method [23-24], Quasi-Newton method [25], and gradient-based algorithm [26], but they will not be discussed in detail here.

Over the past two decades, the digital image correlation method has been well developed [27–29] and high accurate, fast and robust commercial software, such as LaVision [30], VIC-3D [31], ARAMIS [32] and Q-400 [33] are used for image processesing.

3.3.2 The Principle of Digital Image Correlation

Digital image correlation utilizes the basic principle of deformation theory [34]. Unlike the other optical techniques, DIC uses purely computational methods. This technique is based on comparing the images acquired at different stages of the deformation. For this purpose, a high resolution camera system is employed to photograph the surface of the specimen. The digital images of the sample captured by the camera system during the test contain intensity measurements and they are made up of a rectangular array of grey pixels. These pixels are assigned a bit value; for instance, if 12 bit camera is used, the dynamic range of the count will be 4095 and thus the number for grey levels ranges from 0 (black) to 4095 (white).

Since the image correlation technique is based on matching pixel grey level values between two digital images taken at different times in a deformation process, it can

be achieved in theory by using a pixel and its characteristic features in an undeformed image and searching for the pixel which maximizes a similar function in deformed images. Mostly, this function is based on a least squares formulation. The pixel which is searched in the deformed images can be discriminated among the other pixels by its grey-value, grey value derivatives or the colour. In practise, since a single grey value is insufficient to distinguish a pixel from other pixels, the neighbouring pixels are used. Such a collection of pixels is called a sub-region of the correlation window. The resulting displacement obtained from each sub-region is an averaged value of the pixels in the sub-region. Each sub-region can contain 8×8, 16×16, 32×32, 64×64 pixels etc. and the size of the sub-region depends on the deformation magnitude. For example, in the case of plastic deformation, a sub-region is usually chosen with more pixels in order for two images to be correlated before and after deformation.

Figure 3.6 illustrates schematically the deformation process of a square pixel array with 20 pixels in the X direction and 20 pixels in the Y direction. One of the sub-regions with 6×6 pixels is shown in this array where the dashed line symbolizes a reference (undeformed) sub-region and the solid line symbolizes the corresponding deformed sub-region. If a reference point (x_0, y_0) and as well as a nearby point (x, y) are selected from this sub-region as shown in Figure 3.6, and if the deformation is sufficiently small, the point of the nearby position after deformation (x', y') can be approximated by a first order Taylor series as follows;

$$x'-x = u + \frac{\partial u}{\partial x}dx + \frac{\partial u}{\partial y}dy, \tag{3.1}$$

$$y'-y=v+\frac{\partial v}{\partial x}dx+\frac{\partial v}{\partial y}dy, \tag{3.2}$$

in which u and v are displacement components to be measured in the X and Y directions respectively, dx and dy are the position differences between the reference and nearby points prior to deformation. As only 2D dimensional deformation is considered here, the displacement components and the first order displacement components for the first order Taylor series are described by the position of a nearby point.

Especially for large deformations, the positions of the reference and the nearby points in deformed images are not located at the pixel points of the digital image, so they do not have grey values. Thus, interpolation is required to gain grey values so that the intensity pattern of the sub-region can be reconstructed as a continuous grey value distribution in the deformed images. Generally higher order interpolation provides more accurate results, but requires more computation time. The selection of the interpolation depends on different requirements. Bi-linear interpolation, bi-cubic interpolation and bi-cubic spline interpolation are widely used. For instance, in bi-linear interpolation, the grey level value $f(x,y)$ at a point located between four neighbouring pixel points is acquired as

$$f(x,y)=c_1x+c_2y+c_3xy+c_4 \tag{3.3}$$

In which c_1, c_2, c_3 and c_4 are constants which can be determined from the grey level values of the four nearby pixel points.

With the help of the assumption explained above, the displacements and displacement gradients are determined by a cross-correlation coefficient or least

squares correlation coefficient. For simplicity, this least squares correlation coefficient C is defined such that $f(x,y)$ and $fd(x',y')$ are the grey value distributions of the undeformed and deformed image, respectively. For a sub-region S, a correlation coefficient C is defined as

$$C = \sum_{i,j=-S/2}^{S/2} \left[f(x_i, y_j) - fd(x_i'-y_j') \right]^2 . \tag{3.4}$$

The size of the sub-region is represented as $S \times S$. When $C=1$; the two sub-regions are correlative fully, and when $C=0$, the two subsets are not correlative. Therefore, minimization of the coefficient C provides the best estimation of the correlation. Minimization of the correlation coefficient C is a non-linear optimization process, which can be achieved by using iterative methods.

3.3.3 Procedure of Data Acquisition

Since digital image correlation involves complicated mathematical procedures, it is challenging for experimentalists. However, by means of sophisticated software packages the mapping process becomes automatic. In this dissertation, all of the computational analyses have been performed by using the DIC software Strainmaster package, DAVIS, developed by LaVision [30], which was originally developed for particle image velocimetry [35].

This software involves image pre-processing, correlation, displacement vector processing and visualisation. The algorithm of the software uses cyclic Fast Fourier Transform (FFT) with iterative decreasing and deforming search array procedure [30]. With this technique, the algorithm is much faster than the conventional cross correlation method [36]. This feature enables use of multiple iterations, thus it is

possible to get the highest correlation between the initial sub-region prior to deformation and the translated or deformed sub-region.

Prior to displacement vector calculation using DAVIS software, some image processing needs to be completed. Although there are many processes available for different purposes in the software, only two of them, which were routinely used in our experiments, will be briefly mentioned here. The first process prior to displacement calculation is called shift-correction. Following acquisition of the first image there is generally a shift and/or rotation of subsequent images, and the effect of this on the final displacement result must be removed. This is achieved by choosing a point on the first image and ensuring the subsequent images are shifted relative to that selected point. In other words, the displacement value at the end of the image processes will be obtained relative to that point. Following the shift-correction process, the second procedure is to define a work space so that the displacement vector process can be implemented in the particular region of most interest without analysing out of that region. This process is thus a time saver.

Once these procedures have been completed, displacement vector processes are employed. For this purpose, the correlation mode is defined. For 2D displacement measurement by DIC, typically two different approaches, auto-correlation and cross-correlation are utilized. The techniques of the two modes are given in Figure 3.7. In the auto-correlation mode the original image contains a single frame as a double exposure. The algorithm calculates the auto-correlation of all the sub-regions in this original image by using the FFT. The highest peak obtained from this process is always at the zero displacement (0/0) owing to the self-correlation [30] thus, this

peak is ignored. The second highest peak in the auto-correlation is generally representative of the displacement vector *ds*. Since the auto-correlation is symmetric and results in a direction uncertainty, it is not usually preferable as an assessment method. Therefore, the cross-correlation mode is used because of the more accurate calculation of the displacement vector. In cross-correlation mode, the original image contains two frames, upper (first frame) and lower (second frame) part. The first frame contains the first exposure whereas the second frame contains the second exposure. The algorithm computes the cross-correlation of all sub-regions between first and second frames. The highest peak in the cross-correlation image is usually the displacement vector *ds*. There is no peak value at the zero-displacement (0/0) [30].

The iterations for calculating the displacement vectors can be done by a single pass or multiple passes. Single pass is the simplest and quickest choice as vector calculation is done in only one pass. During the process, the sub-region size remains constant. The accuracy of the calculation of the vector field with a single-pass is usually not high. If multi-pass is chosen, calculation of the vector field is achieved with a number of iterations specified. In each pass a reference vector is calculated at each sub-region. The calculated vector field is utilized as a reference vector field for the next pass. By means of the information from the previous pass the position of the sub-region in the new pass is shifted. This helps to compare matching particles and improves the signal-to-noise ratio. In addition to multi-pass, the size of the sub-region can be selected to be smaller after the initial iteration. Hence, the computed vector results in the first pass are used as a best-choice sub-region shift. With the

help of this, the sub-region shift is sufficiently improved to calculate the vectors in the next steps more precisely and more consistently [30].

Splitting the images into regular sub-regions is essential and the size of the sub-region chosen has an effect on the resolution and accuracy of the computed displacements. Once again, each sub-region gives a single average displacement value and this displacement can be mathematically obtained by correlating the sub-regions in subsequent images. In fact the higher number of the features in each sub-region, the lower the uncertainty in strain/displacement calculation. However, choosing a higher number of pixels for sub-regions reduces the spatial resolution. Fortunately, by means of overlap, a large enough sub-region can be chosen without losing spatial resolution. Table 3.1 shows the accuracy of the calculated vector for different size of the sub-regions for DAVIS software. For instance, if the sub-region size is chosen as 64×64 with a 25% overlap, so the actual density of a sub-region in an image is (64×64)×(75%) = (48×48). The vector error from the table is then 0.05, and the error in the strain is calculated as 0.05×2/48=0.002=0.3% where 2 is used because two vectors are used.

Table 3.1 Accuracy of the calculated vector by strain master software [30]

Size of the sub-region	Accuracy of the calculated vector
128×128	down to 0.01 – 0.03 pixel
64×64	down to 0.02 – 0.05 pixel
32×32	down to 0.05 – 0.2 pixel
16×16	Larger than 0.1 – 0.3 pixel

3.3.4 Some Experimental Issues in Digital Image Correlation

There are several important experimental issues that need to be taken into account during the experimental setups. In this section, some of them will be given briefly.

- Illumination and contrast

In the DIC technique ordinary incoherent light is sufficient for the measurements. However, the illumination must be distributed onto the surface uniformly and constantly during the experiment in order to get accurate results because surface contrast is directly related to quality of the lighting system. High contrast is vitally important as explained above; each sub-region must have unique characteristic features in order to track it in the subsequent images. Digital images with high contrast can also be enhanced by applying a random speckle pattern on the surface of the sample using paint or other means.

- Calibration

Calibration of the optical magnification is an important step for further image processing in DIC, because the cameras count pixels rather than the actual dimensions of the specimen. Therefore, the pixel size for each particular field of view prior to each experiment has to be calculated. In addition, the calibration has to be repeated if the distance between object and camera has changed.

- The effect of rigid body motion

The incidence of rigid body motion is a common problem for almost all optical techniques. Especially, if the testing conditions are not stable, image decorrelation can occur. Rigid body motions arise due to vibration in the system, poorly mounted

fixtures or jumpy motion of the system. However, the effect of rigid body motion is not a very important problem for the DIC technique since it can be removed during the analysis. In order to do so, a shift-correction procedure is implemented by choosing a point on the image, and the displacement can be obtained relative to that point. In applications where larger deformations or rigid body motions are expected images must be taken more frequently so that decorrelation can be minimised.

Sjodahl [37] showed from experiments and analyses that the random error, e, from the use of the DIC algorithm is

$$e = \frac{k\sigma^2}{B}\sqrt{\frac{1-\gamma}{\gamma}}, \tag{3.5}$$

in which σ is the speckle size, B is the sub-region size, k is a constant and γ is the magnitude of the correlation peak. It can be seen from Eq. (3.5) that the error reduces with smaller speckles and/or a larger sub-region as confirmed from Table 3.1.

- Error due to out-of-plane displacement

In a system set up for measuring in-plane displacement of the specimen, any out-of-plane displacement such as, a change in distance between the lens and the surface, will result in a change of magnification of the imaging system, and hence induce apparent in-plane displacement [38]. This apparent in-plane displacement would cause measurement error in the normal sense.

3.3.5 Obtaining Strain Maps from Displacement Maps

As explained in the sections 3.3.2 and 3.3.3, DIC methods actually calculate displacement rather than strain. Therefore, the strain value must be computed by using the strain-displacement relations. Consider the in-plane displacement vector u in the x direction and v in the y direction, and then the resulting strain tensor for 2D is obtained as

$$\varepsilon_{xx} = \frac{\partial u}{\partial x};\ \varepsilon_{yy} = \frac{\partial v}{\partial y};\ \varepsilon_{xy} = \frac{1}{2}\left(\frac{\partial u}{\partial y} + \frac{\partial v}{\partial x}\right). \tag{3.6}$$

These strain fields can be calculated by using a simple finite difference method. Strainmaster software package, DAVIS, enables the calculation of the strain values at each of two neighbouring sub-regions. In the present work, in order to have more flexibility in the calculation of strain values from the displacement fields, a MATLAB script was programmed to calculate strain field. This script computes first the displacement values in the longitudinal direction along the gauge length of the specimen, and the strain field, by choosing a suitable differentiation range and overlap. A number of successive displacement data points (e.g. 3, 4, 5) at each column are extracted and converted into a strain value via the differentiation range. The next set of displacement values are determined by the overlap (e.g. 1, 2, 3) and the strain values are calculated. This provides a smooth variation of the strain field. The resulting strain field is then averaged and a one-column strain matrix is obtained. Furthermore, the program allows determination of Young's modulus, proof stress for any percentage, elongation at yield, ultimate strength and failure along the gauge length of the sample. The schematic diagram summarising the steps of the script is given in Figure 3.8.

3.4 Implementation of DIC on 2024-T351 Aluminium Alloy

In this section, the tests to determine the variation of mechanical properties in a 2024-T351 aluminium alloy under tensile loading are presented. Since the DIC system existing in our laboratories was used for the first time during the present work, a strain gauge was also used during the tensile test in order to see the level of agreement between the results obtained by the DIC system and the strain gauge. In addition, the stress-strain curves that were extracted from various regions of the sample were used to determine the variations of modulus of elasticity, and proof stresses at different levels of strain.

3.4.1 Material and Specimen

AA2024-T351 is a tremendously prevalent alloy for aerospace applications due to its damage tolerant characteristics [39-40]. T351 indicates the heat treatment condition of the alloy; in general the T3 temper signifies that the alloy is solutionised, quenched, and allowed to age naturally. In its naturally aged condition the alloy shows an excellent combination of strength, ductility, fracture toughness, and crack propagation resistance features. T×51 shows that the alloy has been stress relieved by stretching by 1-3% prior to ageing. The resistance characteristic of the alloy for crack propagation is almost three times more than that of the 7xxx series of alloys [41].

The specimen used for this study was cut out from a large plate of 2024-T351 aluminium alloy with 10 mm thickness. For this purpose, an Electro Discharge Machine (EDM) fed with 0.1 mm diameter standard brass wire was used. The final

size of the specimen used for the experiment was reduced to 50 mm gauge length, 9.7 mm gauge width, and 3.16 mm thickness. A picture of the specimen with its dimensions is given in Figure 3.9.

3.4.2 Experimental Procedures

The AA2024-T351 tensile test was carried out using the Digital Image Correlation (DIC) and strain gauge techniques. A KYOWA strain gauge [42] with 15 mm gauge length, 120Ω resistance, uni-axial load at one edge and 23 linear expansion coefficient matched to aluminium was glued onto the surface of the specimen. The strain gauge channels were wired by soldering and connected to a static strain gauge indicator.

One side of the specimen was strain gauged and the other side was used for DIC measurements. The tensile test was performed using a screw driven tensile testing machine (Instron 3367) with a calibrated 30kN capacity load cell at room temperature. A photograph of the Instron machine and DIC setup for the experiment can be seen in Figure 3.10.

A high resolution (4 Mega-pixels at 12 bit) monochromatic progressive scan camera (LaVision Image Pro 4) [30] was utilized to photograph the surface deformation of the specimen throughout the tensile test. A Rodenstock macro lens, with variable zoom between 0.8X and 4.0X, and a working distance of 90mm, was used in the experiment. The surface of the sample for the experiment was not polished as the EDM cutting process gave a good contrast on the surface.

After the specimen was clamped by grips, the camera was positioned and an initial image prior to the test was calibrated. In addition, the strain gauge indicator was balanced so that the strain value prior to deformation showed zero strain. Moreover, another camera was employed to capture load values from the Instron machine and strain values from the strain gauge box corresponding to each image captured. The crosshead speed of the Instron machine was chosen as 0.2 mm/min and every 2.5 seconds an image was captured during the test. In total, 275 images were obtained and all of them were stored in the PC running the LaVision software. The size of each pixel was calculated to be 8.84μm.

3.4.3 Data Analysis

After all images were stored in the computer, the data analysis was carried out. Since the images captured during the experiment may involve some rigid body motion as explained in the section 3.3.3, by choosing a reference point on the first image, the rest of the images were shifted. Then the area of most interest was extracted from each image to make the analysis quicker.

Following these steps, vector calculation was carried out. The integral strain field where all of the images obtained during the experiment were correlated relative to the first image was used to get the total deformation. Multi-pass analysis with a decreasing interrogation sub-region size option was chosen to calculate the vector field with three numbers of the iterations. The initial sub-region size was defined as 64×64 pixels with a 25% overlap. After the reference vector field was calculated in the first pass, the sub-region size was reduced to 32×32 pixels for the rest of the passes.

Subsequent to the vector analysis step, the calculated displacement field was exported from the software and input into the MATLAB data manipulation script file. The displacement vectors were used to compute the strain component in the tensile test direction along the gauge length by choosing an appropriate differentiation range and overlap as explained in the section 3.3.5. Since a homogeneous material was chosen for the experiment each row in the strain arrays was then averaged across the width of the specimen by assuming that the strain variation along the transverse direction is constant. As a result, one-column strain data were obtained. The stress-strain data curves for each averaged sub-region along the gauge length of the specimen were obtained. The MATLAB script was then used to calculate the elastic modulus and proof stress at several values of the offset strain.

3.4.4 Results and Discussions

Figure 3.11 presents the post-processing steps of the analysis performed for the specimen. As can be seen from Figure 3.11 (a), high resolution images were obtained by using the 12 bit CCD camera. Note that the wires appearing behind the image were for the strain gauge measurement implemented on the other face of the specimen. As can be seen from this figure, all images consisted of not only part of the specimen but also the background. Thus, the region which was to be investigated by the DIC method was extracted from each image after the shift and correction procedure was carried out, to remove the effects of any rigid body motion on the calculated displacements.

Following the shift-correction procedure and extraction of the relevant region, the resulting image can be seen in Figure 3.11 (b). By choosing three iterations number

with a sub-region size 64×64 pixels for the first iteration and 32×32 pixels for the next two iterations, with a constant overlap 25%, the vector calculation was carried out as explained in the section 3.3.3. The resulting displacement vector field for nominal strain of 0.37 % at an applied stress of 270 MPa can be seen in Figure 3.11 (c). From the displacement field, the corresponding strain field was calculated and the strain map for nominal strain of 0.37% at an applied stress of 270 MPa is given in Fig 3.11 (d). It can be seen from the strain map that most of the region has a similar magnitude of strain due to the homogeneous material that was used in this experiment.

In order to see the agreement level of the two techniques on the stress-strain curves for the elastic region, a plot line of averaged DIC results is compared with the strain gauge measurement in Figure 3.12. An excellent agreement was found. Note that the averaged DIC results in this figure were obtained from the MATLAB script by choosing differentiation gap distance of 4 and overlap of 2 data points. Then the calculated strain values were averaged in order to correlate with the strain gauge value.

Variation of the Young's modulus along the gauge length of the specimen was determined, which is given in Figure 3.13. It can be seen that the Young's Modulus varies between 66-74 GPa. Each data point on the graph represents the position on the specimen (i.e. sub-regions) where Young's Modulus was calculated. Uncertainty bar is also added into the figure. In order to calculate the uncertainty on the Modulus of elasticity, Table 3.1 was used. Since the sub-region size was 32×32 pixels and 25% overlap, the resulting error in the strain was found to be 1.66 %. Then using

this uncertainty in the strain, the corresponding uncertainty in the Modulus of Elasticity was calculated for each point in the figure.

Figure 3.14 shows the stress-strain curves obtained from the average DIC results and the strain gauge measurement. Very good agreement was found between the two independent strain measurement techniques. Note that since the sample for this experiment was chosen as a homogeneous material, the resulting stress-strain curves obtained along the gauge length were very similar. Therefore, showing the stress-strain curves along the gauge length on the same plot may not be necessary.

In order to see the differences between the results of strain calculations obtained from the LaVision software and the MATLAB script, the proof stress variations at 0.2%, 0.5%, 1%, 2%,and 3% along the gauge length of the sample were plotted. Here, the differentiation gap and overlap were chosen to be 4 and 2 respectively for the MATLAB script. The proof stress variations obtained from the LaVision software show some fluctuations. This is due to the fact that the Lavision software calculates the strain values at each neighbouring sub-region. In contrast, the MATLAB script calculated the strain value for each four sub-regions (owing to choosing the differentiation gap size as four). Hence, smother variations of the proof stresses from the MATLAB script can be observed. In addition, it can be clearly seen from the figure that the variation of the proof stress along the gauge length is almost constant due to the homogeneity of the sample.

3.5 Conclusion

In this chapter, the importance of optical methods in the full field measurement of displacement and strain fields was explained. Then, brief descriptions of some of the optical techniques that are widely used in experimental mechanics were presented. Next, the principle of the digital image correlation method (DIC) was given in detail. Finally, the experimental verification of DIC with the help of a strain gauge measurements on a tensile specimen made of 2024–T351 aluminium alloy was presented.

3.6 REFERENCES

[1] ASTM E2208 (2002). Standard Guide for Evaluating Non-Contacting Optical Strain Measurement Systems. In: ASTM international, West Conshohocken, PA, USA

[2] Hearn E.J. (1997). Mechanics of Materials 1. An Introduction to the Mechanics of Elastic and Plastic Deformation of Solids and Structural Materials, 3rd Edition. Butterworth-Heinemann, Oxford, UK.

[3] The Open University course T357 (2007). Structural Integrity: Designing against Failure. The University Press, Cambridge.

[4] Sciammarella C.A. (1982). The Moiré Method, a Review. Experimental Mechanics, vol. 22, pp. 418.

[5] Department of Materials Engineering webpage, The Open University, UK. http://materials.open.ac.uk

[6] Durelli A.J. and Parks V.J. (1967). Moiré Fringes as Parametric Curves. Experimental Mechanics, vol. 7 (3), pp. 97-104.

[7] Post D. (1982). Developments in Moiré Interferometry. Optical Engineering., vol. 21 (3), pp. 458-467.

[8] Huntley J.M. (1998). Automated Fringe Pattern Analysis in Experimental Mechanics, a Review. Journal of Strain Analysis for Engineering Design, vol. 33(2), pp.105-125.

[9] Wykes C., Jones R., Creath K. and Chen X.L. (1998). Part VII, Speckle Methods. Optical Methods of Engineering Analysis, Editor Cloud G.L. Cambridge University Press.

[10] Leendertz J.A. (1970). Interferometric Displacement Measurement on Scattering Surfaces Utilizing Speckle Effect. Journal of Physics E: Scientific Instruments, vol. 3, pp. 214-218.

[11] Butters J.N. and Leendertz J.A. (1971). Speckle Pattern and Holography Techniques in Engineering Metrology. Optics and Laser Technology, vol. 3(1), pp. 26-30.

[12] Macovski A, Ramsey S.D. and Schaefer L.F. (1971). Time-Lapse Interferometry and Contouring Using Television System. Applied Optics, vol. 10, pp.2722-2727.

[13] Kennedy D.M., Schauperl Z. and Greene S. (2004). Application of ESPI-Method for Strain Analysis in Thin Wall Cylinders. Optics and Lasers Engineering, vol. 41, pp. 585-594.

[14] Sirohi R. S. (1993). Speckle Metrology. New York: Marcel Decker.

[15] Macy W.W. (1983). Two Dimensional Fringe-Pattern Analysis. Applied Optics, vol. 22, pp.3898-3901.

[16] Creath K. (1985). Phase Shifting Speckle Interferometry. Applied Optics, vol. 24, pp. 3053–3058.

[17] Dally J.M. and Riley W.F. (2005). Experimental Stress Analysis, 4th Edition. College House Enterprises LLC, Tennessee, USA.

[18] Peter W.H. and Ranson W.F. (1982). Digital Imaging Technique in Experimental Mechanics. Optical Engineering, vol. 21(3–4), pp.427-431.

[19] Sutton M.A., Wolters W.J., Peters W.H., Ranson W.F. and McNeill S.R. (1983). Determination of Displacements Using an Improved Digital Image Correlation Method. Image and Vision Computing, vol. 1(3), pp.133–139.

[20] Chu T.C., Ranson W.F., Sutton M.A. and Peter W.H. (1985). Applications of Digital-Image-Correlation Techniques to Experimental Mechanics. Experimental Mechanics, vol. 25(3), pp. 232-244.

[21] Gao J.X. and Zhou X.G. (1995). Principle and Applications of Digital Speckle Correlation Method. Acta Mechanica, vol. 27(6), pp.724–731.

[22] Vendrous G. and Knauss W.G. (1998). Submicron Deformation Field Measurement: Part 2 Improved Digital Image Correlation. Experimental Mechanics, vol. 38(2), pp.86-92.

[23] Bruck H.A., McNeill S.R., Sutton M.A. and Peters W.H. (1989). Digital Image Correlation Using Newton–Raphson Method of Partial Differential Correction. Experimental Mechanics, vol. 29, pp.261-267.

[24] Chapra S.C. and Canale R.P. (1998). Numerical Methods for Engineers. McGraw-Hill Companies Inc.

[25] Wang H.W. and Kang Y.L. (2002). Improved Digital Speckle Correlation Method and its Application in Fracture Analysis of Metallic Foil. Optical Engineering, vol. 41(11), pp. 2793-2798.

[26] Zhang J., Jin G.C., Ma S.P. and Meng L.B. (2003). Application of an Improved Subpixel Registration Algorithm on Digital Speckle Correlation Measurement. Optics and Lasers Engineering, vol. 35(7), pp. 533-542.

[27] Lu H. and Cary P.D. (2000). Deformation Measurements by Digital Image Correlation: Implementation of a Second-Order Displacement Gradient. Experimental Mechanics, vol. 40, pp.393-400.

[28] Jin G.C., Wu Z., Bao N. and Yao X. (2003). Digital Speckle Correlation Method with Compensation Technique for Strain Field Measurements. Optics and Lasers Engineering, vol. 39, pp.457-464.

[29] Yoneyama S., Morimoto Y. and Takashi M. (2003). Automatic Determination Method of Stress Intensity Factor Utilizing Digital Image Correlation and Nonlinear Least Squares, Editors Wu Z. and Abe M. Structural Health Monitoring and Intelligent Infrastructure. Swets & Zeitlinger, pp. 1357-1367

[30] Strain Master Commercial Software, LaVision. (http://www.lavision.de/).

[31] Vic-3D Digital Image Correlation Program. Correlated Solutions, Inc. (http://www.correlatedsolutions.com/).

[32] ARAMIS Commercial Software. GOM. (http://www.gom.com/).

[33] Q-400 Commercial Software. Dantec Dynamics. (http://www.dantecdynamics.com/).

[34] Fung Y.C. (1965). Foundation of Solid Mechanics, Prentice-Hall, Inc., Englewood Cliffs, N.J.

[35] Stanislas M., Kompenhans J. and Westerweel J. (2000). Particle Image Velocimetry: Progress towards Industrial Application. Kluwer, Dordrecht.

[36] Fincham A.M.. and Spedding G.R. (1997). Low Cost, High Resolution DPIV for Measurement of Turbulent Fluid Flow. Experiments in Fluids, vol. 23, pp. 449-462.

[37] Sjodahl M. (1997). Accuracy in Electronic Speckle Photography. Applied Optics, vol.36, pp. 2875–2885.

[38] Asundi A.K. (1993). Speckle Metrology, Editor Sirohi R.S. Marcel Dekker, New York, 1993, pp. 325.

[39] Lequeu P., Lassince P., Warner T. and Raynaud G.M. (2001). Engineering for the future: Weight Saving and Cost Reduction Initiatives. Aircraft Engineering and Aerospace Technology, vol. 73(2), pp. 147-159

[40] Dif R., Bes B., Daniel D., Lassince P. and Ribes H. (2000). Improving the Forming Characteristics of Aluminium Sheets for Aerospace Application. Materials Science Forum, vol. 331-337, pp. 483-488.

[41] I.J. Polmear (1989). Light Alloys, 2nd Edition, Editor Arnold E., Melbourne.

[42] www.kyowa-ei.co.jp

3.7 Figures

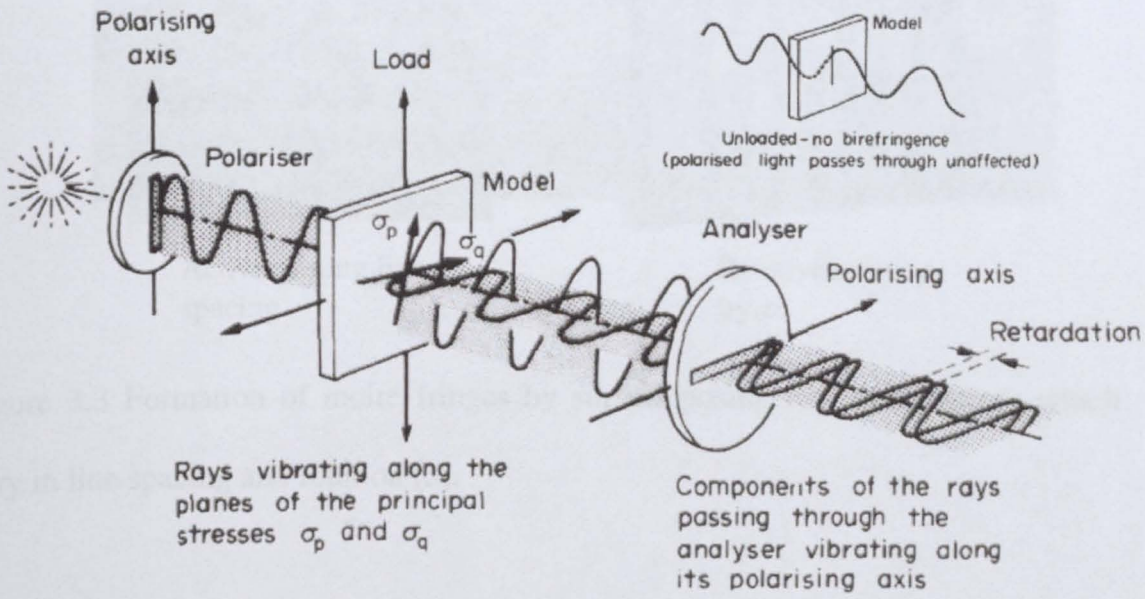

Figure 3.1 Optical arrangement of birefringence for the unstressed and stressed models [2].

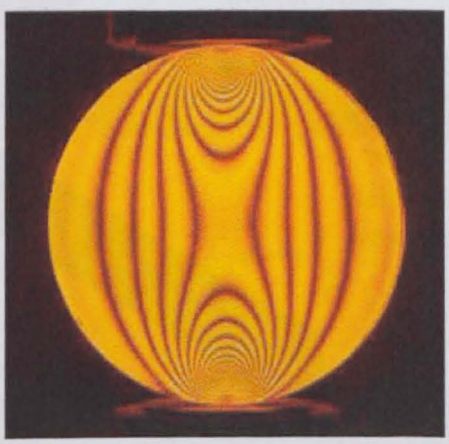

Figure 3.2 Isochromatic fringes in a disc of uniform thickness compressed across its vertical diameter [3].

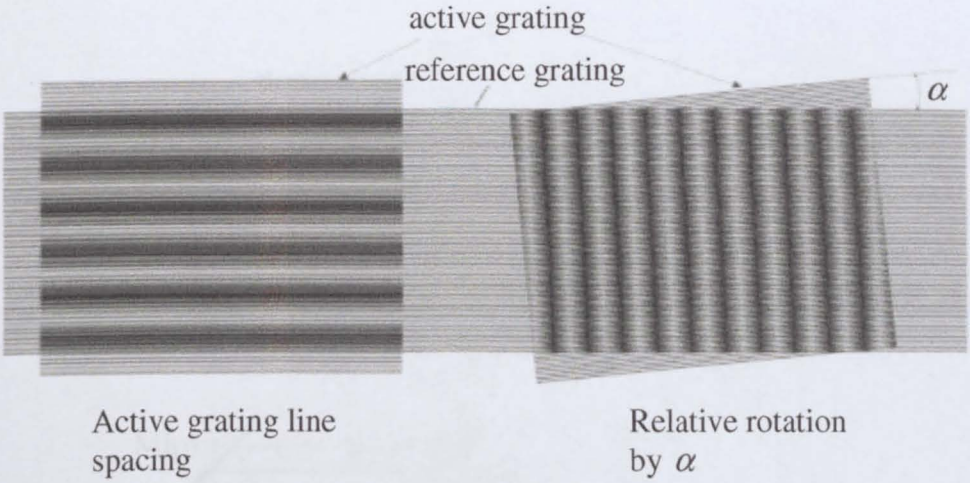

Figure 3.3 Formation of moiré fringes by superimposing two line patterns which vary in line spacing and rotation [5].

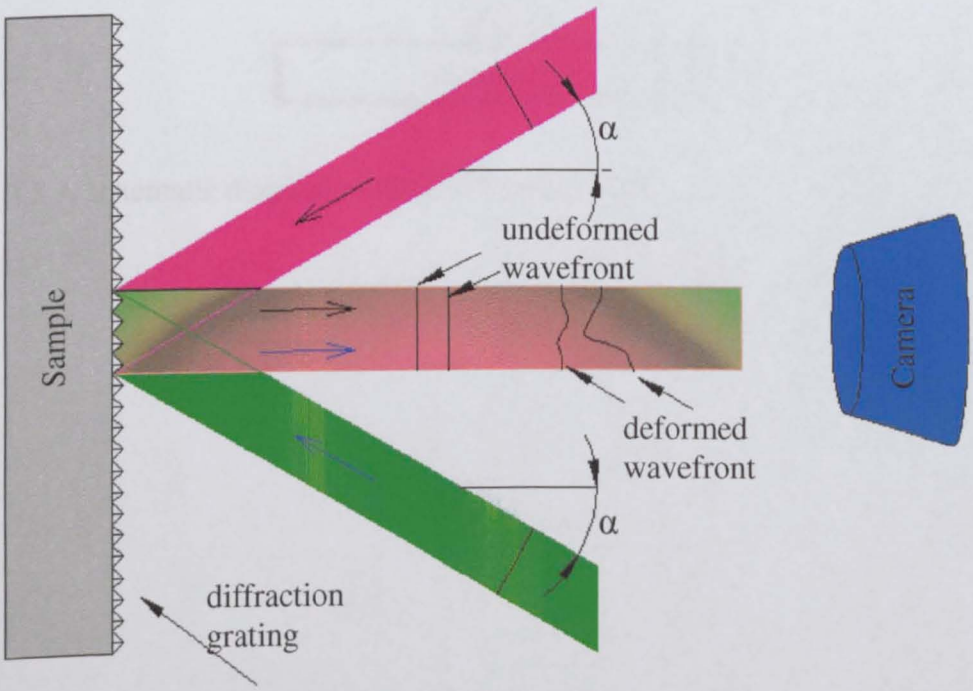

Figure 3.4 A schematic of the moiré interferometry system [5].

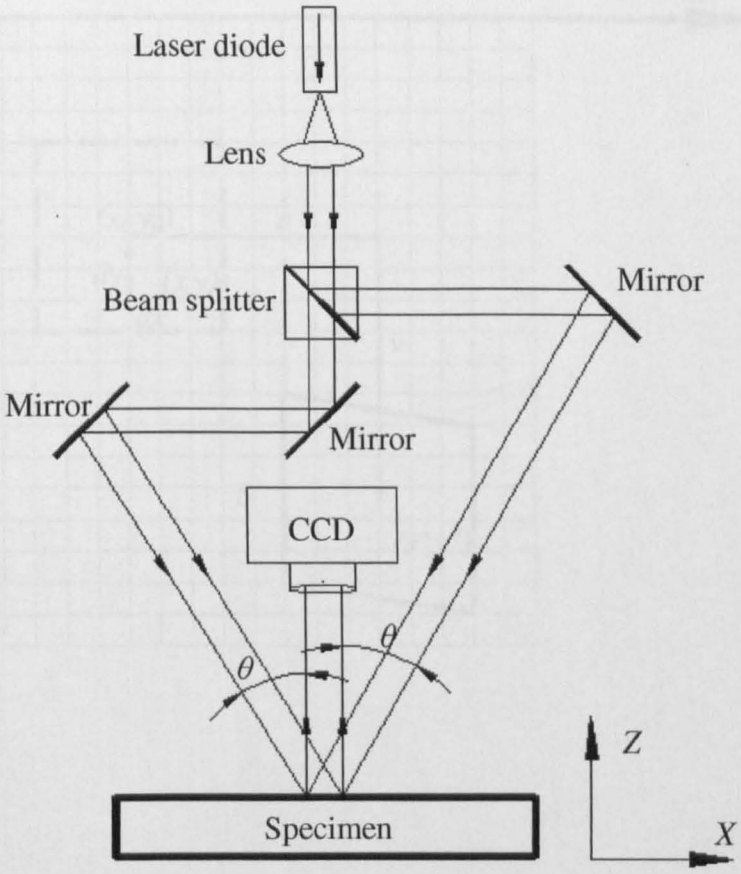

Figure 3.5 A schematic diagram of the ESPI system [13].

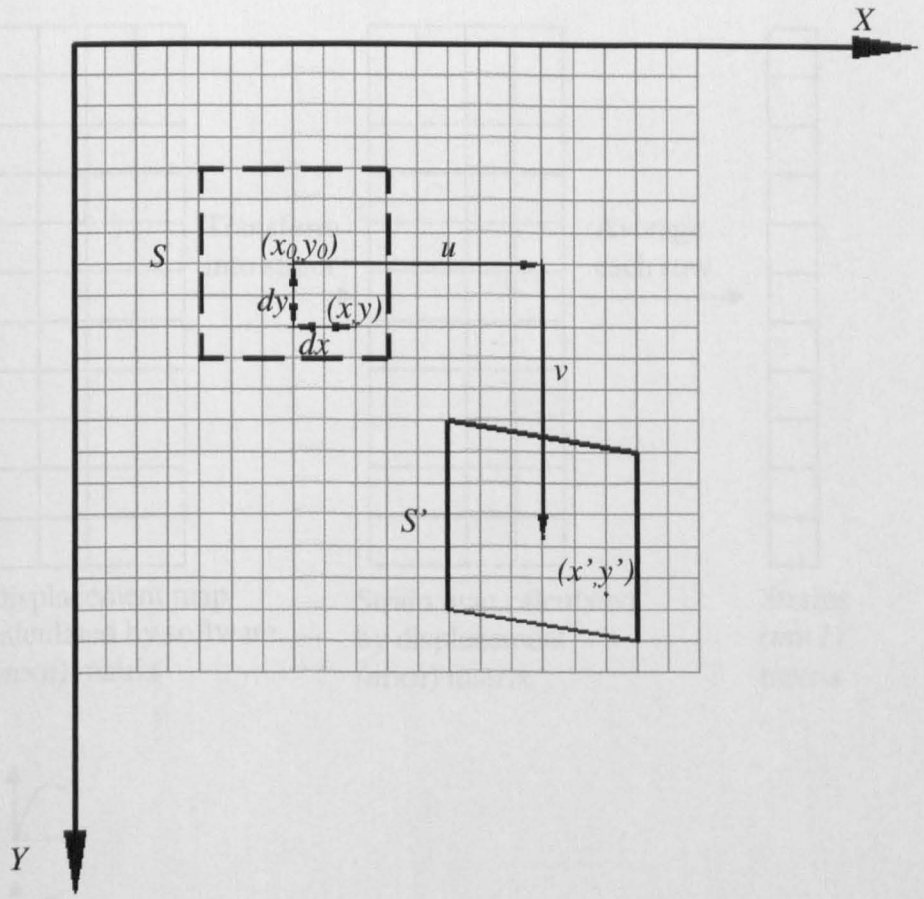

Figure 3.6 Schematic diagram of deformation process for planar object.

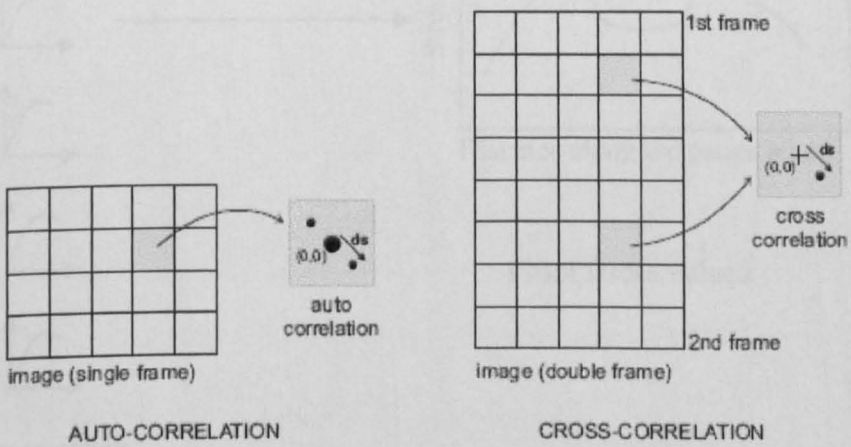

Figure 3.7 Schematic diagrams of auto and cross correlation [30].

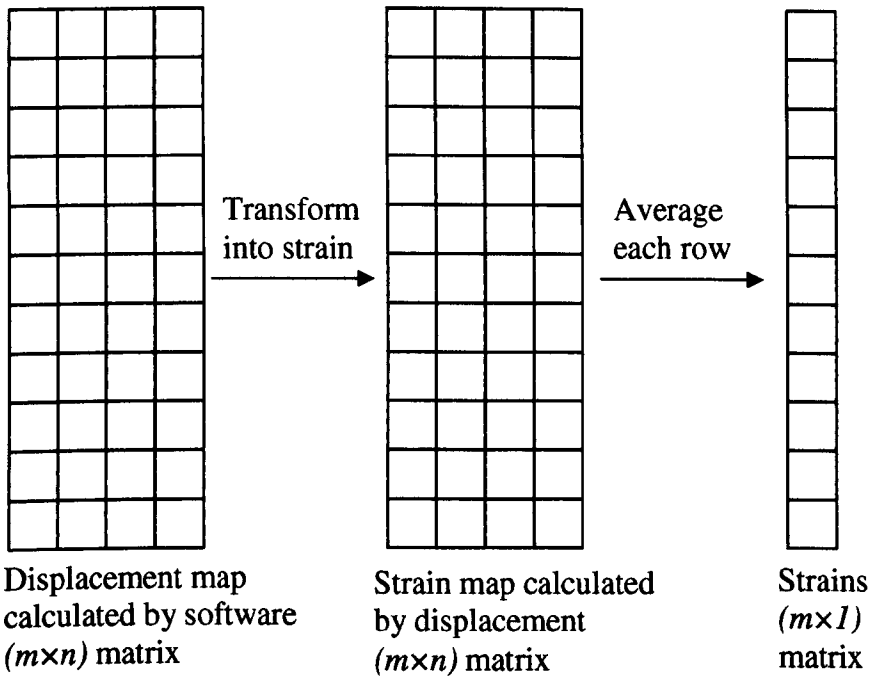

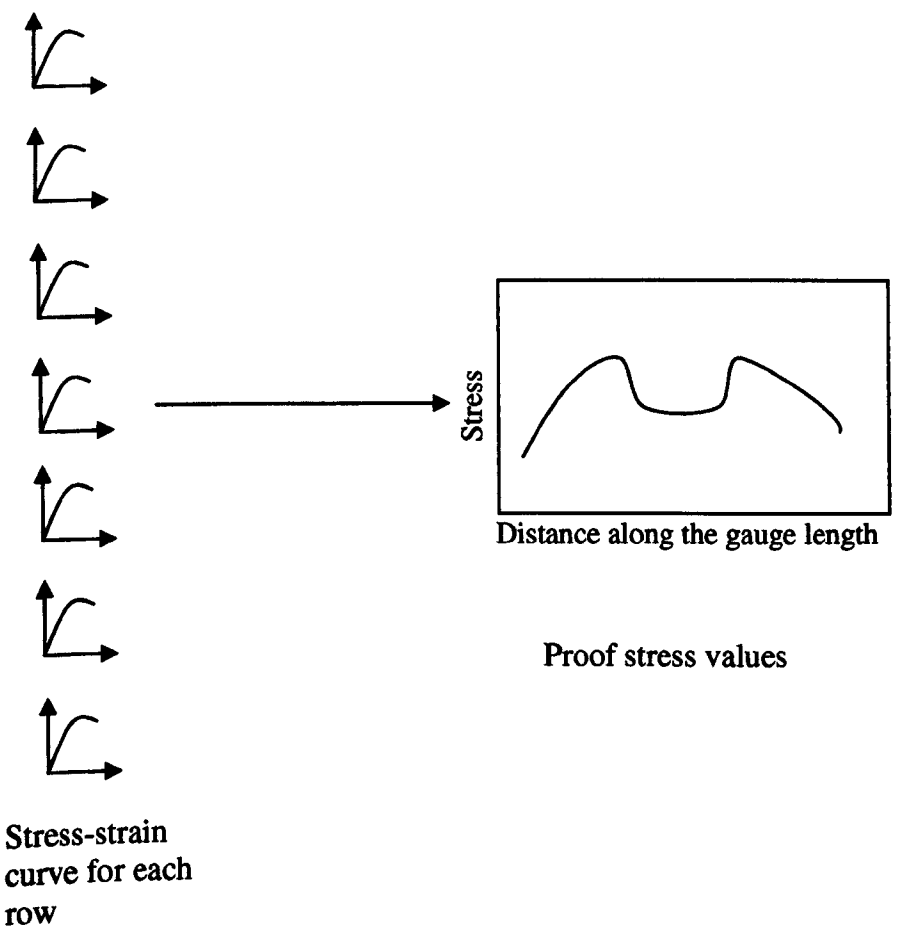

Figure 3.8 Schematic diagram showing the data analysis steps carried out by data manipulation package written in MATLAB.

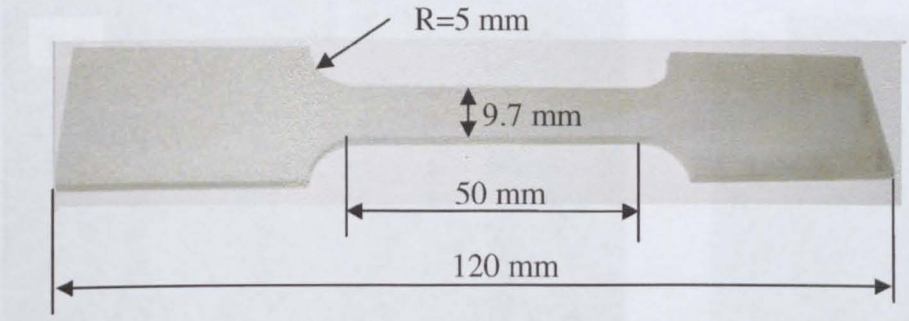

Figure 3.9 A picture of the 2024-T351 aluminium specimen with its dimensions.

Figure 3.10 A view of the Instron tensile test machine and DIC set up for the full field strain measurement on the AA2024-T351 sample.

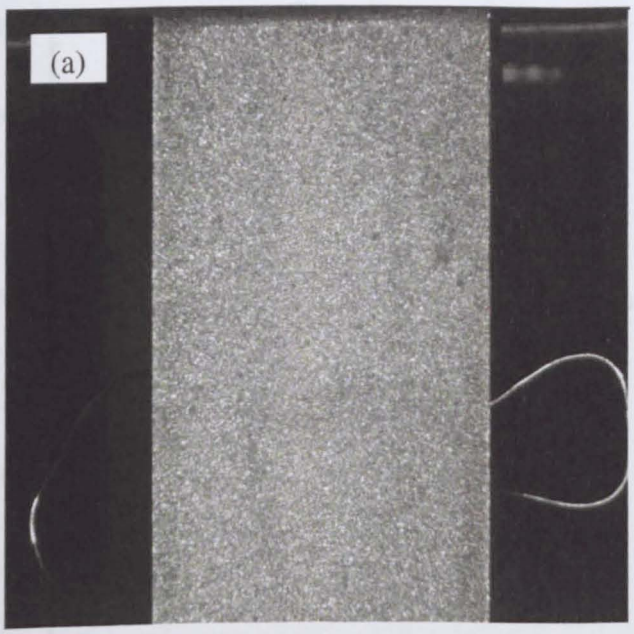

An initial Image

Extract the gauge length of the sample

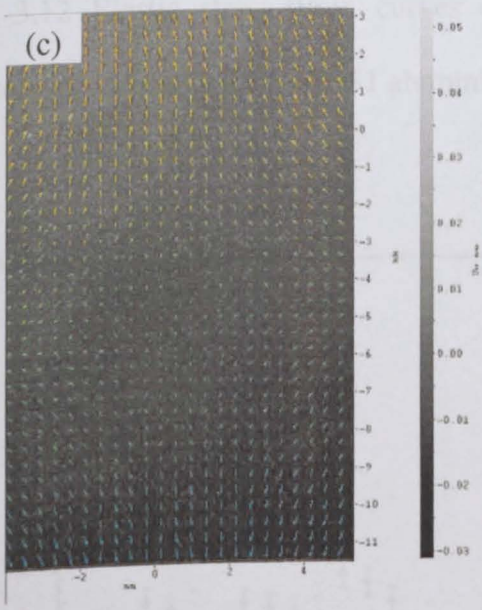

Vector calculation (32 pixels sub-region)

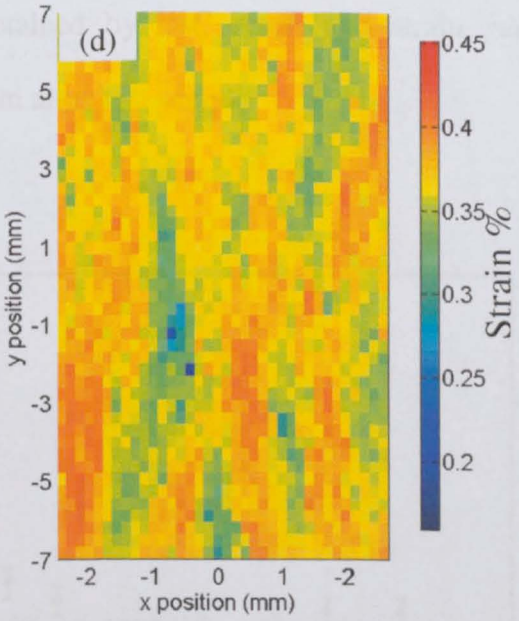

Strain map

Figure 3.11 The post-processing steps of the analysis performed for the specimen.

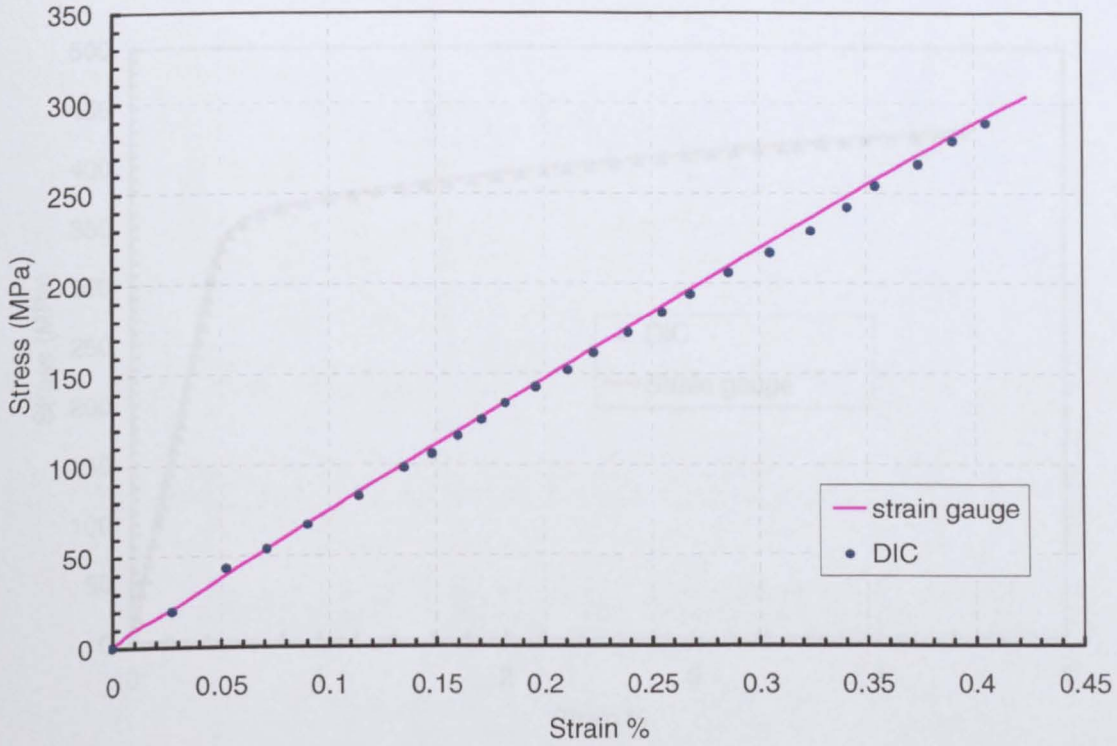

Figure 3.12 Elastic stress-strain curves obtained by DIC result and strain gauge measurement for the AA2024-T351 aluminium alloy test sample.

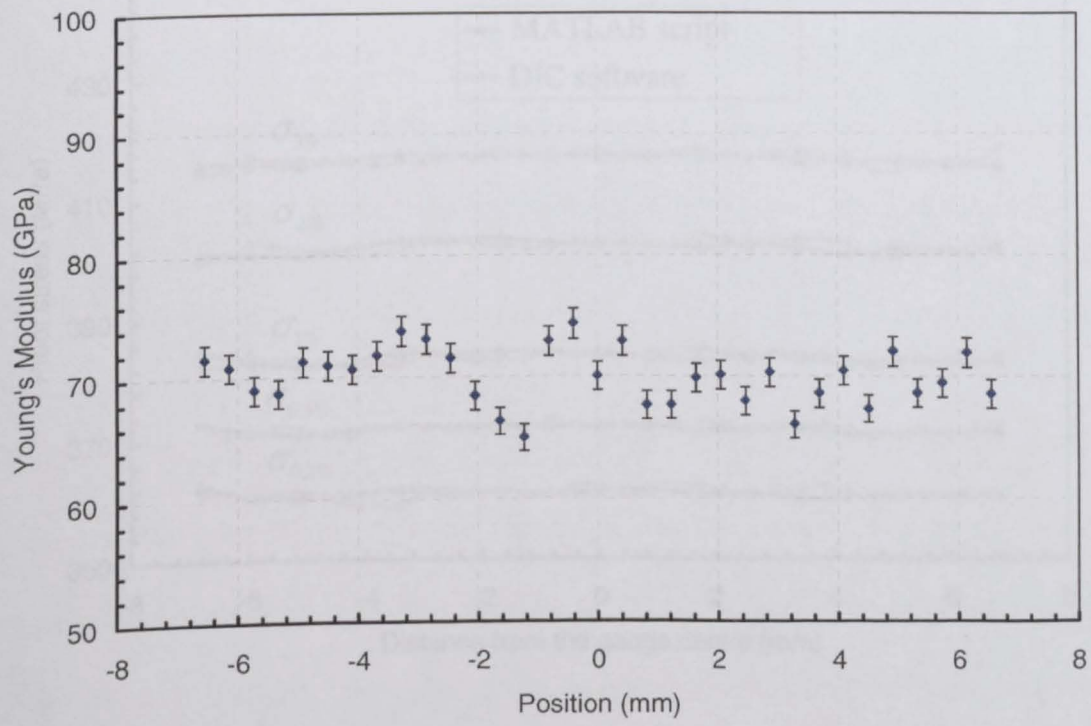

Figure 3.13 The variation of Modulus of Elasticity along the gauge length of the AA2024-T351 tensile test sample.

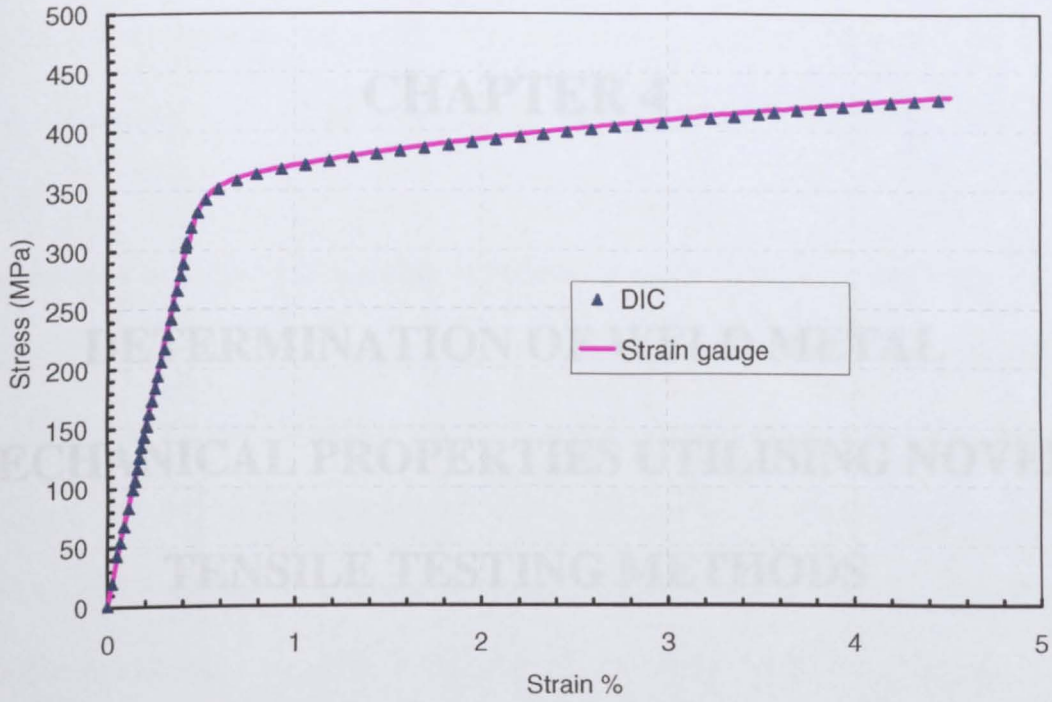

Figure 3.14 Stress-strain curves obtained by DIC result and strain gauge measurement for the tensile test sample.

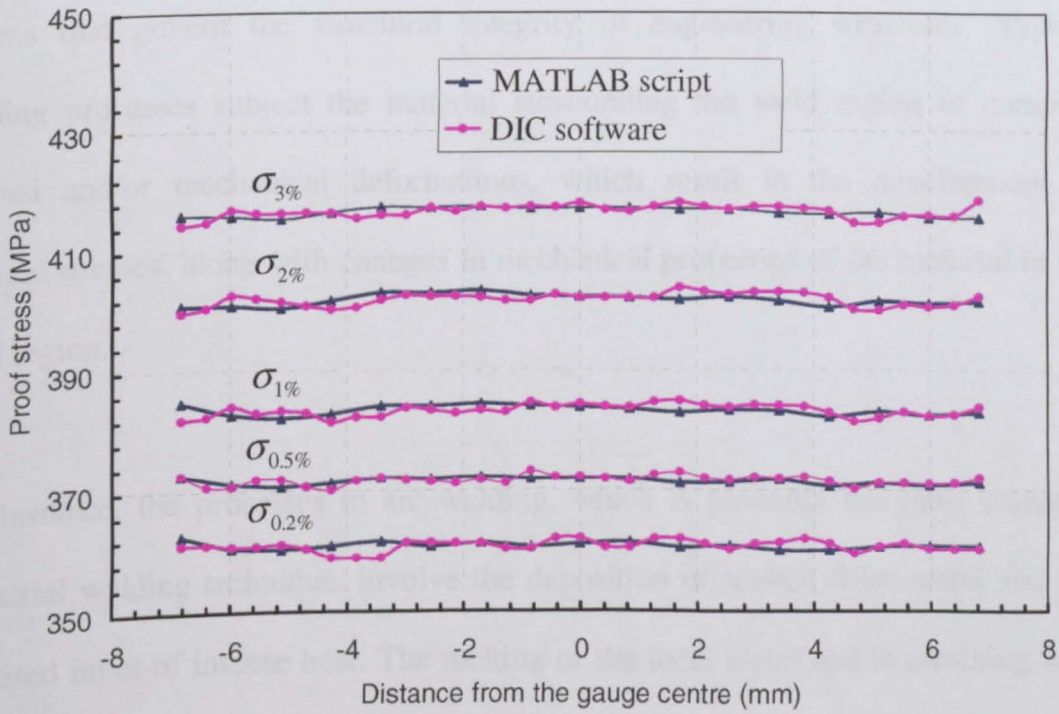

Figure 3.15 Variation of proof stress along the length of the specimen.

CHAPTER 4

DETERMINATION OF WELD METAL MECHANICAL PROPERTIES UTILISING NOVEL TENSILE TESTING METHODS

4.1 Introduction

Welds, whether produced by fusion or solid-state welding, are often the most critical regions that govern the structural integrity of engineering structures. Typical welding processes subject the material surrounding the weld region to complex thermal and/or mechanical deformations, which result in the development of residual stresses, along with changes in mechanical properties of the material in the weld region.

For instance, the processes in arc welding, which is probably the most common industrial welding technique, involve the deposition of molten filler metal and the localised input of intense heat. The melting of the local metal and intermixing with the filler metal will result, upon cooling, in a different microstructure than the parent metal. Since the area of the parent metal adjacent to the weld will be subjected to somewhat different heating and cooling cycles during the welding processes, the

weld (fusion zone) and the surrounding material (heat affected zone – HAZ) will end up with a heterogeneous microstructure, and hence, varying mechanical properties across the region.

Development of improved welding processes requires accurate knowledge of the variation in material properties caused by those processes. It is essential to investigate the mechanical response of material at the local level so that welding processes can be optimized and modelled. The global response of the welded structure can then be determined by successfully implementing the constitutive stress-strain response in the weld region, together with the residual stress information, into numerical modelling codes.

A number of recent articles studying the mechanical properties of friction stir welds [1-5] and a laser weld [6] have reported that digital image correlation (DIC) is an effective technique for the measurement of the local variations in stress-strain response across the weld. In these studies, DIC was used to measure strain variations on standard tensile specimens that were cut perpendicular to the weld line, such that the gauge length of the specimen contained the fusion zone and the HAZ. Genevois et al. [4] also cut micro-tensile test specimens, parallel to the weld line, from different regions of a welded joint and compared these results with standard tensile test samples. They found good agreement between the strain data obtained by micro-tensile tests and standard tensile tests.

The present study investigates the variation of mechanical properties in a stainless steel pipe girth weld manufactured by multi-pass arc welding. For this purpose,

micro-tensile samples, from each region (fusion zone, HAZ and parent material), were cut from slices taken from the pipe in two orientations: parallel and normal to the weld line directions. The stress-strain curves obtained from those micro-tensile samples were used to determine the variations of modulus of elasticity, proof stress and tensile stress by using the digital image correlation technique. Then, DIC was used to obtain the full-field strain map of a standard tensile test sample that was cut from the slice along the direction normal to the weld line. In order to verify the DIC measurements, strain measurements on the back surface of the tensile specimen were made using Electron Speckle Pattern Interferometry (ESPI), which is also an optical technique providing full field displacement maps. Finally, the results obtained from micro-samples were compared to those obtained by the standard tensile specimen.

4.2 Material and Specimens

4.2.1 Material

All specimens used in this study were extracted from a girth weld pipe with dimension of 432 mm outside diameter [7]. The pipe, which was supplied by British Energy and manufactured for two power station headers (Header 1D1/3 (cast 55882A) and Header 2C2/2 (cast 69431)), is made of 316H stainless steel whose nominal chemical composition is given in Table 4.1.

Table 4.1 Chemical compositions of power station headers

Element	C	Si	Mn	P	S	Cr	Ni	Mo	Co	Nb	Ti	V	W	N
1D1/3 cast 55882A	0.06	0.32	1.45	0.02	0.01	17.18	10.92	2.32	0.08	-	-	-	-	0.08
2C2/2 cast 69431	0.07	0.39	1.01	0.03	0.02	17.10	11.60	2.32	0.08	<0.01	0.01	0.05	0.05	0.03

These kinds of welded pipe applications are widely used in industry. For example, this pipe closely denotes the geometry and materials of 19mm thick stainless steel welds that are now operating in UK gas cooled reactors [8].

The fabricating processes of the two headers involved the following stages. The headers were first bore-machined to an average wall thickness of 19.6 mm. In order to remove any residual stresses remaining from original fabrication of the headers, the headers were subjected to a stress relief treatment at 1050°C for 1 hour followed by air cooling. Then, one side of each header was machined out further in order to produce a *J*-groove which is typically used in manufacturing of plant pipe welds [7]. The geometry of the *J* groove includes two slopes as shown in Figure 4.1. The first slope makes an angle of 25° with the horizontal plane and the second angular span of the slope between the side walls and vertical plane is 15°. By matching the sections of two headers where the *J* groove was introduced, the headers were butt welded. The welding process involved two steps: the Tungsten Inert Gas (TIG) method was used to join the headers in the first pass. Then, following passes were made by using manual metal arc (MMA) welding with a target of the heat input of about 1.35 kJ/mm. The structure of the fusion boundary and the relative positions of the TIG and MMA weld passes are shown in the macrograph in Figure 4.2. The assembly of the welded pipe with dimension of 830 mm total length is depicted in

Figure 4.3. The summary of the geometrical parameters, material properties and weld features are given in Table 4.2.

Table 4.2 Summary of the geometrical parameters, material properties and weld features [7].

Components		**Characteristics**
Global geometry	Outer radius, R_0 (mm)	216
	Wall thickness, t (mm)	19.6
Parent Material	Stainless steel	AISI Type 316H
	0.2% Proof stress (MPa)	212
	1% Proof stress (MPa)	272
Weld characteristics	Designation	Girth
	Weld type	MMA
	Number of passes	16
	Average arc energy (kJ/mm)	1.35
	Weld material	316L
	1% Proof stress (MPa)	446
Geometry of welds	Arc-length, L (degrees)	360
	Groove width (mm)	22
	Depth d (mm)	19.6

4.2.2 Specimens

The 'as-received' material for this study was cut in the form of a 190 mm long semi circle pipe section as shown in Figure 4.4. To extract test material from the pipe for this work, first of all transverse slices were machined from the weld section with dimensions of 19.6 mm wide (the pipe's wall thickness) × 190 mm long (along the length of the pipe) × 15 mm thick (along the circumference).

Before machining out the specimens, one of the slices was metallographically examined to determine the variation of the microstructure across the weld. First of all, the slice was rough ground by SiC from grit size 220 up to 4000 finish followed by fine automatic polishing first in 6μm diamond suspension then finishing in 1μm

diamond suspension. Afterwards, etching was done by immersing the specimen for less then 30 seconds in a solution containing NaOH and NaF in water. These processes also helped to determine the location of the slices where the standard and micro tensile test specimens would be extracted.

The effect of the welding process on the mechanical properties across the weld material was studied using very small specimens. These micro-tensile specimens, with a gauge length of 3.75 mm, width of 0.7 mm and thickness of 0.7 mm (Figure 4.5), were machined using electro-discharge wire machining (EDM), from various regions of the weld at two orientations. The longitudinal specimens (orientated in a direction normal to the weld line) were extracted from five regions of the weld: fusion zone, HAZ, and within the parent material at varying distances from the weld line (i.e. parent1 at 20 mm, parent2 at 30 mm and parent3 at 90 mm) as shown in Figure 4.6 a. Specimens in the weld line direction (in the wall thickness direction of the pipe) were machined from three regions: fusion zone, HAZ, and parent material at a distance of 90 mm from the weld line as shown in Figure 4.6 (b). So, eight micro samples, five in the longitudinal direction and three in the weld line direction were analysed in this study.

In order to investigate whether micro-samples machined out from different regions of the pipe were necessary for determining mechanical properties or only one standard sample containing the all regions of the weld is reliable to use, a standard tensile specimen was machined from one of the slices such that the important regions of the weld (e.g. weld and HAZ) are contained within the specimen gauge. The dimensions of the standard tensile test specimen and its machining position on

the slice is shown in Figure 4.7. The specimen, which is 10 mm wide and 3 mm thick in the 80 mm long gauge region, was also machined using EDM.

4.3 Experimental Procedures

4.3.1 Micro Tensile Test Specimens

The tensile tests for the micro tensile test specimens were performed using a screw driven tensile testing machine (Instron 3367) with a calibrated 30kN capacity load cell at ambient temperature.

Digital image correlation was used to monitor the full field displacement maps in the gauge sections during the tensile tests. A high resolution (4 Mega-pixels at 12 bit) monochromatic progressive scan camera (LaVision Image Pro 4) [9] was used to capture the surface deformation of the specimens during the tensile tests. A telescopic lens with a variable zoom and a working distance of 90 mm (Rodenstock macro CCD vario-lens) was used in the tests, so that the whole gauge length of the specimens were contained in the field of view at maximum possible resolution. A conventional extensometer equipped with a wire spring was used in all micro-sample experiments. Figure 4.8 depicts the micro tensile test specimen placed in the grips and Figure 4.9a and 4.9b show the two different aspects of the DIC set up: a micro specimen, grips, the telescopic lens, an illumination system and an extensometer. The illumination during all experiments was distributed onto the surface uniformly and constantly in order to get high accuracy result as surface contrast is directly related to quality of the lighting system. The surfaces of all the

samples for the experiments were not polished since the EDM cutting processes gave a good contrast on the surface.

At the beginning of each test, the camera had to be positioned and an initial image prior to each test was calibrated since each specimen shows very different mechanical properties in the plastic zone. In this manner, the magnification was taken such that when the specimen plastically deforms, it still stayed within the imaging frame. The ductility of the material around the weld was found to increase with the distance from the weld line. For instance, the failure strain of the parent3 sample is about twice as much as that of the sample taken from the weld zone. Since the field of view of the camera for the parent material will include a larger area than that for weld material, lower resolution was obtained for the parent3 sample than that of the weld sample. At each test, the applied load and the displacement of the test machine's cross–head were recorded. During the testing of the micro-tensile specimens, an extensometer monitored the specimen extension which was used as a verification of the cross-head displacement and the global extension determined by the DIC software.

The micro-tensile specimens were tested under a constant displacement rate of 0.225 mm/min. The reason for choosing such a low displacement rate was due to the short gauge lengths. The corresponding strain rate was in the order of 1×10^{-3} s^{-1}. One image per second was captured during the test. All images were stored in a desktop computer running LaVision software [9]. The total number of images taken in the duration of the tensile test varied between 300 and 700 depending on the ductility of the material. The magnifications varied for the test samples. For example the pixel

size was calculated as 4.8 μm for the parent3 sample and 3.8 μm for the micro-sample extracted from the weld region.

4.3.2 Standard (cross-weld) Specimen

Two independent non-contact full-field strain measurement techniques, digital image correlation and electron speckle pattern interferometry, were utilized to analyse the strain variation in the cross weld specimen when it was subjected to tensile loading.

The ESPI unit at the Manchester Materials Science Centre was used for this experiment. Figure 4.10 shows the design of the ESPI unit. The ESPI sensor (left side of the figure) was joined to a movable pulley system on the screw-driven test machine. This mechanism allowed the pulley system and ESPI sensor to move at half of the cross-head speed. Consequently, the centre of the sample was tracked by the ESPI sensor during the experiment [10]. This helped to minimize the effects of rigid body motion.

ESPI systems consist of a laser source, mirrors and a CCD camera. The laser source illuminates the surface of the sample and speckle patterns are generated. The direction of illumination is controlled by the mirrors, and images of the speckle patterns are recorded by a CCD camera. The whole system is controlled by a computer and 3D ESPI software produced by Ettemeyer [11] was used to measure the displacements of the longitudinal, transverse and out of plane strain components.

For DIC, a high resolution (2048×2048 pixels at 12 bit) monochromatic progressive scan camera (right side of the sample) was used to capture the surface deformation of the cross-weld specimen during the tensile tests. A Nikon 50 mm lens with a variable zoom was used in the test. The position of the camera was adjusted by using an *XYZ* translation system. Since in a typical tensile testing configuration one end of the specimen is fixed and the other end is displaced by the cross-head movement, the centre of the specimen gauge length, which contains the fusion zone, moves within the field of view of the camera as the specimen extension becomes significant in the plastic region. This movement would reduce the correlation area, in particular in the test of the standard specimen as the magnification was optimized to obtain maximum possible pixel size, and part of the gauge area will move out of camera view. To alleviate this problem, in the test of the standard tensile specimen, the camera was moved at half of the cross head distance at every minute in the direction of the cross-head by means of the translating stage so that the camera position tracked the centre of the specimen.

Polishing the surface for optical correlation and laser speckle is not desirable since DIC requires a contrast surface in order for the analysis software to distinguish the sub-region movements, and ESPI requires having surface which shows a matt finish. Since all the specimens used in this study were cut by EDM, they already had a surface finish suitable for having contrast surface for DIC and the generation of a speckle pattern. As a result, there was no need for further surface preparation for the specimens.

The tensile test was carried out using a twin-screw type 1196 Instron tensile testing machine with a calibrated load cell of 30kN capacity. The tests were conducted at room temperature. One side of the sample was used for ESPI and the other side for DIC. In order to preserve the surface on which the DIC experiment was carried out from the reflection of the laser, the surrounding sample was covered by thick cartons.

After the specimen was placed into the tensile test machine and aligned, the cameras were positioned so that their line of the sight was normal to the specimen surface, in order to minimize out-of-plane affects. Once the cameras were positioned and calibrated, the acquisition of images for both the DIC and ESPI commenced.

The acquisitions for DIC were automatic, whereas the camera for the ESPI system was operated manually. The experiment was stopped when a total strain of 30% was reached, which corresponded to about 400 images for DIC. Data collection was controlled by the data acquisition system and digital images were stored in the LaVision computer.

Image acquisition for the ESPI system was governed by a PC running ISTRA, software produced by Ettemeyer [11], and the PC was connected to the load cell which allowed each phase image to obtain the corresponding load reading. For this experiment, the pixel size was 41 μm for DIC and each fringe represented 1.07 μm of displacement for the ESPI technique.

4.4 Data Analysis

4.4.1 Digital Image Correlation

Once the tensile tests were completed, all the images captured during the tests were processed using the LaVision software to obtain the displacement vectors. While performing the experiments, the specimen is subject to rigid body motions. If not corrected, these motions would cause errors in the measurements since the software will not discriminate between actual deformations and the apparent displacements due to rigid body motions. It is hence necessary to remove the effect of the rigid body motion before beginning data analysis and the LaVision software enables removal of this effect. This issue was explained in detail in Chapter 3. In addition, the regions of most interest were extracted from the images to make analysis quicker. For all experimental results, an integral strain field option where all images are correlated relatively to the first image to obtain total deformation was used. The multi-pass with decreasing interrogation sub-region size option was chosen to calculate the vector field with three iterations. The initial sub-region size was chosen as 64×64 pixels with 25% overlap. After the reference vector field was calculated in the first pass, the sub-region size was reduced to 32×32 pixels for the following passes. Figure 4.11 presents the post-processing steps of the analysis performed for one of the selected micro samples.

The vector field data was then transferred to a MATLAB script where the data was analysed to determine first the displacement values in the longitudinal direction along the gauge length of the specimen, to compute the strain field along the longitudinal direction, and so to calculate the strain variation along the gauge length

by choosing a suitable differentiation range and overlap: a number of successive displacement data points (e.g. 3, 4, 5) were extracted and converted into a strain value via an appropriate differentiation range. Overlap (e.g. 1, 2) goes back and extracts next data points. This provides a smooth variation for the strain field. For all experiments, differentiation range and overlap were selected as 4 and 2 respectively. Justifications of these two parameters were given in the results section of Chapter 3. Therefore the spatial resolution was around 0.2 mm for the micro-samples and 2 mm for standard sample.

Since the main object of this study was to investigate the mechanical properties along the gauge length of the specimens, each row in the resulting strain arrays was averaged over the width of the region where mechanical properties are to be determined. In other words, the variations in mechanical properties along the weld direction were not the concern of this investigation. Furthermore, averaging the strain data over the width of the region of interest provided convenient comparison between the ESPI and DIC results as their spatial resolutions were different from each other. Consequently, one-column strain data were obtained: each row of which represented the averaged strain data for each sub-region. The resulting stress-strain data curve was determined for each row. The MATLAB script was then used to calculate the elastic modulus, proof stress and ultimate tensile strength (UTS) for each region.

4.4.2 Electron Speckle Pattern Interferometry

The ISTRA software [11] was used for data analysis of the speckle pattern in order to create displacement maps from the speckle pattern images obtained using the

ESPI technique during the tensile test of the standard specimen. For this purpose, each subsequent image which was obtained during the test was subtracted from the reference image that was taken before the loading commenced. The resultant patterns show fringes of bright and dark speckles. Figure 4.12a shows the image of the cross weld tensile test specimen captured by the ESPI unit during the experiment. The corresponding phase map of the cross weld specimen is given in Figure 4.12b. The rectangular areas on the images demonstrate the region from which measurements were taken.

The ISTRA software was used to obtain the longitudinal displacement arrays from the phase maps. The resulting displacement vectors were then analysed using MATLAB scripts, in a similar manner to DIC analysis. A MATLAB script was first used to average the longitudinal displacement data along the width of the region where the mechanical properties are to be determined. Then the strain was calculated by differentiating the displacement data along the gauge length. The resulting stress-strain curves along the length of the specimen were obtained at each point. Finally, the proof stress values across the weld were calculated by means of a MATLAB script.

4.5 Results and Discussion

Figure 4.13 shows the stress-strain curves of micro-specimens extracted from five different regions of the slice with the loading orientation normal to weld line (i.e. Weld, HAZ, parent1, parent2, and parent3). It can be seen that the weld micro-sample shows the highest yield strength and the lowest initial work hardening rate amongst five micro-samples. The lowest yield strength is observed for parent3

material. The stress-strain curves of the three micro-specimens cut out from the weld, HAZ, and parent3 zones in weld line direction are given in Figure 4.14. Once again, the weld region exhibits a higher yield strength and lower initial work hardening rate than the others. Note that the averaged strain values of the DIC results were calculated by taking an average of all sub-regions were used.

In order to verify the DIC results with conventional strain measurement for the micro-sample tests, an extensometer was attached onto the grips. Good agreement was found for all the micro samples. The agreement between the extensometer and the DIC result for a parent3 region in the longitudinal direction (normal to weld line) is illustrated in Figure 4.15. Here, the averaged strain value DIC result is given by the marker in the figure. The solid line represents the stress-strain curve obtained by extensometer measurement.

Figure 4.16 shows the Young's modulus distribution along the length of the gauge of the micro specimen extracted from the HAZ region in the weld line direction. It can be seen that the Young's modulus varies between 194-208 GPa. Each data point on the graph shows the position of the specimen (i.e. each sub-region) where the Young's modulus was calculated. As can be seen from the figure, uncertainty bar for each point was calculated. As sub-region size was 32×32 pixels with 25% overlap, the error in the strain value was calculated to be 1.66% from the Table 3.1in Chapter 3 and corresponding uncertainty in Modulus of Elasticity for each sub-region was determined. Note that the gauge length of the micro-samples is very small, and only 6-7 data points could be measured in the elastic zone until the specimens reached the yield point.

After the complete stress-strain curves were determined for every sub-region for each micro tensile test specimen, the proof stress variation along the gauge length was calculated for the micro-tensile test specimens. Figure 4.17 shows the variation in 0.2%, 0.5%, 1%, 2%, and 5% proof stress versus position along the gauge length of the micro-specimen extracted from the parent3 region in the weld line direction.

The variation of 0.5% proof stress along the length of the micro-samples at two orientations is plotted in Figure 4.18. It can be seen that the longitudinal specimens (in a direction perpendicular to the weld line) in the weld region indeed represents the worst case (very heterogeneous); the variation in all the other cases is not so steep. Figure 4.18 also shows the effect of orientation on the proof stress in different regions. There does not seem to be a trend with orientation, but the change in proof stress is more pronounced with the HAZ; the strength of material in this region in the direction perpendicular to the weld line is considerably higher than that in the direction parallel to the weld line. It is also clear that proof stress distribution for the micro samples in the longitudinal direction continuously gets lower when remote from weld centre. This trend maintains till the furthest region from weld centre.

Plots of proof stress and UTS versus the distance from the weld centre, showing all the micro-sample results from different regions are given in Figure 4.19. Here, since the plot shows the mechanical properties along the direction normal to the weld line, only one value in each region can be shown for 0.5% proof stress of micro samples in the weld direction, thus the averaged values of micro samples extracted in the weld direction were used. Therefore, scatter bars were used to represent the proof stress variations of the micro-specimens in the weld direction. A summary of all the

mechanical properties of the weld material obtained from the micro tensile test specimens is given in Table 4.3. It can be seen from the table and/or its graphical version Figure 4.19 that the proof stress and UTS show significant variations. In general, the strength values decrease away from the weld. One of the interesting tensile properties found in these experiments was that the UTS value of the micro sample extracted from the parent3 zone in the longitudinal direction is the lowest whereas it has the highest value in the welding direction.

Table 4.3 Mechanical properties of cross weld material obtained by tensile tests of micro-specimens

	%0.5 Proof stress (MPa)	Ultimate tensile strength (MPa)
Weld in the longitudinal direction	389 – 465	567
Weld in the weld line direction	413 – 453	545
HAZ in the longitudinal direction	392 – 433	582
HAZ in the weld line direction	298 – 341	528
parent1 in the longitudinal direction	305 – 346	557
parent2 in the longitudinal direction	272 – 304	549
parent3 in the longitudinal direction	250 – 267	492
parent3 in the weld direction	288 – 322	572

One of the most significant features of this DIC study for the cross-weld test was to compare the experimental results obtained by ESPI for standard samples and DIC for micro-samples. Investigation of the mechanical properties of the pipe girth weld material by a cross weld sample using the DIC technique, as can be seen in the literature, is powerful. However, verifying these results with the micro-samples and other independent optical methods would be even better.

Figure 4.20 shows an example of the longitudinal strain distribution in the gauge of the standard tensile specimen using DIC and ESPI techniques at an applied stress of 455 MPa. There is an excellent agreement between the two optical methods used. It can be seen that the deformation in the weld is relatively small compared to the HAZ and the parent material. The level of strain seems to increase away from the weld. That means the strength of the weld is higher than the parent material. Indeed, the stress-strain curves extracted from each main region, by using the data from both standard and micro-tensile specimens (Figures 4.13 and 4.21), confirm that the strength of material increases towards the weld.

The comparisons of stress-strain curves obtained from micro-specimens with the corresponding areas extracted from the standard tensile test specimen are given in Figure 4.21. The stress-strain curves extracted from the weld, the HAZ, the parent1, and the parent2 of the standard specimen agree well with the stress-strain curves obtained by the micro-tensile specimens. However, the correlation between cross weld specimen and micro sample for the region parent3 is not available since the data extraction region for parent material on the standard tensile specimen could not be obtained from a part that is exactly corresponding to the part where the micro specimens were cut. The corresponding region was further away from the gauge of the standard specimen. Figure 4.21 shows that the zone affected by the welding extends further away from the weld line than anticipated when extracting specimens from the pipe. The comparison of the stress-strain curves determined by ESPI for the cross-weld specimen for different regions is also given in Figure 4.21. Since the length of the gauge monitored by ESPI technique could only be under 40 mm due to the large deformation involved during the test, only weld and HAZ regions in large

plastic deformation were able to be compared by using two independent optical methods. Nevertheless, fairly good agreement can be observed between the DIC (markers) and ESPI (dash lines) methods for these two regions.

The comparison of the local 0.5% proof stress variations, in the direction of the gauge length, between micro-samples and the corresponding areas extracted from standard specimens by using DIC and ESPI are given in Figures 4.22 and 4.23. Because the image resolution of the standard specimens was relatively low (larger pixel size), fewer data points (sub-regions) could be extracted, whereas more points could be obtained from the high resolution data of the micro specimens.

The variations of the 0.5% proof stress within the weld region for all experimental results generated by using the plastic strain data of the micro sample experiments are given in Figure 4.22. As can be seen, there is a considerable variation across the width of the specimens, which was captured by both types of specimen. Although results obtained from standard specimens agree well, there are some differences between them and the micro-samples. The differences in the data can be attributed to the fact that the micro-sample cut out from the weld in the longitudinal direction can be elongated freely under the plastic deformation. In contrast, in the standard sample, the surrounding material may constrain the weld material and not allow it to elongate freely.

Figure 4.23 shows the 0.5% proof stress variations for the regions HAZ, parent1 and parent2 for micro and standard specimens. Unlike the weld region where there are differences between micro and standard samples on the variation of proof stress, all

results are in very good agreement within these regions. Step changes found in the weld region are not observed in these other regions.

The variation in proof stress for the results obtained by DIC and ESPI is clearly seen in Figure 4.24, which plots the variation of 0.5% proof stress with distance perpendicular to the weld line, along the gauge length of the standard tensile specimen. Figure 4.24 also shows that the proof stress variation with distance from the weld line does not level off to a constant value, i.e. does not quite reach the weld-unaffected zone, within the gauge length of the standard tensile specimen. This explains the large discrepancy observed between the stress-strain curves obtained by micro and standard tensile specimens given in Figure 4.21, as discussed earlier. Furthermore, it is obvious from Figure 4.24 that the strength variation with perpendicular distance from the weld line is not symmetrical on each side. This may be due to the fact that the effect of the welding might not be symmetric, i.e. the thermal strain and plastic strain during the welding process might not transfer to base material equally on both sides.

Figure 4.25 shows a picture of one of the cross weld samples after the experiment. It can be seen that the necking starts end of the gauge length. The reason for the necking at that point is that the UTS decreases when remote from the weld centre as can be seen from Figure 4.19 and since somewhere around the end of gauge length reaches the UTS value first, necking begins there.

4.6 Conclusion

In this study, tensile properties in different regions of a girth weld in a stainless steel pipe have been investigated. Although it has been seen that the mechanical properties of the frictional stir welds and a laser weld have been reported using the image correlation method in the literature [1-6], the main difference of this work distinguishing it from these previous studies is the use of two independent optical techniques, digital image correlation and electron pattern speckle interferometry. These have been applied to cross-weld tensile specimen to investigate measurement reliability, and image correlation has also been used with micro tensile test specimens extracted from different zones of girth welded pipe for comparison with results from standard tensile tests. These sets of comparisons had not been done by previous researchers. Tensile properties in different regions of a girth weld in a stainless steel pipe obtained using micro tensile test specimens have been found to be in good agreement with those determined by full field strain mapping on a standard tensile specimen whose gauge contained all the regions of the weld. In addition, it has been found that the results obtained from the DIC and ESPI methods are in very good agreement.

Strain mapping proves to be an effective way of determining the mechanical properties of the material across the welded region. It has been found that Digital Image Correlation is a powerful technique and with the use of high resolution optical setup, very accurate full field strain variations can be obtained within materials with heterogeneous properties.

4.7 References

[1] Lockwood W.D., Tomaz B. and Reynolds A.P. (2002). Mechanical Response of Friction Stir Welded AA2024: Experiment and Modelling. Materials Science and Engineering A, vol. A323, pp. 348-353.

[2] Lockwood W.D. and Reynolds A.P. (2003). Simulation of the Global Response of a Friction Stir Weld Using Local Constitutive Behaviour. Materials Science and Engineering A, vol. A339, pp. 35-42.

[3] Sutton M.A, Yang B., Reynolds A.P. and Yan J. (2004). Banded Microstructure in 2024-T351 and 2524-T351 Aluminium Friction Stir Welds. Part II. Mechanical Characterization. Materials Science and Engineering A, vol. A364, pp. 66-74.

[4] Genevois C., Deschamps A. and Vacher P. (2006). Comparative Study on Local and Global Mechanical Properties of 2024-T351, 2024-T6 and 5251-O Friction Stir Welds. Materials Science and Engineering A, vol. A415, pp. 162-170.

[5] Hatamleh O. (2008). Effect of Peening on Mechanical Properties in Friction Stir Welded 2195 Aluminium Alloy Joints. Materials Science and Engineering A. In Press.

[6] Boyce B. L., Reu P.L. and Robino C.V. (2006). The Constitutive Behaviour of Laser Welds in 304L Stainless Steel Determined by Digital Image Correlation. Metallurgical and Materials Transactions A, vol. 37A, pp.2481-2492.

[7] Bouchard P. J., George D., Santisteban J. R., Bruno G., Dutta M., Edwards L., Kingston E. and Smith D. J. (2005). Measurement of the Residual Stresses in a Stainless Steel Pipe Girth Weld Containing Long and Short

Repairs. International Journal of Pressure Vessels and Piping, vol. 82, pp. 299-310.

[8] Santisteban J. and Edwards L. (2004). Boiler Spine Residual Stress Measurements Programme Task 1.3: Measurement of Multi-pass Repair Weld Structural End Effects Using Neutron Diffraction. British Energy Generation Limited.

[9] Strain Master Commercial Software, LaVision GmbH, Anna-Vandenhoek-Ring 19, Gottingen, Germany

[10] da Fonseca J. Q., Preuss M., Ryan P. and Withers P. J. (2004). Mechanical Property Mapping Using Image Correlation and Electronic Speckle Interferometry. Advances in Experimental Mechanics, vol. 1-2, pp. 147-152.

[11] Dantec Ettemeyer. Dantec Ettemeyer GmbH, Kassbohrerstr., 18D-89077 Ulm, Germany.

4.8 Figures

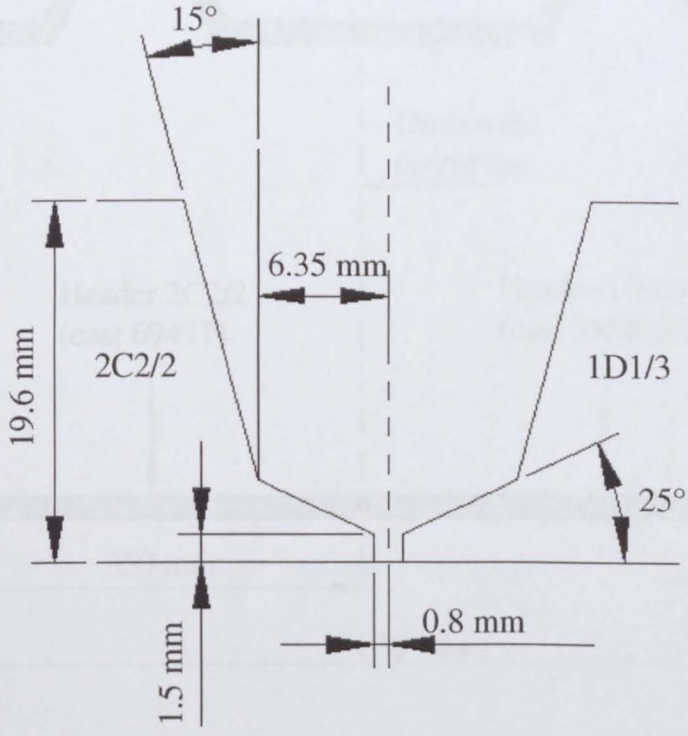

Figure 4.1 Girth groove weld geometry

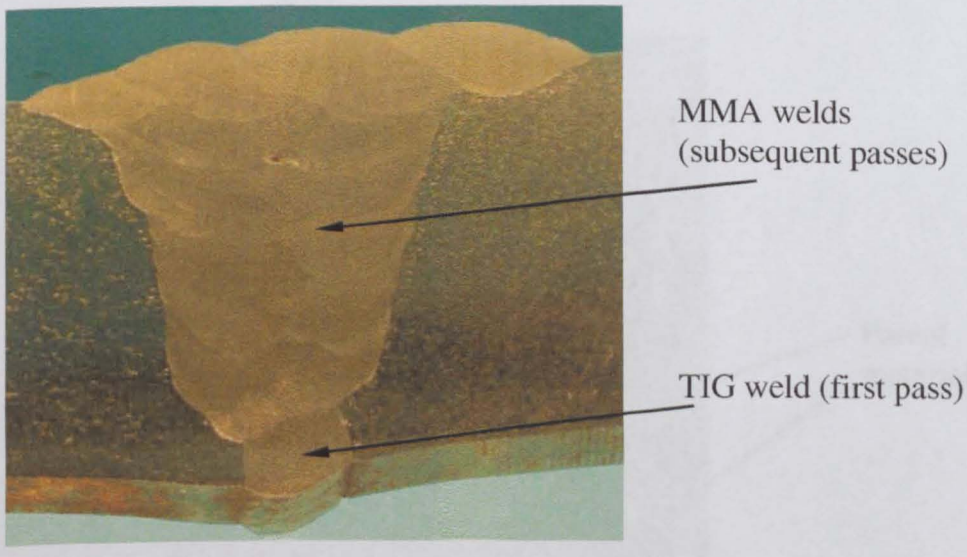

Figure 4.2 A macrograph showing the fusion boundary of weld and the positions of TIG and MMA welds.

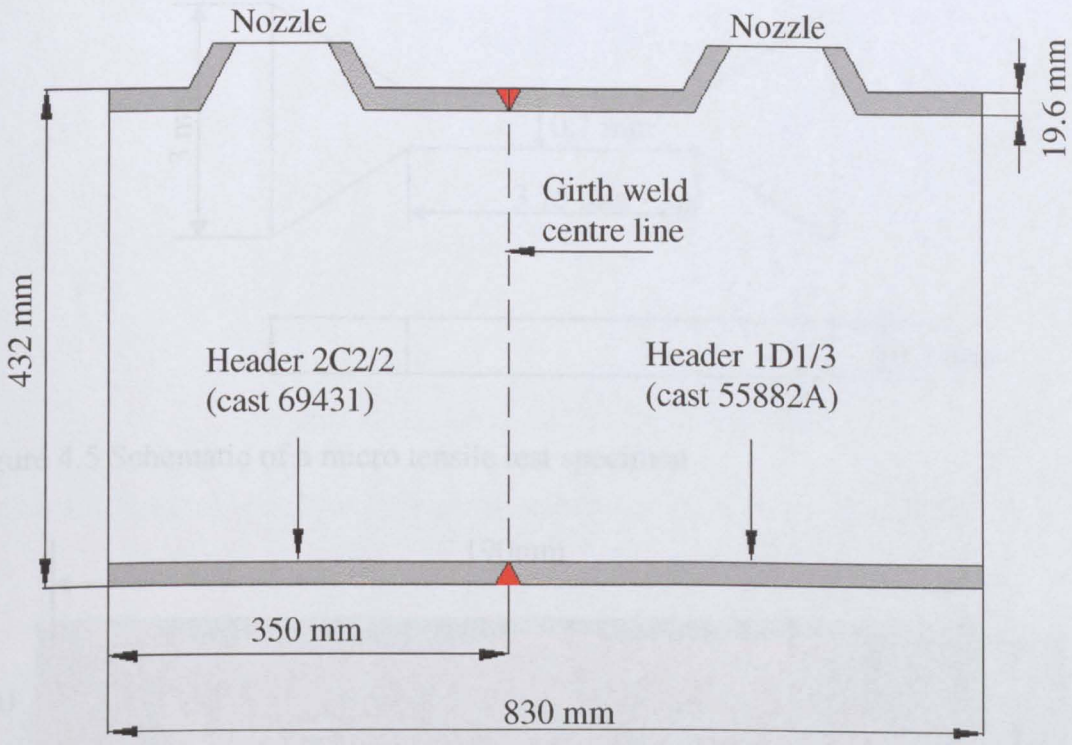

Figure 4.3 Schematic of the girth welded pipe

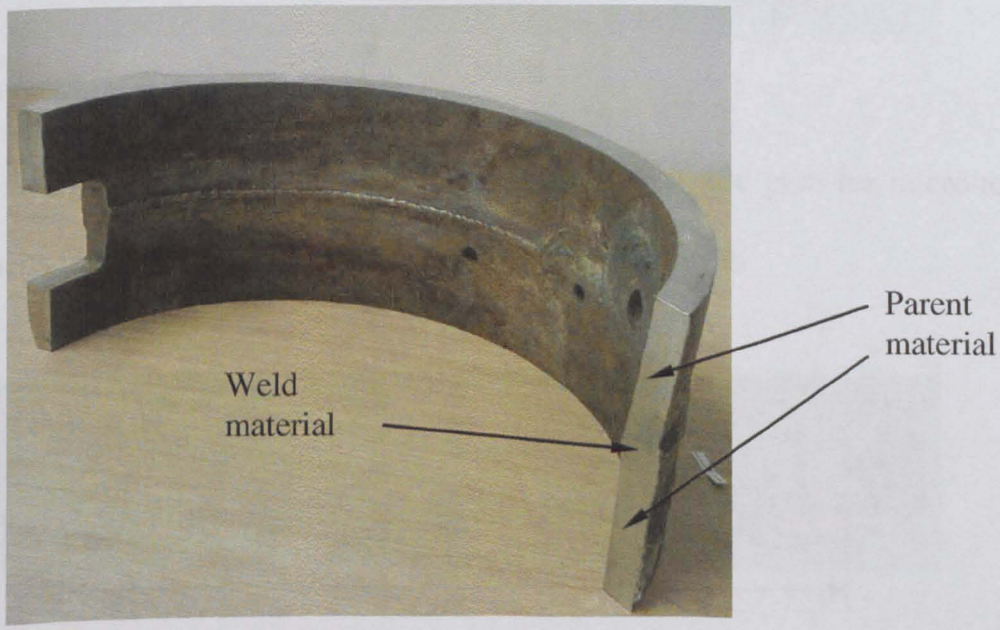

Figure 4.4 A photograph of the semi girth welded pipe.

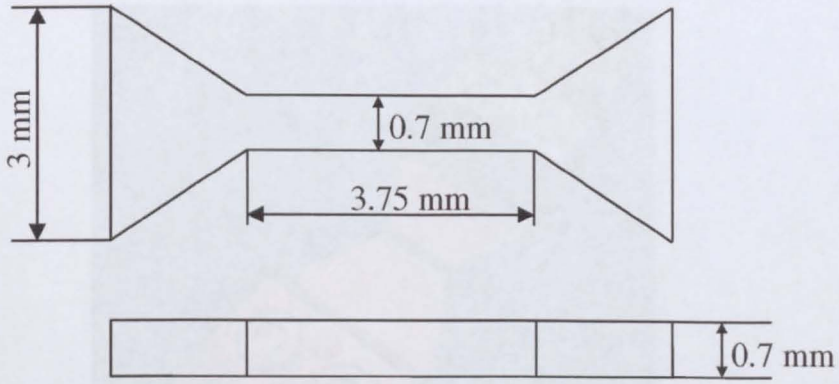

Figure 4.5 Schematic of a micro tensile test specimen

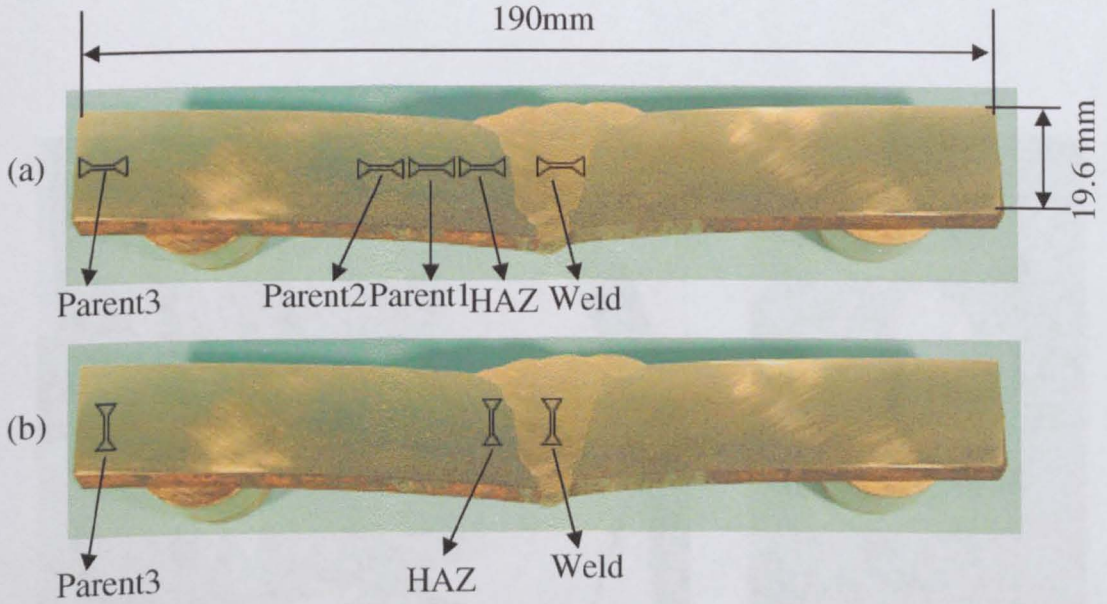

Figure 4.6 Machining positions on the slice taken from the pipe for micro-tensile specimens in (a) the longitudinal and (b) weld line directions.

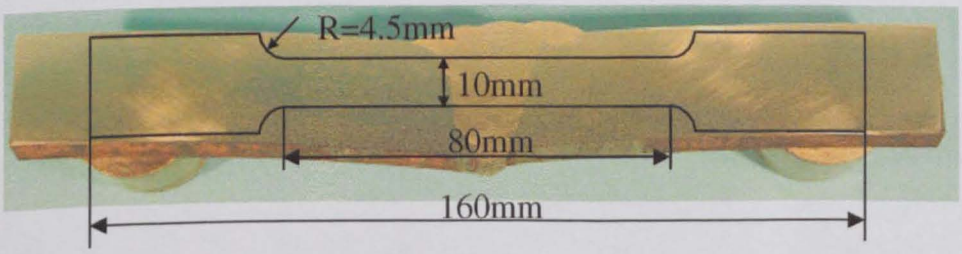

Figure 4.7 The dimensions of the standard tensile test specimen and its machining position on the slice taken from the girth weld.

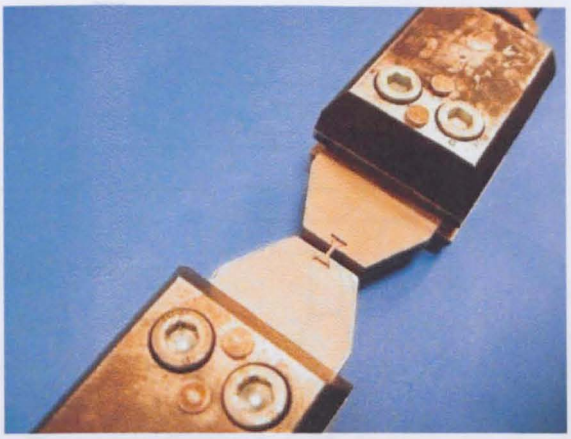

Figure 4.8 A micro tensile test specimen and the grips used for experiments

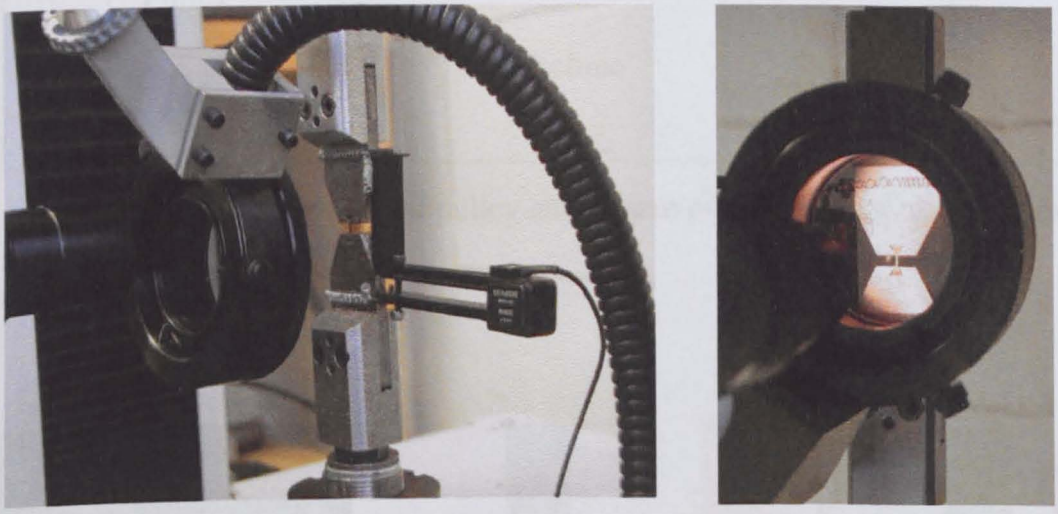

Figure 4.9 DIC set up for the full field strain measurement on the micro sample.

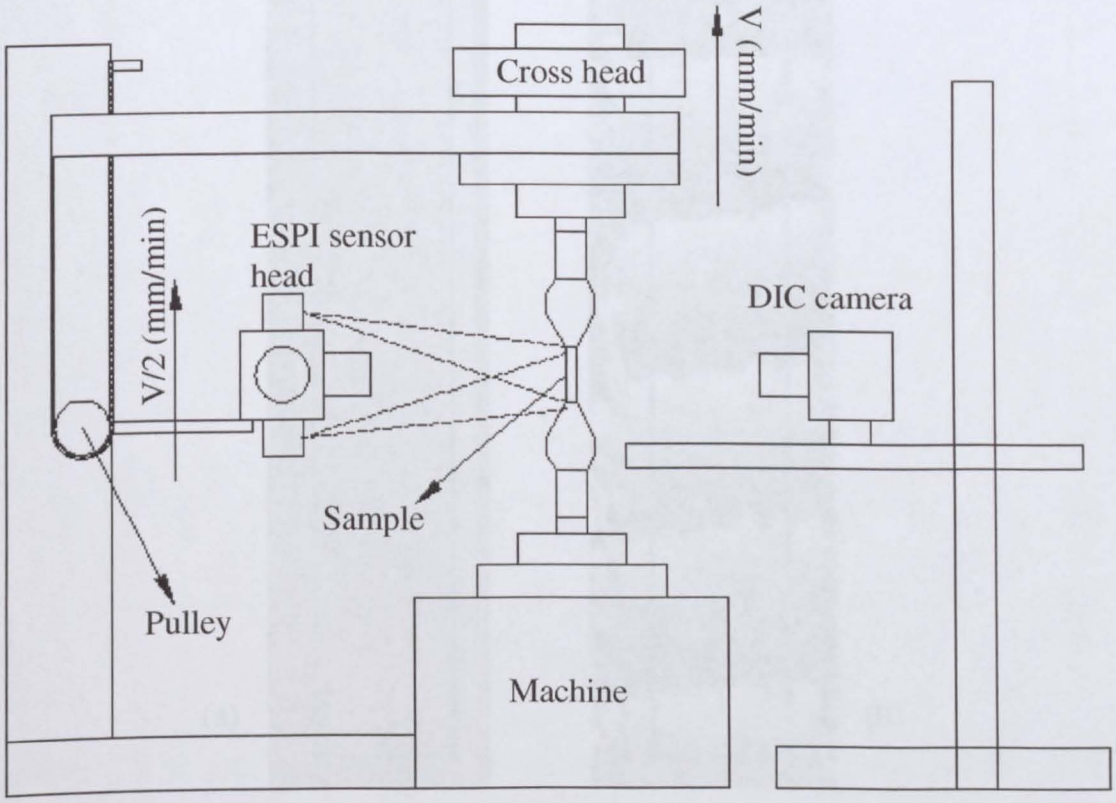

Figure 4.10 Schematic showing of pulley attachment of ESPI sensor to cross-head of tensile testing machine

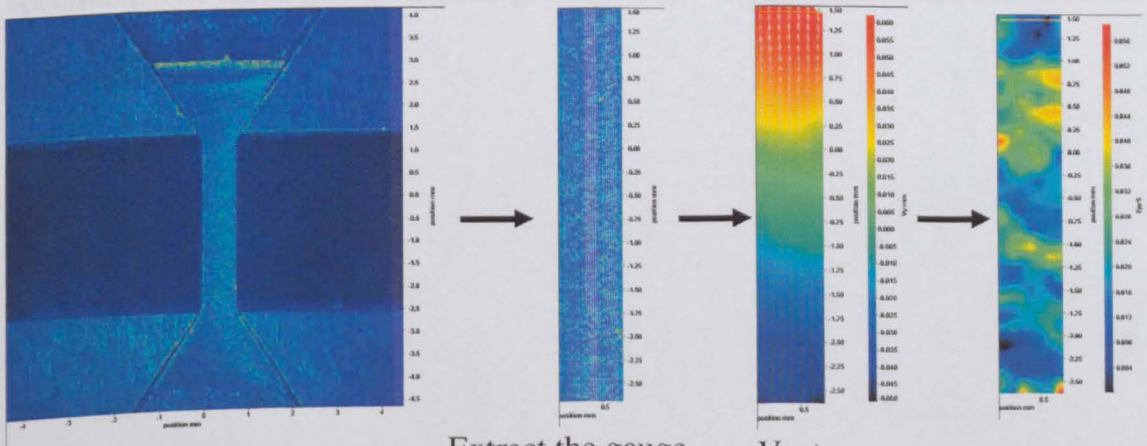

Figure 4.11 The post-processing steps of the analysis performed for one of the selected micro samples.

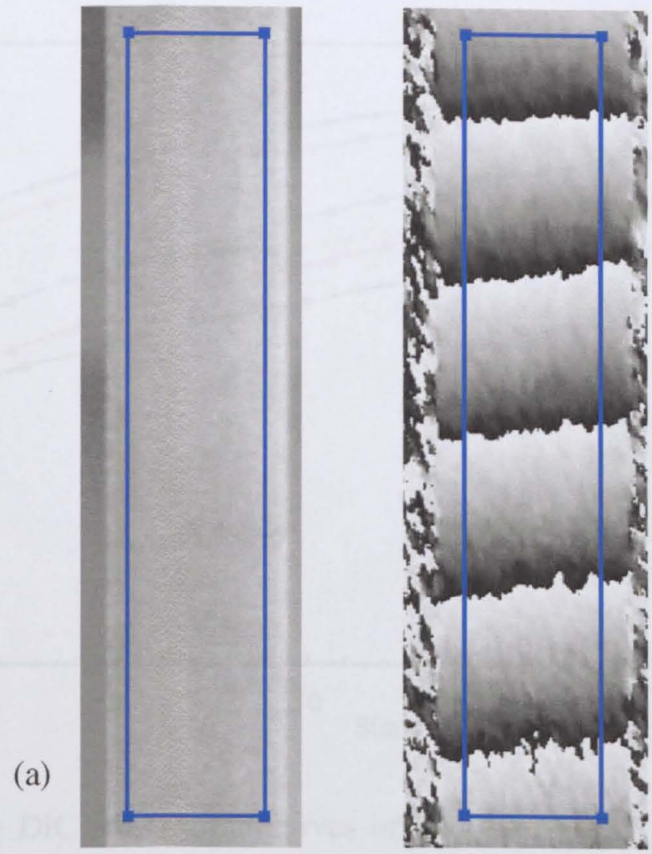

Figure 4.12 (a) The image of the cross weld tensile test specimen captured by the ESPI unit during the experiment. (b) The corresponding phase map of the cross weld specimen. The rectangles on the images denote the region from which measurements were taken.

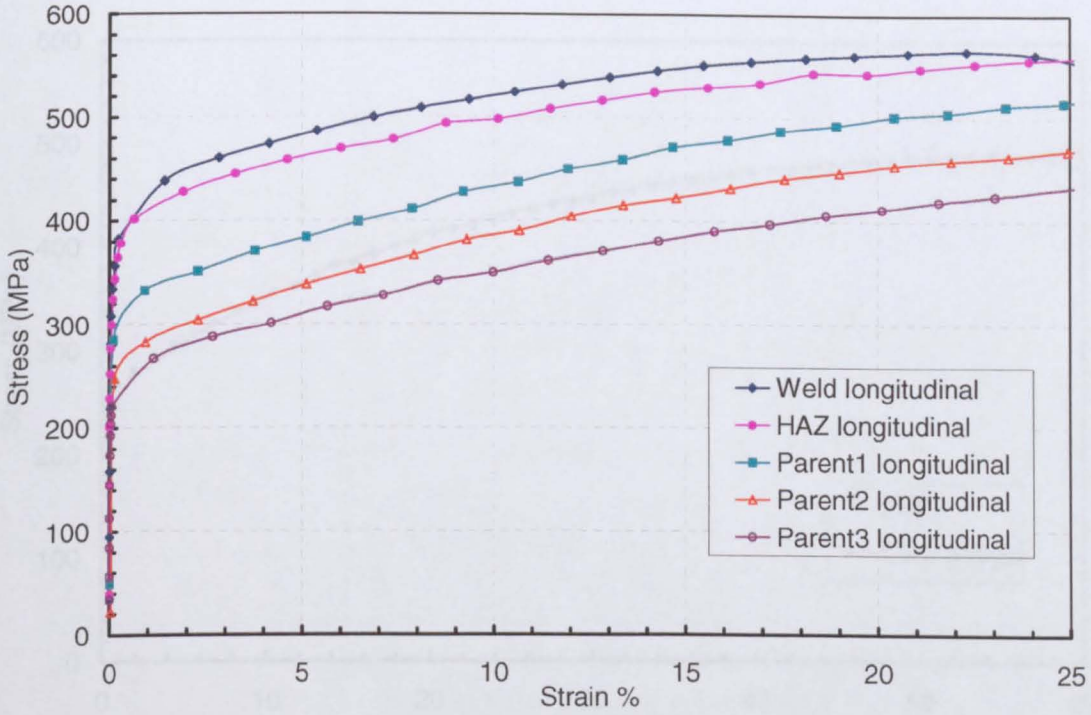

Figure 4.13 The DIC stress-strain curves of micro-specimens extracted from five different regions with the orientation normal to weld line (i.e. Weld, HAZ, parent1, parent2, and parent3)

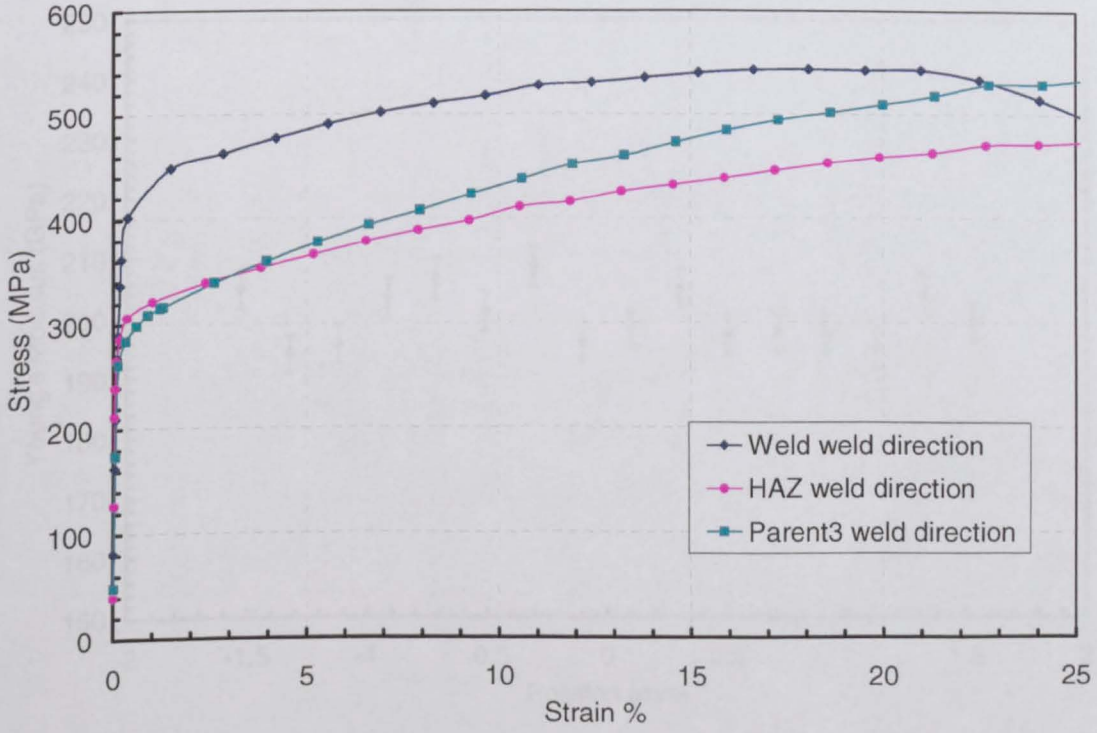

Figure 4.14 The stress-strain curves of micro-specimens extracted from three different regions in the weld line direction (i.e. Weld, HAZ, and parent3)

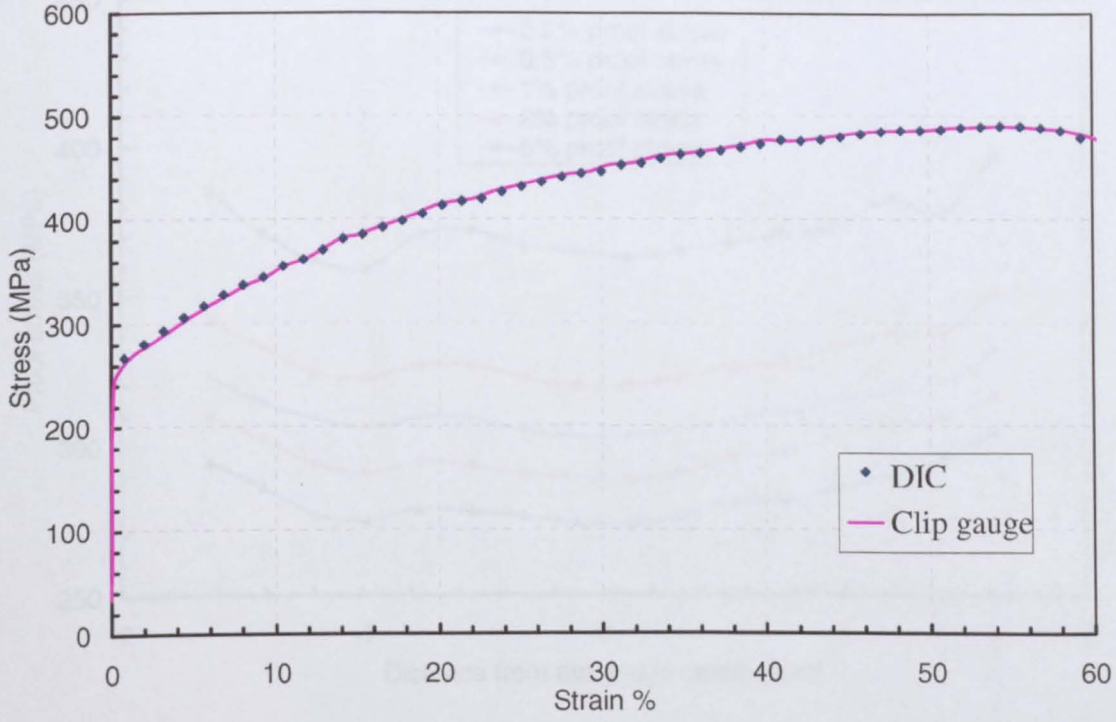

Figure 4.15 Stress-strain curves obtained by DIC result and Extensometer measurements for the micro tensile test sample cut out from the parent 3 region in the longitudinal direction.

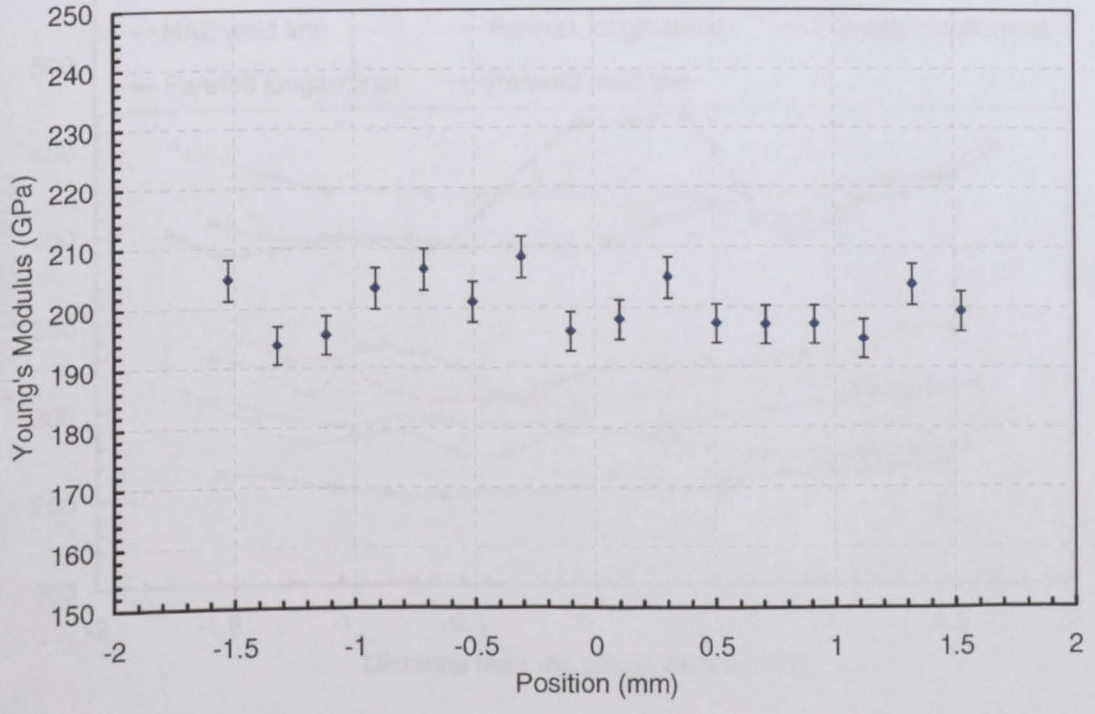

Figure 4.16 The variation of Modulus of Elasticity along the micro tensile test sample extracted from the HAZ region in the weld line direction.

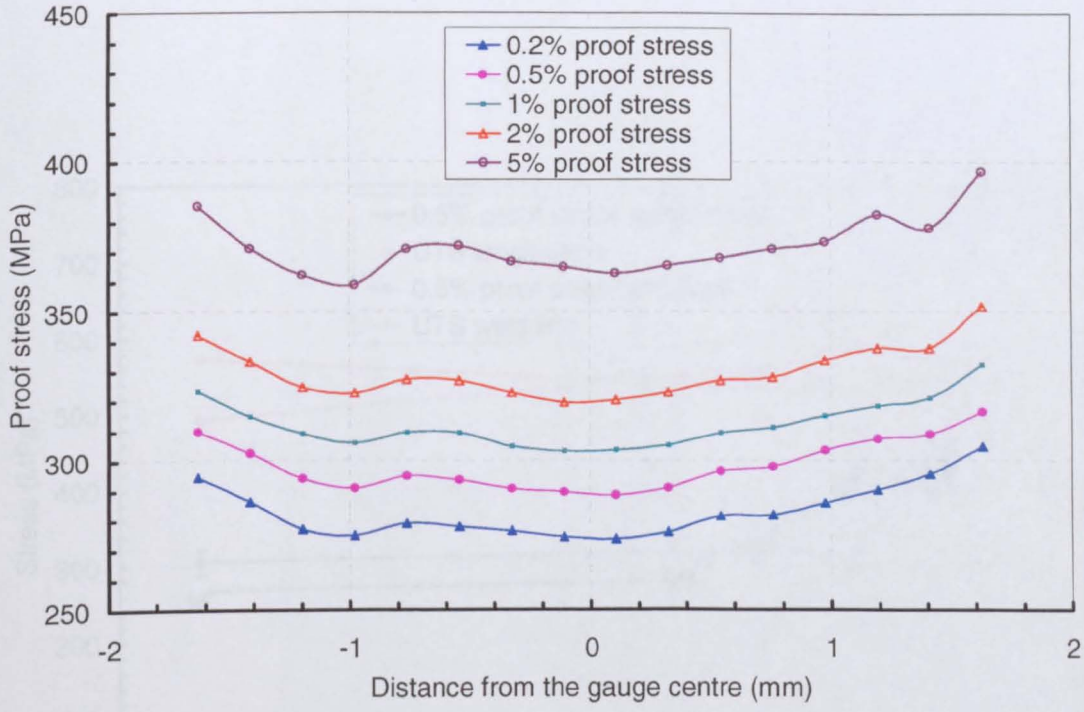

Figure 4.17 Proof stress variations at 0.2%, 0.5%, 1%, 2%, and 5% strains versus position along the gauge length of the micro-specimen extracted from parent3 region in the weld line direction.

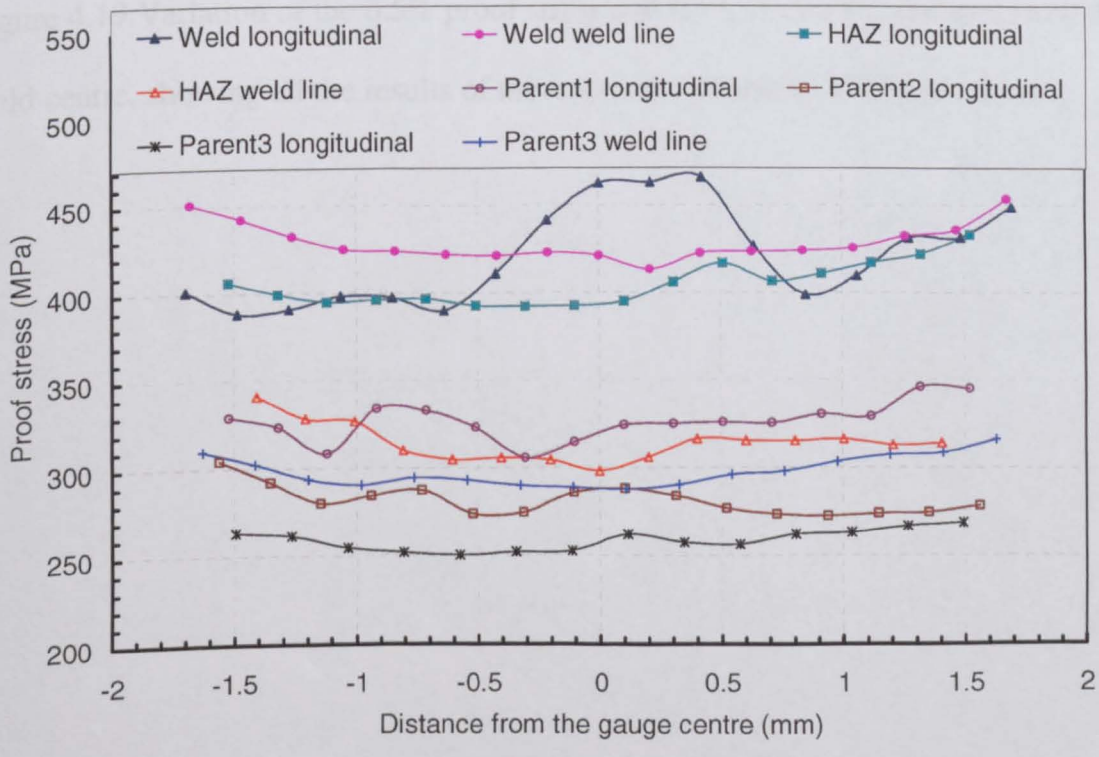

Figure 4.18 Variation of 0.5% proof stress along the length the micro-samples at two orientations within the representative regions of the weld.

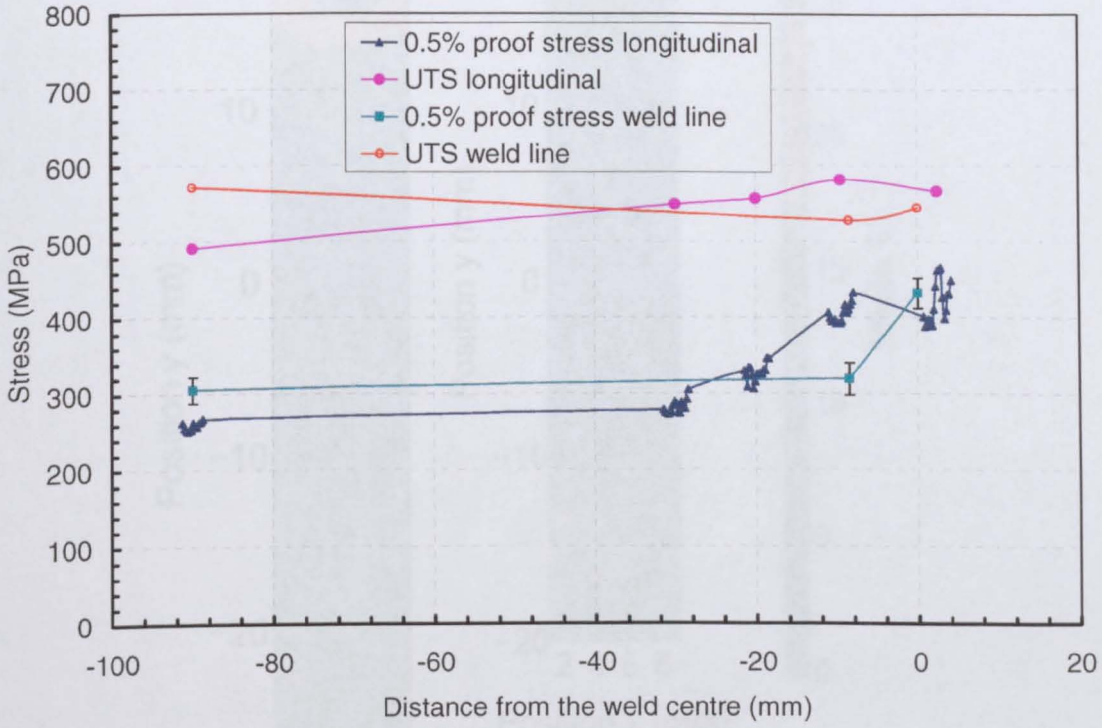

Figure 4.19 Variation of the 0.5% proof stress and UTS versus the distance from the weld centre, showing all the results of the micro-samples from different regions.

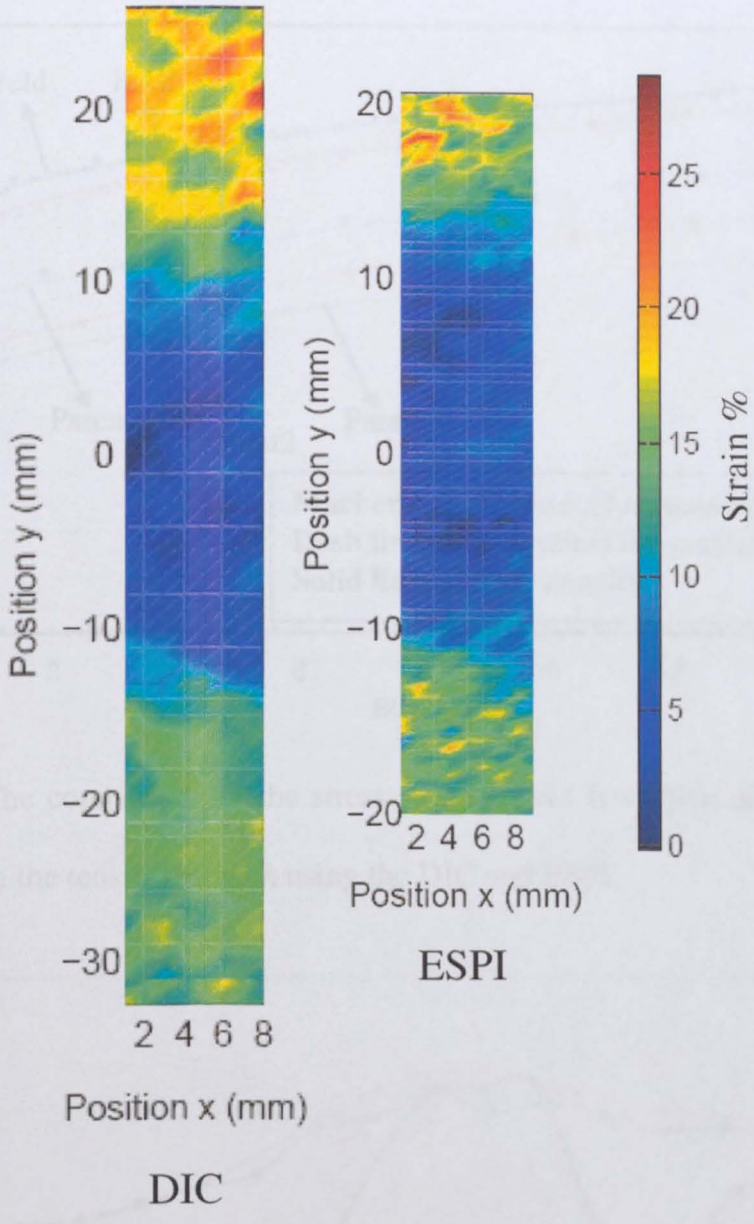

Figure 4.20 Longitudinal strain distributions in the gauge of the standard tensile specimen using DIC and ESPI techniques at an applied stress of 455 MPa.

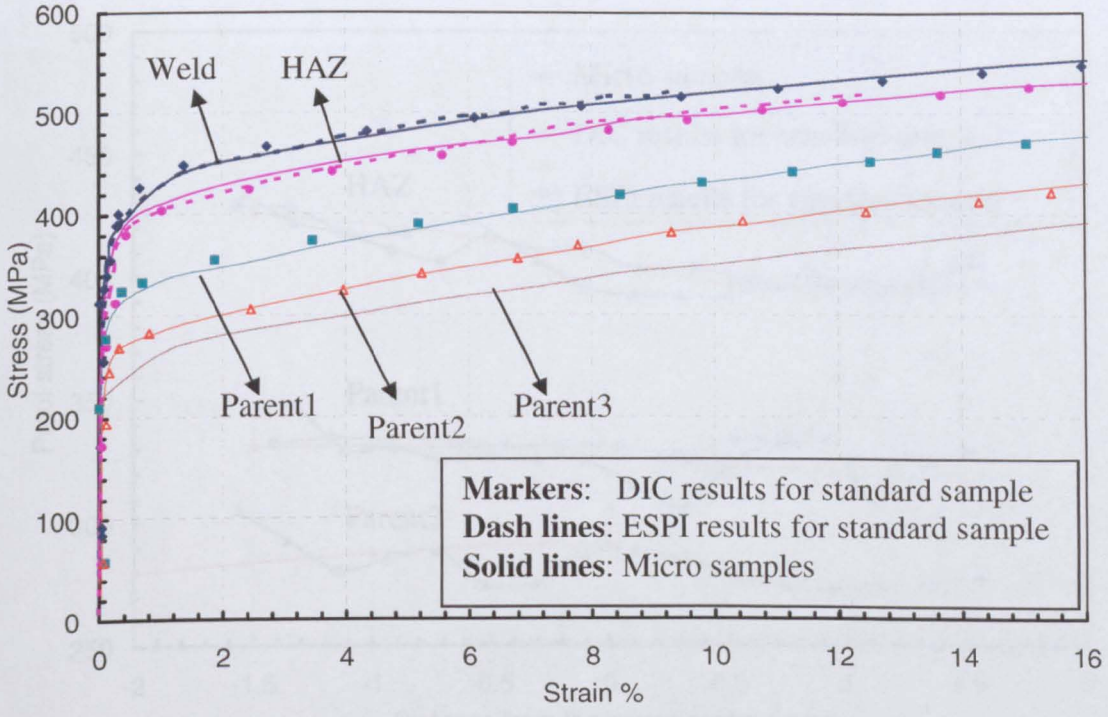

Figure 4.21 The comparison of the stress-strain curves from five different regions, extracted from the tensile test data using the DIC and ESPI.

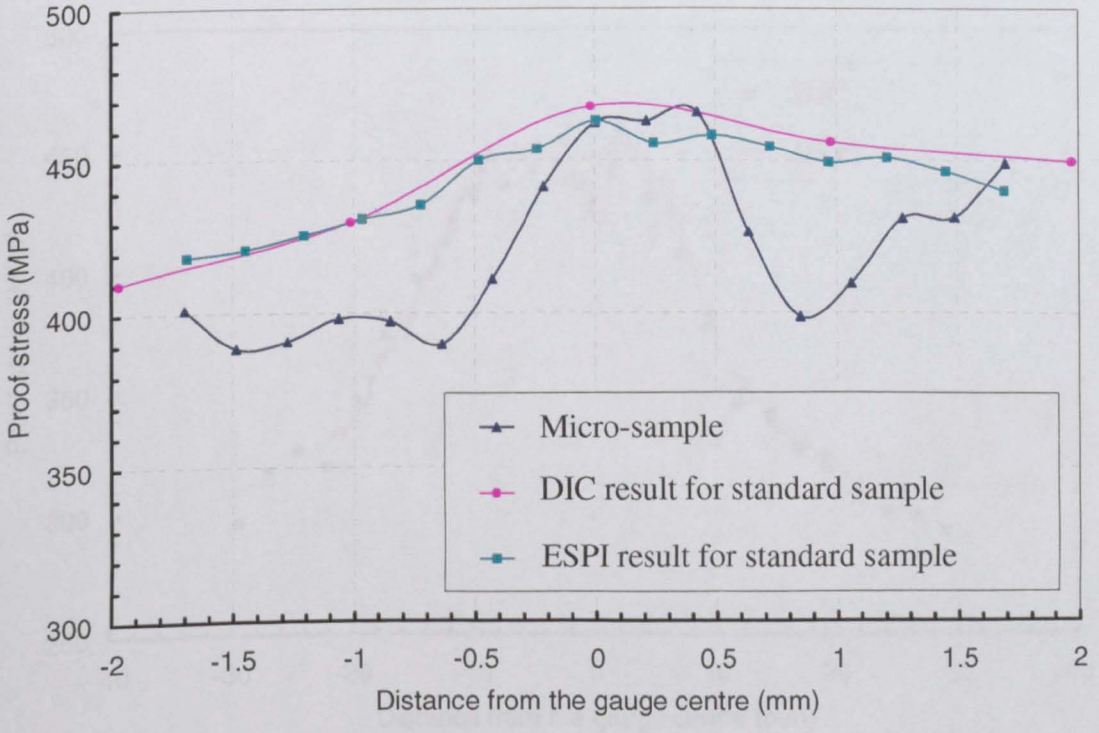

Figure 4.22 Variation of proof stress within the weld regions

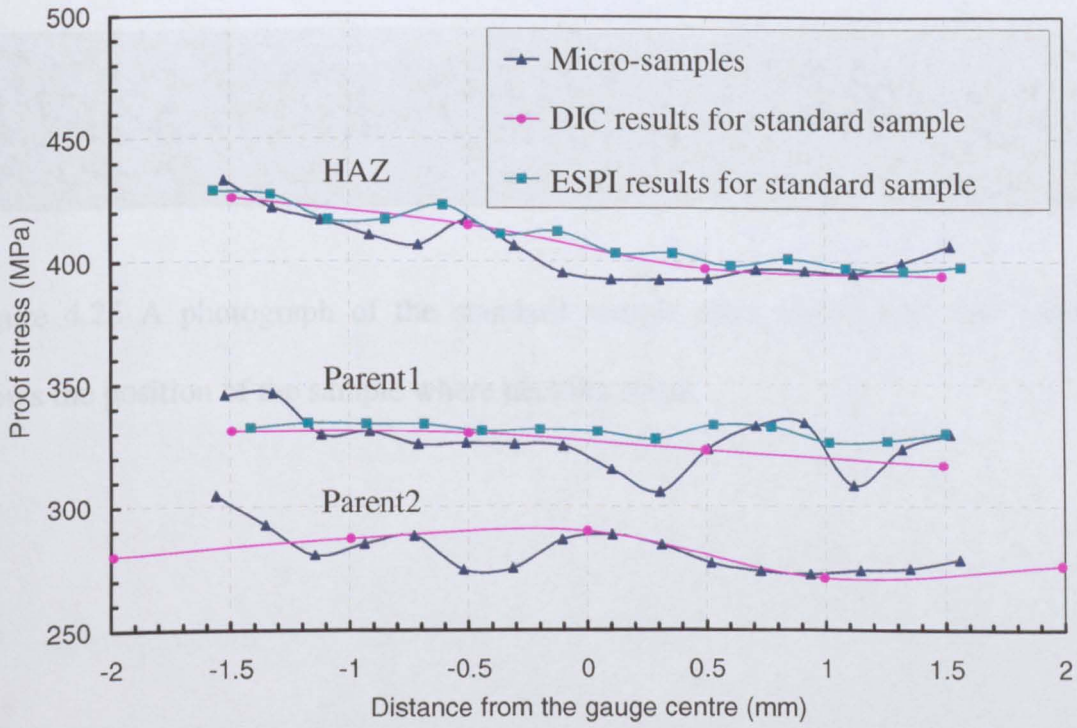

Figure 4.23 Variation of proof stress within the HAZ, parent1 and parent2 regions

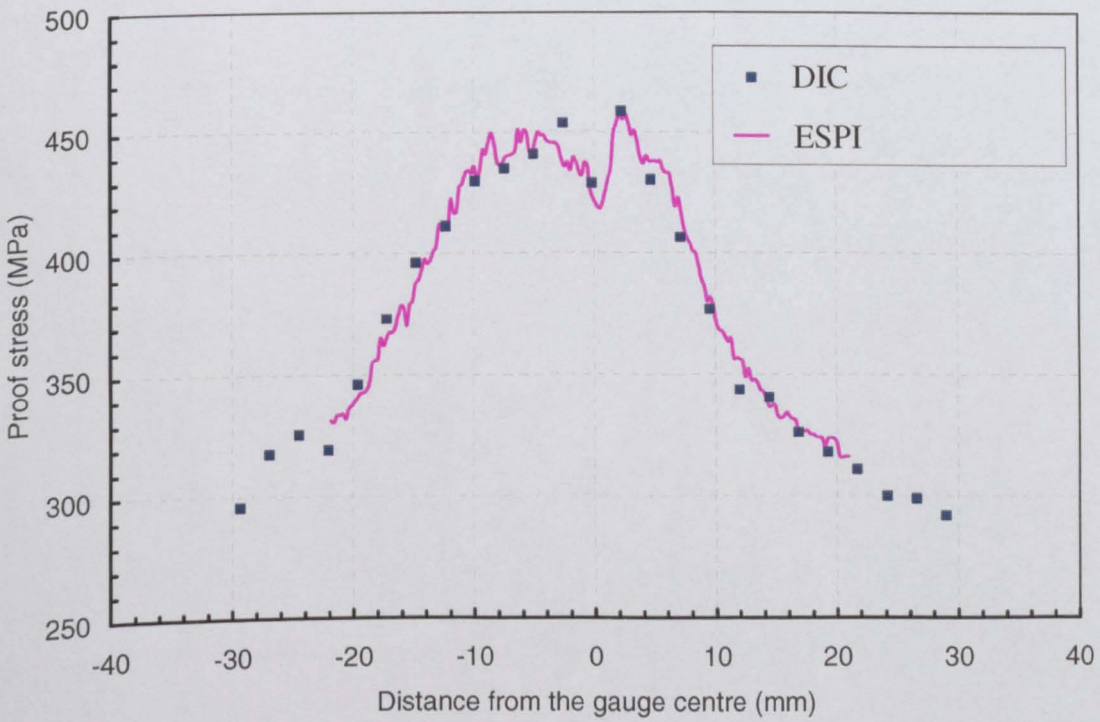

Figure 4.24 Variation of 0.5% proof stress along the length of the standard specimen

Figure 4.25 A photograph of the standard sample after tensile test. The marker shows the position of the sample where necking starts.

CHAPTER 5

DETERMINATION OF THE RESIDUAL STRESS USING THE CONTOUR METHOD

5.1 Introduction

The recently invented contour method is a destructive method, but has many advantages [1-4]. Unlike other sectioning methods, such as hole drilling, it can map the residual stress distributions in large cross sectional areas with a single cut.

The principle of the Contour Method is based on Bueckner's superposition principle [5]. A specimen having residual stresses is cut into two parts and the resulting relaxed surface contour is measured. The measured surface contour is then brought back to its original flat profile in a finite element model, replicating the original residual stress field. This procedure allows the full-field residual stress normal to the cut to be measured along the cut plane. The contour method involves four main steps: specimen cutting, measurement of the relaxed surface profile, data smoothing and finite element analysis to reconstruct the initial residual stress field.

The contour method allows the residual stress maps to be obtained directly from displacement maps with minimum time and computational cost. Furthermore, this

method is not sensitive to microstructure and does not require complex equipment. Since residual stress is directly determined by measured displacement, the contour method does not require complex analytical equations or inverse solution. However, like all residual stress measurement techniques the contour method also has some limitations. The main disadvantage with the contour method is that only one residual stress component can be obtained. Nevertheless, this is not a major drawback since many measurement applications show that only one of the normal components predominates and contributes to failure.

In this chapter, the theory of the contour method will be described first. Next, the fundamental steps of the contour method and their experimental procedures will be explained. Then the contour method will be applied in 2D and 3D situations in order to numerically validate the technique. Finally, the contour method will be applied on 1-pass and 3-pass groove weld specimens. The results will be compared with results obtained using the neutron diffraction technique.

5.2 Methodology

The principle of the contour method for measuring residual stresses is based on Bueckner's superposition principle. Therefore, Bueckner's superposition principle as applied to the contour method will be described here. In order to simplify an illustrative description of the contour technique, a two dimensional body will be utilized in this section although application of the contour method is equally valid for a three dimensional body.

Consider a 2D body possessing the arbitrary residual stress components $\sigma_{xx}(x,y)$, $\sigma_{xy}(x,y)$, and $\sigma_{yy}(x,y)$ as shown in Figure 5.1. In step A, the 2D body prior to the cutting process has both initial tension and compressive residual stresses. When the body is sectioned into two halves along the line $x = 0$, the residual stresses are fully released and new traction-free surfaces are created. The boundary conditions of the new traction free surfaces require that the normal and shear stress components along the line $x = 0$ are zero. Therefore, this condition due to relaxation of the residual stresses results in deforming of the body on both cut surfaces (step B).

The displacement vector on the stress-free surfaces along the line $x = 0$, $\vec{u}(0,y)$, can be expressed as the change in position of each point before and after cutting and it can be calculated as follows

$$\vec{u}(0,y) = u_x\vec{i} + u_y\vec{j}, \tag{5.1}$$

in which u_x, u_y are the displacement components in the x and y directions respectively.

The deformations caused by residual stress relaxation on both cut surfaces are assessed by assuming equivalence of the surface tractions. In other words, the surface tractions which enable to return the deformed surface to return back its original shape are equal and of opposite sign to those that caused the residual stresses which are released by sectioning. The relations between these surface-tractions and the residual stresses can be written as

$$T_x = -\sigma_x n_x, \qquad T_y = -\sigma_{xy} n_x, \tag{5.2}$$

where n is a unit normal vector, and on the flat surface $n_x = 1$ and $n_y = 0$.

Since the traction free boundary conditions certify that the normal and shear stress components along the surface are zero, the displacement vector $\vec{u}(0,y)$ given by Eq. (5.1) on the cut surface is a result of the residual stress relaxation (by assuming elastic relaxation) in Eq. 5.2 and hence the initial residual stresses can be calculated by applying displacement vector in the opposite direction to an unstressed half part as boundary conditions. The displacement and surface tractions can be seen in Figure 5.1 on the point A which is an arbitrary point on the cut surface.

As an experimental procedure, only the x component of the displacement vector u_x can be measured on the relaxed surface. In other words, the initial y coordinate of each point is unknown. However, it is still possible to determine the initial normal component of the residual stresses $\sigma_{xx}(0,y)$, if additional computation effort is taken.

In order to determine the initial residual stress component from the measured displacement, measured displacements can be expressed as a sum of the two displacement components as follows

$$\vec{u}(0,y) = \vec{u}_{normal}(0,y) + \vec{u}_{shear}(0,y), \tag{5.3}$$

in which $\vec{u}_{normal}$ is a displacement vector caused by the release of the normal stress component σ_{xx} and $\vec{u}_{shear}$ is a displacement vector caused by the release of the shear stress component σ_{xy}. In the plane of the cut, the displacement result of the normal stress relaxation is always symmetric

$$\vec{u}_{normal}^{left}(0,y) = \vec{u}_{normal}^{right}(0,y)\,. \tag{5.4}$$

Whereas, the displacement due to release of the shear stress is non-symmetric and in the half plane, the left side is always equal to opposite sign of the right side. That is;

$$\vec{u}_{shear}^{left}(0,y) = -\vec{u}_{shear}^{right}(0,y)\,. \tag{5.5}$$

Therefore, if the measured displacements on the both surfaces are averaged, the displacement due to shear stress relaxation will cancel out, and the average displacement will be equal to the normal stress relaxation.

The description of the contour method is valid with the assumption that the effect of the transverse displacement on the measured normal displacement is negligible. Preliminary FEA study [1] has shown that the effect of the transverse displacement is small enough to be ignored. Actually experimental error during the contouring of the relaxed surfaces has a greater effect ignoring the effect of the transverse displacement on the measured normal displacement [1].

Implementation of the contour method to a 3D body is similar to a 2D plane. In a three dimensional body, another spatial direction z needs to be taken into account during the measurement processes and the other three further residual stress components σ_{xz}, σ_{yz},and σ_{zz} will exist within the body. In this case, the traction free boundary conditions also require that shear stress component $\sigma_{xz}(0,y,z)$ is to be zero on the cut plane. Therefore, the measured normal displacement on the cut surface involves the contribution of the displacement due to this shear stress component $\sigma_{xz}(0,y,z)$. However, similar to 2D case, the averaged value of the

displacement due to this shear stress component $\sigma_{xz}(0, y, z)$ will be always zero on the half plane.

5.3 Implementation of the Contour Method

Implementation of the contour method involves four steps: sample cutting, contour measuring, data smoothing and stress computation. In this section, we will discuss them in detail.

5.3.1 Specimen Cutting

Specimen cutting is the first, and possibly the most critical step for the contour method since the final result depends upon the quality of the cut. There are four main assumptions for specimen cutting in the contour method. (This is normal in any destructive residual stress technique). First of all, it is assumed that only elastic relaxation occurs during the cutting. Next, deformation on the cut surfaces is entirely due to residual stress relaxation and no significant stress is introduced by the cutting. Then, there is no additional removal of material from the cut surface. Finally, one additional assumption that the contour method requires is flat cutting. This assumption is very important for implementation of the contour method because the plane of interest will deform from its original configuration due to stress relaxation during the cutting process and this relaxation may bring about deviation from the original plane of the a cut to different path. Therefore, specimens must be clamped firmly to avoid deviation from the original plane of the sectioning surface. Previous studies [1-4] have proven that these assumptions can be satisfied by the use of appropriate clamping.

An electro discharge machine (EDM) is typically used for the contour method since EDM has been shown very effective cutting for contour method [1-4]. EDM uses electrical discharges (sparks) to remove material from a work piece made of any material which conducts electricity. Rapid direct current electrical pulses are generated between the work piece and the wire electrode, in deionised water. At a certain applied voltage the material melts and vaporizes. A schematic of the EDM machining process is given in Figure 5.2. In order to avoid introducing thermal stresses into the material due to high temperatures during the cutting processes, the specimen and clamps are submerged into a cycling liquid in the EDM tank. In the project, samples have been sectioned by using a FANUC ROBOCUT α-O'B CNC (computer numerically controlled) wire electric discharge machine.

5.3.2 Contour Measuring

Following the specimen cutting, the next step in the contour method is to accurately measure the surface profile (topography) of the two cut surfaces. In this way, the mutual displacements normal to the cut plane due to the stress release are measured. Since the magnitude of the displacements for typical contour experiments are so small (between 0.02 mm and 0.2 mm) due to the very small ratio of σ/E for engineering components, measuring of the surface displacement requires very high precision equipment. The use of a coordinate measurement machine (CMM) provides adequately accurate measurement for a variety of specimens [1-4].

Coordinate measuring machines are designed to measure the surface of a complex shape with high precision. CMMs comprise four components which are the machine itself, a measuring probe, a computing system and the measuring software.

Measurements can be carried out in 3D using a probe which moves along three axes. The machine used for the contour measurement in this project is a Mitutuyo Crystal Plus 574 co-ordinate measuring machine with a ruby-tipped Renishaw touch probe, Φ 1mm. An overview of the CMM Mitutuyo Crystal Plus 574 co-ordinate measuring machine is given in Figure 5.3

5.3.3 Data Analysis

The initial step of the data analysis is to remove noise or pollution data caused by defects during manufacturing or the EDM cutting processes or due to uncertainty in the measurements. The removal process is applied on both the sectioned surfaces. Then, the contour measurement points of both surfaces are averaged. As explained in the section 5.2, this is essential in order to cancel out any shear stress effects on the cut surfaces and any deviations from a straight cut [1]. The resulting averaged surface is then numerically smoothed before inputting the data into a finite element simulation. The smoothing analysis involves fitting the measured and averaged displacements to smooth surfaces. There are numerous smoothing methods such as Fourier, polynomial, moving average or splines.

Data smoothing is vital since any variation in the averaged profile due to surface roughness produces an amplified effect during the calculation of residual stresses. One of the most popular data smoothing techniques is a 3D cubic-spline based algorithm [6]. The algorithm is based on joining polynomials at constant intervals (knots) to form a smooth spline. The knot spacing is adjusted to determine the best fit to the data by means of the least squares analysis.

5.3.4 Determination of Stress

Once measured and averaged displacements have been smoothed to minimize the effect of the EDM surface roughness on the residual stress profile, half of the sectioned part is modelled as initially flat and stress free surface rather than the deformed shape as this is a simpler approach. The opposite of the averaged and smoothed data is applied as displacement boundary conditions to nodes on the surface which represents the cut. An equilibrium step is taken and the resulting residual stress normal to the cut surface is obtained. Boundary conditions can be applied on either a deformed or a flat surface. Since the displacements applied on the cut surface as boundary conditions are small enough, results obtained by applying the boundary conditions on deformed surface and flat surface are equivalent [1].

5.4 Numerical Validation of the Contour Method

In this section, finite element simulation is used for the validation of the contour method in the 2D and 3D bodies. Validation of the contour method by FE simulation involves two steps. In the first step, residual stresses are generated within a body (step A). Subsequent to this process, the EDM cutting is simulated and the resulting displacements caused by release of the residual stresses on the 'cut' surfaces are 'measured' (step B). In the second step, half of the geometry is modelled and the opposite sign of the displacements recorded in the first step are applied on the unstressed and flat surface as boundary conditions. Finally, the result of the purely elastic FE analysis calculation is compared with the known residual stress values.

For our contour method simulations, the eigenstrain concept is used for generating initial residual stresses in a body. Previous studies have demonstrated that residual stresses in a body are due to an incompatible strain field which is the so-called inherent strain [7-9] or eigenstrain [10-11]. Eigenstrain was defined as anisotropic thermal expansion coefficients. In this way the full eigenstrain tensor could be introduced into the FE model. After the equilibrium step is taken, the corresponding residual stresses are obtained. Much greater detail about eigenstrain will be given in the following chapter 6. In this chapter, eigenstrain was used for merely generating residual stress field within the 2D and 3D bodies.

5.4.1 Numerical Experiment: 2D Contour Method

In order to illustrate the validity of the contour method in a 2D body, a beam with 200 mm length and 100 mm of width in the *xy* plane was used where the length of the beam is in the x direction (longitudinal) and the width of the beam is in the y direction (transverse).

A 2D body is considered to be treated with continuous processing along the x direction (the variation of the eigenstrain along the x direction is constant). Therefore, the compatibility equation in 2D

$$\frac{\partial^2 \varepsilon_{xx}}{\partial y^2} + \frac{\partial^2 \varepsilon_{yy}}{\partial x^2} = 2\frac{\partial^2 \varepsilon_{xy}}{\partial x \partial y}, \tag{5.6}$$

shows that only x direction component of eigenstrain ε^*_{xx} causes to residual stresses within the body as the other components of the eigenstrain simply satisfy the compatibility condition, i.e. their partial derivatives with respect to x are zero. Note that continuously processing along the one of the principle axis is not a requirement

of the contour method. Here, continually processing was used to simplify the equations.

Because of the symmetrical characteristic of the system, only half of the beam was modelled using the FE code ABAQUS. The material was assumed to be linearly elastic and isotropic with an elastic Young's modulus of 200 GPa and a Poisson's ratio of 0.3. The mesh was characterised by linear shape four node reduced integration points, and plane stress case. In order to accomplish the cutting simulation, a constraint boundary condition was applied on the cut line.

The longitudinal component of an arbitrary eigenstrain with the following formula was then introduced into the model:

$$\varepsilon_{xx}^{*}(y) = -\frac{500MPa}{E}\exp\left[-3\left(\frac{2y}{w}\right)^{2}\right], \tag{5.7}$$

in which w is the width and E is the elastic Young's modulus of the 2D body. Solving the equilibrium gave the known residual stress within the body. The residual stress component normal to the cut plane was recorded for later comparison with the contour method. Following recording of the residual stress, the constraint boundary on the cut line was released in order to simulate the 'cutting'. The resulting displacement on the mid-plane due to residual stress relaxation was 'measured'.

The next step was to simulate the contour method. For this purpose, half of the geometry with undeformed and unstressed conditions was modelled by keeping all the parameters (mesh density, material) the same. The 'measured' displacement from the first simulation was applied as displacement boundary conditions with

opposite sign. The resulting residual stress component normal to the cut plane was compared with the known value of the residual stress obtained from the first model.

5.4.2 Numerical Experiment: 3D Contour Method

For the validation of the contour method in a 3D body, a block of dimensions 120 mm long, 60 mm wide and 15 mm thick was modelled. It was assumed that the specimen was isotropic and linear elastic with a Young's modulus of 200 GPa and a Poisson's ratio of 0.3. The mesh size was chosen as 0.5 mm × 0.5 mm with reduced integration point 4 nodes, and linear shape. For this simulation, the principal direction normal to the cut plane was z, the long transverse direction was x and the short transverse direction was y. The block was assumed to be continuously processed in z direction so that the eigenstrain variations in the z direction are constant. Once again, continuously processed body in one of the principle directions is not a requirement of the contour method.

The block was considered to have normal and shear stresses along the plane of the cut so that the accuracy of the contour method in the event of having multiple components of residual stress on the cut plane can be seen with this numerical experiment. Similar to the 2D simulation, the residual stresses within the body were generated by inputting arbitrary eigenstrains into the model. Since each component of the eigenstrain can produce residual stresses within the body, all eigenstrain components for the simulation of contour method in three dimensions were input into FE model with the following formula:

$$f(x) = \sin(2\pi x / w)/2, g(y) = \cos(2\pi y / t)/2, \tag{5.8}$$

$$\varepsilon^*_{xx}(x,y) = \varepsilon^*_{xy}(x,y) = \varepsilon^*_{xz}(x,y) = \varepsilon^*_{yy}(x,y) = \varepsilon^*_{yz}(x,y) = \frac{1}{250} f(x)g(y), \qquad (5.9)$$

where w is the width and t the thickness of the sample. The cross-sectional profile variation for the five components of eigenstrain (except for ε^*_{zz}) is shown in Figure 5.4. Since the effect of ε^*_{zz} on residual stress is much more than the other components the magnification of ε^*_{zz} was chosen to be smaller than the others. Defining anisotropic thermal expansion coefficients as a function of x and y positions, all six eigenstrain components were input into the FE model as a pseudo thermal strain. The resulting known residual stress component that is normal to the sectioned surface was recorded (before the 'cut'). Then, the model was 'cut' into two halves and the deformation on both surfaces was 'measured' and averaged. Next, one of the halves, undeformed and unstressed, was modelled and the inverse sign of the displacements recorded from first simulation were applied on the cut surface as boundary conditions. The resulting residual stress component normal to the cut surface was recorded.

5.4.3 Results and Discussion

Figure 5.5 denotes the 2D model with the residual stress variation caused by the eigenstrain with the formula given by equation 5.7. Here, the deformation magnification is 300 for the figure. After EDM simulation of the model, the displaced values of the deformations on the cut line were recorded. The displacement variation generated by the eigenstrain on the cut line is given in Figure 5.6. As is expected from Figure 5.5 where the residual stress value is positive in the middle of the cut line and negative at the edges, the displacement value has opposite variations along the cut line.

The comparison between the known initial residual stress obtained from the first simulation and the measured residual stress acquired from the contour simulation through the cut line is given in Figure 5.7. As can be seen, there is very good agreement between them. The maximum error between the known and measured values is only 0.077 MPa. Since the cut line did not initially contain significantly large shear stress (maximum 2 MPa), there was no need to average the cut pairs and to model the full size of the 2D body. In the event of having only the normal component on the plane of interest, the displacements from both sides are identical.

Figure 5.8 shows the displacement on the surface caused by the release of the residual stresses subjected to the cut simulation for 3D body contour method verification. The resulting contour maps of the known and measured residual stresses are given in Figure 5.9. Contour measurement obtained from the average of the cut pairs, the left displacements only and the right displacements only are also given in the same figure. As can be seen here, the contour method result obtained from the average of two cut surfaces is in good agreement with the known initial residual stress map. Although similar results were acquired by taking only one pair of the surfaces (left or right), there are still differences that can be observed. Especially, near to the top line and bottom line at the surfaces, the differences are visible and they are different from the initial known residual stress. From the plots, it can be inferred that the use of only displacements from one side would bring about wrong results.

In order to compare the line plots of the known residual stress and calculated contour results obtained from the averaged displacements, residual stress values

were extracted from the FE model along the line at y =7.5 mm. It can be seen from the Figure 5.10 that the contour result using the averaged displacement is in good agreement with the known residual stress. The small differences between the calculated and known residual stresses stem from the mesh size for the cut simulation, which was not able to be less than 0.5mm as the pseudo thermal analysis for generating the eigenstrain is highly computationally massive. It was also observed from this numerical validation that the finer mesh was chosen the smaller error was obtained between the known and measured value. In addition, the difference is attributed to the geometrical simplicity that was mentioned in the methodology of the contour method.

5.5 Residual Stress Measurements in Single and Multi-Pass Groove Weld Specimens Using Neutron Diffraction and the Contour Method

In this section, the contour method was performed on 1-pass and 3-pass groove weld specimens. Residual stress measurements on the same specimens were carried out using the neutron diffraction technique by Turski and Edwards [12]. The stress results of the two independent techniques were compared to see the agreement level of these methods on groove weld specimens. Furthermore, measurements of residual stresses made in a single pass compared to those in the 3-pass groove weld specimen, has allowed the effect of successive weld passes on the final residual stress field to be examined.

5.5.1 Material and Specimens

The groove weld specimens were machined from a 316L austenitic stainless steel with 50 mm thickness. Dimensions were reduced to a $200\times180\times25mm^3$ sized blank. Then, each blank was subjected to a stress relief solution heat treatment in order to remove any leftover residual stress. Then one side of each blank was machined out further to produce the groove. Figure 5.11 denotes a schematic of the groove weld blank and the geometry of the groove.

Welding was carried out using the manual metal arc process, with a target heat input of about 1.8kJ/m. Specimens were fabricated with 1, 2 and 3 single pass weld beads. However, only the single pass and the 3-pass samples were studied here.

5.5.2 Experimental Procedures

5.5.2.1 Neutron Diffraction Measurements

Turski and Edwards [12] measured the residual stresses in the groove welded specimens using neutron diffraction, which was carried out on the ENGIN-X instrument at the ISIS facility at the Rutherford Appleton Laboratory, UK [13].

Measurements in the 1-pass and 3-pass welded specimens were carried out in the three principal directions (longitudinal, transverse and normal to the weld bead). SscanSS software [14], programmed by The Open University, was used to plan and control the experiments. This software helps for positioning of the point in an accurate way. The measurement positions were defined prior to the experiment using a virtual model of the sample.

The origin of the coordinate system was chosen at the root of the groove as shown in Figure 5.12. For each specimen, residual stress measurements using neutron diffraction were carried out along three different lines: Scan A, scan B, and scan C. The position of each measurement point for the 1 and 3 pass specimens have also been drawn in the Figure 5.12. Scan A is the line through the thickness at $x = 0$, scan B and scan C are the lines in the transverse direction at $y = 2.9$ mm, and $y = 7$ mm respectively. In all cases measurements were made using a $4\times4\times4mm^3$ gauge volume.

5.5.2.2 The Contour Method

Cross sectional mapping of the longitudinal residual stresses of both the 1 and 3 pass groove weld specimens at the mid-length of the weld (Figure 5.11) were obtained by applying the contour method.

For the very first step of the contour method, the groove weld specimens were sectioned in half by wire electro discharge machining (EDM) using a 0.1 mm diameter brass wire. In order to minimize movement of the specimens as stresses were relaxed during the cutting processes, holes were drilled at the end of the specimens. It was assumed that these holes did not alter the residual stress distribution at the mid-length of the weld (measurement plane). The holes enabled specimens to be clamped firmly by bolts. To prevent additional thermal stresses during the cutting, the specimens were submerged into temperature-controlled deionized water. Figure 5.13 shows a picture of the 1 and 3 pass groove weld specimens after the cuts. Also the holes can be seen in the same picture.

Subsequent to EDM cutting, the surface contours of each of the two cut pairs of the specimens were measured. Each cut surface was measured on a 0.5 mm spaced grid, resulting in ~17,000 measurement points for each surface.

After the measurements, data reduction steps were employed. For this purpose, measured data from the both sides were translated till they were aligned in a common coordinate system. Then they were interpolated on a regular grid in order to make sure that the averaging process of the cut surfaces was done between corresponding locations. Next, the contour positions of both cut sides were averaged. This averaging step is essential as it allows the effect of shear stresses and any imperfections in the cut to be removed. The resulting surface contour was subsequently smoothed before being applied in the FE analysis. The smoothing of the data is necessary as any variations in the surface contour due to the surface roughness of the EDM cut is amplified during the process of calculating stress from displacements. Smoothing was carried out by curve fitting, using a 3D cubic spline based algorithm [6]. In this work the knot spacing for fitting was set to be identical in both directions for each specimen. For this work 3.5, 5, 7 and 10 mm knot spacing intervals were used to fit the measured and averaged displacements for both specimens.

The stresses were finally calculated from the surface measurements by applying the contours as boundary conditions, but with reversed sign, as a series of displacements to the previous flat cut face of a one-half plate the finite element model representation of each grooved plate specimen. The whole analysis is assumed to behave elastically. The elastic constants used were: E=196 GPa and υ=0.3. Finally,

stress values obtained from the contour measurements were extracted from the FE model at the corresponding positions where each neutron diffraction measurement was carried out and compared with the neutron diffraction results.

5.5.3 Results and Discussion

To see the contour measurements on the cut surfaces of the 1-pass and 3-pass groove welded samples, the measured and averaged displacements are given in Figure 5.14. Choices of a suitable fitting order and an interval to define the surface feature accurately are very important. There should be a balance between the accuracy and smoothness of the fitting data. Therefore, using different sets of the knot spacings over which the data were fitted, as explained in the section 5.3.3, the data analysis was carried out. In order to illustrate the smoothed data of the contoured and averaged surfaces, the 5×5 mm cubic spline data that was used for fitting to the averaged data for the 1 and 3 pass groove weld specimens are given in Figure 5.15.

Preliminary contour results of the 1-pass and 3-pass groove weld specimens [15] are given in Figure 5.16. Residual stresses were found to be tensile in and around the weld region and compressive remote from the weld region. The peak tensile residual stresses are about 400 MPa for the 1-pass and 425 MPa for the 3-pass specimens. It can be also seen from the figure that there were very high compressive residual stresses near to the top surface of the specimens with peak values around -400 MPa. In a previous study [15], these high compressive stresses were attributed to machining residual stresses.

In order to find out whether the residual stress field along the cut plane had been successfully determined using the contour method, additional analyses were carried out. For this purpose, the measured and averaged raw data, and their smoothed data obtained from the various knot spacing splines for the 1 pass groove weld specimen were compared along the line x=0 mm x=8 mm. Figure 5.17 (a-b) shows the comparisons between the averaged data and the 3.5×3.5 mm, 5×5 mm, 7×7 mm, and 10×10 mm splines along the line x=0 mm x=8 mm. These figures show that none of the cubic splines was able to fit the sharp gradient of the averaged value especially when y>0. Note that these figures denote the measured data in its gridded form (since this is the form where the cubic splines are fitted to the data) thus the presence of extrapolated data at regions beyond the surface plane, while this data is not applied to the FE model to generate the measured stresses.

Therefore, in contrast to the preliminary results in Kartal et al. [15] where the high compressive stress close to the top surface was attributed to machining residual stress, the actual reason is due to poor fitting of the sharp measured profile close to the top surface resulting in the generation of artefacts in the final stress maps.

The reason for the presence of a sharp gradient in the measured data around the groove wall may be due the fact that the thickness of the weld region is different from the parent region. Also, since a wire is electrically charged with respect to the workpiece, and spark erosion removes material during the cutting process, the finite (non-zero) width of the cut would vary in the weld region. In other words, cut-width in the weld region will be larger than that in parent region. The effect of a change in thickness at the cut surface may be investigated by means of a stress-free sample of

varying thickness. Since the original residual stress would be zero in the sample, the variation of the measured displacement in thicker and thinner regions would be the result of the cut-width.

Figure 5.18 denotes a similar problem when the same comparison is made along the line $y = 7$ mm. This problem again results in deviation of the cubic splines from the measured data.

It is known that the accuracy of the final FE results in the contour method is limited by the ability of the smoothing techniques. Different polynomial functions other than the splines would be used to smooth the averaged value if they would provide a better fit and results. However, comparisons of the different smoothing techniques are not the object of this investigation.

The other way to fit the measured data appropriately is to remove some measured points which cause the poor fit and the high compressive residual stress along the line of the top surface. Since this process was convenient to apply for our problem which provides a good fit especially in the zone ($0<y<7$) where scans B and scans C were carried out, two lines of the measured points on the top surface were removed before the row data was averaged. The comparisons between the averaged data and the four different splines along the lines x=0 mm x=8 mm after removal these data points are given Figure 5.19 (a-b). In this way, much closer agreement was found between the averaged data and the fit for the different splines. The figure also shows that the best fits were obtained by using the 3.5×3.5 mm and 5×5 mm splines.

The longitudinal residual stress maps measured by the contour method for different densities of the cubic splines for the 1 pass groove weld specimen are shown in Figure 5.20. The averaged data was smoothed by cubic splines with 3.5 mm, 5 mm, 7 mm and 10 mm knot spacings after removing the data points which caused high compressive residual stress on the top surface. The figure shows the largest stress is less than 350 MPa at the base of the welded groove and compressive residual stress less than – 200 MPa on the top of the one pass specimen.

Figure 21 shows a comparison of the longitudinal residual stress measurements made along Scan A for the 1 pass groove weld specimen. Results from all the spline fits have been presented in order to illustrate the sensitivity of the cubic spline densities on the final result. The measurements show that the stresses vary between 50-300 MPa at the base of the plate with peak stresses of 300 MPa just beneath the welded groove. It can be seen from the Figure that the same general shape of the profile is captured by both the neutron diffraction measurements and the contour method.

For clarity, contour method results are presented using two separate figures for the comparison between the two techniques for each scan (scan B and scan C). Figure 5.22 (a-b) show the comparison between the neutron diffraction and contour method along scan B for 1 pass groove weld. The measured stresses along line B with peak stresses 200-250 MPa adjacent to the welded groove, these stresses fall to ~ -50 MPa at 40 mm from the centre of the weld.

In the case of scan C (Figure5.23 a-b) peak stresses of 175-225 MPa are found close to the groove wall, which fall to -60 MPa at 60 mm from the weld centre. Agreement between the two measurement techniques is generally good for scans A-C for the 1 pass specimen. The best agreement is found for scan B, while the greatest differences (up to 100 MPa discrepancy) are found for scan A.

Because the same problem of compressive residual stress was found near to the top surface due to the poor fitting of the sharp gradient in the 3-pass groove weld specimen, some data points on the top surface were removed before carrying out the data analysis.

The FE results obtained from the contour method for all four different spline densities after filtering of the data for the 3-pass groove weld specimen are given in Figure 5.24. It is found that tensile residual stress exists with a peak value of around 400 MPa in and around the weld, and compressive residual stress is present remote from the weld region with a peak value of -250 MPa. The residual stresses are hence tensile throughout the thickness of the specimen in the middle of the specimen, balanced by a large region of compressive stress from about $x = \pm 40$ mm until the far edges of each side of the specimen.

Figures 5.25-5.27 show comparisons between contour and neutron diffraction measurements along scans A, B and C for the 3 pass plate respectively. All figures show that peak stresses in the welded region are 50-100 MPa higher than those found in the 1-pass specimen. Agreement between the two measurement techniques is much closer than that found for the 1-pass plate, with most measurements lying

within 50 MPa of one another. This can be explained due to the simpler geometry of the 3-pass welded plate, and in the case of the single-pass plate data in the vicinity of the unfilled groove which resulted in cut-with error is not described well by the smoothing spline causing the stress in this area determined by the contour method to have a high error attribute.

FE results obtained from the contour method for both 1 pass and 3 passes groove weld specimens show that the residual stress map determined from the 3.5×3.5 mm cubic spline demonstrates very short range variations in stress, which was actually indicative of over fitting of the noise in the original surface contour data. Very short range fluctuations on the cut surface were not expected in the macro stress variation.

In contrast to the 3.5×3.5 mm cubic spline, the same residual stress map determined from the 5×5 mm cubic spline indicates a much smoother variation in residual stress. Figure 5.20 and 5.24 show the same maps of stress determined from 7×7 and 10×10 mm cubic splines, these maps show no significant improvement in the distribution of stress over the 5×5 mm cubic spline map, apart from a general increase in smoothing. Profile comparisons between the various cubic splines and measured data (similar to those shown in Figures 5.19) also suggest that the 5×5 mm cubic spline represents the best compromise between smoothing the noise in the measured data and fitting the underlying surface profile. For this reasons the 5×5 mm cubic spline stress map was found as the optimum result amongst the various cubic spline densities employed in this study, and represents the final results for the 1-pass and 3-pass groove weld specimens.

5.6 Conclusion

In this chapter, the theory of the contour method and its fundamental link with experimental procedures was explained. Then validation of the contour method was shown using 2D and 3D geometries. Finally, the contour method was applied on 1-pass and 3-pass groove weld specimens. Comparisons between two measurement techniques, the contour and neutron diffraction methods, have shown good general agreement, increasing the level of confidence for these measurements.

It should be pointed out that the efficacy of the method is not only limited by spline fitting. Other assumptions and errors also may affect the final results obtained from the contour method. In particular, analysis of the cutting assumptions may benefit from further investigation. In order to find out whether only elastic relaxation occurs during the cutting process, especially for materials possessing large residual stress, elastic-plastic finite element analysis can be carried out to investigate the measurement error from inelastic deformation. Such analysis has been performed by Lee and Hill [16], showing minimal plasticity effects even for large stresses. In addition, non-destructive residual stress measurement techniques could be used to investigate the agreement level between this analysis and the contour results, which would indicate whether significant stress is introduced by cutting.

The cutting flatness is the most important criterion for the cutting induced error. The error due to the cutting flatness can be evaluated from the stress-free sample which would be cut under the same condition as the residually stressed specimen where residual stresses are to be measured. Measured displacements on the stress free

sample are imposed into the finite element model as displacement boundary conditions and the resulting residual stress would give the cutting induced error.

5.7 References

[1] M.B. Prime (2001). Cross-Sectional Mapping of Residual Stresses by Measuring the Surface after a Cut. Journal of Engineering Materials and Technology, vol. 123, pp. 161-168.

[2] Zhang Y., Fitzpatrick M.E. and Edwards L. (2002). Measurement of the Residual Stresses around a Cold Expanded Hole in an EN8 Steel Plate Using the Contour Method. Materials Science Forum, vol. 404-407, pp. 527-534.

[3] Zhang Y., Ganguly S., Edwards L. and Fitzpatrick M.E. (2004). Cross-Sectional Mapping of Residual Stresses in a VPPA Weld Using the Contour Method. Acta Materialia, vol. 52, pp. 5225-5232.

[4] Zhang Y. (2004). Numerical and Experimental Exploration of the Contour Method for Residual Stress Evaluation. PhD Thesis, The Open University, UK.

[5] Bueckner H. F. (1958). The Propagation of Cracks and the Energy of Elastic Deformation. Trans. ASME, vol. 80, pp. 1225-1230.

[6] DeBoor C. (2000). MATLAB, Spline Toolbox User's Guide. The Math Works, Inc., Natick, MA, USA.

[7] Ueda Y., Fukuda K., Nakacho K. and Endo S. (1975). A New Measuring Method of Residual Stresses with the Aid of Finite Element Method and

Reliability of Estimated Values. Transaction of the JWRI (Japanese Welding Research Institute), vol. 4(2), pp. 123-131.

[8] Ueda Y. and Fukuda K. (1986). New Measuring Method of Axisymmetric Three-Dimensional Residual Stresses Using Inherent Strains as Parameters. Journal of Engineering Materials and Technology, vol. 108(4), pp. 328-334.

[9] Ueda Y.M. and Fukuda K. (1989). New Measuring Method of Three Dimensional Residual Stresses in Long Welded Joints Using Inherent Strains and Parameters. Journal of Engineering Materials and Technology, vol. 111, pp. 1-8.

[10] Mura T. (1987). Micromechanics of Defects in Solids. Kluwer, Massachusetts

[11] Hill M.R. (1996). Determination of Residual Stress Based on the Estimation of Eigenstrain. PhD Thesis, Stanford University, USA.

[12] Turski, M. and Edwards L. (2006). Boiler Spines Residual Stress Measurements Programme Task 2.1: Residual Stress Measurements by Neutron Diffraction on Groove Weld Specimens. British Energy Generation Limited.

[13] Santisteban, J.R., Daymond, M.R., James, J.A. and Edwards, L. (2006) ENGIN-X: a third generation neutron strain scanner, Journal of Applied Crystallography, vol. 39, pp. 812-825.

[14] James J. A., Santisteban J.R., Daymond M.R. and Edwards L. (2004) A Virtual Laboratory for Neutron and Synchrotron Strain Scanning", Physica B, vol. 350, pp. E743-E746.

[15] Kartal M.E, Turski M., Johnson G., Gungor S. Fitzpatrick M.E., Withers P.J. and Edwards L. (2006). Residual Stress Measurements in Single and

Multi-Pass Groove Weld Specimens Using Neutron Diffraction and the contour Method, Materials Science Forum, vol. 524-525, pp. 671-676.

[16] Lee M.J. and Hill M.R. (2007). Intralaboratory Repeatability of Residual Stress Determined by the Slitting Method. Experimental Mechanics, vol. 47, pp.745-752.

5.8 Figures

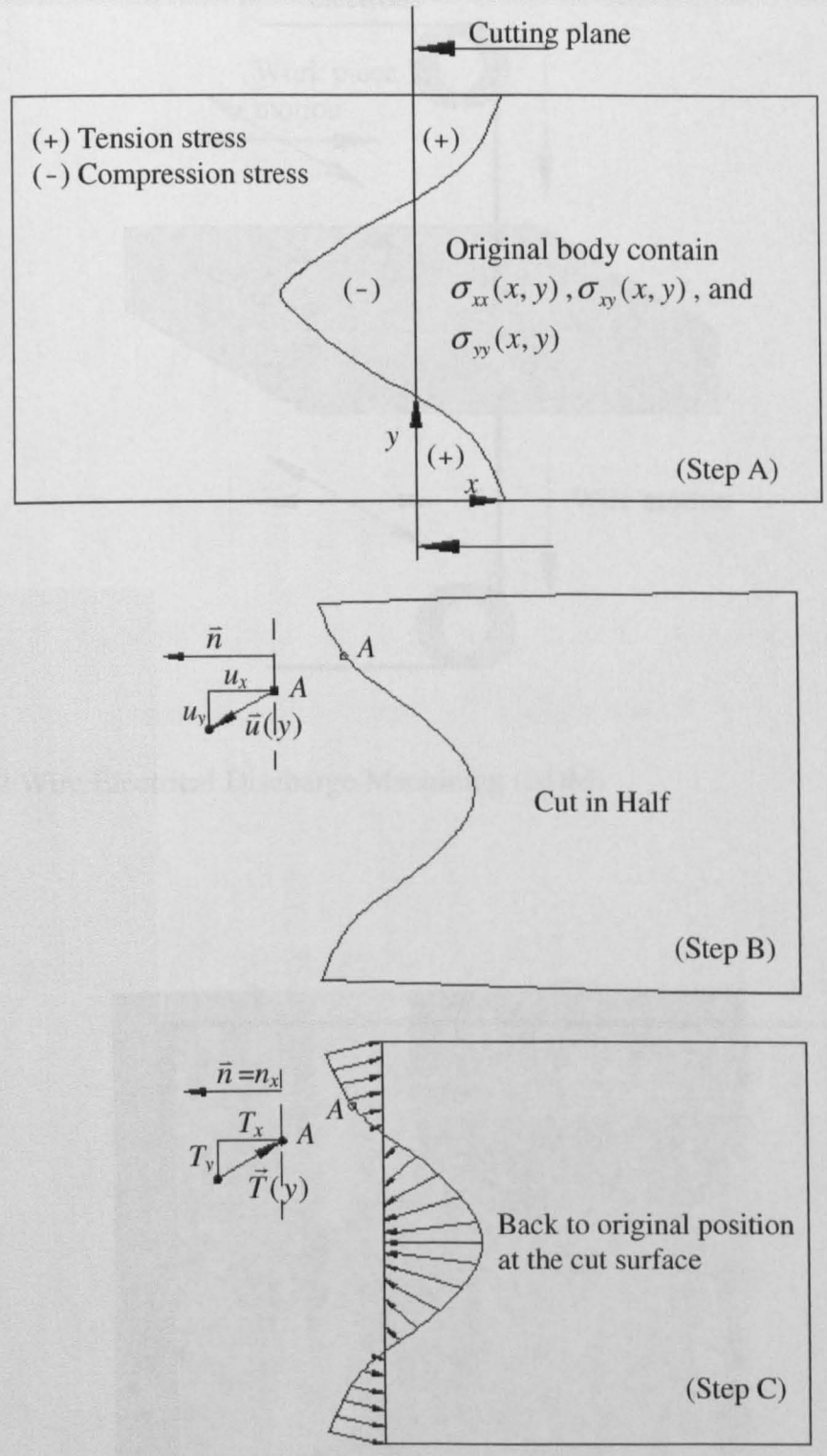

Figure 5.1 Illustration of Bueckner's superposition principle. Point *A* symbolizes any arbitrary point on the cut plane with its displacement and surface traction components.

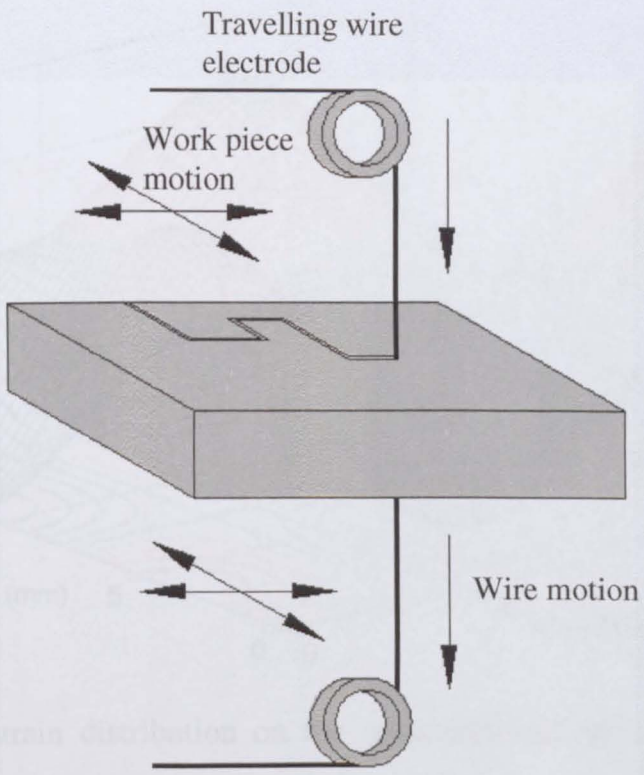

Figure 5.2 Wire Electrical Discharge Machining (EDM)

Figure 5.3 Overview of Coordinate Measurement Machine.

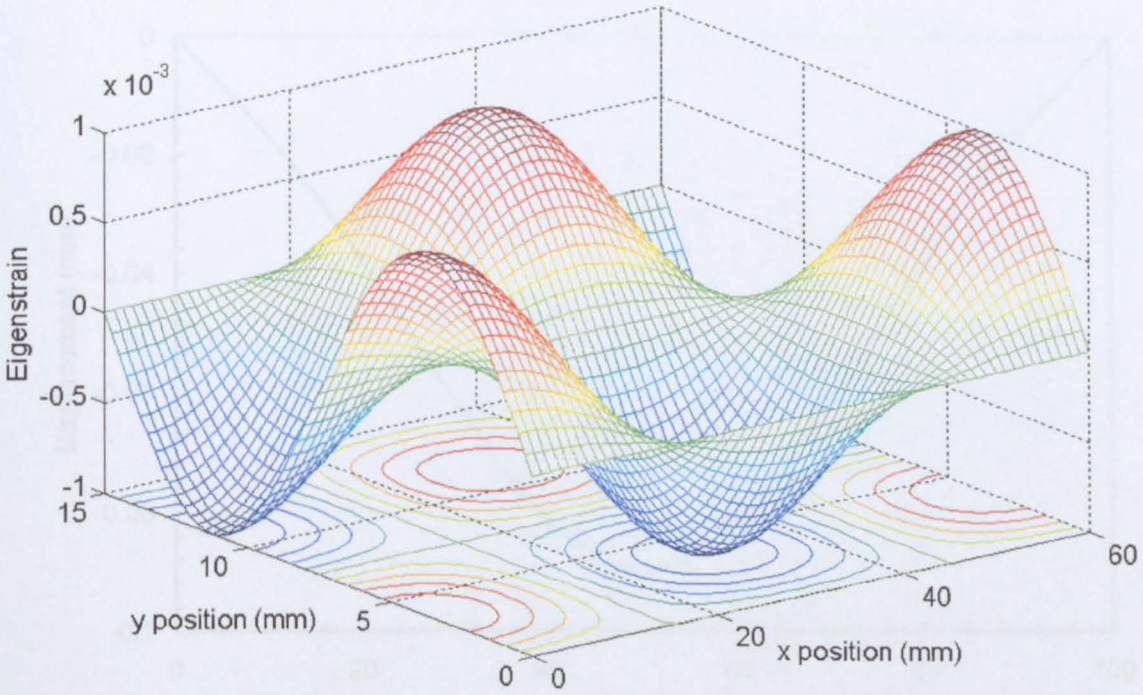

Figure 5.4 Eigenstrain distribution on the cross-sectional area for the numerical validation of the contour method in a three dimensional model.

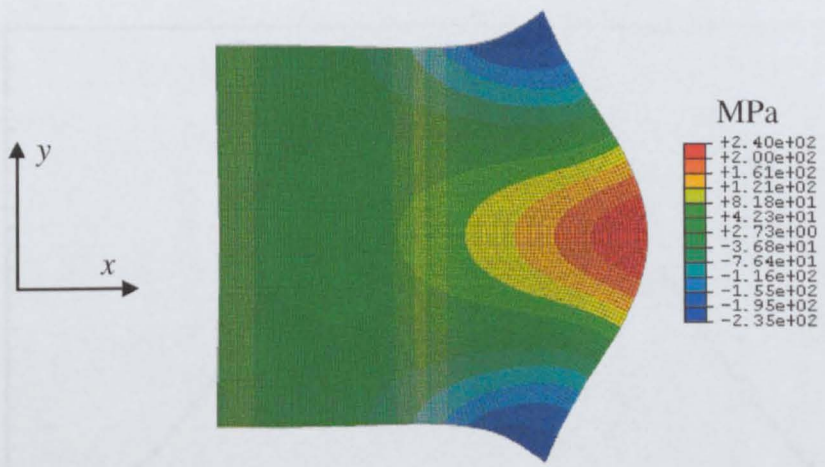

Figure 5.5 Map of the residual stress σ_{xx} for 2D numerical validation of the contour method. Magnification of deformation is 300.

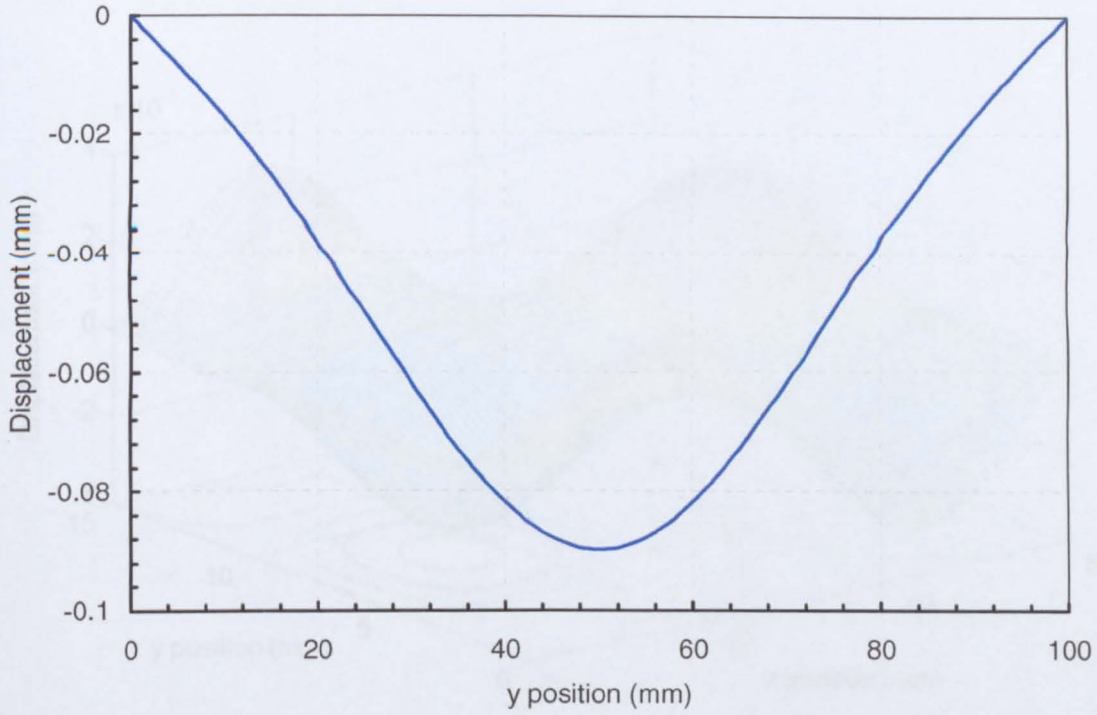

Figure 5.6 Displacement along the 'cut' line for 2D numerical verification of the contour method.

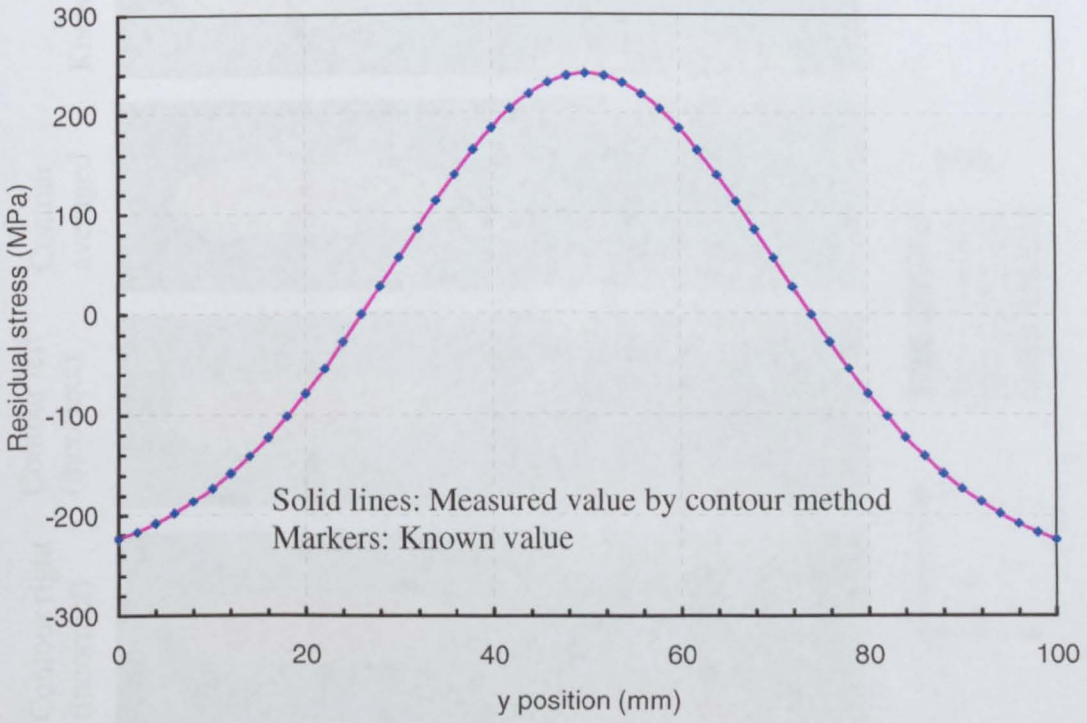

Figure 5.7 Comparison of known and measured residual stress for 2D numerical verification of contour method along the cut line

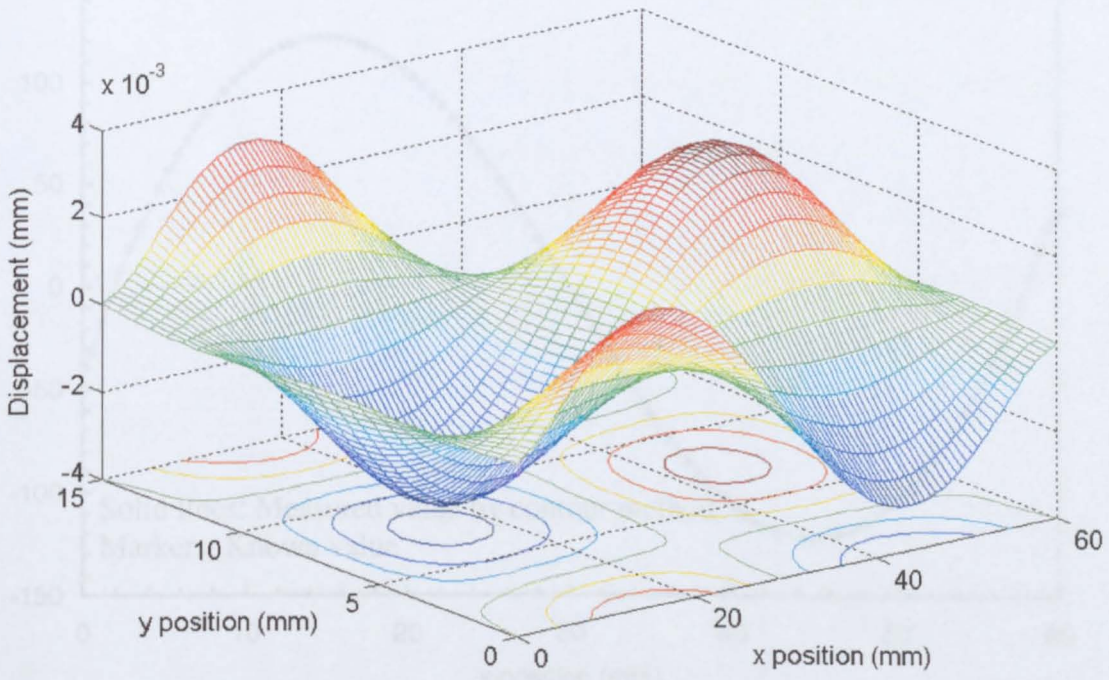

Figure 5.8 Displacement variations on the plane of interest for 3D numerical experiment.

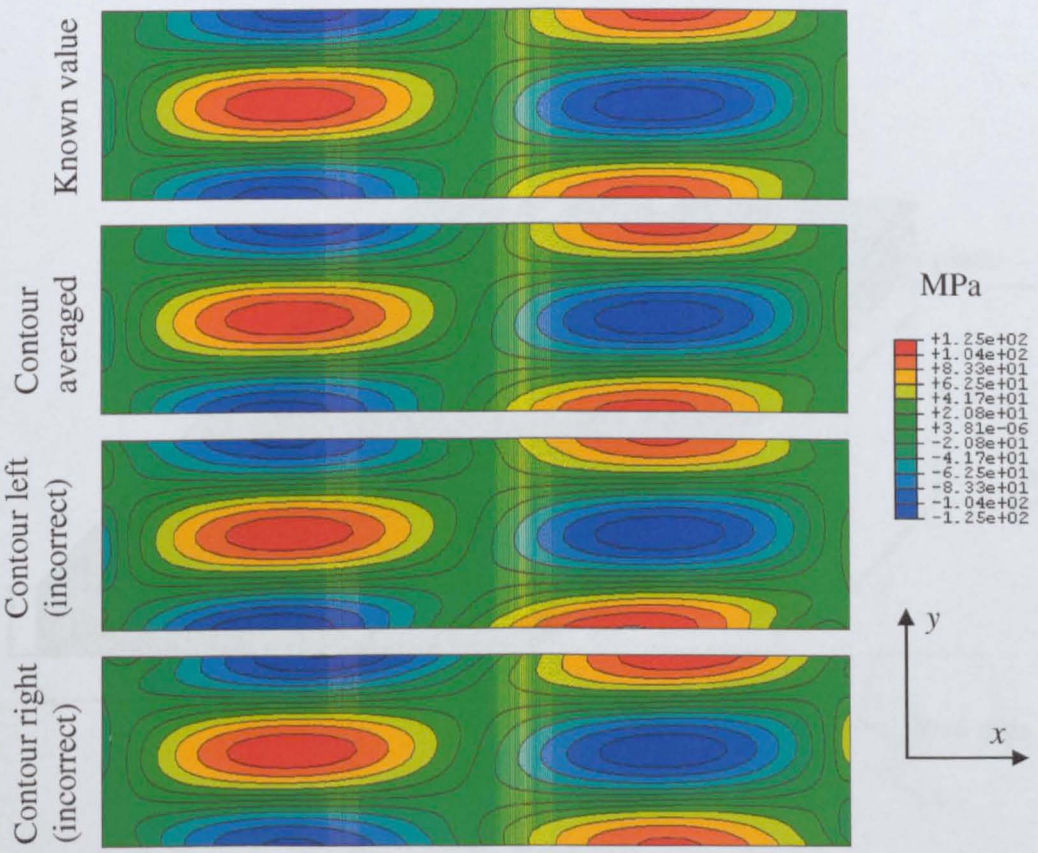

Figure 5.9 Known and calculated residual stress profiles.

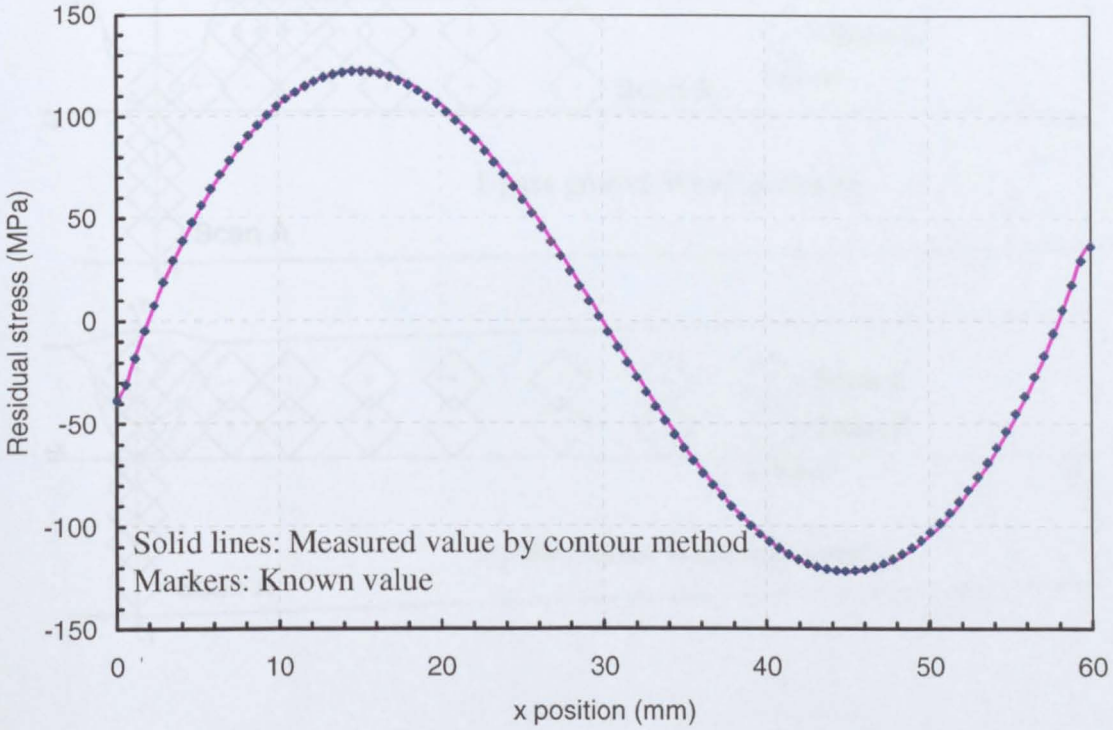

Figure 5.10 Comparison known and measured residual stress component normal to the cut surface for 3D numerical verification of contour method along the line y=7.5 mm.

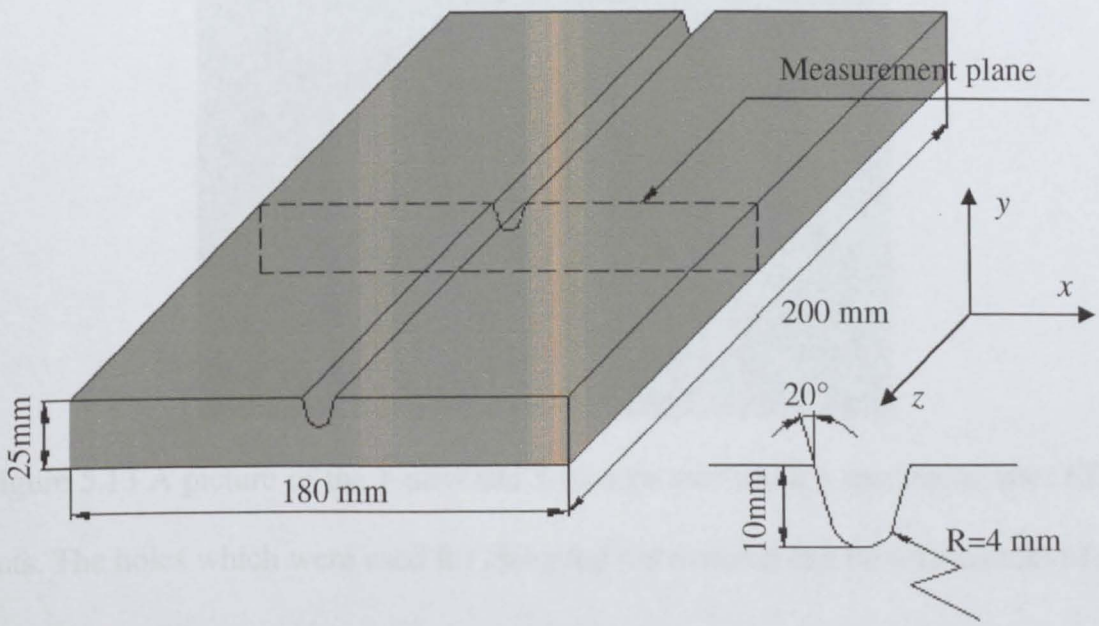

Figure 5.11 Schematic of the groove weld blank before welding and the geometry of the groove.

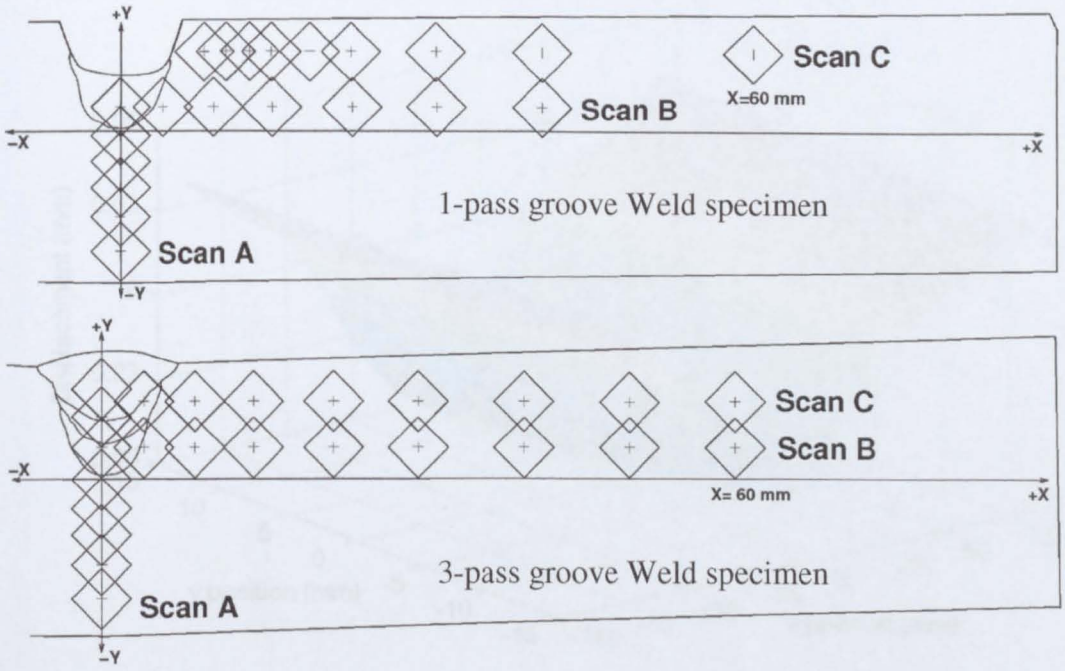

Figure 5.12 Schematic showing neutron diffraction measurement positions within each pass groove weld specimen, at the measurement plane.

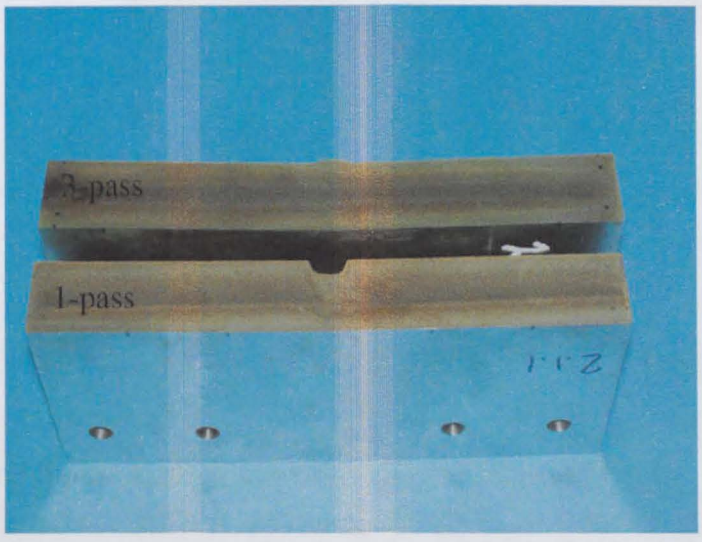

Figure 5.13 A picture of the 1-pass and 3-pass groove welded specimens after EDM cuts. The holes which were used for clamping the material can be seen bottom of the specimen in figure.

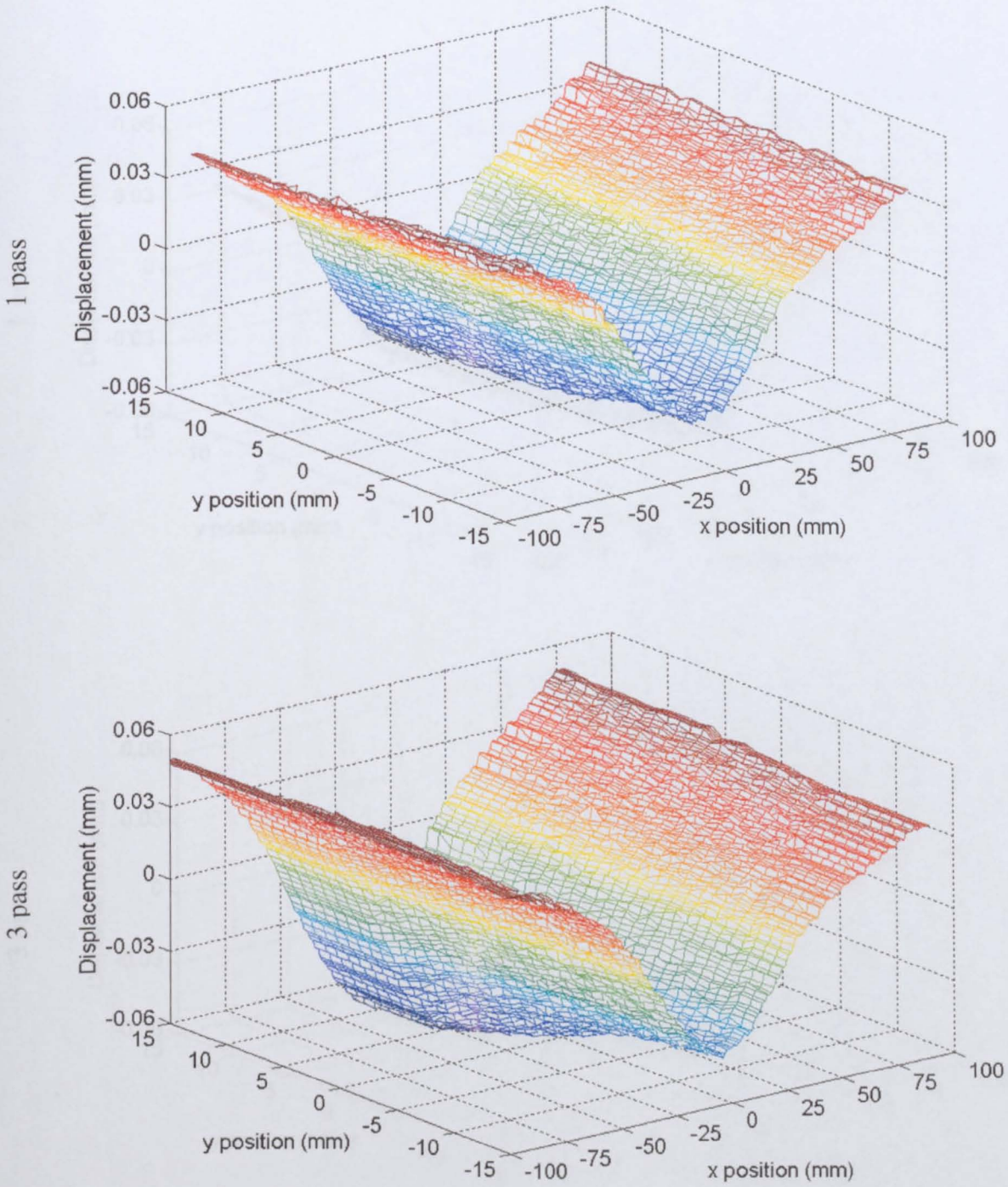

Figure 5.14 1 and 3 pass averaged surface contour measurements.

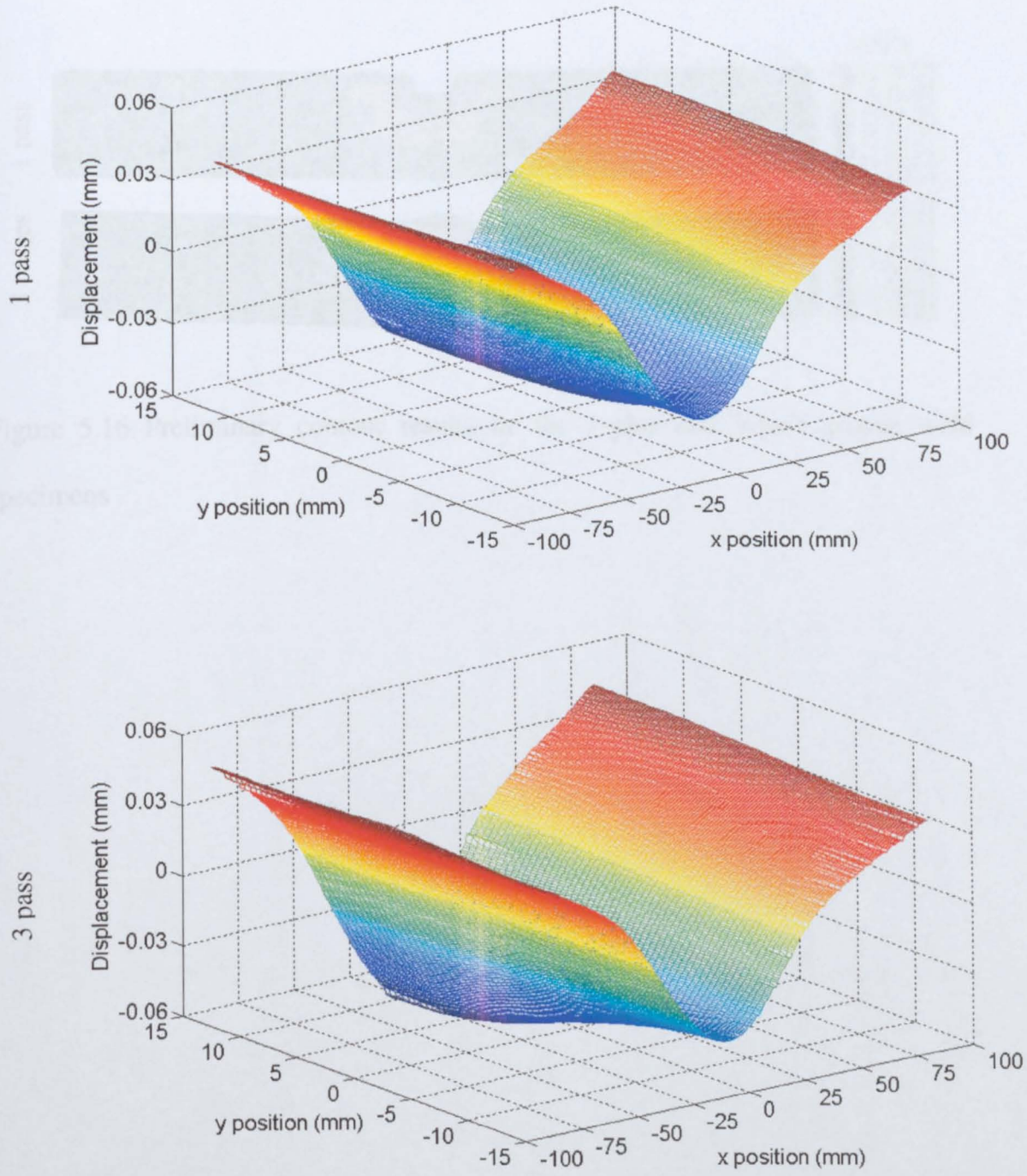

Figure 5.15 5×5 mm cubic spline function fitted to 1 and 3 pass averaged surface contour measurement.

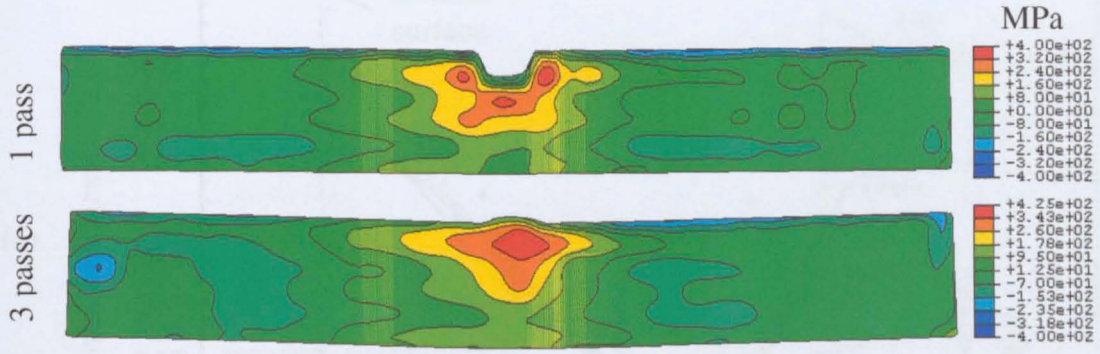

Figure 5.16 Preliminary contour results on the 1-pass and 3-pass groove weld specimens

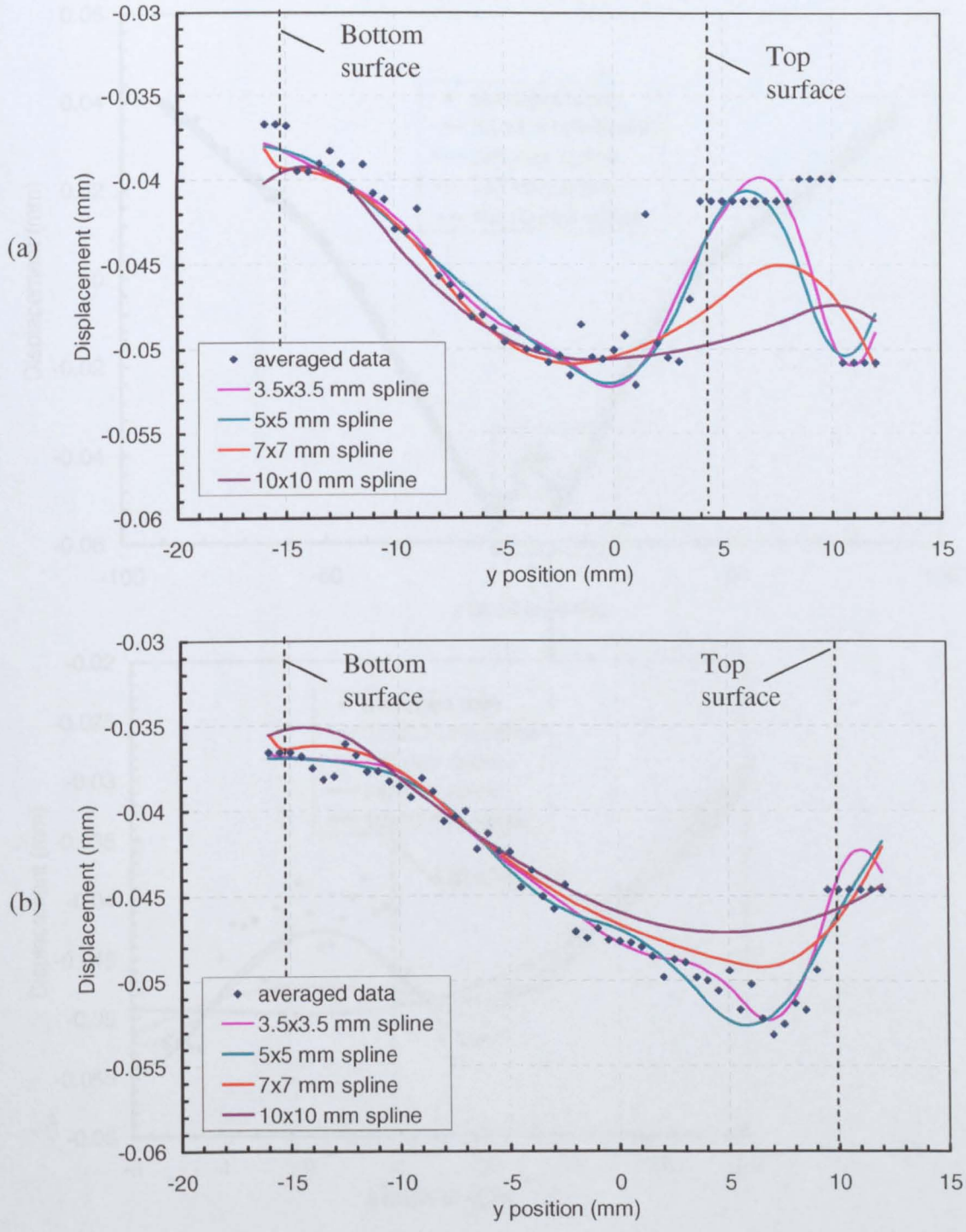

Figure 5.17 The comparison between the averaged data and four different spline knot spacings for the 1-pass groove weld specimen along the lines (a) x=0 mm and (b) x=8 mm.

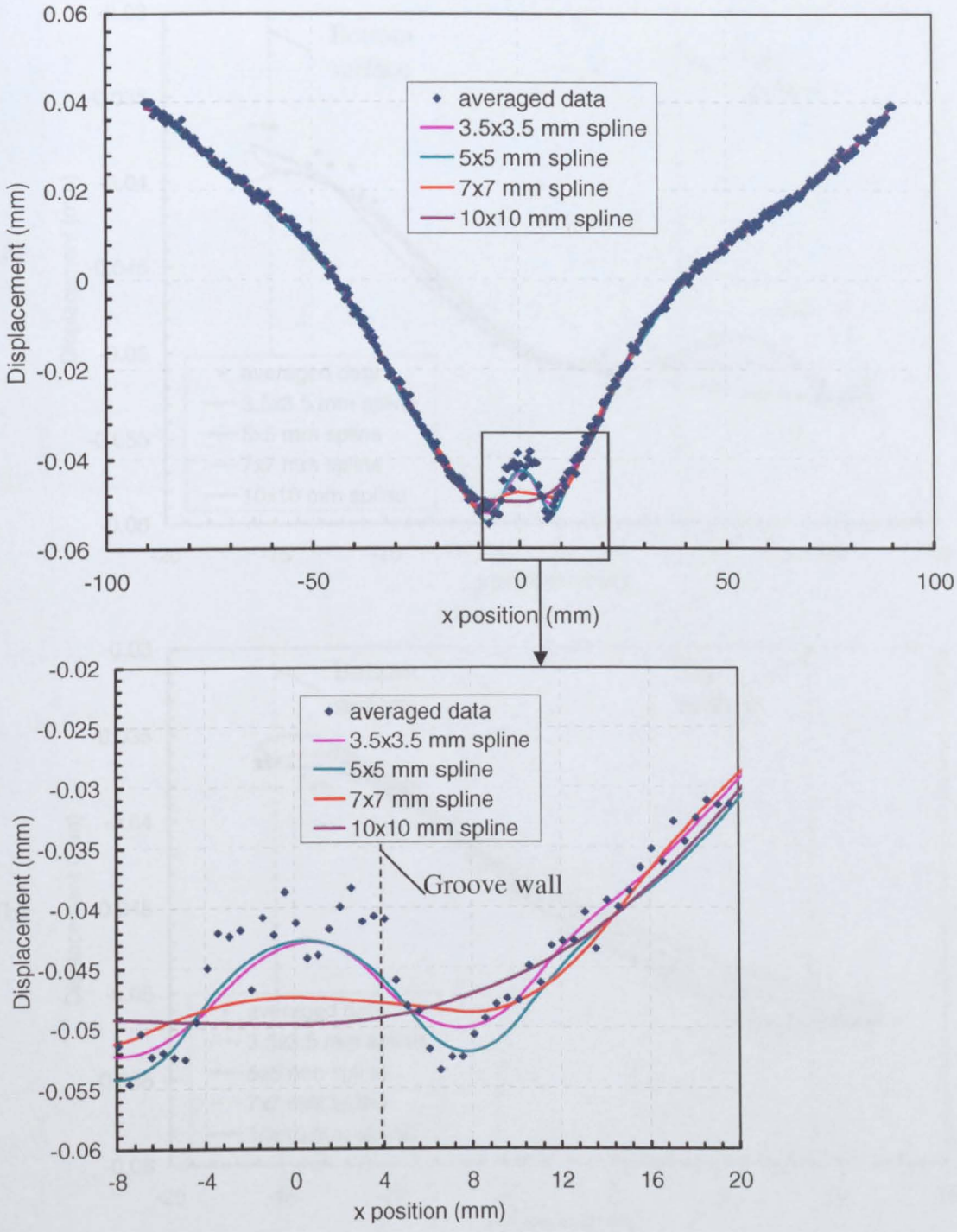

Figure 5.18 Comparison of raw and smoothed data along y=7 mm, of the 1 pass specimen.

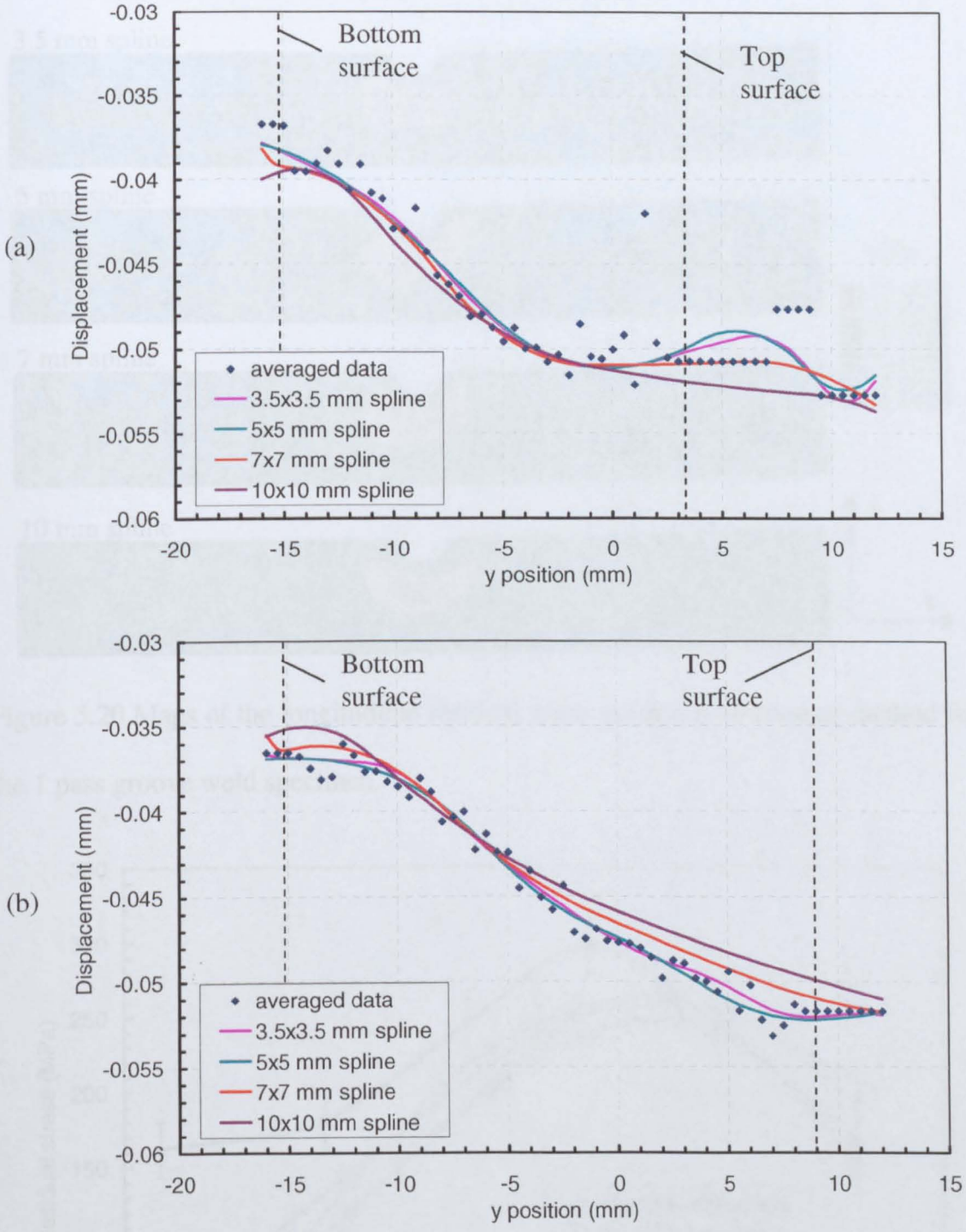

Figure 5.19 The comparison between the averaged data and four different spline knot spacings for the 1 pass groove weld specimen along the lines (a) x=0 mm and (b) x=8 mm (after removing the rows of data points on the top surfaces).

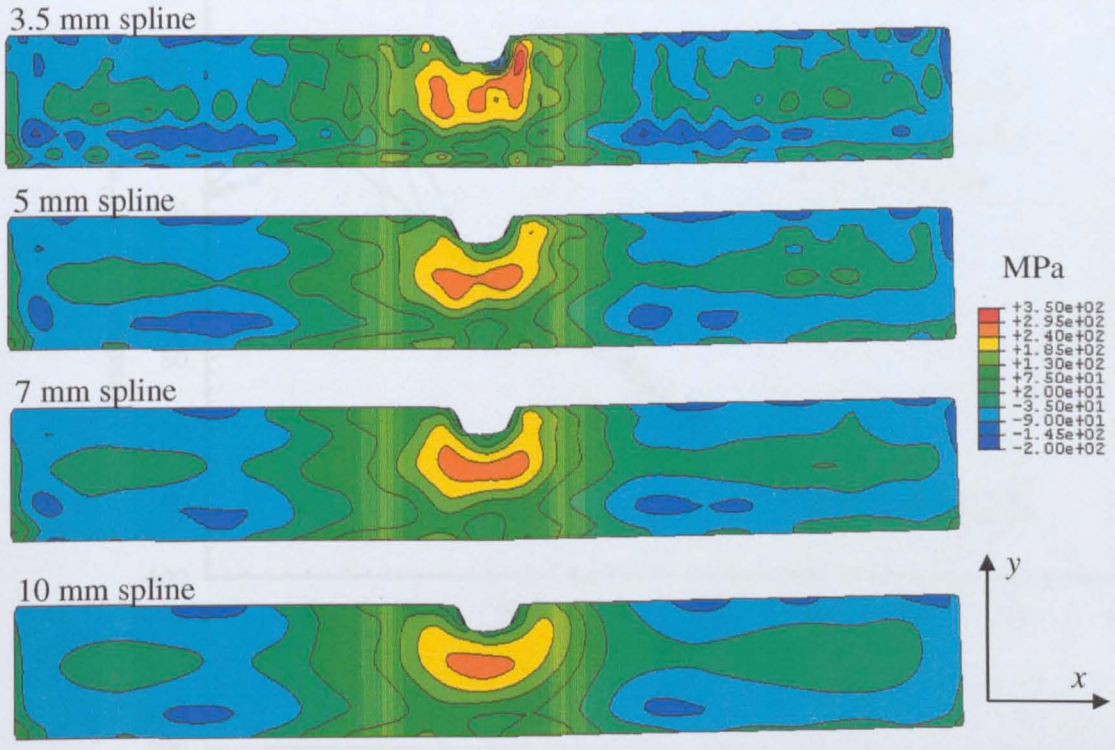

Figure 5.20 Maps of the longitudinal residual stress produced by contour method for the 1 pass groove weld specimen.

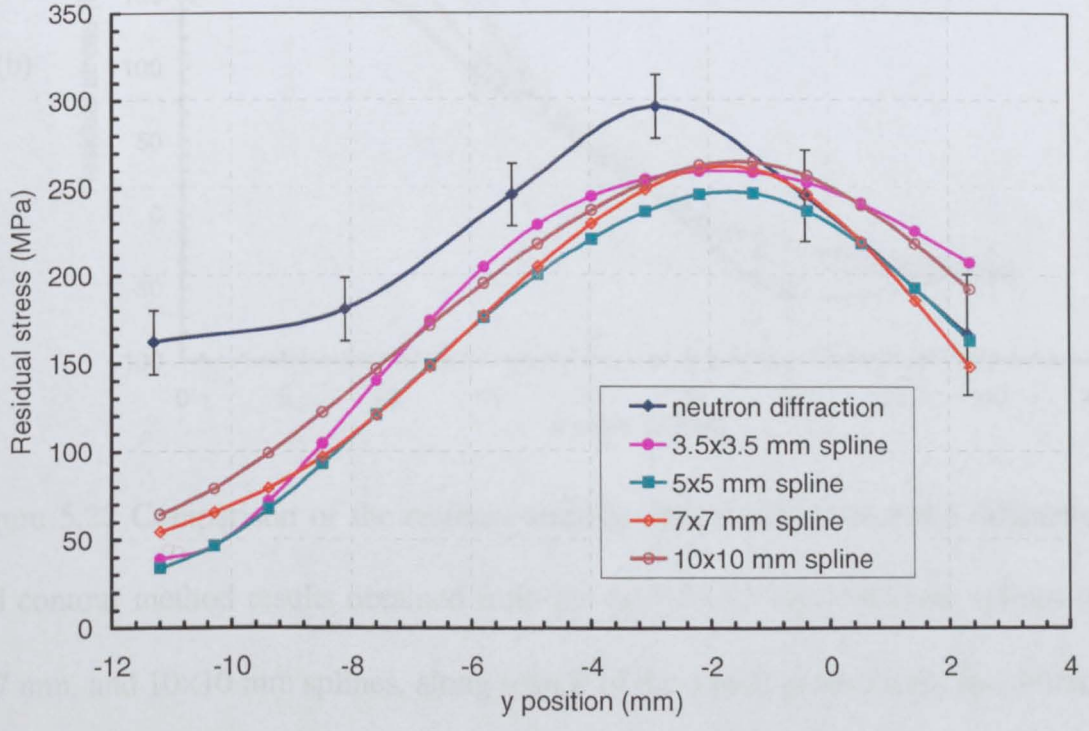

Figure 21 Comparison between neutron diffraction and contour method residual stress measurements made along scan A of the 1 pass groove weld specimen.

(a)

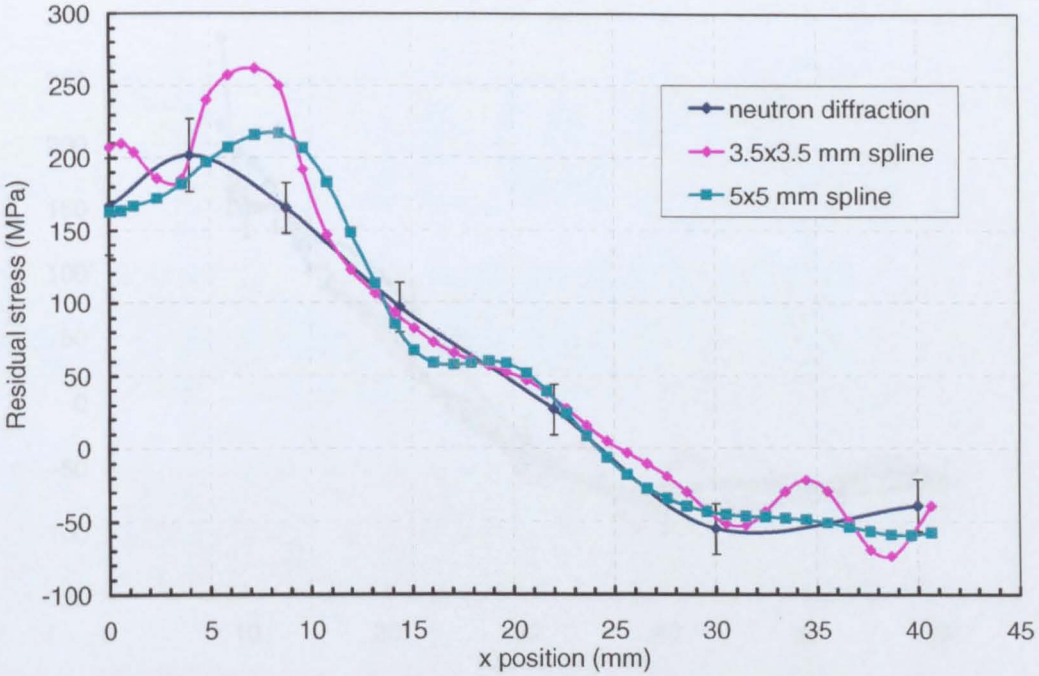

(b)

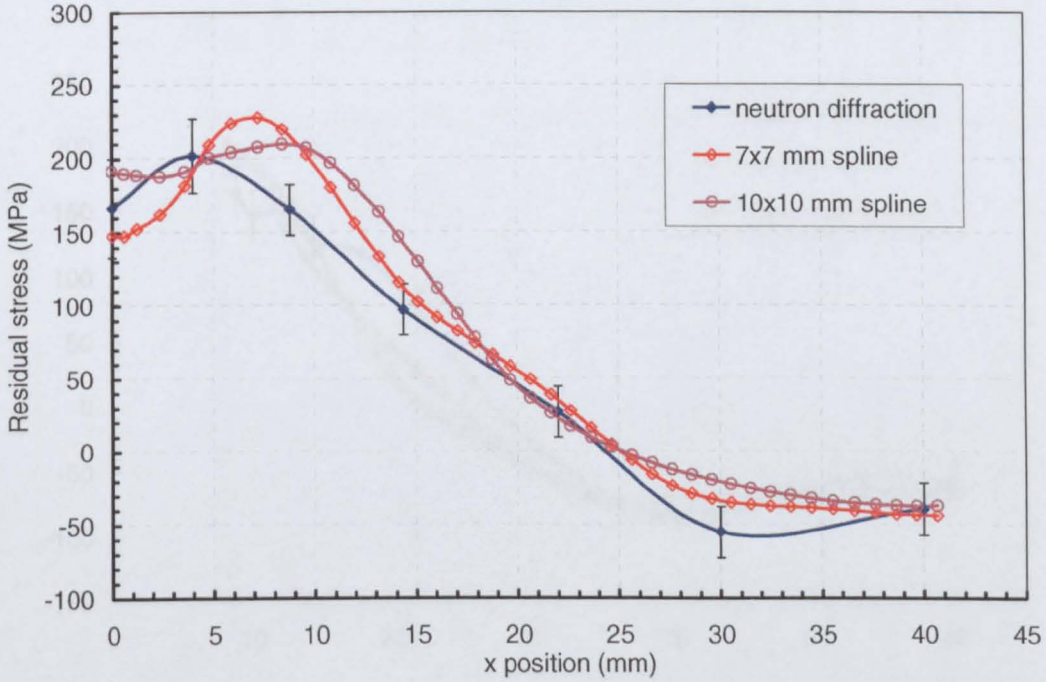

Figure 5.22 Comparison of the residual stresses detemined by neurtron diffraction and contour method results obtained from the (a) 3.5×3.5 mm, 5×5 mm splines (b) 7×7 mm, and 10×10 mm splines, along scan B of the 1 pass groove weld specimen.

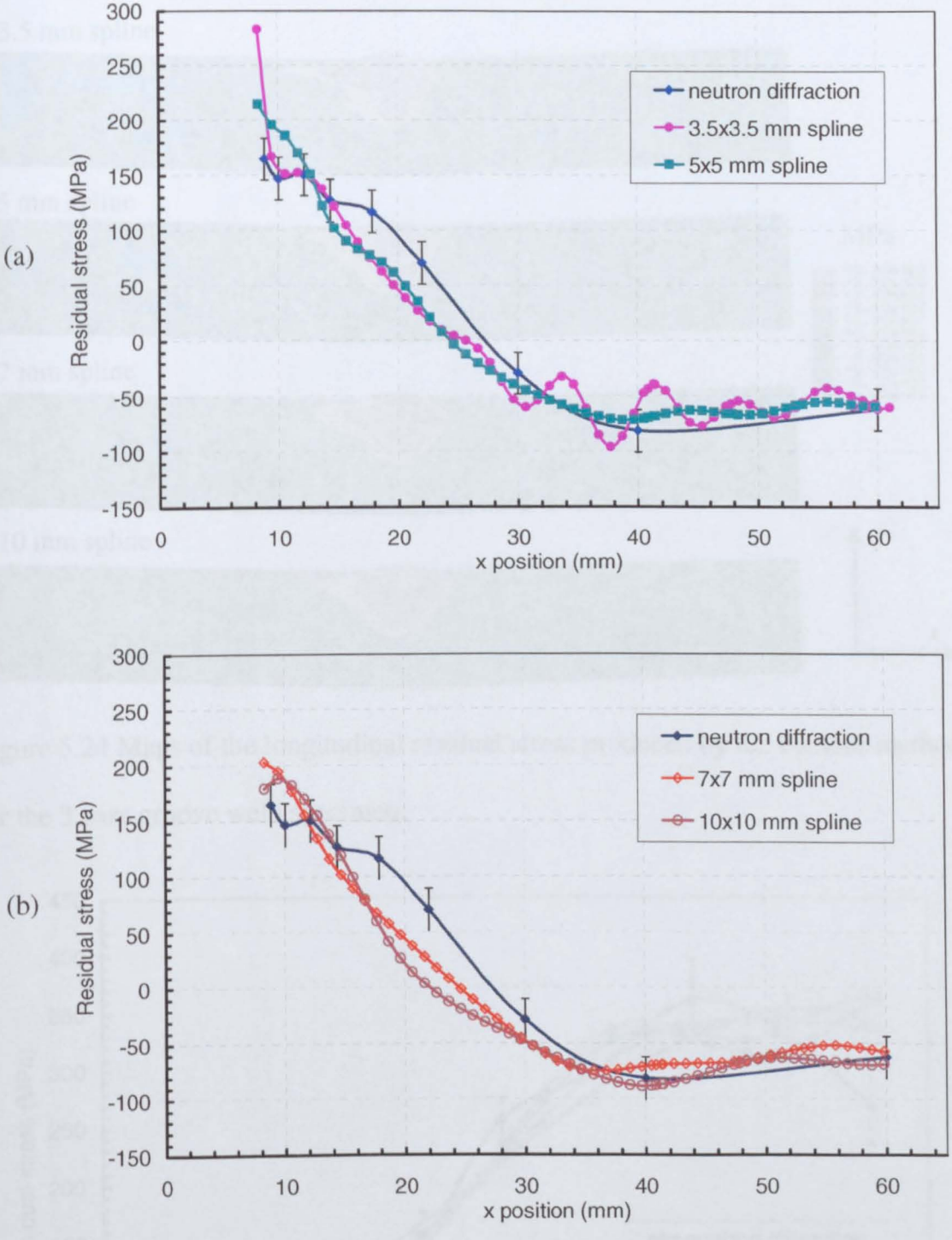

Figure 5.23 Comparison of the residual stresses detemined by neurtron diffraction and contour method results obtained from the (a) 3.5×3.5 mm, 5×5 mm splines (b) 7×7 mm, and 10×10 mm splines, along scan C of the 1 pass groove weld specimen.

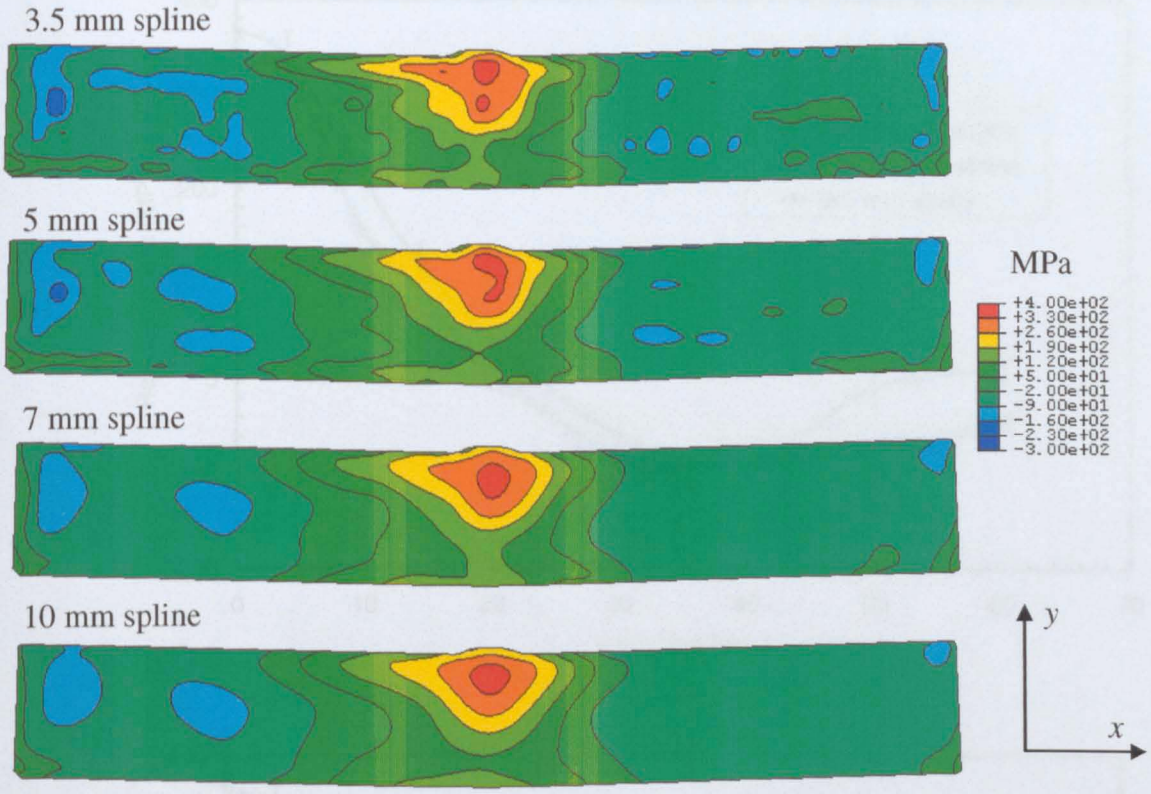

Figure 5.24 Maps of the longitudinal residual stress produced by the contour method for the 3 pass groove weld specimen.

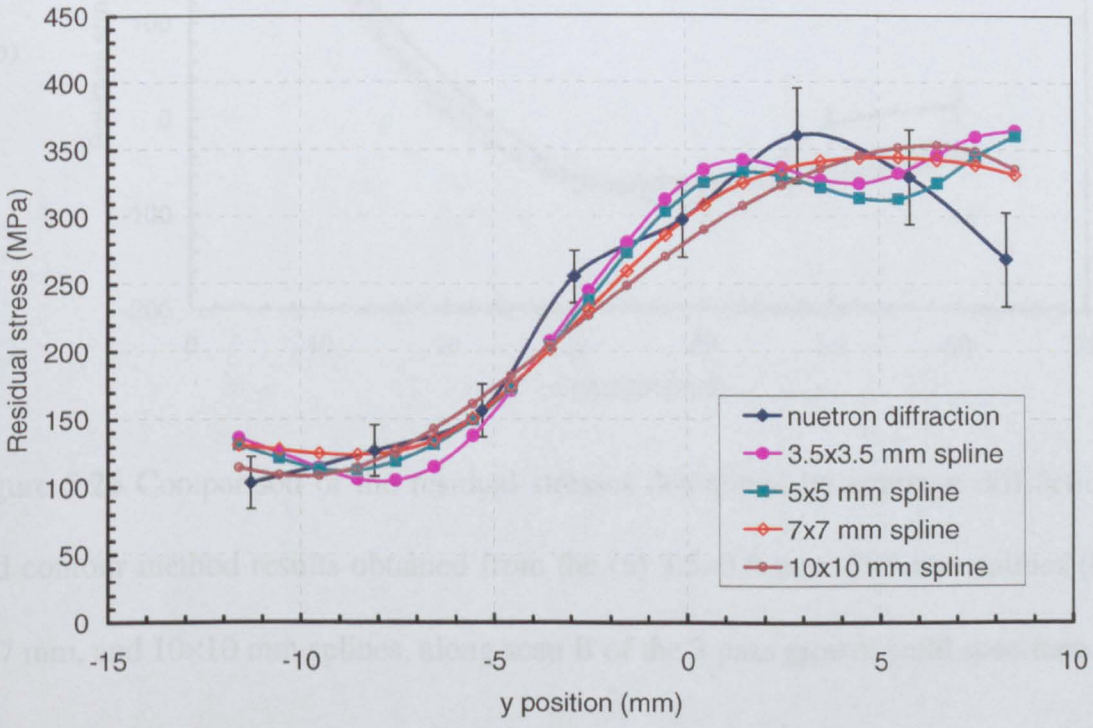

Figure 25 Comparison between neutron diffraction and contour method residual stress measurements made along scan A of the 3 pass groove weld specimen.

(a)

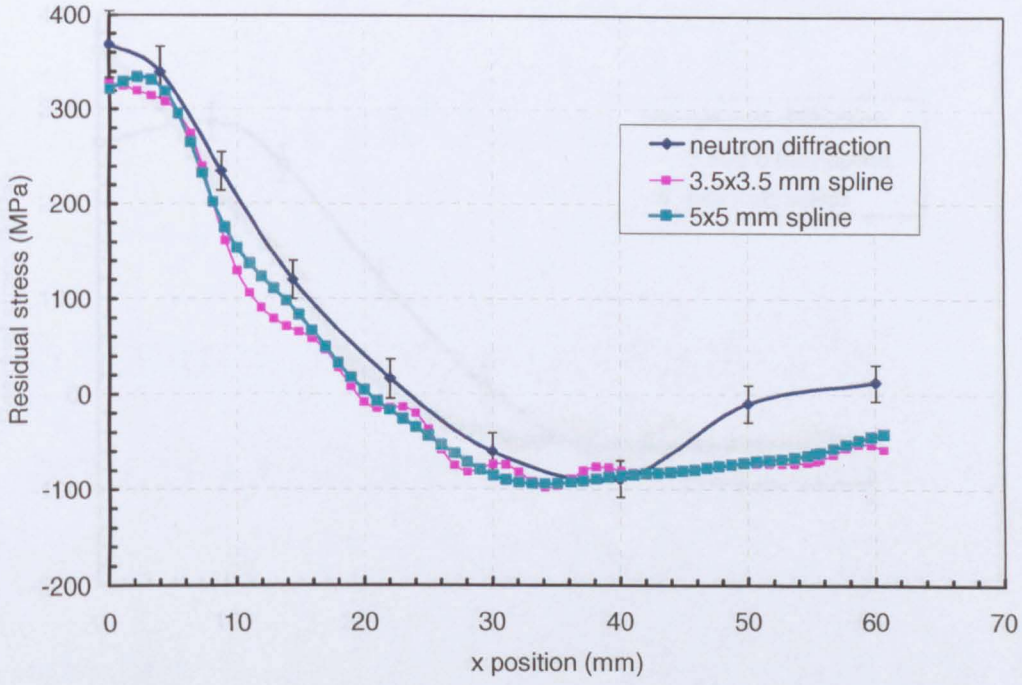

(b)

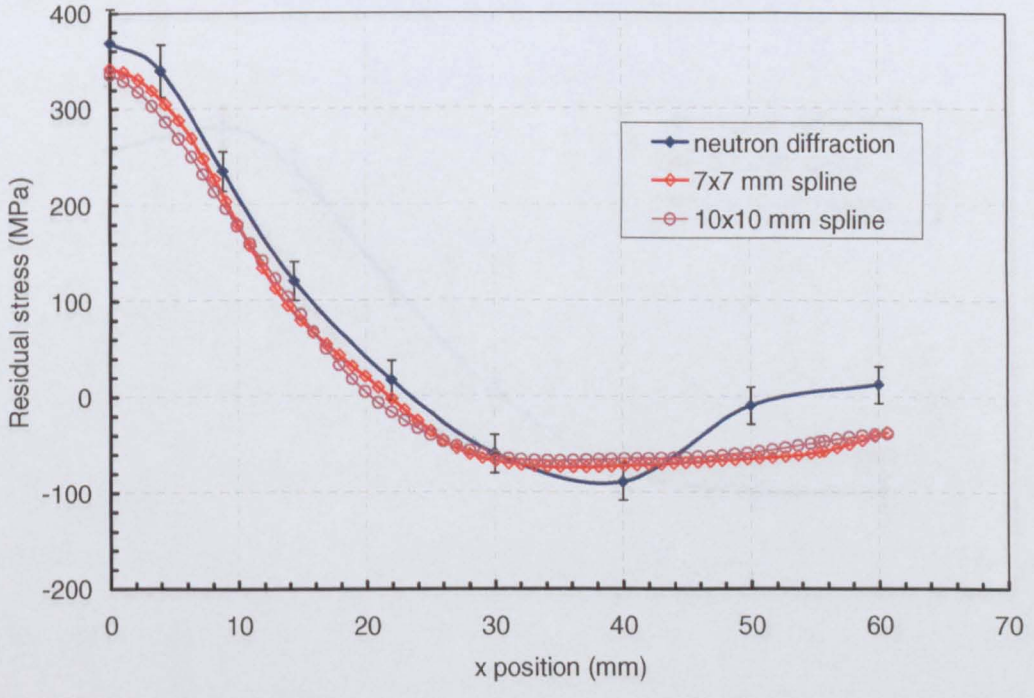

Figure 5.26 Comparison of the residual stresses detemined by neurtron diffraction and contour method results obtained from the (a) 3.5×3.5 mm, 5×5 mm splines (b) 7×7 mm, and 10×10 mm splines, along scan B of the 3 pass groove weld specimen.

(a)

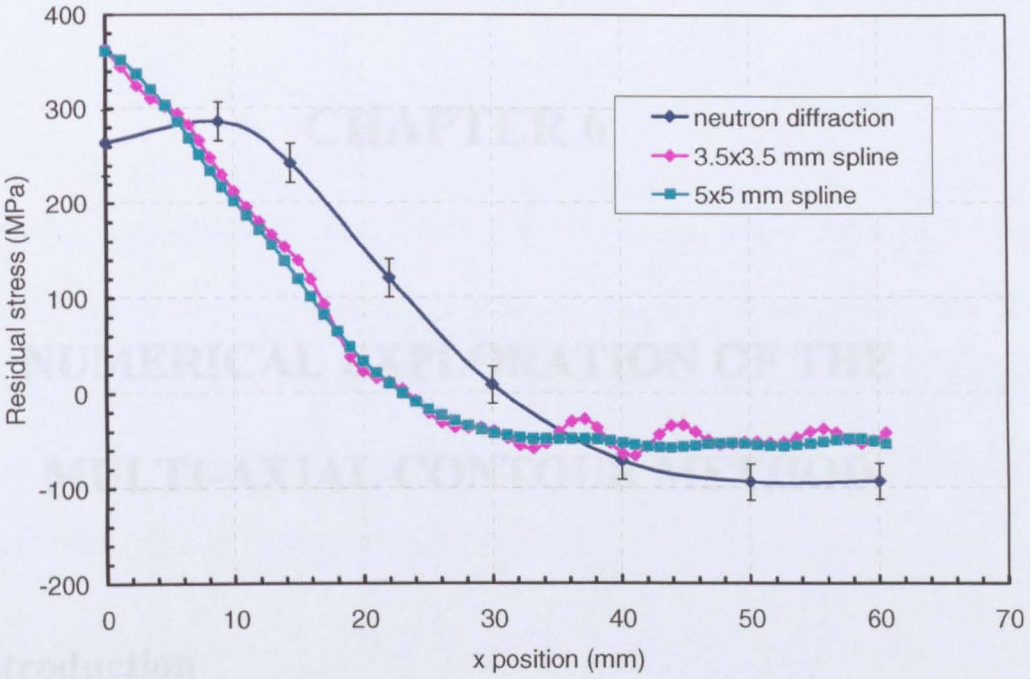

(b)

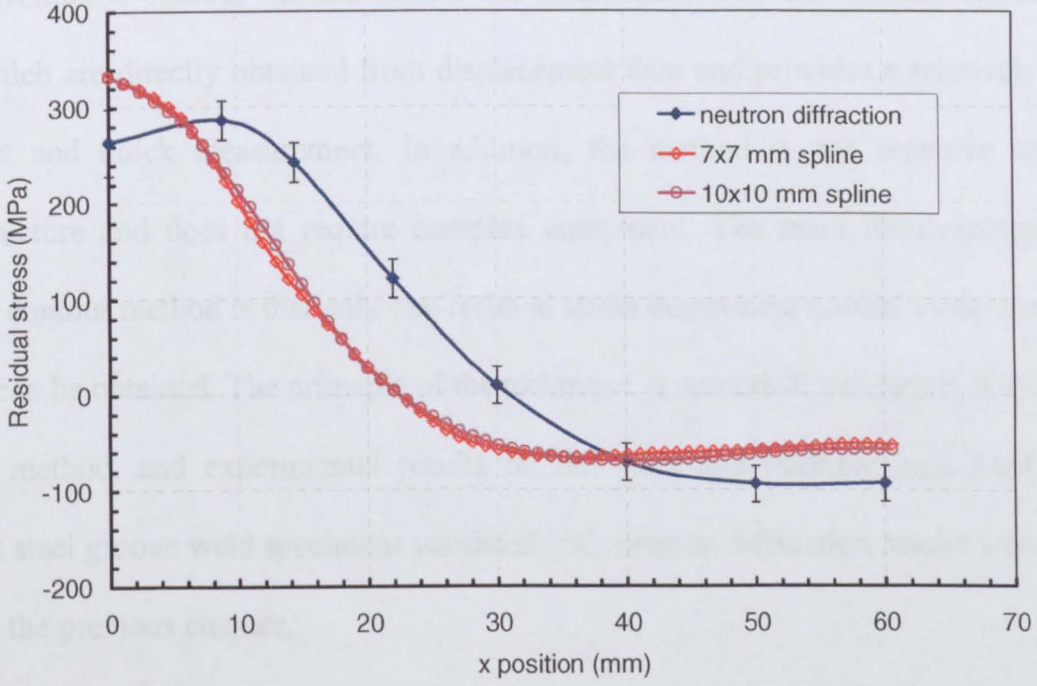

Figure 5.27 Comparison of the residual stresses detemined by neurtron diffraction and contour method results obtained from the (a) 3.5×3.5 mm, 5×5 mm splines (b) 7×7 mm, and 10×10 mm splines, along scan C of the 3 pass groove weld specimen.

CHAPTER 6

NUMERICAL EXPLORATION OF THE MULTI-AXIAL CONTOUR METHOD

6.1. Introduction

The conventional contour method allows the determination of 2D residual stress maps which are directly obtained from displacement data and provides a relatively low cost and quick measurement. In addition, the method is not sensitive to microstructure and does not require complex equipment. The main disadvantage with the contour method is that only one residual stress component normal to the cut surface can be obtained. The principle of the technique, a numerical validation of the contour method, and experimental results on one pass and multiple pass 316L stainless steel groove weld specimens validated with neutron diffraction results were given in the previous chapter.

Numerical and experimental investigations of the conventional contour method are still being undertaken. However, there appear to be only a few investigations in the literature measuring multiple residual stress components by using the capability of the contour method. One of the most successful studies has been undertaken by DeWald and Hill [1]. They used the information from two additional 45° cuts under

the assumption of a continually processed specimen to calculate the full original residual stress tensor.

In contrast, Pagliaro et al. [2] used an additional cut on an orthogonal plane after the original part was sectioned into two halves to obtain two components of residual stress. This method allows another residual stress component, that normal to the second cut plane, to be measured. However, this approach enables the determination of only one component of residual stress on each cut.

The aim of this chapter is to investigate the capability of the conventional contour method to obtain multiple residual stress components by using information from an additional two cuts, assuming a continually-processed part, and calculating the full original stress tensor on the first cut of the specimen. In contrast to the conventional contour measurement, in which displacement is directly used to determine the residual stress distribution, in this technique the displacement is used to calculate eigenstrain then the eigenstrain result is converted to residual stress by computational techniques via the finite element Method (FEM).

In the present chapter, the definition of eigenstrain and the methodology of the multi-axial contour method will be given in detail. Then a numerical validation of the technique for 2D and 3D geometrical specimens will be undertaken using finite element simulation. In the subsequent chapter, the experimental implementation of the multi-axial contour method will be discussed and comparisons with neutron diffraction will be made.

6.2. Eigenstrain

Eigenstrain is an incompatible strain field which results in the residual stress in a body. The term 'eigenstrain' was adapted from a German article [3] by Mura [4]. This incompatible strain is also known in the literature as inherent strain [5]. Eigenstrain can be any kind of strain caused by any nonelastic process such as plastic deformation, thermal expansion, and almost all manufacturing processes. Since the inherent strain defined by Ueda [5] is as a source of residual stress and is equivalent to eigenstrain [4], the residual stress corresponding to that eigenstrain field can be calculated by using numerical analyses (FEM).

In principle, eigenstrains can be divided into two sets: effective and non-effective [6]. Effective eigenstrains arise when an incompatible strain field is introduced to a body, and a corresponding residual stress field due to this effective eigenstrain will exist in the body. However, a non-effective eigenstrains will not produce any residual stress in the body as they are compatible strains and only cause deformation such as uniform tension or uniform shear (i.e. constant or linearly varying eigenstrain). Therefore, there is most interest in effective eigenstrains when investigating the residual stress distribution in a body.

In manufacturing applications, the main cause of eigenstrain is due to thermal strain and plastic strain. Residual stress in a quenched material is, for example, the result of plastic strain. In the case of welding, the eigenstrain is due to thermal strain (temperature) and plastic strain (constraint from the material surrounding the weld region).

Consider the incompatible eigenstrain caused by only thermal strain in a body. The actual strain can be expressed as

$$\varepsilon_{ij}^{*} = \alpha \Delta T, \tag{6.1}$$

where ε^{*} is actual strain which is equal to eigenstrain, α is thermal expansion coefficient and ΔT is temperature increment. This equation (6.1) allows eigenstrain components to be input into a finite element model system, and the resulting residual stress corresponding to the eigenstrain is then calculated by means of the theory of elasticity. Of course, eigenstrains may not only be thermal strains, but may arise from any source of incompatible strain fields such as plastic strains and misfit strains in discontinuous bodies.

Eigenstrain can be input to conventional elastic stress analysis as inelastic strain fields as [4]:

$$\sigma_{ij} = C_{ijkl}\left(\varepsilon_{kl} - \varepsilon_{kl}^{*}\right), \tag{6.2}$$

in which σ_{ij} is stress tensor, C_{ijkl} is the anisotropic elastic tensor, ε_{kl}^{*} the eigenstrain tensor and ε_{kl} is the total strain. Therefore, the value in the parentheses in Eq. (6.2) is pure elastic strain. Hooke's Law for isotropic bodies is

$$\sigma_{ij} = \frac{E}{1+\nu}\left(\left(\varepsilon_{ij} - \varepsilon_{ij}^{*}\right) + \frac{\nu}{1-2\nu}\delta_{ij}\left(\varepsilon_{kk} - \varepsilon_{kk}^{*}\right)\right), \tag{6.3}$$

where E is modulus of elasticity and ν is Poisson's ratio. In elasticity, eigenstrain can be considered as body forces, Mura [4] states that distributed eigenstrain in a body can be replaced by equivalent body force in the equilibrium equations. Thus:

$$F_i = C_{ijkl}\partial\varepsilon_{kl,j}^{*}, \tag{6.4}$$

in which F_i are body forces, and the comma denotes partial differentiation with respect to the variable x_j. For a 3D body, the compatibility equations [7] are

$$\frac{\partial^2 \varepsilon_{xx}}{\partial y^2} + \frac{\partial^2 \varepsilon_{yy}}{\partial x^2} = 2\frac{\partial^2 \varepsilon_{xy}}{\partial x \partial y}, \tag{6.5}$$

$$\frac{\partial^2 \varepsilon_{xx}}{\partial z^2} + \frac{\partial^2 \varepsilon_{zz}}{\partial x^2} = 2\frac{\partial^2 \varepsilon_{xz}}{\partial x \partial z}, \tag{6.6}$$

$$\frac{\partial^2 \varepsilon_{yy}}{\partial z^2} + \frac{\partial^2 \varepsilon_{zz}}{\partial y^2} = 2\frac{\partial^2 \varepsilon_{yz}}{\partial y \partial z}, \tag{6.7}$$

$$\frac{\partial^2 \varepsilon_{xx}}{\partial y \partial z} = \frac{\partial}{\partial x}\left(-\frac{\partial \varepsilon_{yz}}{\partial x} + \frac{\partial \varepsilon_{xz}}{\partial y} + \frac{\partial \varepsilon_{xy}}{\partial z}\right), \tag{6.8}$$

$$\frac{\partial^2 \varepsilon_{yy}}{\partial x \partial z} = \frac{\partial}{\partial y}\left(\frac{\partial \varepsilon_{yz}}{\partial x} - \frac{\partial \varepsilon_{xz}}{\partial y} + \frac{\partial \varepsilon_{xy}}{\partial z}\right), \tag{6.9}$$

$$\frac{\partial^2 \varepsilon_{zz}}{\partial x \partial y} = \frac{\partial}{\partial z}\left(\frac{\partial \varepsilon_{yz}}{\partial x} + \frac{\partial \varepsilon_{xz}}{\partial y} - \frac{\partial \varepsilon_{xy}}{\partial z}\right). \tag{6.10}$$

The eigenstrain fields which satisfy equations (6.5-10) will produce stress free deformation in a body. In other words, any kind of strain which is constant and a linear function of the distance will not create any residual stress in the body.

6.3 Principle of the Multi-Axial Contour Method

The principle of the multi-axial contour measurement is based on determination of the eigenstrain (inherent strain) field existing in the body. The motivation for using eigenstrain to determine residual stresses in the contour method is that the eigenstrain remains constant upon residual stress re-distribution. In other words, a change in geometry of a body alters the residual stress distribution but not the eigenstrain. By means of this feature, multiple cuts can be made without changing the eigenstrain distribution. Moreover, as long as the eigenstrain variation in the

body is known, the residual stress can be calculated for any configuration sectioned from this body. To illustrate this concept, an FE simulation of a sample before and after sectioning into several pieces was undertaken. The eigenstrain distribution and corresponding residual stress is depicted in Figure 6.1. As may be seen, the residual stress distribution in the sample redistributes after cutting whilst the eigenstrain remains unaffected.

The one additional assumption over those used in the conventional contour method is that the body is continually processed. In other words, the variation of eigenstrain in one of the principal directions is constant. Ueda [8] implemented this assumption in welds where the eigenstrain along the longitudinal (welding) direction is assumed to be constant. The principle of the assumption for the particular problem was that if the joint is long enough and welded continuously, then each plane normal to weld direction would have the same thermal history. This assumption is not a major drawback as many engineering products are continually processed, for example by cold rolling or welding.

6.3.1 Two Dimensional Multi-Axial Contour Method

Implementation of the two dimensional case is a simplification of the multi-axial contour method for a 3D body. Consider a 2D *xz* plane in a body which is continually processed in the *z* direction as shown in Figure 6.2. The compatibility equation given in (6.6) is valid for this plane and this equation tells us that only the $\varepsilon^*_{zz}(x)$ component of eigenstrain may cause a residual stress in this plane. The other eigenstrain components $\varepsilon^*_{xx}(x)$ and $\varepsilon^*_{xz}(x)$ just satisfy the compatibility requirement.

In other words, the partial derivatives of these two components with respect to z are zero. Since the z direction is continuously processed the variation of $\varepsilon_{zz}^{*}(x)$ through the z direction is assumed to be the same and varies in only the x direction. However, the misfit strain $\varepsilon_{zz}^{*}(x)$ results in multiple residual stress components $\sigma_{xx}(x,z), \sigma_{zz}(x,z)$ and $\sigma_{xz}(x,z)$ in the body.

The principle of the 2D multi-axial contour measurement is similar to the conventional contour method. The continuously processed plane is cut into two halves. The deformation due to stress relaxation is contoured and the measured displacement is used to calculate the unknown eigenstrain distribution $\varepsilon_{zz}^{*}(x)$ using a smooth basis function. Since the basis function which is used to calculate the eigenstrain component is smooth there is no need to perform further data smoothing for the implementation of this method. Note that a single cut is sufficient to evaluate the unknown eigenstrain $\varepsilon_{zz}^{*}(x)$ for a 2D plane, but multiple cuts are essential to carry out the 3D multi-axial contour method.

The computation of the unknown eigenstrain through measured displacement can be achieved by using an inverse solution technique such as is commonly used for residual stress measurement techniques such as incremental hole-drilling [9] and crack compliance [10]. It is assumed that the unknown eigenstrain variation $\varepsilon_{zz}^{*}(x)$ can be defined as the sum of the basis functions:

$$\varepsilon_{zz}^{*}(x) = \sum_{i=0}^{n} A_i^{zz} P_i(x), \tag{6.11}$$

in which P_i is a functional series such as a polynomial, and A_i^{zz} are unknown coefficients of the functional series expansions which are the basis functions to be determined. Here, the i index is the order of the polynomials in the x direction (ranges from *0* to n). With the form of the unknown eigenstrain component given by equation (6.11), determination of this eigenstrain component is accomplished by determining a number of unknown coefficients ($n+1$).

These unknown coefficients are found from the displacement measured on the cut plane. Assuming elastic behaviour and using superposition, this measured displacement can be expressed by a linear combination of unknown coefficients as

$$u_m(x_j) = \sum_{i=0}^{n} A_i^{zz} C_{ji}, \tag{6.12}$$

where u_m is the measured displacement on the cut plane, and C_{ji} is the compliance matrix which *would* be 'measured' for each term in the polynomial series P_i. This compliance matrix is a "measured" and averaged displacement caused by eigenstrain distribution given by

$$\varepsilon_{zz}^{*}(x) = P_i(x) \cdot 10^{-3}, \tag{6.13}$$

and the relation can be expressed as

$$C_{ji} = u\big|_{\varepsilon_{zz}^{*}(x)=P_i(x)\cdot 10^{-3}}, \tag{6.14}$$

where u is an averaged displacement caused by Eq. (6.13). In this case, the measured displacement u_m is a single-column matrix including all displacement data points on the cut surface, and the compliance matrix C will have one column for each term in the polynomial series and rows for all data points computed on the sectioned surface. Here, since the interval of the polynomials such as [−1,1] is much larger

than the expected strain values, each term in the series is divided by 1000 to make them of the same order of magnitude as the expected strain values.

In order to create the compliance matrix, half of the plane is modelled owing to the symmetrical feature of the overall system, by imposing the constrained boundary condition along the x direction (Figure 6.2). Then each term in the polynomial series is input into the model, equilibrium is employed and the resulting residual stress is obtained. By removing the boundary condition on the line, deformation due to the residual stress is fully released and is 'measured' for each basis function term. There is no need to average both halves since shear stress is always zero at the symmetrical line for 2D deformation.

In the matrix form, Eq. (6.12) can be written as

$$[u_m] = [C][A^{\sigma}]. \tag{6.15}$$

If the number of the point which is measured on the cut surface is equal to the order of the polynomial series then the compliance matrix will be a square matrix and if there is non-singularity of the system then this matrix can be solved. Non singularity is achieved as long as there are no values that produce zero displacement. Singularities arise if any eigenstrain variation caused by one of the known basis function terms produces no stress. Some terms in the polynomial series satisfy the compatibility and give a stress-free result. Therefore, these terms are removed from the compliance matrix manually to avoid having singularities present during the rest of the analysis. If the number of the measured points is less than the order of the polynomial series, then the displacement can be spatially interpolated. If the number

of measured points exceeds the order of the polynomials then additional computational effort is required. In this case, least squares are employed which allows the minimization of error between the measured and fit data [5]. Hence, the number of the unknown coefficients of the basis function can be calculated by least squares as

$$[A^{zz}] = \left\{[C]^T[C]\right\}^{-1}[C]^T[u_m] \tag{6.16}$$

Once the unknown coefficients of the polynomial series have been calculated, Eq. (6.11) is employed to determine the unknown eigenstrain component $\varepsilon^*_{zz}(x)$. Finally, the initial equilibrium step in finite element method gives the initial values of residual stress distribution.

6.3.2 Three Dimensional Multi-Axial Contour Method

Extension of the multi-axial contour method to a 3D body is similar to that for a 2D plane except that, first of all, each eigenstrain component may not satisfy the compatibility equations given in Eqs. (6.5-10) and bring about residual stress in the body. Secondly, another spatial direction y needs to be taken into account for the whole computation processes, which requires polynomial series that vary in the y direction. Finally, it involves multiple cuts in different orientations of a continuously processed prismatic specimen (as shown in Figure 6.3), and each couple pair needs to be averaged to cancel out shear stress affects.

Initially, the specimen is cut into two halves (θ=0° cut) as in the conventional contour method. Both of the new cut surfaces are measured and the results are averaged. Then, the two halves are cut along their diagonal (i.e. θ = 45° and θ = -

45°). The displacements normal to the cut surfaces are contoured and averaged. Note that the length of the specimen is chosen twice as long as its width so that the cuts along their diagonal can be ±45°.

After all the measurements are completed, a data reduction step is carried out to determine the eigenstrain components from these three different measured and averaged surfaces. The data reduction method is explicitly explained in the following paragraphs.

It is assumed that each unknown eigenstrain variation (as a function of (x,y)) can be expressed as

$$\varepsilon^*_{xx}(x,y) = \sum_{i=0}^{(m+1)(n+1)} A_i^{xx} S_i(x,y), \tag{6.17}$$

where ε^*_{xx} are the unknown eigenstrain components (here, only one component of eigenstrain is denoted; other unknown eigenstrain components can be expressed in a similar manner), A_i^{xx} are unknown coefficients of the series for the unknown eigenstrain component ε^*_{xx} to be calculated, and S_i represent bivariate polynomials which are the dot product of two polynomials as basis functions such that

$$S_i(x,y) = P_k(x)P_l(y). \tag{6.18}$$

Here, the k index is the order of the polynomials in the x direction (ranges from 0 to m), l index is the order of polynomials in the y direction (ranges 0 to n), and $i = k + (l+1)n$.

Determination of each eigenstrain component is again accomplished by solution of a number of unknown coefficients (*(m+1)(n+1)*). Note that only three eigenstrain components ε_{xx}^{*}, ε_{zz}^{*} and ε_{xz}^{*} are used to create the compliance matrix, since previous work [1] has shown that the other three components of eigenstrain do not contribute residual stresses significantly and cause instability in the inverse solution of (Eq.6.16). Assuming elastic behaviour and using superposition, the measured displacement u_m can be expressed by a linear combination of unknown coefficients as

$$[u_m] = [C][A], \tag{6.19}$$

where the measured displacement u_m is a one column matrix including all displacement data points for all three cut and averaged surfaces such that

$$[u_m] = \left\{[u_m]_{\theta=0}, [u_m]_{\theta=45^\circ}, [u_m]_{\theta=-45^\circ}\right\}^T, \tag{6.20}$$

where $[u_m]_{\theta=0}$, $[u_m]_{\theta=45^\circ}$, and $[u_m]_{\theta=-45^\circ}$ are measured displacement vectors on the θ=0°, θ=45°, and θ=–45° surfaces respectively. The matrix A is an unknown coefficient matrix involving all unknown values for each eigenstrain component:

$$[A] = \left\{[A^{xx}], [A^{zz}], [A^{xz}]\right\}^T, \tag{6.21}$$

in which $[A^{xx}]$, $[A^{zz}]$, and $[A^{xz}]$ are unknown coefficients of the basis function for the ε_{xx}^{*}, ε_{zz}^{*} and ε_{xz}^{*} unknown eigenstrain components respectively. The compliance matrix C constitutes the resulting displacements induced by each eigenstrain component for each term in S_i and will have one column for each eigenstrain component, and rows for all data points computed from the three different surfaces as follows:

$$C=\begin{Bmatrix} [C^{xx}]_{\theta=0} & [C^{zz}]_{\theta=0} & [C^{xz}]_{\theta=0} \\ [C^{xx}]_{\theta=45^\circ} & [C^{zz}]_{\theta=45^\circ} & [C^{xz}]_{\theta=45^\circ} \\ [C^{xx}]_{\theta=-45^\circ} & [C^{zz}]_{\theta=-45^\circ} & [C^{xz}]_{\theta=-45^\circ} \end{Bmatrix}. \tag{6.22}$$

Here, the compliance matrix consists of 9 components of sub-matrix each of which is a displacement vector for different planes and different eigenstrain components. For instance, $[C^{zz}]_{\theta=0}$ is an averaged displacement vector induced by the eigenstrain component ε_{zz}^{*} for each term in S_i on the θ=0° surface and can be generated as:

$$[C^{zz}]_{\theta=0}=u(x,y)\big|_{\varepsilon_{zz}^{*}=S_i\cdot 10^{-3}} \tag{6.23}$$

The other components can be expressed likewise. In order to create the compliance matrix, the full size geometry is modelled since there are no symmetrical features. Each eigenstrain component which constitutes the compliance matrix is then imposed into the FE model. After an initial equilibrium step, deformation due to residual stress on the cut surfaces is 'measured' and averaged. The simplifications used to calculate the compliance matrix are that the displacement distributions on both θ=45° and θ=−45° surfaces caused by ε_{xx}^{*} and ε_{zz}^{*} eigenstrain components for each term in the bivariate polynomials series are identical (i.e., $[C^{xx}]_{\theta=45^\circ}$ = $[C^{xx}]_{\theta=-45^\circ}$ and $[C^{zz}]_{\theta=45^\circ}$ =$[C^{zz}]_{\theta=-45^\circ}$). Therefore, to measure the displacement distribution on either of the cut surfaces (θ=45° or θ=−45°) is sufficient to determine the other one. Furthermore, $[C^{xz}]_{\theta=0}$ will be always zero since ε_{xz}^{*} results in only

shear stress on the θ=0° surface, and hence the averaged displacement produces zero displacement fields. Besides the displacement fields caused by ε_{xz}^{*} at θ=45° and θ=−45° are of inverse sign (i.e. $[C^{xz}]_{\theta=45^\circ} = -[C^{xz}]_{\theta=-45^\circ}$).

Once the compliance matrix has been calculated, the unknown coefficients matrix A is computed by means of a least squares fit which allows minimizing error between the measured and fit data

$$\{A\} = \left([C]^T[C]\right)^{-1}[C]^T\{u_m\}, \tag{6.24}$$

then the eigenstrain distribution can be calculated from Eq. (6.17). This is then read into the FE model, which results in an elastic strain and the initial residual stress field.

6.4 Numerical Validation of the Multi-Axial Contour Method

6.4.1 Legendre Polynomials

Legendre's Differential Equations [11-12] are encountered in many engineering applications, and defined as

$$\left(1-x^2\right)\frac{d^2y}{dx^2} - 2x\frac{dy}{dx} + n(n+1)y = 0, \tag{6.25}$$

Where n is an integer. When n is a positive integer, the solution of these differential equations are called Legendre polynomials. Since the equations (6.25) are second order ordinary differential equation, the general solution involves two set functions as follows

$$y(x) = A_n P_n(x) + B_n Q_n(x), \tag{6.26}$$

in which A_n and B_n are coefficients of Legendre polynomials of the first kind $P_n(x)$ and the second kind $Q_n(x)$ respectively. Nevertheless, $Q_n(x)$ diverges at the value $x=\pm 1$. In order to get a meaningful result for the solution of the Eq. (6.25), B_n is forced to be zero. The first few Legendre polynomials are as follows

$$P_0(x) = 1$$

$$P_1(x) = x$$

$$P_2(x) = \frac{1}{2}\left[3x^2 - 1\right]$$

$$P_3(x) = \frac{1}{2}\left[5x^3 - 3x\right] \qquad (6.27)$$

$$P_4(x) = \frac{1}{8}\left[35x^4 - 30x^2 + 3\right]$$

$$P_5(x) = \frac{1}{8}\left[63x^5 - 70x^3 + 15x\right]$$

$$P_6(x) = \frac{1}{16}\left[231x^6 - 315x^4 + 105x^2 - 5\right]$$

Graphical representation of the first few terms of the Legendre polynomials is given in Figure (6.4).

Series expansion using equations (6.11, 6.17) can be undertaken as polynomial functions such as Legendre polynomials, power series or Fourier expansion. In this study, Legendre polynomials were utilized for describing the basis functions. The reason for using the Legendre polynomials for definition of the basis functions for the work was that they are widely used for the series expansion approach as their higher order terms (i.e. two and more) automatically satisfy equilibrium. Legendre polynomials are valid in the interval [-1:1] and hence the coordinates are

normalised with dimensions of the thickness and the width before computing the values for each eigenstrain component.

6.4.2 Numerical Verification of the Two Dimensional Multi-Axial Contour Method

Finite element simulation was used for the numerical verification of the multi-axial contour method in two dimensions. A 60 mm × 120 mm beam in the *xz* plane as shown in Fig .6.2 was used for this simulation. Due to the symmetry of the system, half of the sample, 60 mm × 60 mm, was modelled by using finite element software ABAQUS 6.6 and a 120 × 120 mesh of reduced integration point 4 nodes, linear shape, and a plane stress assumption. The material behaviour was assumed to be isotropic and linear elastic with a Poisson's ratio of 0.3 and Young's modulus of 200 GPa, typical values for steels.

The initial known eigenstrain distribution $\varepsilon_{zz}^{*}(x)$ given by the equation (6.28) was imposed into the 2D model.

$$\varepsilon_{zz}^{*}(x) = -\frac{1}{400}\exp\left[-3\left(\frac{x}{w}\right)^{2}\right]\left\{\sin\left[\frac{\pi x}{w}\right]+1\right\}, \tag{6.28}$$

where w is the width of the sample. In order to get similar magnitude to the eigenstrain, the expression given by Eq. (6.28) was divided by 400. After the eigenstrain was initialized, known residual stress components $\sigma_{xx}(x,z)$, $\sigma_{zz}(x,z)$ and $\sigma_{xz}(x,z)$ caused by the eigenstrain were recorded along the EDM cut line. Then, one additional step was taken to simulate EDM cutting. For this purpose, the constraint boundary condition was used for the initial step along the line where contour

measurement is supposed to be performed, and by removing this boundary condition in the next step, the deformation due to residual stress is released and the displacement on the line was 'measured'.

After the known residual stresses (before the 'cut') and the known displacements normal to the 'cut' plane (after the 'cut') were recorded, the eigenstrain variations corresponding to each term of the Legendre polynomial series (6.27) were input to the model to generate the compliance matrix. The resulting displacements caused by those terms in Legendre polynomials were then 'measured' (after the 'cut'), using the first 20 terms of the basis function. Note that the first two terms of the Legendre polynomials (P_0 and P_1) satisfy compatibility and result in zero displacement. Hence, these two terms were removed from the compliance matrix in order to avoid any singularity in the equation system. Then, the compliance matrix and known displacement distribution were input into Eq. (6.16), and the coefficients of the Legendre polynomials A^{zz} were calculated. These coefficients of the basis functions were utilized to calculate the unknown eigenstrain distribution $\varepsilon_{zz}^{*}(x)$ (6.11). By imposing this eigenstrain into the FE model, the calculated residual stresses were obtained. The comparison between the known and calculated residual stresses will show the precision of the method as there are no experimental errors present in the simulations.

6.4.3 Numerical Verification of Three Dimensional Multi-Axial Contour Method

For the 3D multi-axial contour method simulation, a simulated block of dimensions 160 mm long, 80 mm wide and 7.1 mm thick was used. It was assumed that the specimen was isotropic and linear elastic with a Young's modulus of 72.4 GPa and Poisson's ratio of 0.34, typical values for aluminium alloys.

For the simulation of the multi-axial contour method in three dimensions, all eigenstrain components were input into the FE model using the following formula:

$$f(x) = \exp\left[-3\left(\frac{2x}{w}\right)^2\right], g(y) = -\frac{1}{2}\left[\cos\left(\frac{2\pi y}{t}\right)+1\right], \tag{6.29}$$

$$\varepsilon^*_{xx}(x,y) = \varepsilon^*_{xy}(x,y) = \varepsilon^*_{xz}(x,y) = \varepsilon^*_{yy}(x,y) = \varepsilon^*_{yz}(x,y) = \frac{1}{250} f(x)g(y), \tag{6.30}$$

Where w is the width and t is the thickness of the sample. In order to get similar magnitude with eigenstrain, the expression given by Eq. (6.30) was divided by 250.

The cross-sectional profile variation for all five components of eigenstrain (apart from ε^*_{zz}) is shown in Figure 6.5. Since the effect of ε^*_{zz} on residual stress is much greater than the other components, the magnification of ε^*_{zz} was chosen to be four times smaller than the others. Defining anisotropic thermal expansion coefficients as a function of x and y positions, all six eigenstrain components were input into the FE model as pseudo thermal strain. The resulting known residual stress components on the ($\theta = 0°$ cut) were recorded (before the 'cut' was implemented). Then, the model was 'cut' into two halves and the deformation on both surfaces ($\theta = 0°$ cut) was 'measured' and averaged. Next, the two half-models were 'cut' along the diagonals

(θ = 45° and θ = -45°). The displacements normal to the cut surfaces were 'measured' and averaged.

Once the known displacements on the three surfaces and the known residual stresses on (θ = 0° cut) were recorded, each term in the bivariate Legendre series was input into the FE model as an eigenstrain distribution of each component (ε^*_{xx}, ε^*_{zz} and ε^*_{xz}). Note that only three eigenstrain components ε^*_{xx}, ε^*_{zz} and ε^*_{xz} are used to create compliance matrix, since previous work [1] has shown that the other three components of eigenstrain do not contribute residual stresses significantly and cause instability to the inverse solution (Eq.6.24).

The simulation was then allowed to equilibrate, and the resulting deformations on the three different cut pairs 'measured' and averaged for each term. The resulting displacement for each term and each eigenstrain component constitute the compliance matrix. Once again, Legendre polynomials are valid in the interval [-1:1] and hence the coordinates were normalised with dimensions of the thickness and the width before computing the values for each eigenstrain component. Each term in the bivariate Legendre series is divided by 1000.

After the compliance matrix was created, the unknown coefficients were found by least squares solution of Eq. (6.23). Then, the unknown eigenstrain components for ε^*_{xx}, ε^*_{zz} and ε^*_{xz} were computed. Finally, these three eigenstrain components were input into the finite element model and the resulting residual stress were compared with the initial input.

6.5 Results

6.5.1 Numerical Result of the 2D Multi-Axial Contour Method

The 'measured' displacement components normal (u_z) and transverse (u_x) to the 'cut' surface for 2D simulation and their fit data are plotted in Figure 6.6. The order of the fit was selected as 13. The quadratic mean, which is a statistical measurement of accuracy, was used to calculate the error between the 'measured' and fit data for the normal displacement u_z. Quadratic mean (QM) can be expressed as

$$QM = \sqrt{\frac{1}{r}\sum_{j=1}^{r}\left(u_m - u_f\right)^2}, \tag{6.31}$$

in which r is the number of points measured on the cut surface, and u_f is the fit data which is obtained after computing unknown coefficients of the polynomials A^{zz} by least squares (6.16) and inputting them into Eq. (6.15). Quadratic mean is useful especially when the values consist of negative and positive signs to avoid cancelling each other and getting a zero average. In order to investigate the accuracy of the fit, the first 20 terms of the basis function were used to create the compliance matrix. Figure 6.7 is a log plot of the quadratic mean error versus the order of polynomial fit for the first 20 terms. It can be seen from the figure that there is no significant reduction in error with increasing the order of the fit after the 13th order.

Figure 6.8 shows a comparison between the known initial residual stress obtained from inputting eigenstrain in Eq. (6.28) and the calculated residual stresses acquired from the multi-axial contour method simulation. Here, solid lines symbolize measured values and dotted lines shows initial input values. There is an excellent agreement between the measured and initial values. The longitudinal residual stress

component σ_{zz} is seen to be tensile and reaches 388 MPa in the middle, and is balanced by remote compression stresses. The normalised error between the known and measured residual stress components are shown in Figure 6.9, where normalized error is defined as the difference between the known and measured residual stress divided by the maximum known values. The error for this simulation was found to be less than 0.003%.

6.5.2 Numerical Results of the 3D Multi-Axial Contour Method

The averaged displacements from three different surfaces (θ = 0°, θ = 45°, and θ = -45°) generated by the eigenstrain distribution given in equations 6.29 and 6.30 at y = 3.55 mm and x = 40 mm are depicted in Figure 6.10 and 6.11 respectively. The order of Legendre polynomials was chosen as 6 for both directions. The solid lines of these two figures show the fit displacement acquired by the least squares (Eq. 6.24), and the markers symbolize the known displacement. It can be clearly seen from figures 6.10 and 6.11 that the 6^{th} order is sufficient to give excellent agreement between the known displacements and their fit. Since there is no experimental error for the numerical simulation, any error between known and fit displacement would reduce by choosing higher order of polynomials. However, the average error for the 6^{th} order polynomial fit is low enough to get good agreement between the two results.

The resulting stress tensor contour map on the $\theta = 0^{\circ}$ surface, determined by multi-axial contour measurement, is given in Figure 6.12. In order to compare these results with the measured residual stress values, the stress values at y = 3.55 mm and at x = 40 mm are extracted and plotted in Figures 6.13 and 6.14 respectively. Although all

eigenstrain components were used to generate known residual stresses using equations 6.29 and 6.30, these plots demonstrate that the effect of eigenstrain components ε^*_{xy}, ε^*_{yy}, and ε^*_{yz} on the residual stress are much less than the others. The normalised error between the known and 'measured' residual stress components at $y = 3.55$ mm and at $x = 40$ mm are shown in Figures 6.15 and 6.16 respectively, and in which the normalized error is the difference between the known and measured residual stress and divided by the maximum known values (171 MPa). Those figure show that there is an excellent agreement found between them by choosing 6^{th} order of Legendre polynomial series for both directions, showing that the method is working smoothly.

It can hence be concluded that the full residual stress tensor can be determined with high accuracy by means of calculating an eigenstrain from the measured displacements.

6.6 Discussion

One of the main extensions of this method over the conventional contour method is the use of eigenstrains to determine the residual stress. This makes it possible, by the use of multiple cuts, to obtain data for predicting the full residual stress components in a continuously-processed body. Moreover, since series expansion is utilized in a least squares fit (Eq. 6.24) there is no need to smooth the measured displacement surface. The use of eigenstrain is vital as the residual stress distribution is affected by the $\theta = 45°$ and $\theta = -45°$ cut planes due to the free ends of the body. One drawback, however, is that the creation of the compliance vector, the size of which

depends on the displacement variation on the cut surface, requires substantial computational effort compared with the conventional contour method. For example, in order to create the compliance matrix for the 3D multi-axial contour method, the order of the Legendre polynomials were chosen as 6 for both directions. Therefore, 147 jobs were analysed for numerically creating the compliance vector. In contrast, a half model is sufficient for conventional contour method to calculate the residual stress.

As an addition to previous research [1], numerical validation (by using a different geometry, material and eigenstrain distribution) was undertaken to determine the accuracy of the novel multi-axial contour method. This validation confirmed that the use of only three eigenstrain components ε^*_{xx}, ε^*_{zz} and ε^*_{xz} for creating the compliance matrix was sufficient to get accurate results for any residual stress distribution in the body. Moreover, a 6^{th} order polynomial series for both directions was sufficient to get very accurate results; the averaged error between the known displacements and their fits on the three cut surfaces was found to be less than 0.1%.

The reason for using Legendre polynomials as the basis functions for this work was that they are widely utilized for series expansion approaches as the higher order terms (i.e. two and more) satisfy equilibrium. Perhaps it would be simpler or quicker for the implementation of the multi-axial contour method to use any other basis functions instead of Legendre polynomials. However, Legendre polynomials gave a small error for the non-polynomial numerical example used.

There may be some limitations in the use of polynomial series for least squares fitting. Firstly, a more accurate result will not always be obtained by choosing higher order terms. In other words, the result may not converge more after a certain order. In addition, they may show instability and not fit properly near end points. For example, second and more orders of the Legendre polynomials show dramatic changes near to point ±1 (as shown in Fig. 6.4). This may be the main reason to get errors in the fit as there are lower accuracy results at the ends of the samples. For instance, Figure 6.15 confirms this issue. The normalized residual stress error is around 0.004 in middle, but it becomes around 0.01 near to the end points.

6.7 Conclusion

In this chapter, the novel 'multi-axial contour method' technique for the residual stress measurement was explained. Since this technique uses the eigenstrain concept, first the theory of eigenstrain was given in detail. Then, the principles of the multi-axial contour method for 2D and 3D bodies were explained. Finally, the method was simulated numerically in order to verify that it can accurately reproduce a pre-existing stress field in a sample where the eigenstrain in invariate in one direction. Impressive agreements have been found between multi-axial contour method and the known values that were used for the validation of the technique.

6.8 References

[1] DeWald A.T. and Hill M.R. (2006). Multi-Axial Contour Method for Mapping Residual Stresses in Continuously Processed Bodies. Experimental Mechanics, vol. 46, pp.473-490.

[2] Pagliaro P., Prime M.B. and Zuccarello B. (2006). Multiple Stress Components from Multiple Cuts for the Contour Method. Associazione Italiana per l'Analisi delle Sollecitazioni (AIAS) XXXV Convengo Nazionale 13-16 September 2006.

[3] Reissner H. (1931). Eigenspannungen und Eigenspannungsquellen. Zeitschrift fur Angewandte Mathematik und Mechanik, vol. 11(1), pp. 1-8.

[4] Mura T. (1987). Micromechanics of Defects in Solids. Kluwer, Massachusetts.

[5] Ueda Y., Fukuda K., Nakacho K. and Endo S. (1975). A New Measuring Method of Residual Stresses with the Aid of Finite Element Method and Reliability of Estimated Values. Transaction of the JWRI (Japanese Welding Research Institute), vol. 4(2), pp. 123-131.

[6] Ueda Y. and Fukuda K. (1986). New Measuring Method of Axisymmetric Three-Dimensional Residual Stresses Using Inherent Strains as Parameters. Journal of Engineering Materials and Technology, vol. 108(4), pp. 328-334.

[7] Timoshenko S.P. and Goodier J.N. (1970). Theory of Elasticity, 3rd Edition. New York, McGraw-Hill Book Company.

[8] Ueda Y.M. and Fukuda K. (1989). New Measuring Method of Three Dimensional Residual Stresses in Long Welded Joints Using Inherent Strains and Parameters. Journal of Engineering Materials and Technology, vol. 111, pp. 1-8.

[9] Schajer G.S. (1981). Application of Finite Element Calculations to Residual Stress Measurements. Journal of Engineering Materials and Technology, vol.103, pp.157-163.

[10] Cheng W. and Finnie I. (1985). A method for Measurement of Axisymmetric Residual Stresses in Circumferentially Welded Thin-Walled Cylinders. Journal of Engineering Materials and Technology, vol.107, pp.181-185.

[11] Arfken, G.B. and Weber H.J. (2001). Mathematical Methods for Physicists, 5th edition. A Harcourt Science and Technology, San Diego.

[12] Abramowitz M. and Stegun I.A. (1972). Handbook of Mathematical Functions with Formulas, Graphs, and Mathematical Tables, 9th printing. New York: Dover.

6.9 Figures

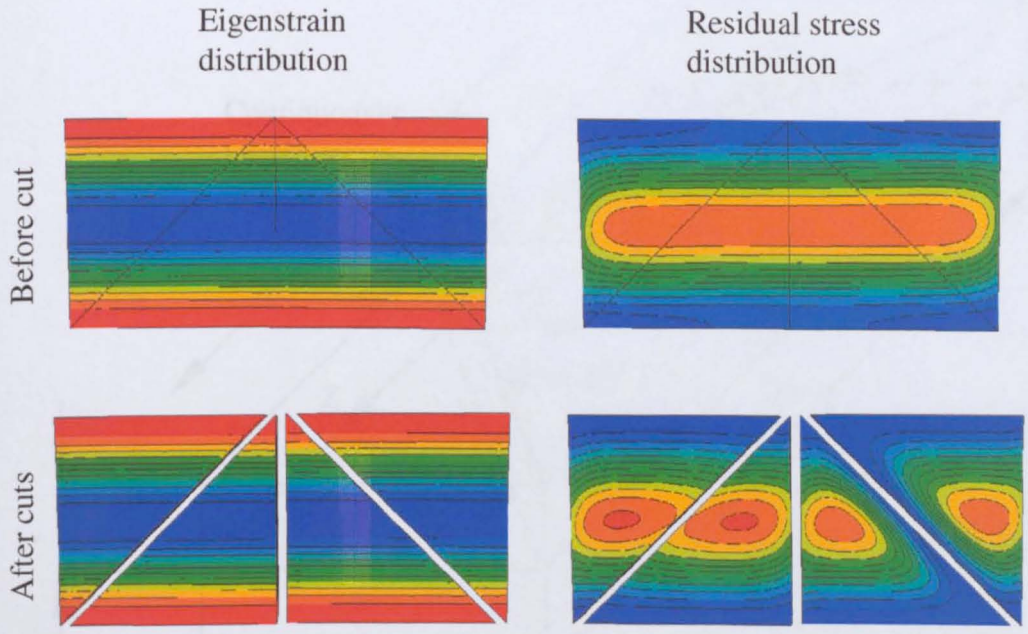

Figure 6.1 Eigenstrain (longitudinal) and corresponding residual stress (von Mises) distributions before and after cuts.

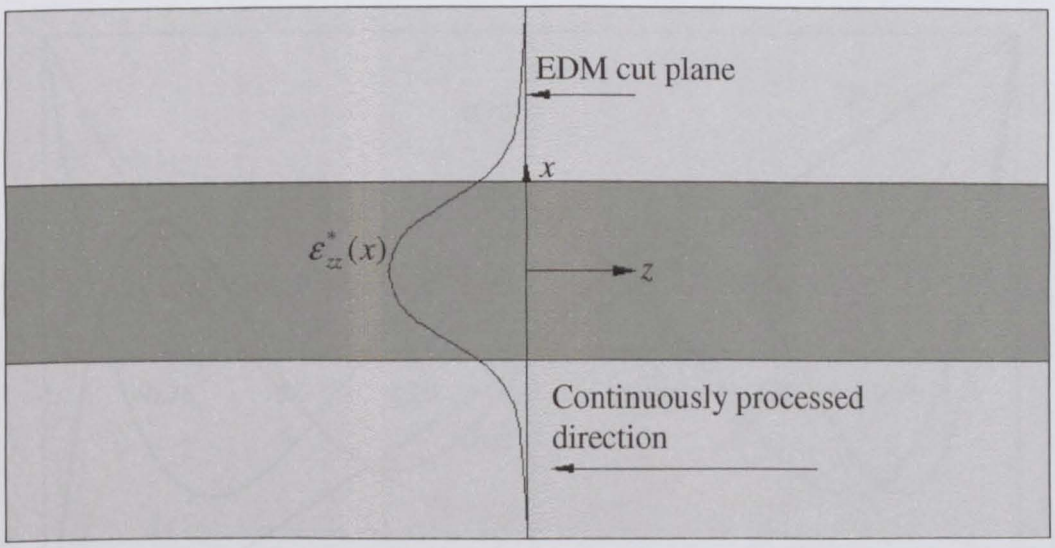

Figure 6.2 Illustration of a 2D continuously processed plane for multi-axial contour measurement.

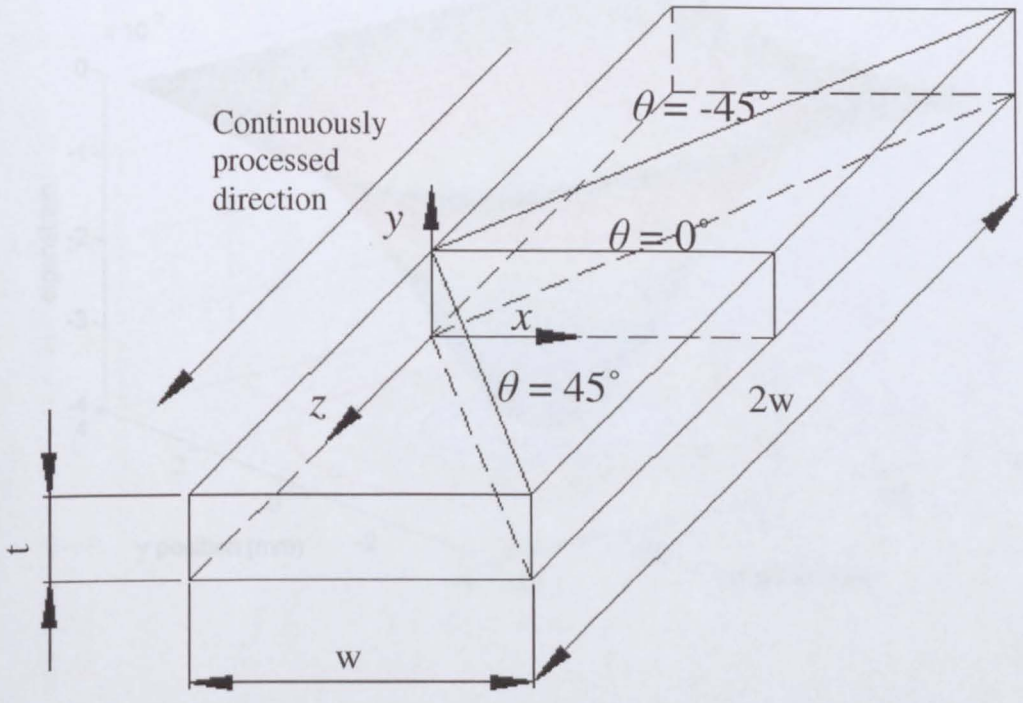

Figure 6.3 Illustration of a continuously processed prismatic sample for multi-axial contour method.

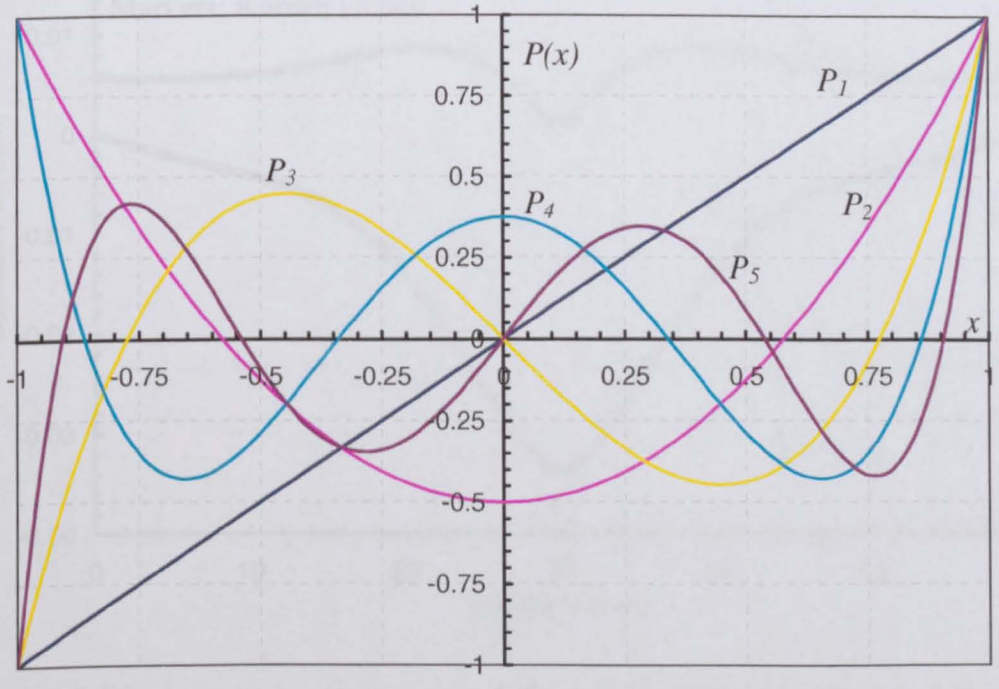

Figure 6.4 The first few terms of the Legendre polynomials

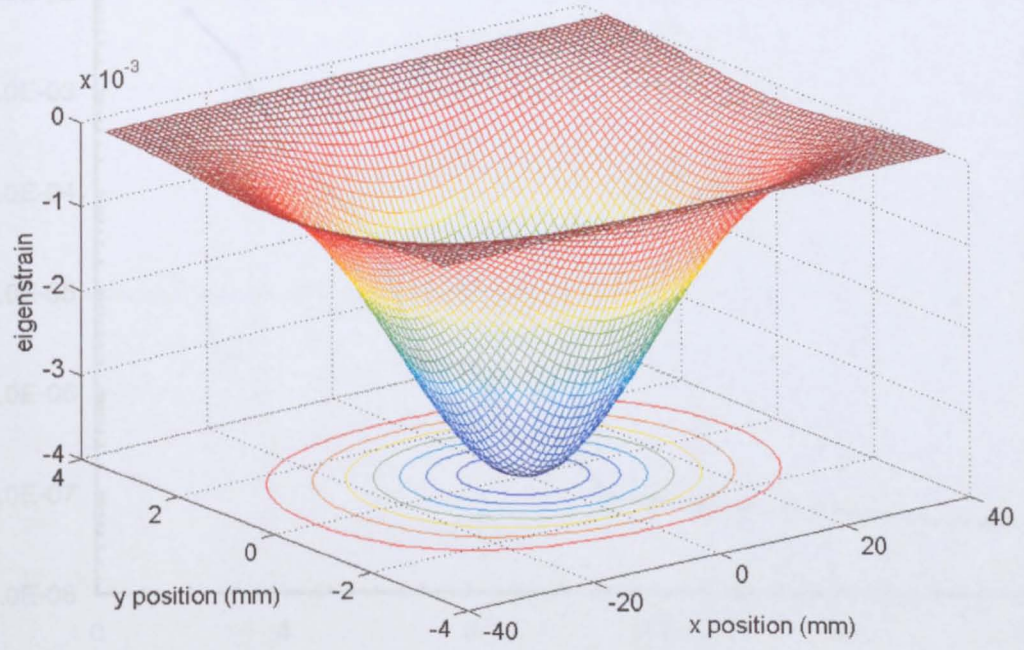

Figure 6.5 Eigenstrain distribution on the cross-sectional area for the numerical validation of the multi axial contour method

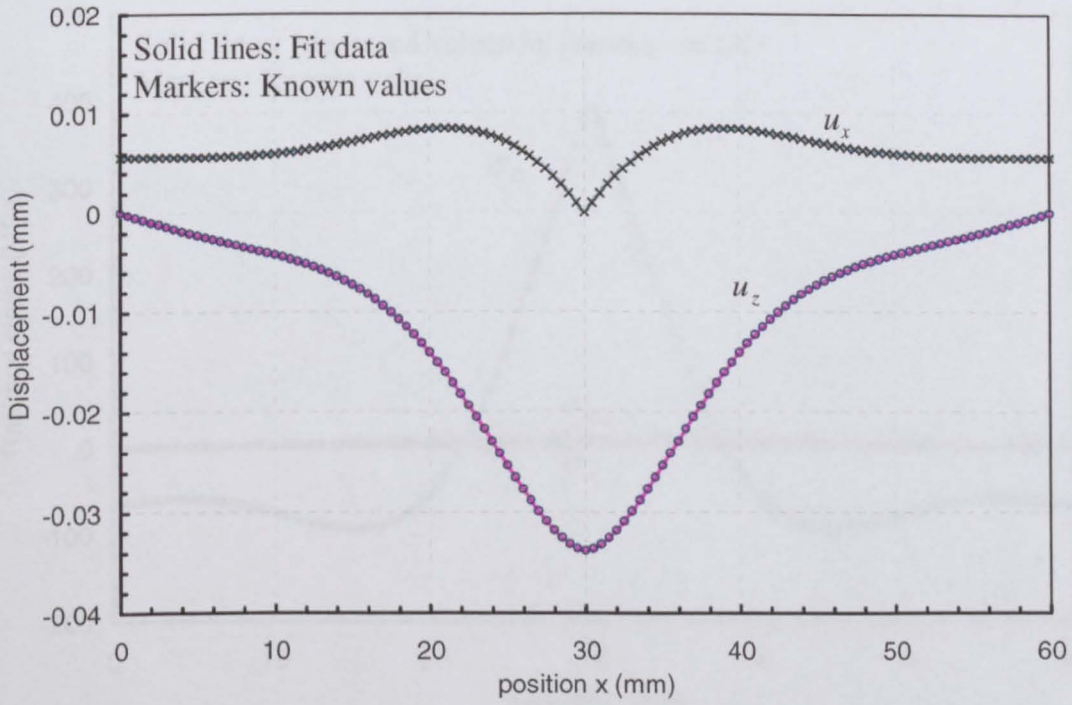

Figure 6.6 Displacement components of the 'cut' surface for 2D simulation of the multi-axial contour method.

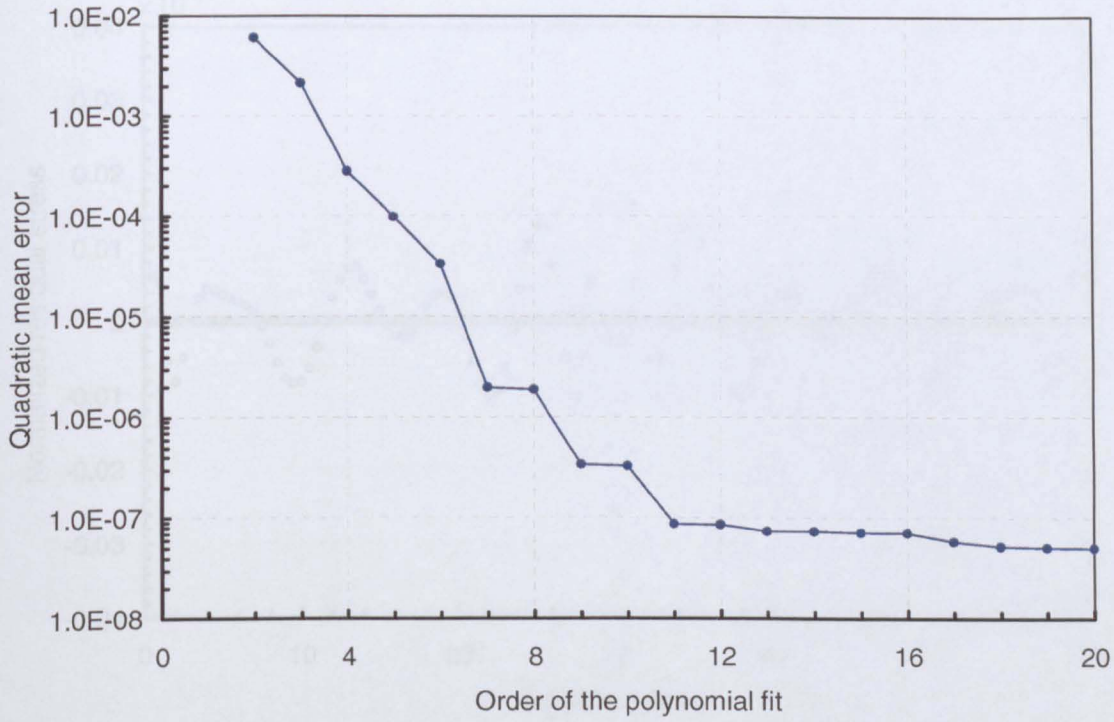

Figure 6.7 Quadratic mean error between the 'measured' and fit displacement for different orders of the fits.

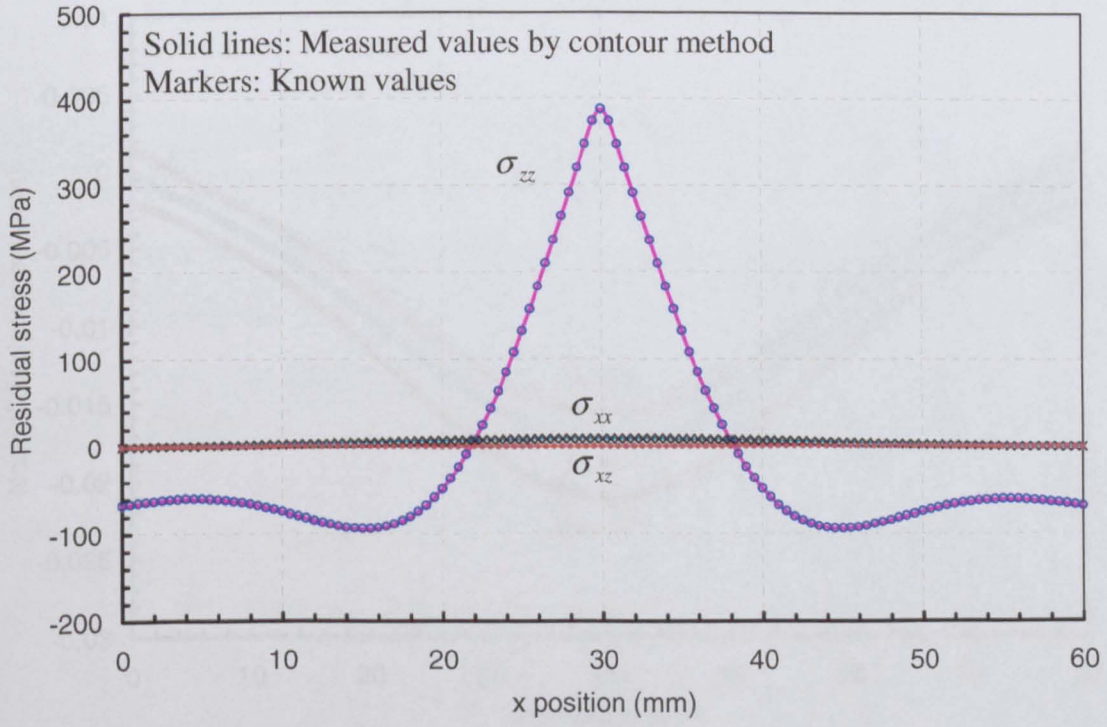

Figure 6.8 Residual stress results for 2D multi-axial contour simulation.

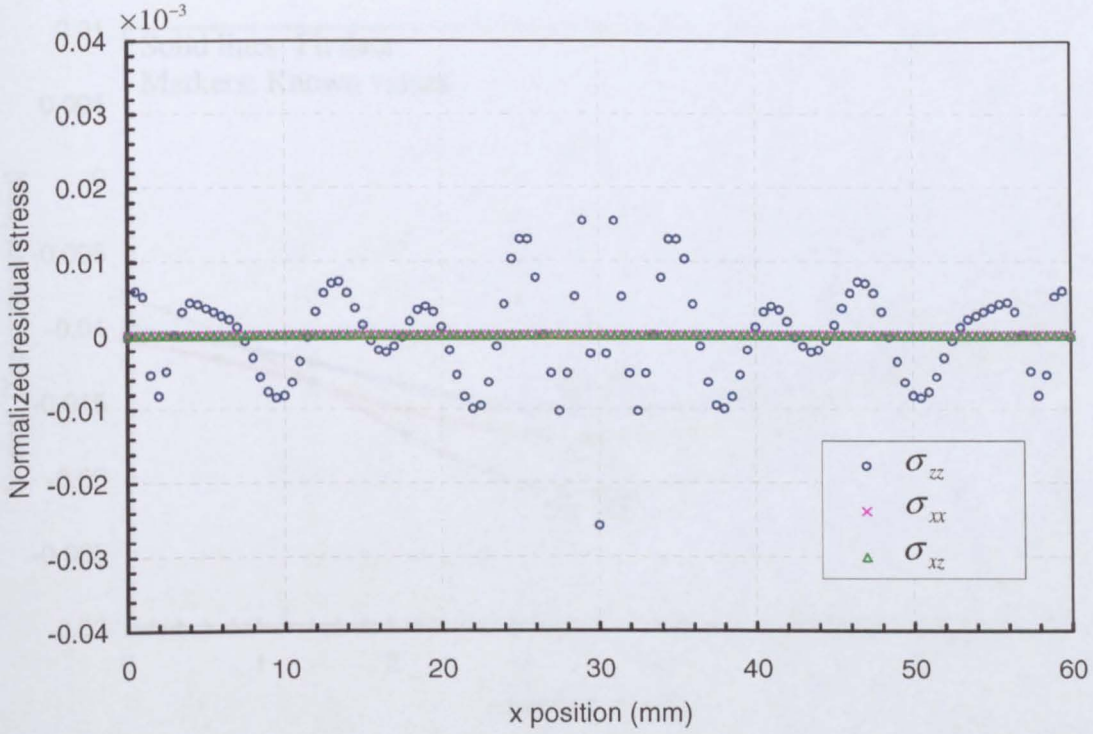

Figure 6.9 Normalised error between known and measured values for 2D multi-axial contour simulation.

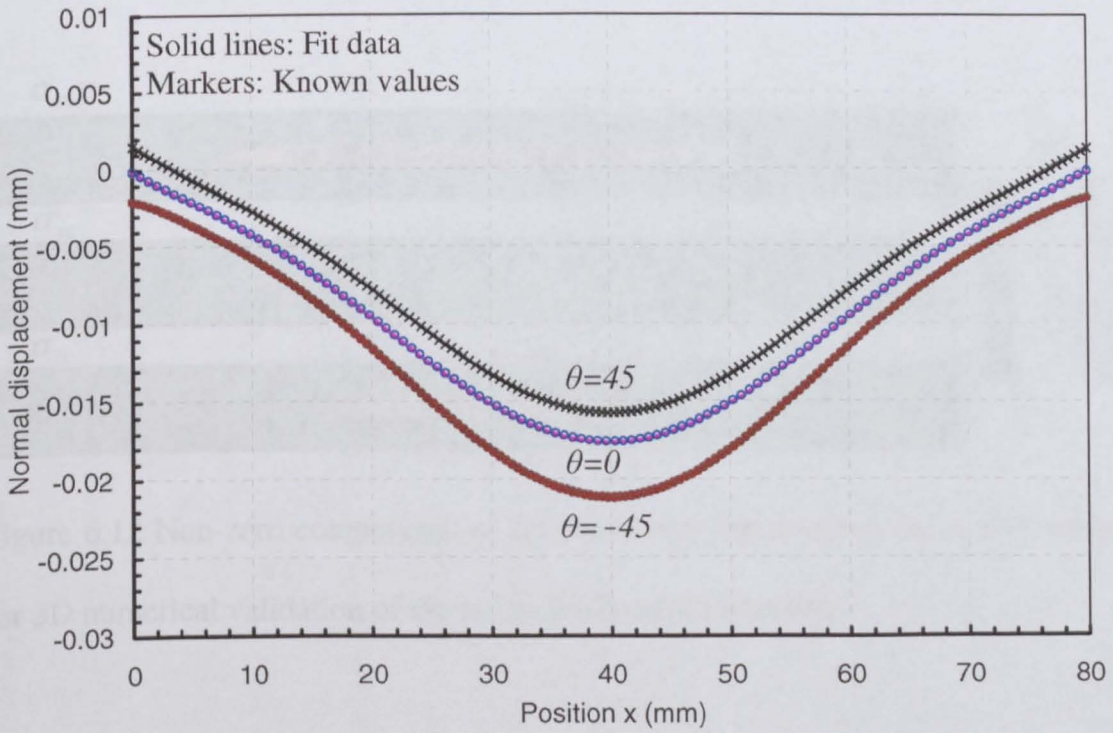

Figure 6.10 Comparison between known and fit data for 3D numerical verification of multi-axial method along the line y = 3.55 mm.

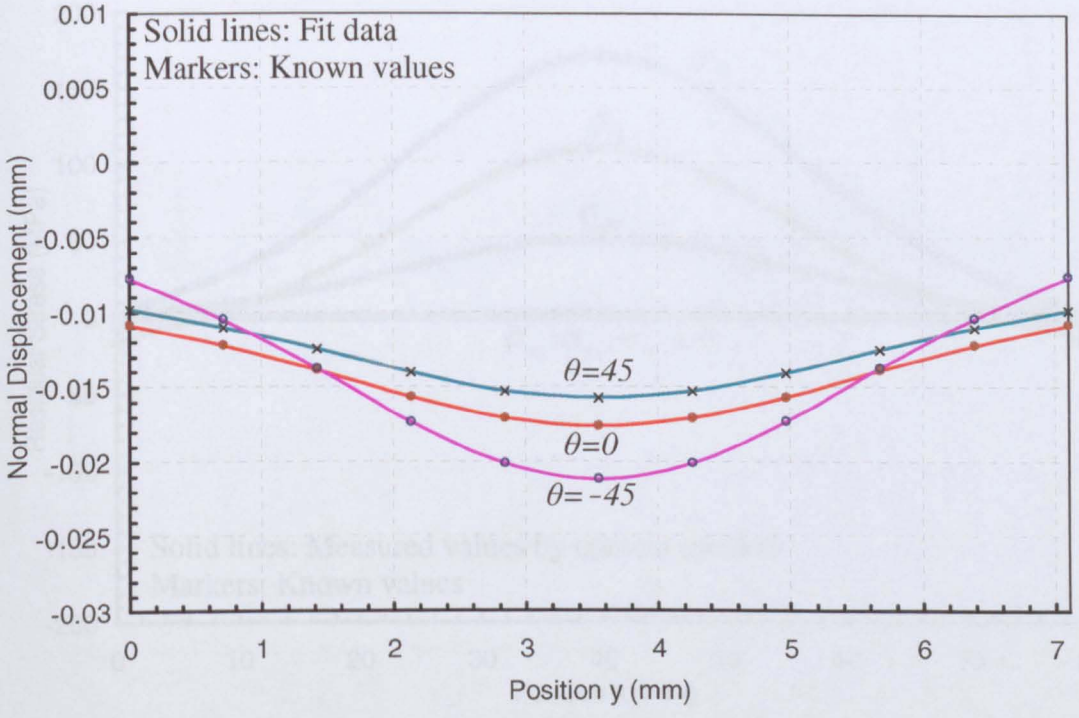

Figure 6.11 Comparison between known and fit data for 3D numerical verification of multi-axial method along the line x = 40 mm.

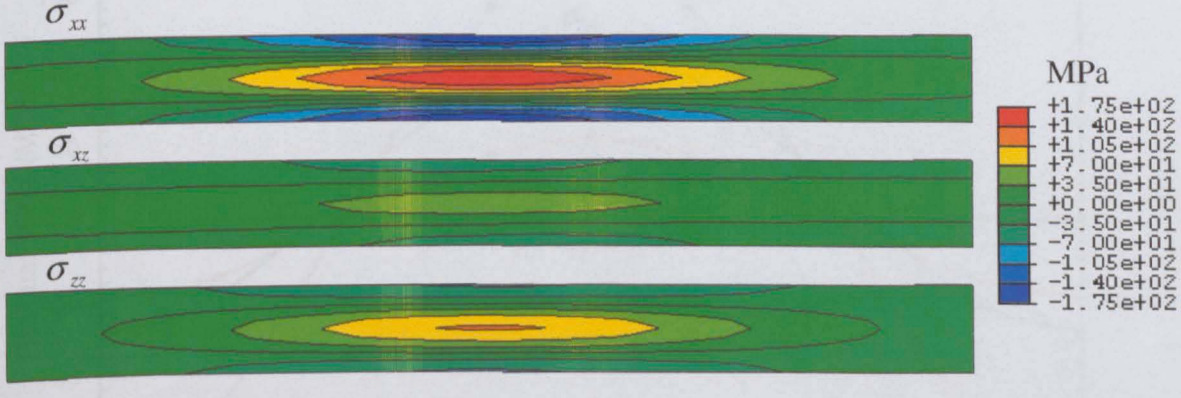

Figure 6.12 Non-zero components of residual stress variation on the θ = 0° surface for 3D numerical validation of the multi-axial contour method.

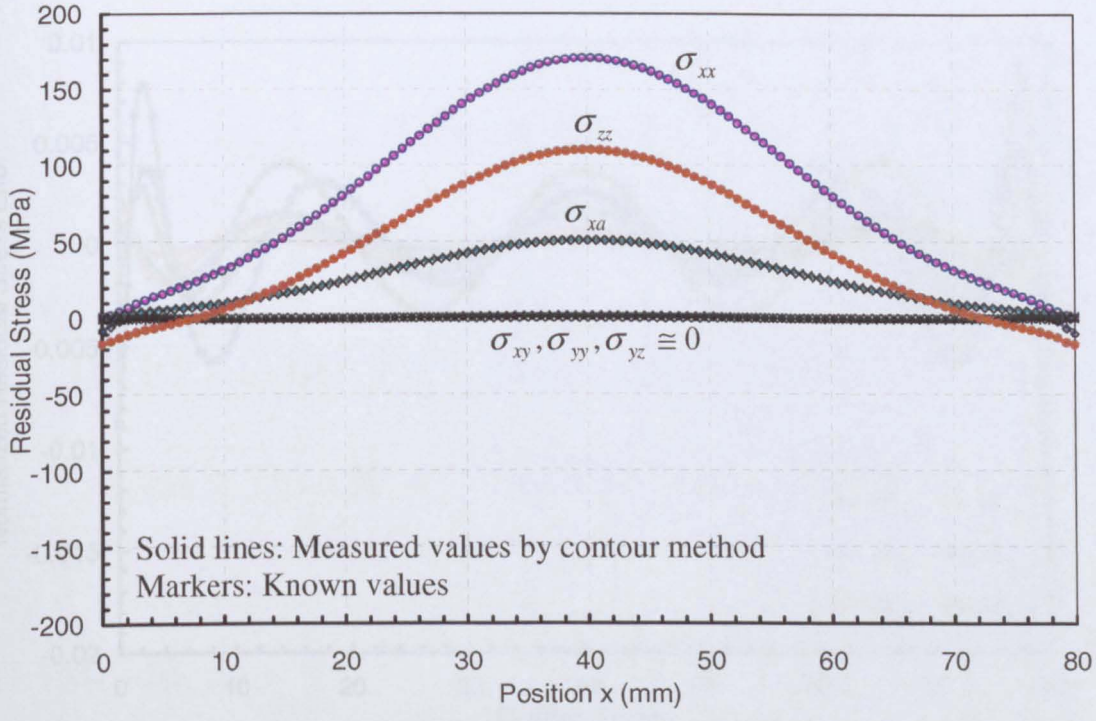

Figure 6.13 Comparison between known and measured residual stress for 3D numerical verification of the multi-axial method along the line y = 3.55 mm

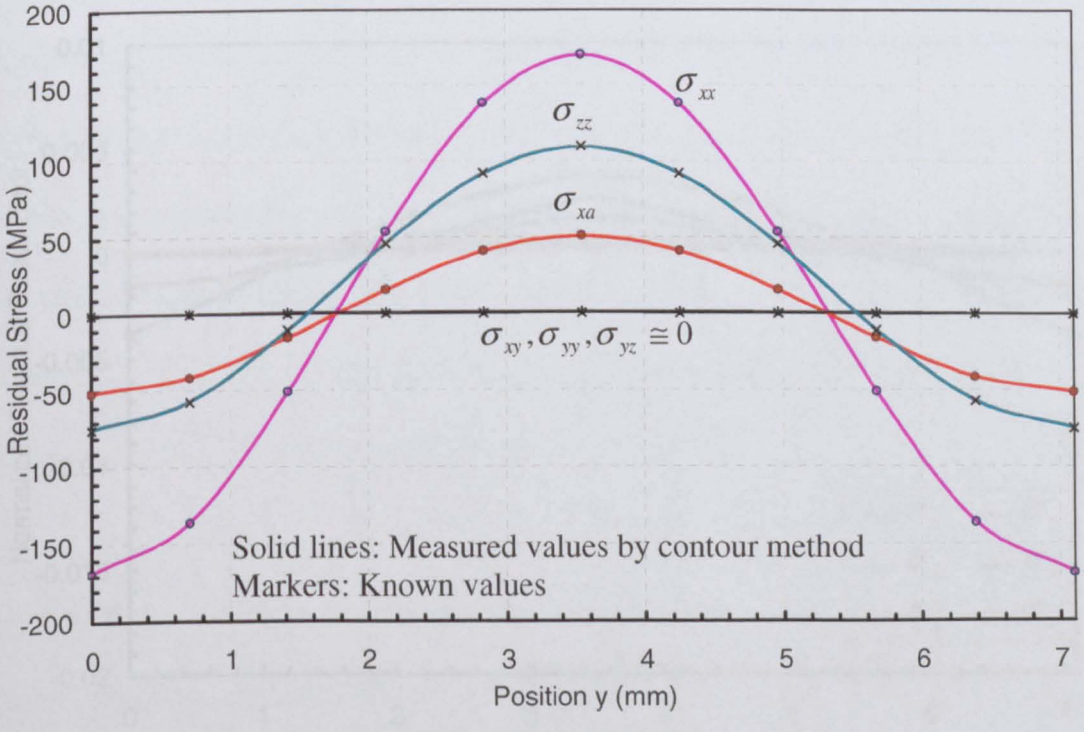

Figure 6.14 Comparison between known and measured residual stress for 3D numerical verification of the multi-axial method along the line x = 40 mm

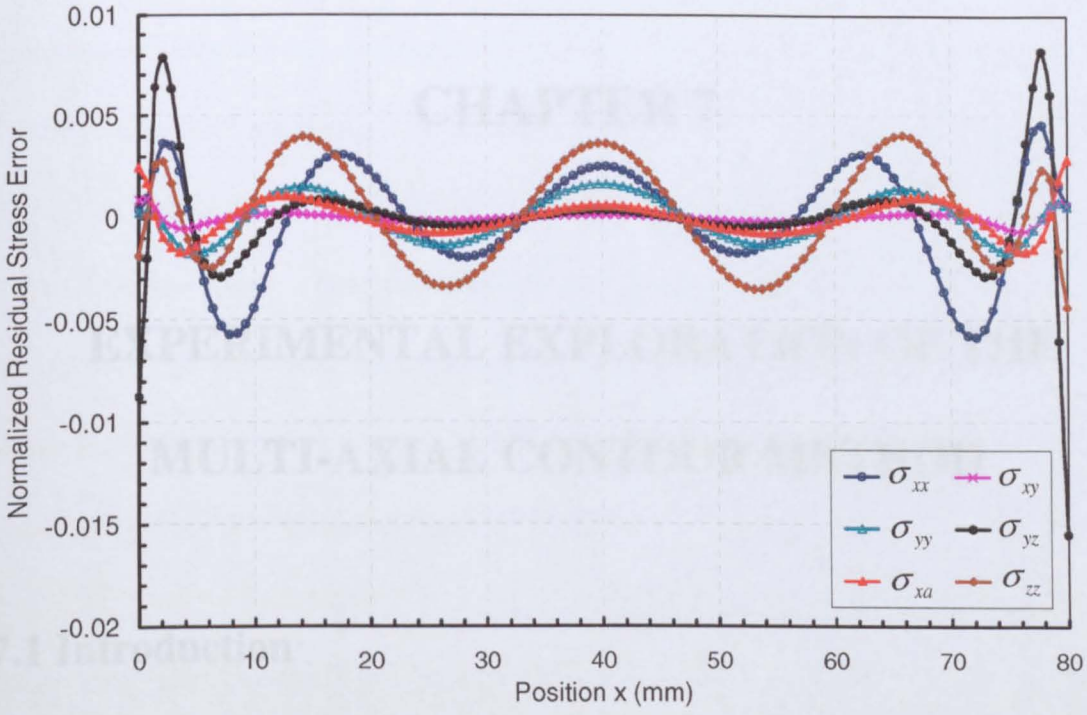

Figure 6.15 Normalised error between known and measured values for 3D multi-axial contour simulation along the line y = 3.55 mm

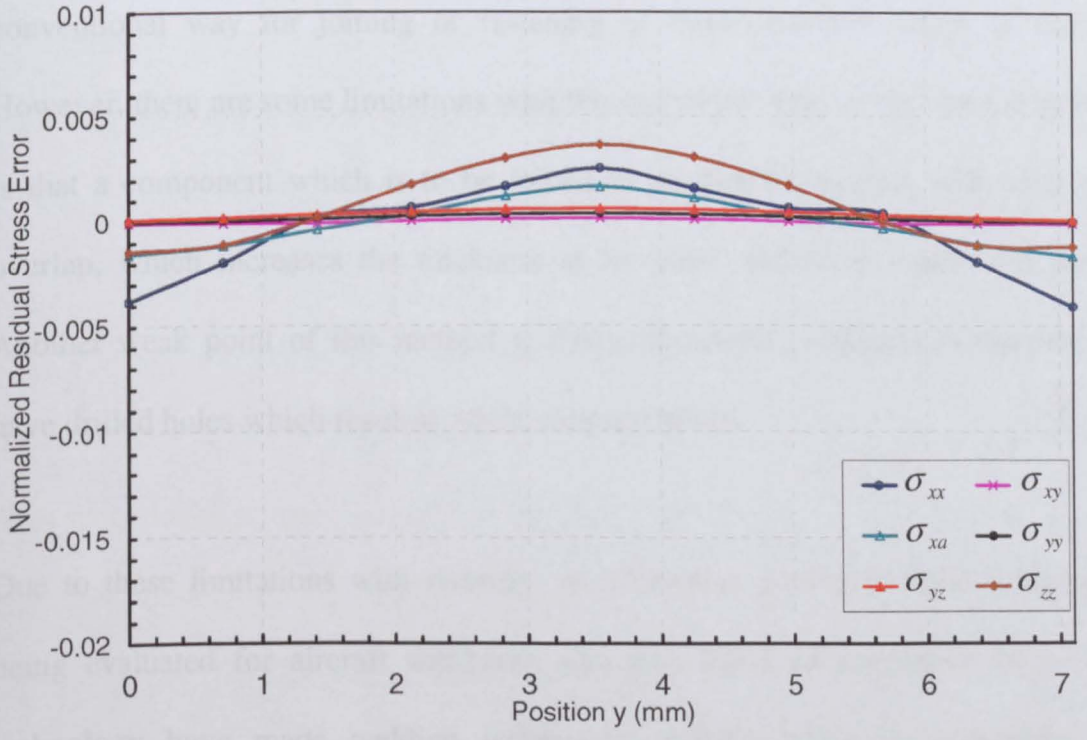

Figure 6.16 Normalised error between known and measured values for 3D multi-axial contour simulation along the line x = 40 mm

CHAPTER 7

EXPERIMENTAL EXPLORATION OF THE MULTI-AXIAL CONTOUR METHOD

7.1 Introduction

With very high strength to weight ratio, the heat treatable aluminium alloys which are 2xxx, 6xxx and 7xxx series are widely used for aircraft applications. Structural components for aircrafts are usually built-up using the different alloys. One conventional way for joining or fastening of those different alloys is riveting. However, there are some limitations with this technique. One of the main drawbacks is that a component which is to be joined to another by riveting will have some overlap, which increases the thickness at the joint and so increases the weight. Another weak point of this method is that components subjected to riveting will have drilled holes which result in stress concentrations.

Due to these limitations with riveting, an alternative joining method, welding, is being evaluated for aircraft structures. Recently rapid advancements in welding technology have made welding techniques valuable tools in maintaining the structural integrity of engineering structures [1]. These developments also bring about the necessity of the understanding and modelling the mechanical response of

welds, and especially the effects of residual stresses as the local residual stress and mechanical response in or around a weld affects the mechanical performance and thereby structural integrity. For instance, aluminium alloys are one of the most complicated metals to weld because of their high thermal expansion coefficients and thermal conductivity. These result in the development of residual stresses along with changes in the weld and surrounding parent metal properties. Hence, the residual stress field introduced by welding needs to be fully characterized as long as the weld region governs the structural integrity of engineering structures.

It has long been known that diffraction techniques such as X-ray, synchrotron X-ray and neutron diffraction for residual stress measurements enable the determination of multiple residual stress components within the body. Nevertheless, these methods are sensitive to microstructural changes, and can be expensive and time consuming. In particular, the structural integrity of dissimilar materials (i.e. parent and weld materials) and microstructural variations for welded materials cause limitations for measurement of residual stress for these diffraction techniques in weld materials [2].

The 'conventional' contour method has emerged as a very effective residual stress measurement as an alternative to diffraction techniques [2-8]. Although it is a destructive method, the contour method does not have the limitations which were explained above for diffraction techniques for residual stress measurements in welded metals. In the conventional contour method, a 2D residual stress map in the direction normal to the sectioned surface can be calculated by means of measuring displacement caused by relaxation of the residual stress on the cut surface. Calculation of multiple residual stress components can be achieved by multiple cuts,

but each cut in a body results in redistribution of the residual stress, and therefore in practice the conventional contour method does not provide any other original residual stress component in the body. This limitation arises from the fact that the displacement in the conventional contour method is directly converted to residual stress by imposing this displacement in the inverse direction as boundary conditions on the cut surface, using Bueckner's elastic superposition principle [9] in a finite element model.

The importance of using the eigenstrain for determination of the residual stress can be seen in the case of having multiple cuts in the body. The eigenstrain distribution remains the same regardless of multiple cuts being made, even if the residual stresses are relaxed. The multi-axial contour method hence uses the assumption that residual stresses are due to an inelastic misfit strain (eigenstrain) which does not change when a sample containing residual stresses is sectioned. The eigenstrain is derived from the measured displacements due to residual stress relaxation when the specimen is sectioned. By carrying out multiple cuts, the full residual stress tensor in a continuously processed body can be determined. In the previous chapter, the theory of the multi-axial contour method was described and finite element simulation of the technique was carried out to numerically verify the method for 2D and 3D bodies.

The aim of this chapter is to investigate the capability of the multi-axial contour method on a residually stressed sample. To provide experimental validation of the multi-axial contour method, a weld which was previously investigated by Ganguly [10] was chosen. The parent material in this work was 2024-T351 aluminium alloy

and the welding was carried out using the variable-polarity plasma-arc (VPPA) process. Investigations using the multi-axial contour method were performed to determine the cross sectional residual stress field in the VPPA 2024 T351 aluminium alloy welded plate in multiple directions. The residual stress components obtained by the multi-axial contour method were compared with the neutron diffraction results obtained previously.

7.2 Materials and Specimen

The material was AA 2024-T351, which is widely used for aerospace applications such as rivets and aircraft wings owing to its damage tolerant characteristics [11-12]. The chemical composition of the 2024-T351 alloy is given in table 7.1 (from [13]). The typical mechanical properties of the AA2024-T351 sheet are shown in table 7.2. The 2024-T351 aluminium alloy used in this study was welded using the newly developed welding technique of variable polarity plasma arc welding (VPPA) by Cranfield University [14].

The "as received" specimen was supplied as a "dogbone" specimen with 160 mm gauge length, 350 mm full length, 80 mm gauge width, and 7.1 mm thickness. The "dogbone" specimen was used for the neutron diffraction measurements to determine the residual stress across the width of the specimen. A picture of the specimen 'as received', the weld lines and the machining position of the specimen which was used for the multi-axial contour method are given in Figure 7.1.

Table 7.1: Chemical composition of 2024-T351 aluminium alloy

Alloy	Si	Fe	Mn	Mg	Cu	Zn	Cr	Ti	Others
2024	0.5	0.5	0.3-0.9	1.2-1.8	3.8-4.9	0.25	0.1	0.1	0.05

Table 7.2: Mechanical properties of 2024-T351 aluminium alloy

Alloy	Modulus of Elasticity (GPa)	Poisson's ratio	Ultimate tensile strength (MPa)	Elongation at failure (%)
2024	72.4	0.34	470	20

7.3 Experimental Procedures

7.3.1 Neutron Diffraction

Ganguly [10] evaluated the residual stresses in this material using neutron diffraction measurements which were carried out on the ENGIN-X instrument at the ISIS facility of the Rutherford Appleton Laboratory, UK [15].

Neutron diffraction is a well-established non-destructive technique to determine strains within metallic structures [16]. The inter-planar atomic lattice distance can be determined from the position of the diffraction peaks using Bragg's Law [17]. Measurements in the welded sample were carried out in three directions (longitudinal, transverse and normal to the weld) to be able to compute the direct stresses. For the longitudinal strain measurements, the gauge a volume was 2×2×2 mm^3. The gauge volume was increased to 2×20×2 mm^3 for measurements in the transverse and normal directions to reduce the overall measurement time.

7.3.2 Multi-Axial Contour Method

After the neutron diffraction measurement, the specimen was machined to produce a 160×80×7.1 mm^3 block to perform the multi-axial contour method. A wire electro-discharge machine (EDM) with a 0.1 mm diameter brass wire was used for this purpose. In order to minimize any movement during the cutting processes, the specimen was clamped firmly by using a steel plate. Each cutting process was performed by submerging the specimen. It took around 1 hour for EDM to complete each cut.

A schematic of the prismatic block used for the experiment, with the Cartesian coordinate system *xyz* is given in Figure 7.2. Note that weld line was chosen in the *z* direction along which the eigenstrain is constant.

The block was first sectioned along the $\theta = 0°$ surface and the deformed surfaces due to residual stress relaxation were measured with the CMM. After the first measurement, the two remaining square blocks were sectioned along their diagonals ($\theta = 45°$ and $\theta = -45°$) and the displacements were measured with the CMM. For these experiments, the density of the contouring the surfaces by CMM was chosen as 0.5 mm for both *x* and *y* directions. Hence, ~2270 data points at each of the $\theta = 0°$ cut pairs and ~3210 measured points at each of the $\theta = 45°$ and $\theta = -45°$ cut pairs were recorded. All surface displacement pairs were then averaged to remove any shear stress relief effects and cut path wandering as explained in the section 5.3.3 in chapter 5. The displacement from all the three cuts was then assembled into the displacement vector (u).

After the experiments were completed, the full size sample was modelled by using the finite element solver ABAQUS with a 0.5 mm × 0.5 mm mesh of reduced integration point 4 nodes, and linear shape. The material behaviour is assumed to be isotropic and linear elastic with Poisson's ratio 0.34 and elastic Young's modulus 72.4 GPa.

For the experimental data the order of the Legendre polynomial series was chosen as 20^{th} order for the x direction and 3^{rd} order for the y direction. The reason for choosing a very high order Legendre polynomial in the x direction will be explained in the next section. A series of known bivariate Legendre polynomial surfaces were input into the model for three eigenstrain components (ε^*_{xx}, ε^*_{zz} and ε^*_{xz}). Therefore, (20+1) × (3+1) × 3 = 252 jobs were analysed for numerically creating the compliance matrix. Each job took about 1 hour for ABAQUS to complete the analysis.

As the model involved 3 cut pairs (6 surfaces) and net displacement due to stress relaxation on each sectioned surface could be calculated by subtracting the deformed surface from the undeformed surface (before 'cut'), 12 surfaces had to be measured for each job. Thus, 252 jobs × 12 surfaces = 3024 surfaces were measured to create the compliance vector. The displacements from the opposite sides of each cut were averaged and the compliance matrix (C) was assembled.

Equation (7.1) was then solved with the inverse solution using a least squares method, and the unknown coefficient matrix (A) was determined.

$$\{A\}=\left([C]^T[C]\right)^{-1}[C]^T\{u\}, \tag{7.1}$$

Once equation (7.1) has been solved, the eigenstrain distributions in the specimen can be calculated for all components using the determined A matrix and equation (7.2).

$$\varepsilon^*(x,y)=\sum AS(x,y), \tag{7.2}$$

where ε^* is the unknown eigenstrain components, A are unknown coefficients of the series for the unknown eigenstrain component ε^* to be calculated, and S represents bivariate Legendre polynomials which are the dot product of two Legendre polynomials ($S\ (x,y)=P(x)P(y)$). Note that much greater details for the theory of multi-axial contour method and the inverse solution for calculating eigenstrain components have been given in the previous chapter 6.

These determined eigenstrain distributions are then included in the FE simulation and the induced misfit results in elastic strains and the residual stresses.

7.4 Results and Discussion

The averaged displacements through the thickness of the $\theta = 0°$, $\theta = 45°$ and $\theta = -45°$ surfaces measured by CMM are depicted in Figure 7.3. Since the displacement along the x-direction as shown in Figure 7.3 varies significantly, the order of the polynomial series had to be fairly high, whereas a 3rd order was adequate in the y-direction to fit. Because Legendre polynomials are smooth functions, the resulting linear combination from the solution of equation (7.1) will be smooth and there is no need for further smoothing. Figure 7.4 shows the data fit for the 12th order

polynomial series to the $\theta = 0°$, $\theta = 45°$ and $\theta = -45°$ surfaces. A very good fit could be obtained to the measured values and the resulting fitted displacements were indeed smooth. The effect of higher orders of the Legendre polynomials in the x-direction (6^{th} and 12^{th}) can be seen in Figure 7.5 where the results at $y = 3.55$ mm for the $\theta = 0°$ cut surface are plotted. It can be clearly seen that the 6^{th} order does not capture the variation of displacement, whereas the 12^{th} order follows the variation in the measured displacements. This smoothness was found to be very important in earlier investigations of the conventional contour method [7].

In order to investigate the best fit for the experiment, the order of the Legendre polynomials was increased up to 20 in the generation of the compliance matrix. It was however found that there was no significant change between the 12^{th} and 20^{th} orders. The average error between the averaged row data and fitted data on the $\theta = 0°$ surface was found to be 2.5 μm for the 6^{th} order and 1.6 μm for the 12^{th} and 20^{th} orders.

The resulting residual stress variations on the $\theta = 0°$ surface for measured non-zero components are given in Figure 7.6. In order to compare the results for the two different independent techniques, the longitudinal residual stress variation through the line at $y = 3.55$ mm was extracted and compared with the neutron diffraction measurements (Figure 7.7). Calculation of the longitudinal stresses by applying the data from the initial cut to the conventional contour method is also presented for comparison.

There are some differences between the results from the standard and the multi-axial contour methods, which can be attributed to the fact that the inverse procedure used for calculating the stress values fits all the eigenstrains simultaneously, and the displacement matrices obtained from the ±45° cuts therefore affect the longitudinal strains calculated. There is slightly better agreement between the neutron diffraction data and the standard contour technique (average root-mean-square discrepancy of 17 MPa for the standard method compared to 21 MPa for the multi-axial technique).

From the comparison of longitudinal stresses measured along the line at y = 3.55 mm at the θ = 0° surface in Fig. 7.7, it can be seen that there is a small difference between the neutron diffraction and the contour results (especially between 60 mm and 70 mm, where the contour results are higher than the neutron results), but overall there was very good agreement between the two sets of results. This difference might be due to the fact that during specimen cutting from one side, there may be local deformation ahead of the cutting wire as a result of the local stress relaxation, which alters the width of the cut and introduces some error into the final stress values. As expected, Figure 7.7 shows that the weld and heat affected zone (HAZ) regions have tensile stress character and this is balanced by compressive residual stress in the parent material.

The transverse residual stress distribution for the line at y = 3.55 mm for neutron diffraction and multi-axial contour method is compared in Figure 7.8. It can be seen that the transverse residual stresses vary between ±50MPa. There is a reasonably good agreement between two independent techniques for transverse residual stress component despite their low variation. The normal residual stress component was

found to be even smaller than the transverse one. Any small discrepancy between the two results is probably due to the relatively small magnitude of this stress or because the measurements were not carried out at exactly the same place as the neutron diffraction data which is averaged over the gauge volume.

Note that the error bars on the neutron data are derived from the reported uncertainties in the Pawley [18] refinement fitting of the diffraction spectra: other uncertainties such as those in the elastic modulus and possible systematic errors in a_0 are not included, and the total uncertainty may therefore be greater than indicated by the error bars.

7.5 Conclusion

The aim of the present work was to apply the methodology developed by DeWald and Hill [19] to a specimen where the residual stresses had been measured with a well-established residual stress measurement technique. Such a validation had not been carried out previously. For this purpose, the multi-axial contour method was performed on a VPPA-welded sample, because the residual stresses in the VPPA weld had been measured previously with different techniques, and the results were consistent for all methods [5,6].

Longitudinal residual stress distributions in for both specimens at their θ = 0° surfaces were obtained as expected. Since typical observations for VPPA weld in aluminium alloys for different thickness of the specimens were previously reported in [5-6, 14], longitudinal residual stress distribution for the weld material along the

width is with the form of *M* shape as shown in Figure 7.7. The peak tensile stress is observed in the HAZ. The reason for a tensile residual stress in and around weld region is due to the fact that the interface between weld and parent material is subjected to heating and the hot material is constrained by the other material during the cooling, which causes tensile stress.

In the multi-axial contour method, a higher uncertainty might be expected in the non-longitudinal stress components, as has been observed in a previous study [20], where an eigenstrain series expansion was used for calculating the residual stress components using a slitting method for fibre-reinforced metal matrix composite material, and the uncertainties were found to be large for the non-longitudinal residual stress components.

One possible criticism of the present work could be that the VPPA specimen used here is not a good application for experimental verification of the multi-axial contour method, since the transverse and normal residual stresses are small in magnitude when compared with the major principal stress. Therefore, it is not clear whether the variation in transverse stresses acquired by neutron diffraction is a true variation or just noise.

Although the multi-axial contour method is a powerful technique in many aspects, it requires great computational effort. If computing cost is taken into account, the multi-axial contour method should only be applied on samples which fully satisfy the assumption of this technique.

7.6 References

[1] Mendez P.F. (2000). New Trends in Welding in the Aeronautic Industry. Proceedings of the conference New Trends for the Manufacturing in the Aeronautic Industry, Hegan/Inasmet, San Sebastián, Spain, pp. 21-38.

[2] Prime M.B., Hill M.R., DeWald A.T., Sebring R.J., Dave V.R. and Cola M.J. (2002). Residual Stress Mapping in Welds Using the Contour Method. Proceedings of the 6th International Conference: Trends in Welding Research, Pine Mountain. Georgia, pp. 891-896.

[3] M.B. Prime (2001). Cross-Sectional Mapping of Residual Stresses by Measuring the Surface after a Cut. Journal of Engineering Materials and Technology, vol. 123, pp. 161-168.

[4] Zhang Y., Fitzpatrick M.E. and Edwards L. (2002). Measurement of the Residual Stresses around a Cold Expanded Hole in an EN8 Steel Plate Using the Contour Method. Materials Science Forum, vol. 404-407, pp. 527-534.

[5] Zhang Y., Ganguly S., Edwards L. and Fitzpatrick M.E. (2004). Cross-Sectional Mapping of Residual Stresses in a VPPA Weld Using the Contour Method. Acta Materialia, vol. 52, pp. 5225-5232.

[6] Zhang Y. (2004). Numerical and Experimental Exploration of the Contour Method for Residual Stress Evaluation. PhD Dissertation, The Open University, UK.

[7] Kartal M.E, Turski M., Johnson G., Gungor S. Fitzpatrick M.E., Withers P.J. and Edwards L. (2006). Residual Stress Measurements in Single and Multi-Pass Groove Weld Specimens Using Neutron Diffraction and the Contour Method, Material Science Forum, vol. 524-525, pp. 671-676.

[8] Prime M.B., Gnaupel-Herold T., Baumann J.A., Lederich R.J., Bowden D.M. and Sebring R.J. (2006). Residual Stress Measurements in a Thick, Dissimilar Aluminium Alloy Friction Stir Weld. Acta Materialia, vol. 54, pp. 4013-4021.

[9] Bueckner H.F. (1958). The Propagation of Cracks and the Energy of Elastic Deformation. Translation of the ASME, vol. 80, pp. 1225-1230.

[10] Ganguly S. (2004). Non-Destructive Measurement of Residual Stresses in Welded Aluminium 2024 Airframe Alloy. PhD Thesis, The Open University, UK.

[11] Lequeu P., Lassince P., Warner T. and Raynaud G.M. (2001). Engineering for the Future: Weight Saving and Cost Reduction Initiatives. Aircraft Engineering and Aerospace Technology, vol. 73(2), pp. 147-159

[12] Dif R., Bes B., Daniel D., Lassince P. and Ribes H. (2000). Improving the Forming Characteristics of Aluminium Sheets for Aerospace Application. Materials Science Forum, vol. 331-337, pp. 483-488.

[13] ASM (1979). Properties and Selection: Nonferrous Alloys and Pure Metals. Metals Handbook. 9th Edition, vol. 2, Ohio, USA.

[14] Serrano G.L. (2003). Variable Polarity Plasma Arc Welding (VPPA) of 12.5mm Thick AA-2024 T351, AA-7150 T651 and AA-7150 W51. 2nd International Conference on Recent Developments and Future Trends in Welding Technology, Cranfield University.

[15] Santisteban J.R., Daymond M.R., James J.A. and Edwards L. (2006). ENGIN-X: A Third Generation Neutron Strain Scanner, Journal of Applied Crystallography, vol. 39, pp. 812-825.

[16] Fiori F, Albertini G, Girardin E, Giuliani A, Manescu A. and Rustichelli F. (2004). Neutron and Synchrotron Radiation Non-Destructive Methods for the Characterisation of Materials for Different Applications. Journal of Alloys and Compounds, vol. 382, pp. 39-45.

[17] Bragg W.L. (1914). The Diffraction of Short Electromagnetic Waves by a Crystal. Proceedings of the Cambridge Philosophical Society, vol. 17, pp. 43-57.

[18] Pawley G.S. (1981). Unit-Cell Refinement from Powder Diffraction Scans. Journal of Applied Crystallography, vol. 14, pp. 357-361.

[19] DeWald A.T. and Hill M.R. (2006). Multi-Axial Contour Method for Mapping Residual Stresses in Continuously Processed Bodies. Experimental Mechanics, vol. 46, pp.473-490.

[20] Prime M.B. and Hill M.R. (2004). Measurement of Fibre-Scale Residual Stress Variation in a Metal-Matrix Composite. Journal of Composite Materials, vol. 38 (23), pp. 2079-2095.

7.7 Figures

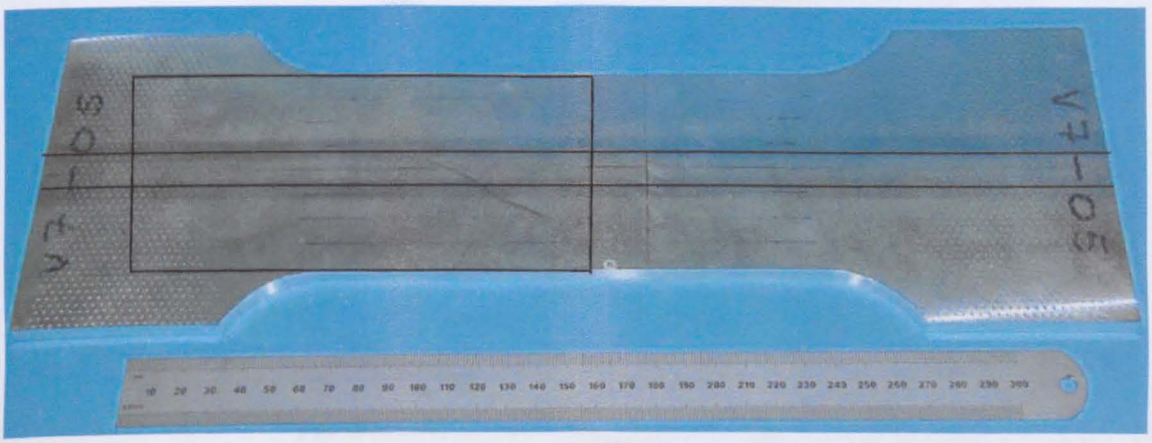

Figure 7.1 A photograph of the "dogbone" sample for the neutron diffraction, the weld line and the machining position of the prismatic block for the multi-axial contour method.

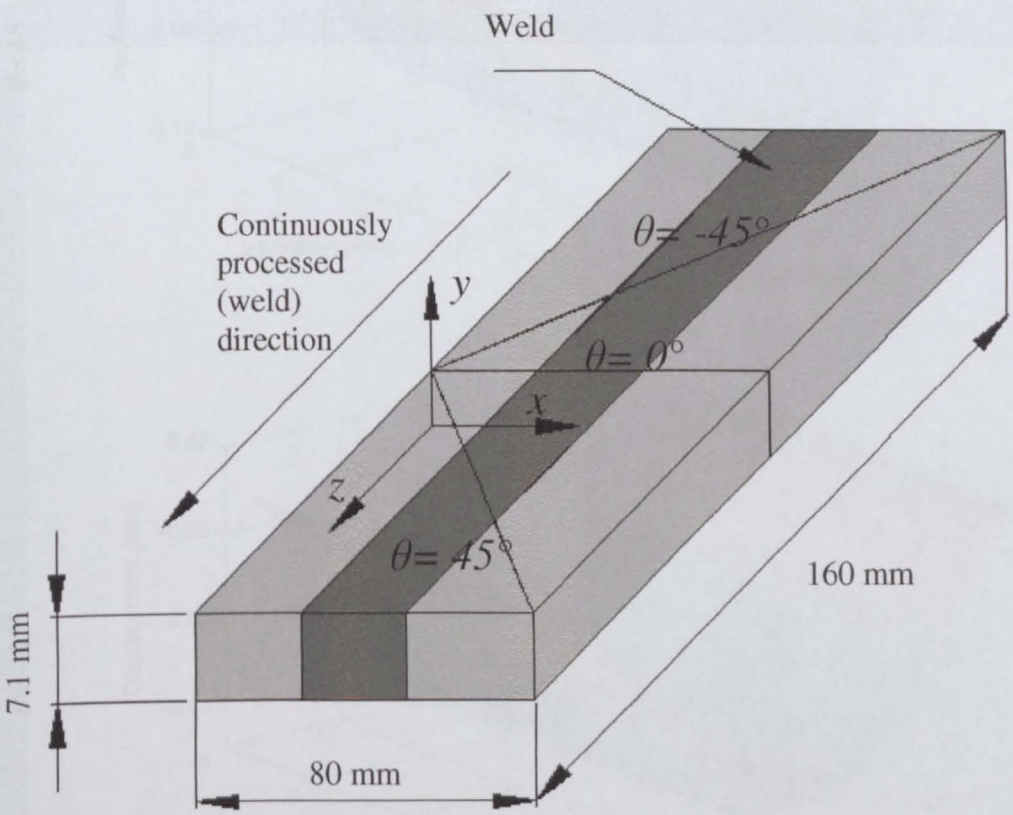

Figure 7.2 VPPA welded 2024-T351 aluminium alloy sample used for multi-axial contour method.

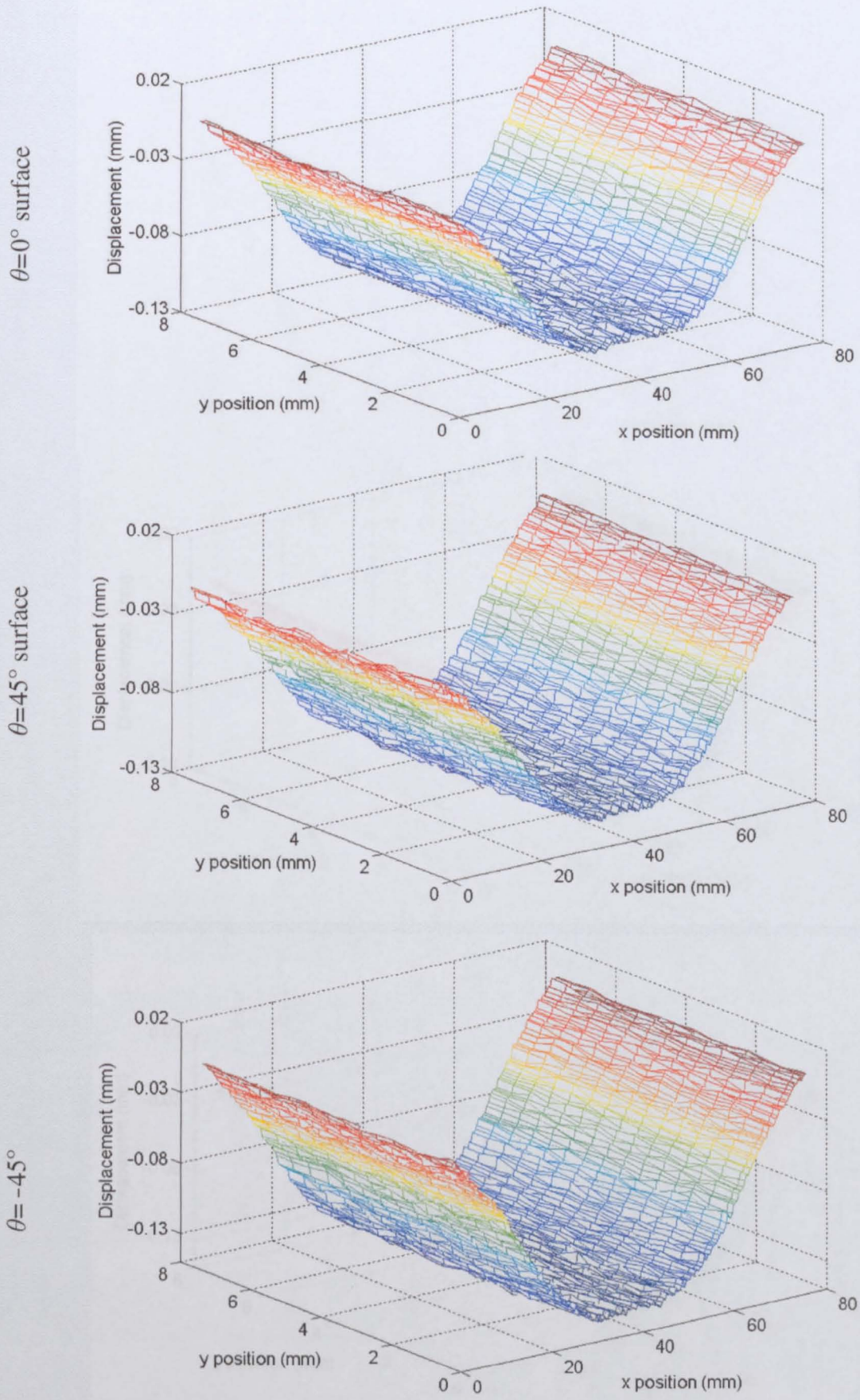

Figure 7.3 Averaged displacement distributions on the $\theta = 0°$, $\theta = 45°$ and $\theta = -45°$ surfaces of the VPPA sample.

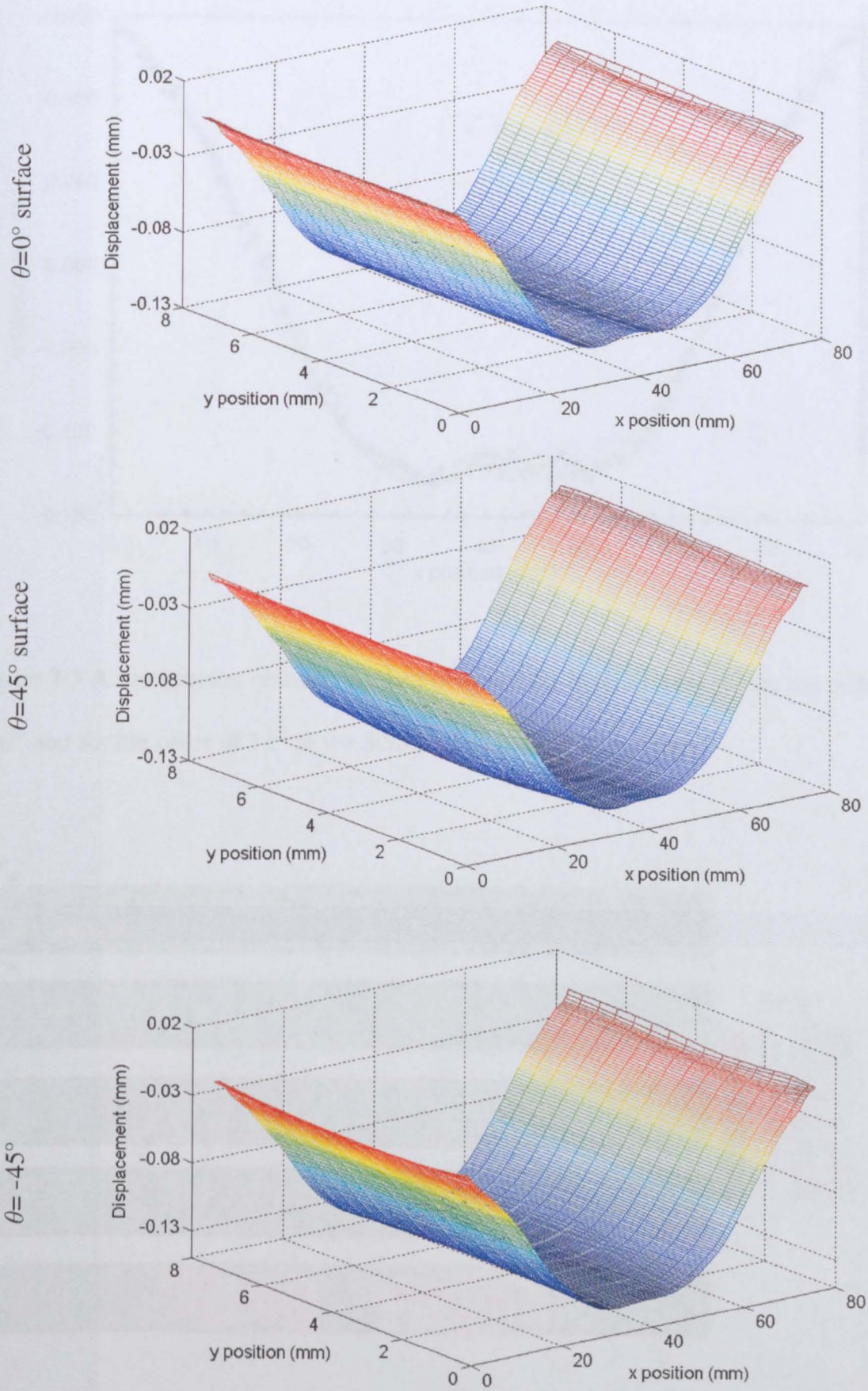

Figure 7.4 Smoothed data as a result of the least squares the $\theta = 0°$, $\theta = 45°$ and $\theta = -45°$ surfaces of the VPPA sample.

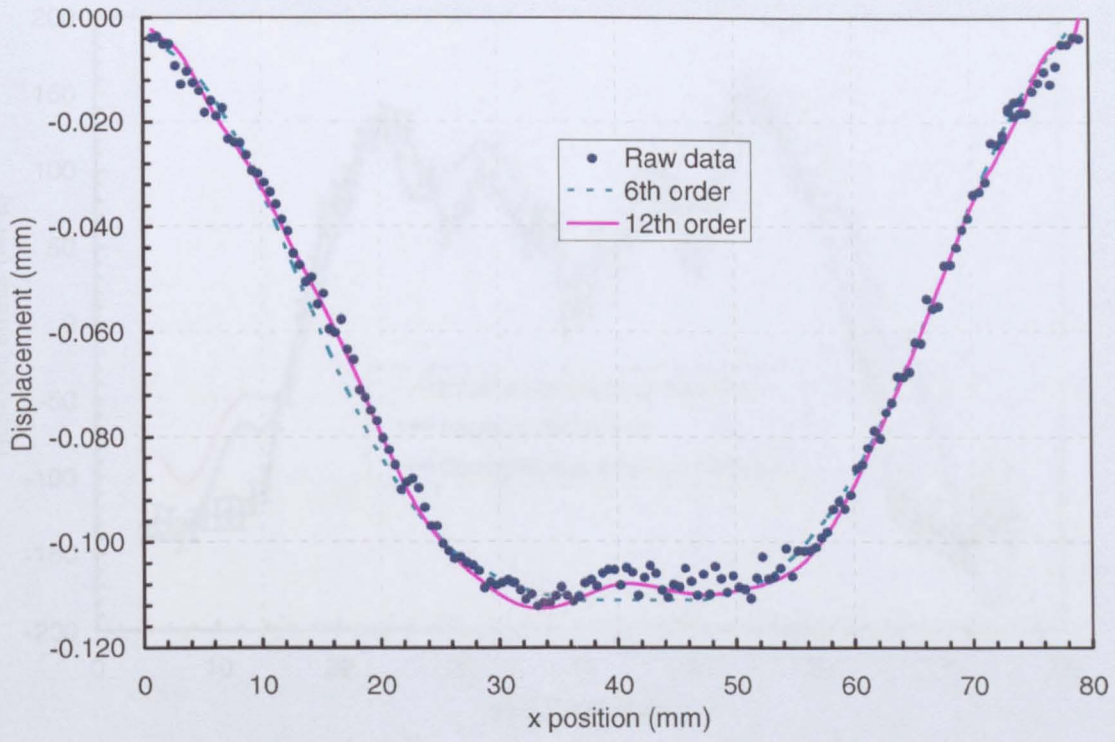

Figure 7.5 A comparison between fit data obtained by inverse solution for the order of 6th and for the order of 12th at $y = 3.55$ mm on the $\theta = 0°$ surface.

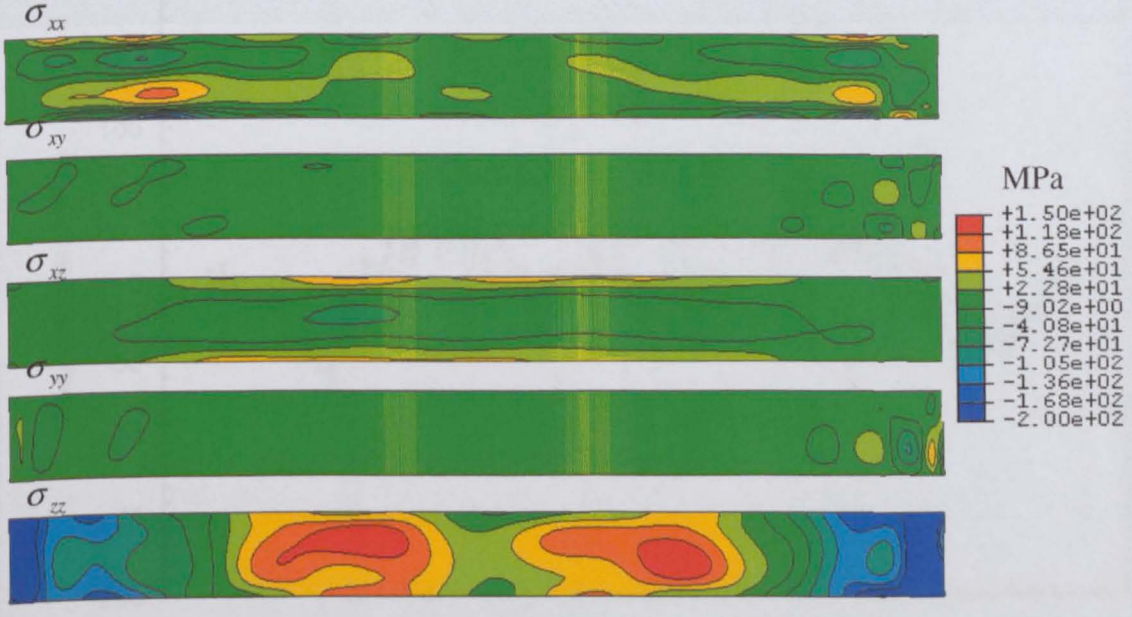

Figure 7.6 Non-zero components of residual stress variation on the $\theta = 0°$ surface for VPPA welded sample.

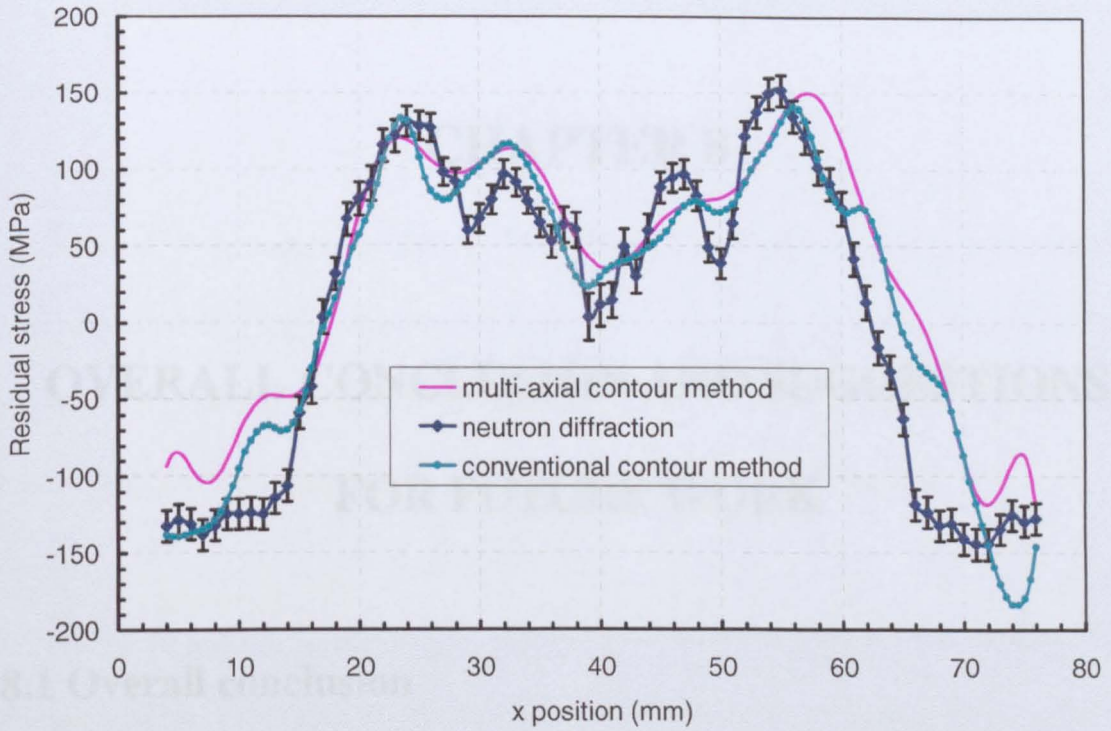

Figure 7.7 Longitudinal residual stress at the $\theta = 0°$ surface along the line $y = 3.55$ mm.

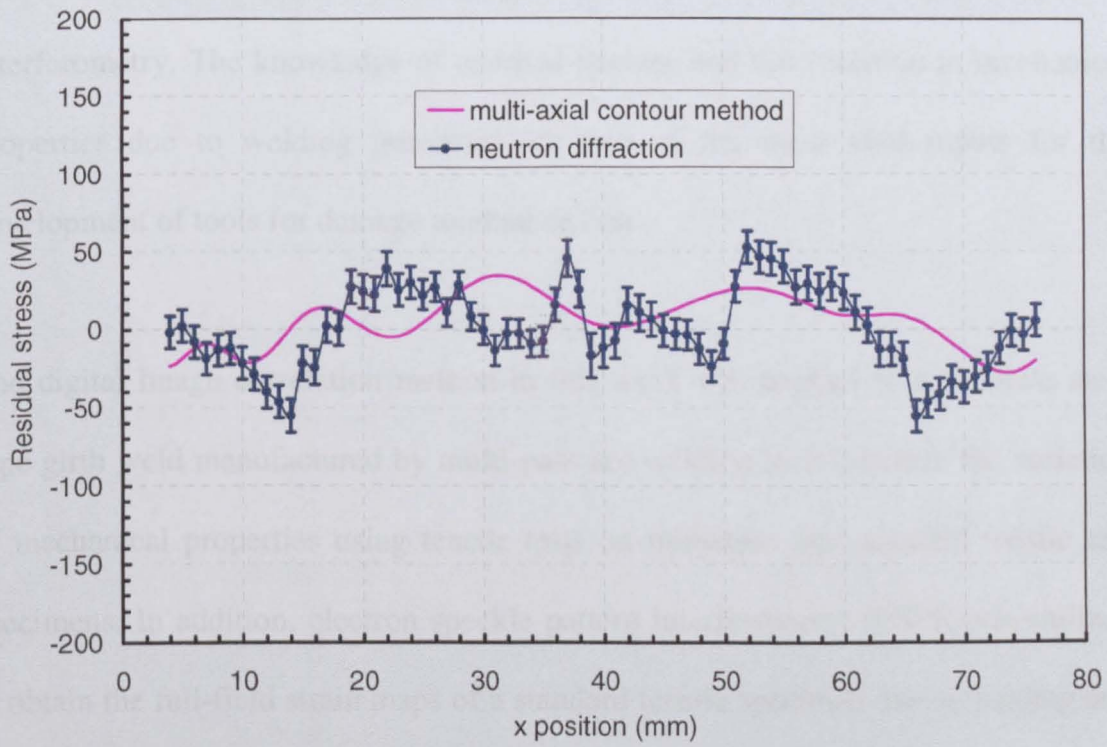

Figure 7.8 Transverse residual stress at the $\theta = 0°$ surface along the line $y = 3.55$ mm.

CHAPTER 8

OVERALL CONCLUSION AND SUGGESTIONS FOR FUTURE WORK

8.1 Overall conclusion

The major aims of this project were to investigate the capability of the contour method to measure the profile of the complete residual stress tensor and to characterize the mechanical properties of welded joints using optical strain measurement techniques: digital image correlation and electron speckle pattern interferometry. The knowledge of residual stresses and the variation in mechanical properties due to welding processes are two of the most vital inputs for the development of tools for damage tolerant design.

The digital image correlation method in this work was applied to a stainless steel pipe girth weld manufactured by multi-pass arc welding to investigate the variation of mechanical properties using tensile tests on miniature and standard tensile test specimens. In addition, electron speckle pattern interferometry (ESPI) was utilized to obtain the full-field strain maps of a standard tensile specimen during loading and compared to those obtained in the same specimen by digital image correlation in

order to see the agreement level between two independent strain measurement methods.

In chapter 5, the principle of the contour method was simulated using both two and three dimensional the finite element methods. In addition, the contour method was applied to 1-pass and 3-pass groove weld specimens and the results obtained by the contour method were compared to those obtained with neutron diffraction.

In chapter 6, the capability of the conventional contour method was numerically investigated to calculate the full residual stress tensor in a body by means of eigenstrain. The experimental exploration of the multi-axial contour method by using the VPPA welded AA2024-T351 alloy was investigated in chapter 7. The overall conclusions drawn from the work shown in the results chapters are presented in the following sections.

8.1.1 The Contour Method

- The numerical and experimental verifications have shown that the conventional contour method has the capability to measure the full cross sectional map of the residual stress component normal to the surface of interest produced by one straight cut.
- It has been demonstrated that the determination of the correct residual stress field can be achieved by averaging the measured displacement field obtained from two halves to cancel out the shear stress effect on the final result.

- The numerical verifications of the contour method in two and three dimensions have demonstrated that residual stress field can be successfully determined even if all components of residual stress or eigenstrain within a body are non-zero.
- The numerical validation of the contour method has shown that use of an initially flat surface in a finite element model to represent the deformed plane gives fairly reasonable results to produce a correct residual stress profile.
- Specimen cutting is the first and possibly the most critical step for the contour method, as the accuracy of the results depends upon the quality of the cut[1].
- Since in most engineering applications, the displacement fields due to relaxation of residual stresses are so small, the accuracy of the contour method depends on the resolution of the displacement measurement machine.
- Data smoothing is vital because any variation in the averaged profile due to surface roughness produces an amplified effect during the calculation of residual stresses. A 3D cubic-spline-based algorithm has been used for fitting the averaged data. Experimental results on 1-pass and 3-pass groove weld specimens have shown that choosing an appropriate knot spacing density is very important. The amount of smoothing in the contour method is chosen by minimizing the uncertainty in the calculated residual stresses. It is expected that there should be an optimum value for interval of the smoothing density. It has been observed that too coarse a knot spacing would fail to capture the features in the surface and too fine a knot spacing would unnecessarily capture noise in the data. In this work, the amount of smoothing was selected by manual judgement.
- It has been found that the contour method results for data smoothed with a 5×5 mm cubic spline density gave the optimum residual stress measurement for both 1 one and 3 pass groove weld specimens.

- Tensile residual stresses in the weld region of the 1 pass and 3 pass specimens have been measured as 250 MPa and 350 MPa respectively.
- Comparisons between the contour method and the neutron diffraction technique have shown good general agreement, increasing the level of confidence for these measurements.
- One of the main limitations with the contour method is that only one residual stress component normal to the cut plane can be measured.

8.1.2 The Multi-Axial Contour Method

- This work shows that the multi-axial contour method has the potential capability to determine the original complete residual stress tensor on the first cut plane of interest.
- The motivation for using eigenstrain to determine residual stresses in the contour method is that the eigenstrain remains constant upon the redistribution of residual stress. Hence, any change in the geometry of a body alters the residual stress distribution but not the eigenstrain. Thus, multiple cuts can be made without changing the eigenstrain distribution.
- Since the multi-axial contour method requires the inverse solution technique and a least squares process to provide a fit to the data, there is no need to smooth the averaged data obtained from the CMM measurement.
- A Legendre polynomial, whose higher order terms (i.e. two and more) automatically satisfy equilibrium, was used in order for the unknown eigenstrain components to be expressed as sum of basis functions.

- Numerical verifications of the multi-axial contour method on two and three dimensional bodies have shown that the Legendre polynomials provide sufficiently accurate results even in the case of choosing non-polynomial eigenstrain variations.
- The numerical validation on a three dimensional prismatic block has demonstrated that only three components of the eigenstrain (ε_{xx}^{*}, ε_{zz}^{*} and ε_{xz}^{*}) were sufficient to create a compliance matrix to obtain highly accurate results. This is due to the fact that these three components contribute the most to the residual stresses in a body.
- The multi-axial contour method was applied to a VPPA welded sample and results were compared with the neutron diffraction results. Very good agreement between the two independent techniques was found, especially for the residual stress in the longitudinal direction. Because of the low transverse stresses in the chosen specimen, the validation is more subtle than it might have been in an optimal application. It may be that the inverse procedure makes the uncertainties larger for the non-longitudinal stresses, which has been observed before with eigenstrain series expansion [2].
- The principle of the multi-axial contour method dictates that the eigenstrain in one of the principle direction is constant in order to simplify the calculations. This is not a major drawback, as many engineering products are continually processed, such as by cold rolling or welding. However, the multi-axial contour method requires considerably more computational time.

8.1.3 High Resolution Strain Mapping Using Digital Image Correlation Technique

- Strain mapping has been shown to be an effective way of determining the mechanical properties of the material across the welded region.
- It has been found that digital image correlation is a powerful technique, and with the use of high resolution optical setup, very accurate full field strain variations can be obtained with materials having heterogeneous properties.
- Tensile properties in different regions of a girth weld in a stainless steel pipe obtained using micro tensile test specimens have been found to be in good agreement with those determined by full field strain mapping on a standard tensile specimen whose gauge contained all the regions of the weld.
- Experimental results have demonstrated that the tensile properties of the stainless steel pipe girth weld were affected by the welding process over a large area around the weld centre.
- It has been found that the most heterogeneous region of the cross-weld specimens were in and around the weld part where the tensile properties of the material change dramatically at every millimetre.
- Small differences between the results obtained from the cross-weld specimen and micro tensile specimens may be due to the fact that the micro-sample cut out from the weld in longitudinal direction can be elongated freely under the plastic deformation. In contrast, in the standard sample, the surrounding material may constrain the weld material under constraint and not allow it to elongate freely.

8.2 Suggestions for Future Work

The multi-axial contour method appears to be a very promising technique. Since the first experimental verifications of this method appear to have been done in this work in the literature, there are many potential applications for the multi-axial contour method to be useful.

Since EDM cutting is the first and hence probably the most important step for implementation of both conventional and multi-axial contour methods, some experimental issues may be investigated. As can be seen from the multi-axial contour method results on the VPPA sample where the contour results are higher than the neutron results, this difference might be due to the fact that during specimen cutting from one side, there may be local deformation ahead of the cutting wire as a result of the local stress relaxation, which alters the width of the cut and introduces some error into the final stress values. Therefore, it would be useful to investigate this effect using stress-free specimen cutting and applying the conventional contour method. In this way, any residual stresses that are measured will be due to the local stress relaxation.

Legendre polynomials have been used for the inverse solution problem in the multi-axial contour method. Perhaps another series expansion rather than the Legendre polynomials such as a Fourier series would provide a better fit for the measured displacement. Hence, it would be interesting to apply the multi-axial contour method by using different series expansions and compare the results.

For the numerical verifications of the multi-axial contour method, a non-polynomial eigenstrain variation has been used as known values. It would be very informative to model more realistic cases for the numerical verifications. For instance, if residual stresses in a welded joint are to be experimentally determined by the multi-axial contour method, then the corresponding welding process can be modelled instead of using arbitrary eigenstrain variation for the numerical verification of the multi-axial contour method prior to numerical cutting process. In this manner, the numerical verification of the multi-axial contour method can be directly compared with the experimental results. This example can be given for the quenching process where the quenching process can be modelled using Finite Element at first, and numerical verification of the multi-axial contour method can be correlated with experimental results.

Incremental hole drilling method would be a very good choice to validate the multi-axial contour results experimentally. However, since rosette strain gauges are used for experiments in hole drilling, there may be some experimental errors stemming from strain gauges. Therefore, it would be very interesting if optical techniques such as digital image correlation or electronic speckle pattern interferometry could be used to measure strains in hole drilling experiments [3-4]. In this way, optical methods can eliminate the majority of experimental errors caused by temperature change, installation of the strain gauge, the measurement of the hole diameter, etc.

It would be very informative to provide an estimate of uncertainty in the experimental multi-axial contour results. The technique used by Prime and Hill [5] is applicable to such an eigenstrain method. It may be that the inverse procedure

makes the uncertainties larger for the non-longitudinal stresses, which has been observed before with eigenstrain series expansion [2]. Since uncertainty is always important for experimental measurements, it would be worth pursuing the issue further.

Although the multi-axial contour method is a powerful technique in many aspects, it requires great computational effort. If computing cost is taken into account, the multi-axial contour method should only be applied on samples which fully satisfy the assumption of this technique.

8.3 References

[1] Cheng W., Finnie, I., Gremaud, M. and Prime, M.B. (1994). Measurement of Near Surface Residual Stresses Using Electric Discharge Wire Machining. Journal of Engineering Materials and Technology, vol. 116 (1), pp. 1–7.

[2] Prime M.B. and Hill M.R. (2004). Measurement of Fiber-Scale Residual Stress Variation in a Metal-Matrix Composite. Journal of Composite Materials, vol. 38(23), pp. 2079-2095.

[3] Schajer G.S. and Steinzing M. (2005). Full-Field Calculation of the Hole Drilling Residual Stresses from Electronic Speckle Pattern Interferometry Data. Experimental Mechanics, vol. 45(6), pp. 526-532.

[4] Steinzing M. and Ponslet E. (2003). Residual Stress Measurement Using the Hole Drilling Method and Laser Speckle Interferometry: Part I. Experimental Techniques, vol. 27(3), pp. 43-46.

[5] Prime M.B. and Hill M.R. (2006). Uncertainty, Model Error, and Order Selection for Series-Expanded, Residual-Stress Inverse Solutions. Journal of Engineering Materials and Technology, vol. 128(2), pp. 175-185.